Starfixers, Inc.

Final Report

Design Synthesis Exercise
Group 9

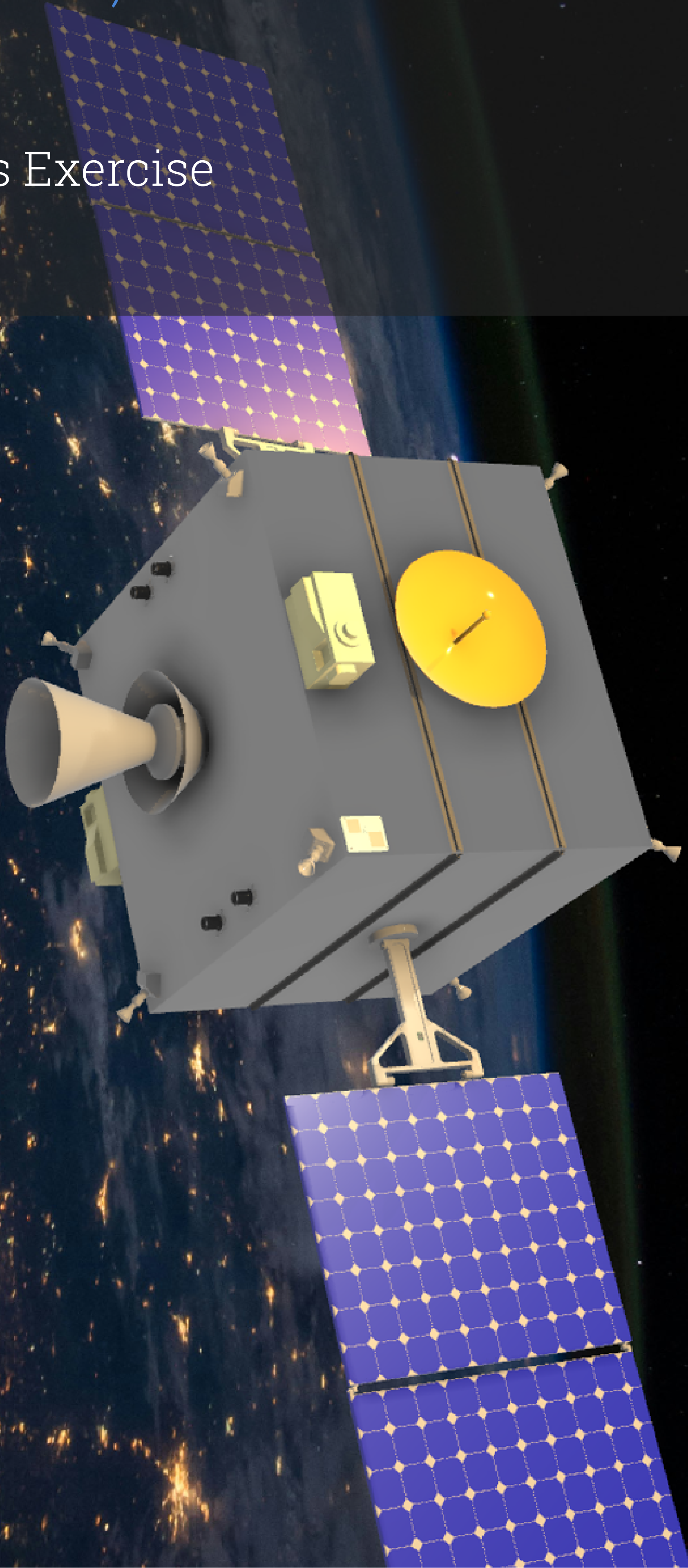

Delft University of Technology

Starfixers, Inc.

Final Report

Group 9

Viktor Zupnik	5708338
Mats den Hartog	5414296
Bastiënne Visser	5545684
Louise Brouwers	5805961
Sibylle Lekens	5444594
Wybe Mijnendonckx	5769094
David Adell Cortés	5799821
Dimitrios Zafeiriou	5681308
Douwe Vis	5273315
Carolina Castro	5482259

The team would like to express sincere gratitude to our tutor and coaches, Steve Gehly, Prem Sundaramoorthy and Mario Badas Aldecocea for their continuous guidance, insightful feedback and encouragement throughout this project. Their support was invaluable in helping Starfixers Inc. navigate complex challenges and deepen our understanding of the Active Debris Removal topic.

We also wish to thank the following individuals for their time and helpful input during various stages of our work: Thomas Kaempfe, Joao De Teixeira da Encarnacao, Rens van der Zwaard, Michel van Pelt, Stefano Speretta, Jeanne Longlune and Calvin Rans.

Tutor:	Steve Gehly
Coaches:	Prem Sundaramoorthy & Mario Badas Aldecocea
Date:	June 18, 2025
Faculty:	Faculty of Aerospace Engineering, Delft

Cover: Canadarm 2 Robotic Arm Grapples SpaceX Dragon by NASA under CC BY-NC 2.0 (Modified)
Style: TU Delft Report Style, with modifications by Daan Zwaneveld

Contents

Nomenclature

Abbreviations

Abbreviation	Definition	Abbreviation	Definition
AC	Accomodation Coefficient	GEO	Geostationary Earth Orbit
ACPL	Accepted Collision Probability Level	GN&C	Guidance, Navigation and Control
ADCS	Attitude Determination and Control System	GNSS	Global Navigation Satellite System
ADR	Active Debris Removal	GSE	Ground Service Equipment
ADOS	Application of Design and Operation Standards	HAS	High Accuracy Service
AIT	Assembly, Integration and Test	HCA	Half Cone Angle
AMoI	Moment of Inertia	HMU	Health Monitoring Unit
BPSK	Binary Phase Shift Keying	IADC	Inter-Agency Space Debris Coordination Committee
C&DH	Command and Data Handling	IMU	Inertial Measurement Unit
CIC	Cell-Interconnect-Coverglass	ISA	International Standard Atmosphere
CNA	Computer Network Architecture	LASA	Low Earth Orbit
CoM	Centre of Mass	LCA	Life Cycle Assessment
COLA	Collision On Launch Assessment	LOOS	Launch and On-Orbit Support
COPUOS	Committee on the Peaceful Uses of Outer Space	LVDS	Low Voltage Differential Signalling
COTS	Commercial Off-The-Shelf	MAI	Manufacturing, Assembly, Integration
CPU	Central Processing Unit	MDT	Mean Down Time
CR	Command Receiver	MEO	Medium Earth Orbit
DC	Direct Current	MLI	Multi-Layer Insulation
DIT	Detectability, Identification and Tracking	MMoI	Mass Moment of Inertia
ECC	Error Correction Code	MPPT	Maximum Power Point Tracking
ECOB	Environmental Consequences of Orbital Breakups	MPMT	Mean Preventive Maintenance Time
EMI	Electromagnetic Interference	MTBF	Mean Time Between Failures
EoL	End of Life	MTBM	Mean Time Between Maintenance
EPS	Electrical Power Subsystem	MTTR	Mean Time To Repair
ESA	European Space Agency	MTTM	Mean Time To Maintain
ESG	Economic, Social and Governance	NASA	National Aeronautics and Space Administration
FDIR	Fault Detection, Isolation, and Recovery	OASPL	Overall Sound Pressure Level
FEM	Finite Element Method	OBC	On-Board Computer
FPGA	Field-Programmable Gate Array	P2P	Point-to-Point
FOV	Field Of View	Pc	Collision probability

Abbreviation	Definition	Abbreviation	Definition
PCU	Power Control Unit	SF	Safety Factor
PECL	Positive Emitter Coupled Logic	SMAD	Space Mission Analysis and Design
PMD	Post Mission Disposal	SNR	Signal-to-Noise Ratio
QPSK	Quadrature Phase Shift Keying	SSA	Space Situational Awareness
RAMS	Reliability, Availability, Maintainability, Safety	SSD	Solid-State Drive
R&D	Research & Development	SSR	Space Sustainability Rating
RDT	Requirements Discovery Tree	SWOT	Strengths, Weaknesses, Opportunities and Threats
RDV	Rendezvous	TLE	Two-Line Element
ROI	Return on Investment	TRL	Technology Readiness Level
RMS	Root Mean Squared	TT	Telemetry Transmitter
RPM	Revolutions per Minute	TT&C	Telemetry, Tracking and Command
RTOS	Real-Time Operating System	UN-OOSA	United Nations Office for Outer Space Affairs
SEU	Single-Event Upset	V&V	Verification and Validation

Symbols

Symbol	Definition	Unit
A	Area	[m^2]
a	Acceleration	[m/s^2]
a_{sm}	Semi-major axis	[m]
B	Bandwidth	[Hz]
BS	Buffer Size	[bits]
c	Distance to Neutral Axis	[m]
C_d	Drag Coefficient	[-]
d	Distance	[m]
D	Pixel Depth per Frame	[bits]
DR	Data Rate	[bits/s]
E	Modulus of Elasticity	[Pa]
FR	Frame Rate	[fps]
F	Force	[N]
g_0	Standard Gravity Acceleration	[m/s^2]
h	Altitude	[m]
H	Angular Momentum	[N]
I	Mass Moment of Inertia	[kg·m^2]
I_A	Area Moment of Inertia	[m^4]
I_{sp}	Specific Impulse	[s]
J	Radiation Intensity	[W/m^2]
k	Stiffness	[N/m]
L	Length	[m]
L_s	Latency	[ms]
M	Mass	[kg]
M_b	Bending Moment	[Nm]

Symbol	Definition	Unit
M_m	Molar Mass	[g/mol]
M_t	Number of Momentum Transfer Manoeuvres Per Debris	[-]
$\dot{m}$	Mass Flow	[kg/s]
N	Number of Debris Objects to be De-orbited	[-]
N_p	Number of Pixels per Frame	[-]
O/F	Oxidiser-Fuel Ratio	[-]
p	Pressure	[Pa]
P	Power	[-]
Q	Heat Energy	[J]
r	Radius	[m]
R	Reliability	[-]
S_r	Relative Distance	[m]
t	Time	[s]
t_w	Wall Thickness	[m]
T	Temperature	[K]
$T_{2\pi}$	Period	[s]
V	Velocity	[m/s]
v	Volume	[m^3]
W	Width	[m]
X	Total Amount of Orbits	[-]
α	Angular Acceleration	[rad/s^2]
α_{ro}	Filtering Roll-off Factor	[-]
α_s	Absorptivity	[-]
ΔV	Delta V	[m/s]
ϵ	Strain	[-]
ϵ_s	Emissivity	[-]
η	Efficiency	[-]
μ	Standard Gravitational Parameter	[m^3/s^2]
ν	Poisson Ratio	[-]
ω	Angular Velocity	[rad/s]
ϕ	Orbital Phase	[rad]
ρ	Mass Density	[kg/m^3]
σ	Stress	[Pa]
τ	Torque	[Nm]
θ	General Angle	[rad]

Summary

The rapid launch and growth of satellite constellations such as Starlink and OneWeb have led to a concerning rise in the number of objects in Low Earth Orbit (LEO), increasing the risk of collisions and worsening the space debris problem. This development resulted in a mission need statement for Starfixers, Inc:

> ”The growing number of satellites and space debris in Earth’s orbit is increasing collision risks and threatening the sustainability of space operations. To preserve a safe and stable orbital environment, there is a pressing need for active debris removal missions capable of targeting multiple objects efficiently.”

This mission need resulted in the following Project Objective Statement:

> Design an active debris removal mission to de-orbit a minimum of 10 spacecraft in one year from LEO orbits between 550-630 km altitude within a budget of €100 million, by 10 students in 10 weeks full-time.

While the global increase in space missions and constellations poses risks, it also provides an opportunity. The growing interest in the space industry is drawing greater attention to the severity of the space debris problem. This global rise in space responsibility and accountability creates a strong demand for Active Debris Removal (ADR) and hence a market.

Market Analysis and Opportunity

Although the enforcement mechanisms are limited for international guidelines on space sustainability, it provides the global baseline for responsible behaviour. As a result, national space authorities can establish more binding regulations. Currently, regulations and insurance companies increasingly require satellite de-orbit plans, especially for mega-constellations and government agencies. Considering the size of current mega-constellations, their operators have the highest potential of being ADR clients.

The ADR market is still in its early phase and obligations for ADR are not truly developed yet. Nonetheless, entities such as ESA, Lockheed Martin and the United States Space Force invested hundreds of millions of Euros in ADR startups. The market size is rapidly expanding and is expected to grow from its €1.13 billion size to €4.76 billion by 2032.

Starfixers Inc. targets this market at the dawn of its development, offering flexible, multi-target removal of uncooperative debris in crowded LEO. Despite current challenges like worldwide funding and legal enforcement of space sustainability, increasing regulatory pressure and market needs make ADR a potentially lucrative, growing opportunity.

Starfixers, Inc. stands out from other ADR startups due to its capability of de-orbiting a higher number of targets, both cooperative and non-cooperative. This allows for a higher flexibility of targets and makes Starfixers, Inc. an attractive option for clients with varying space debris objects.

Besides strengths, the mission also has weaknesses, opportunities and threats. For a full understanding of the mission potential, a SWOT analysis was performed:

- Strengths - Early mover advantage, cost-conscious design and promoting of environmental sustainability

- Weaknesses - Reliance on public sector and limited mission capacity of 10 targets per year which may not meet demand growth
- Opportunities - Market gap and scaling potential for parallel systems and higher removal rates
- Threats - Legal barriers, emerging competition from larger companies and funding gaps

Mission Design and Concept of Operations

The mission consists of a single spacecraft, capable of performing multiple active debris removal operations during its lifetime. It will be the first ADR spacecraft to de-orbit multiple targets as well as become the first in-space application of the method known as gas shepherding. In gas shepherding, the spacecraft uses its main thruster to direct a controlled plume of exhaust at uncooperative debris targets. This thrust transfers momentum to the debris, gradually reducing its orbital energy and lowering its altitude until atmospheric drag becomes sufficient to ensure rapid reentry and complete burn-up in Earth's atmosphere.

The mission begins with launch and orbit insertion into an orbit identical to that of the target debris, within the 550–630 km range. The spacecraft then performs sequential rendezvous and close proximity operations until at least 10 (defunct) satellites are de-orbited. For the simulations and calculations in this report, the targets were assumed to be 10 Starlink V1 satellites at 600 km altitude due to being a majority in LEO compared to other satellites or debris bodies, especially when considering future constellation deployment trends. Each target is first observed using the spacecraft's GN&C sensors, and the ADCS aligns the spacecraft for optimal operational positioning. The debris shall approach the spacecraft with a calculated ideal relative velocity of up to 8 m/s, to maximise the contact time between the thruster plume and the debris while maintaining a minimum safety distance of 3m. At a distance of 9m, the main thruster is activated, gradually slowing the target's orbit while accelerating the spacecraft itself until their relative distance is larger than 9m again. Of course, the momentum imparted on the debris per rendezvous heavily depends on the efficiency of the momentum transfer and only lasts up to 6 seconds. Hence, multiple rendezvous are required to lower a target's orbit to an altitude of 381km, leading to a total number of 153 rendezvous for 10 targets.

To perform all these momentum transfers and gradually lower the perigee of the debris, a detailed orbital operational procedure was defined. After each interaction, the spacecraft will assess if enough ΔV was applied to the debris and whether or not they should meet again. Between two rendezvous, the ADR spacecraft will adapt its orbit to be able to meet with the target after two orbits from the last rendezvous. Eventually, when a debris is de-orbited, it will align with the next debris by correctly timing this next transfer. This procedure will be repeated until all debris are safely de-orbited. It is important to note that the operational timeline spans one year, including initial commissioning, target acquisition, and de-orbit operations. Therefore, the spacecraft will perform all its manoeuvres within the first two months after which all targets will use the remaining time to passively de-orbit within the next nine months due to atmospheric drag. In addition, the analysis accounted for external factors such as atmospheric drag, possible tumbling behaviour of the debris and collision avoidance manoeuvre which may affect mission performance. Moreover, the adaptability of this mission was assessed and an sequence optimisation tool was developed.

Risk and Reliability

To improve the design of the spacecraft and mission operations, an extensive list of risks was developed. Each risk was assessed on its likelihood of occurring and the severity of the consequences. Based on this, mitigations and contingencies were constructed to minimise severe consequences. All these aspects are presented in a risk bow-tie diagram and were taken into account for the rest of the design process.

Technical Subsystems Summary

Each subsystem has been developed in detail to support the mission operations and sustainability goals.

The GN&C subsystem consists of multiple sensors: a GNSS receiver and antennas to obtain an accurate orbit position knowledge within 20cm, two narrow field of view infrared cameras for long-range debris tracking, two wide field of view infrared cameras for close proximity livestreaming and two LiDAR sensors. The LiDAR sensors are crucial for measuring the relative attitude and motion of the debris to ensure safe rendezvous and de-orbiting operations.

The ADCS is closely connected to the GN&C subsystem, and is responsible for the spacecraft's attitude determination and control. It consists of two star trackers, four sun sensors, two inertial measurement units, four reaction wheels and eight cold nitrogen gas thrusters. The nitrogen gas thrusters allow for rotational and translational adjustments during rendezvous.

The main thruster on the spacecraft is a 465 N bi-propellant vectored thruster designed by researchers at the University of Padova. It will make use of H_2O_2 and kerosene as propellant, which is both green and non-toxic. To increase the efficiency of the momentum transfer and maximise the contact between plume and target, the thruster shall have a narrow half-cone angle of <15 degrees. The adverse thruster, mentioned above, is a smaller version of the main thruster and is mounted opposite to it (symmetrically) to enable fine velocity adjustments to optimise relative speed with regard to the debris.

The electrical power subsystem was developed by analysing the power requirements during each phase of the mission. The EPS will provide power, making use of two 0.76m x 1.28m solar arrays, capable of generating over 424W during daylight and a battery pack of 56 small Li-ion batteries to accommodate operations during eclipse. Moreover, a power control unit is on board to ensure the power flows correctly between destinations, and a maximum power point tracker maximises the power output of the solar panels.

For communications with Earth, stations from the ESA Estrack Network's core and cooperative ground networks were selected. Telemetry and command functions will operate through a shared dual S-band antenna while the LiDAR data and infrared images are transmitted via X-band. To ensure a live downlink of the wide field of view infrared camera, the momentum transfer operations have to take place while in direct contact with a ground station, or the spacecraft will have to relay communications with other satellites.

The C&DH subsystem handles all data and command flow within the spacecraft and consists of the following key modules: onboard computer, data storage unit, health monitoring unit, command receiver and telemetry transmitter. Data will be collected and either stored in a NAND Flash card, for later transmission to the Ground Segment or passed through an SRAM unit for live transmission, after which it will be deleted. Considering that the Starfixers' mission is a data-heavy mission, comprising many different information paths and subsystem dependencies, a very reliable and concrete C&DH subsystem is required, and therefore designed.

The spacecraft bus is an aluminium 7075-T6 rectangular prism bus with dimensions 1000x1000x823 mm^3, which is optimised for mass efficiency and launch survivability. The four cylindrical bi-propellant fuel tanks serve as pillars and carry axial loading through an outside cylindrical connector. Additional strength is provided by stiffeners and lateral rods between the tanks. Thermal control is achieved passively through surface coatings and multi-layer insulation. A detailed thermal analysis ensured all components remain within operational limits during both eclipse and daylight phases. Radiation shielding is provided by 3 mm bus walls that guarantee an acceptable radiation environment throughout the mission.

Python code for significant calculations can be seen in Final Branch of Starfixers Inc. Repository. All subsystems and components combined, the spacecraft has a final total mass of 646kg, consisting of

263.9kg of dry mass and 382.1kg of fuel. The values include a 10% safety margin on the dry mass and a fuel margin that allows for a single additional de-orbiting. The structural layout of the spacecraft is presented in Figure 1.

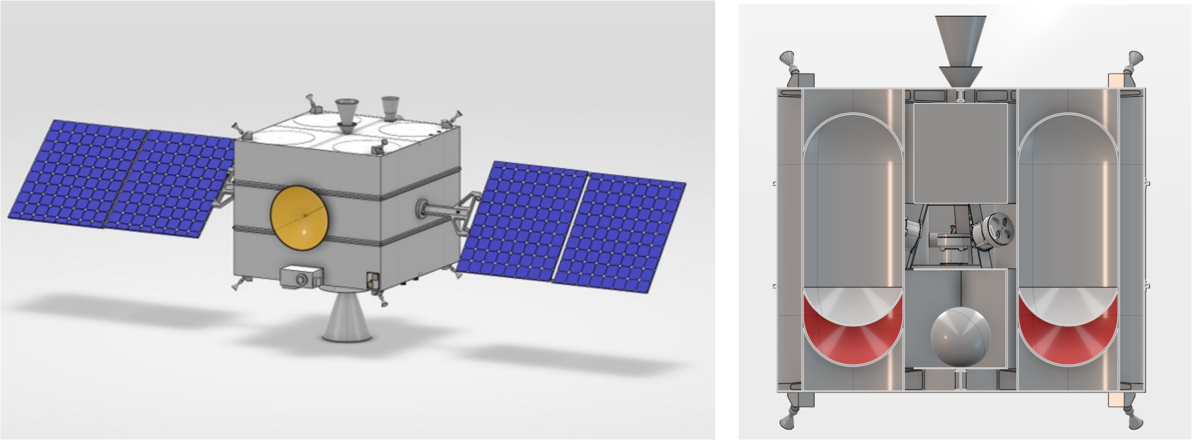

(a) 3D Render of the Starfixer Spacecraft.

(b) Cross Section of the Starfixer Spacecraft.

Figure 1: Structural Layout.

Verification, Validation and Sustainability

All requirements have been verified by one of the following methods: testing, inspection, demonstration, analysis or comparison. The programs and codes that were used to design the current spacecraft have also been thoroughly verified, and while not all have been validated, a detailed validation plan has been set. Moreover, a sensitivity analysis has been performed to investigate the effect of changing the user requirements on the outcome of the design.

Regarding sustainability, the mission's purpose is to contribute to space sustainability and remove space debris. The current design achieves a platinum space sustainability rating as well as a bonus gold star based on its high levels of data sharing, communication and manoeuvrability in case of collision avoidance manoeuvres.

The mission will remain within a €100 million budget, of which 15% is allocated as reserve. While this mission serves as a demonstration of the gas shepherding concept and its ADR potential, future missions will be less expensive, as non-recurring costs drop. For the current budget, it is estimated that 60% will be recurring costs and 40% are non-recurring. This significantly improves the scalability of future missions at a unit cost of €7.2 million per de-orbit.

Future Development

The future development of the ADR satellite was also addressed through a detailed RAMS analysis, examining its reliability, availability, maintainability, and safety aspects. In addition, a Manufacturing, Assembly, and Integration Plan was created, outlining the key processes and strategies for building and assembling the satellite. A forward-looking development plan was also proposed, describing the intended approach for continuing the satellite's technical advancement beyond the current project phase.

This mission will be the first multi-target active debris removal spacecraft and perform the first in-orbit gas-shepherd manoeuvre, pioneering this novel ADR technique. By maintaining low cost, high flexibility, and sustainability in every aspect of the mission, Starfixers, Inc. stands at the dawn of a new era of sustainable space.

1 Market Analysis

This chapter will explore the market for Starfixers Inc.'s project, highlighting key drivers such as demand and regulation for the design. Section 1.1 will explain the problem of space debris, while Section 1.2 will delve deeper into how regulations and laws drive the design process. Then, potential customers for the service will be identified in Section 1.3 and the market size will be estimated in Section 1.4, followed by an evolution of this technology for the future. The competitive aspect of this new technology will be discussed in Section 1.5, while Section 1.6 will explain how market requirements drive the design. Section 1.7 and Section 1.8 will discuss the user requirements and SWOT (Strengths, Weaknesses, Opportunities and Threats) analysis, respectively.

1.1 Orbital Congestion and its Risk

The most recent report from the European Space Agency (ESA)[1] on orbital debris identifies 14 050 satellites currently in orbit, with approximately 11 200 remaining operational, leaving 2 850 defunct satellites drifting without an active de-orbit plan. This debris poses significant risks to future missions. Many of these satellites reside in Low Earth Orbit (LEO), but also in Medium Earth Orbit (MEO), Geostationary Orbit (GEO) and also highly elliptical orbits. The continuous growth in the number of satellite launches, as shown in Figure 1.1, reinforces the urgent need for responsive and flexible debris removal missions, especially at LEO, where the orbits are the smallest and are considered among the most useful and valuable due to their suitability for a wide range of space missions [21].

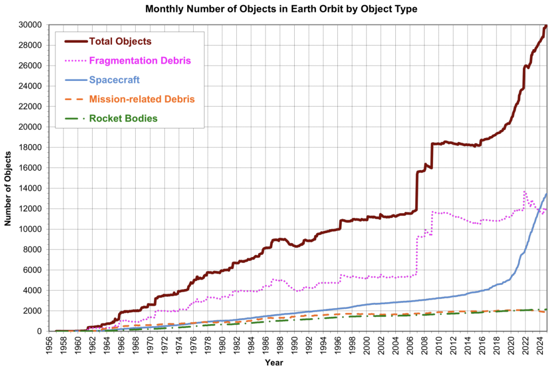

Figure 1.1: Monthly Number of Catalogued Objects in Earth Orbit by Object Type as of 9 January 2025. This chart displays a summary of all objects in Earth orbit officially catalogued by the U.S. Space Surveillance Network [74].

The space debris problem has worsened due to the launch of satellite constellations deployed by companies such as SpaceX (Starlink), Qianfan (SSST), and Amazon (Kuiper), among others. Even though SpaceX did establish procedures for de-orbiting their satellites[2], the large number of launched units (almost 9000 in June 2025 [3]) makes it inevitable that some will fail despite the best contingency measures. The likelihood of collisions between inactive satellites and other objects in space, therefore, continues to grow. This issue calls for the development of Active Debris Removal (ADR) systems.

---

[1] `https://www.esa.int/Space_Safety/Space_Debris/ESA_Space_Environment_Report_2025`

[2] `https://shorturl.at/aPdvZ`

[3] `https://planet4589.org/space/con/star/stats.html`

For a better understanding of the long-term consequences of orbital debris growth, NASA used Monte Carlo simulations to predict debris evolution over the next century under varying scenarios of PMD effectiveness. The analysis, visualised in Figure 1.2, emphasises that maintaining a PMD success rate of 99.9%, which is very high, is essential to limit large debris accumulation. A success rate lower than this threshold would lead to a significantly higher debris population, which intensifies collision risks and further escalates the demand for an ADR service. Currently, no functional ADR system has been deployed. Furthermore, most of the developing systems are cost-inefficient and must be custom-designed for each individual debris.

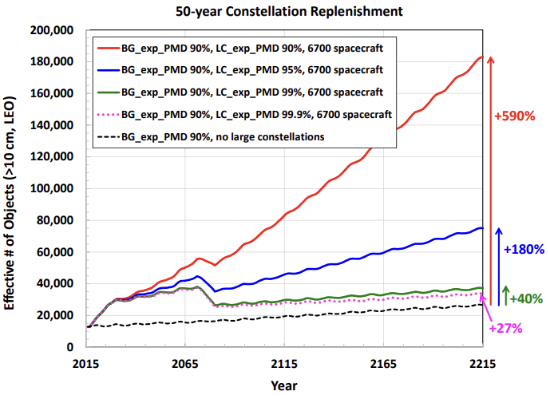

Figure 1.2: Results From Large Constellation (LC) Scenarios Where the LCs Maintain Full Operations With Spacecraft Replenishment for 50 years [73].

The Starfixers Inc. mission will operate in the LEO region due to its high satellite density and importance for space operations. Additionally, most of the new mega-constellations are planned to be launched in LEO[4]. However, existing Post-Mission Disposal (PMD) strategies struggle to maintain debris control and orbital safety. The cluster of inactive objects within constellations is steadily growing, and ESA estimates a high number of constellation satellites as well as miscellaneous small satellites at a 500 km altitude (Figure 1.3), highlighting an expanding market opportunity for Starfixers Inc. to provide services for targeted debris removal in an orbital region that is highly congested.

Starfixers Inc. will operate in LEO, where satellite density is highest and the region plays a critical role in space operations. Most planned mega-constellations are also expected to be deployed in this orbital region. However, current PMD strategies are struggling to keep pace, leading to increasing risks related to debris and orbital congestion. In particular, inactive satellites within constellations continue to accumulate. Moreover, according to ESA, a significant number of constellation satellites and various small satellites are concentrated around 500 km altitude (Figure 1.3). This growing congestion underscores a strong market opportunity for Starfixers Inc. to offer targeted debris removal services in one of the most densely populated orbital zones.

---

[4] `https://uppcsmagazine.com/satellite-mega-constellations-the-future-of-global-connectivity/`

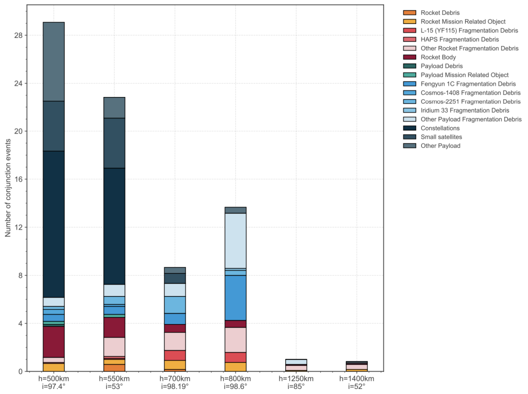

Figure 1.3: Conjunction Events With Collision Probability Above 10^{-6} and Corresponding Chaser Classification for a Set of Representative Targets Over 2023 [35].

In addition to the environmental incentive, there is a large financial motivation to enter the market, the viability of which has been rigorously assessed. A thorough cost-effectiveness study by NASA demonstrates in Figure 1.4 that de-orbiting large debris objects, through controlled or uncontrolled reentry, can yield a cost-benefit ratio ranging from 1:10 (€1 spent yields €0.10 in benefit) to 10:1 (€1 spent yields €10 in benefit) over 30 years, depending on operational assumptions [66]. High profit potential highlights that ADR services pose attractive commercial opportunities if the mission cost is sufficiently low. These findings strongly support the current Starfixers Inc. market positioning, in particular given the high traffic density in LEO.

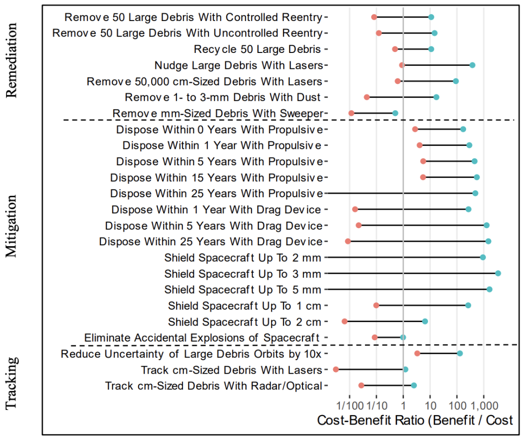

Figure 1.4: The Estimated Range of Cost-benefit Ratios Associated With Each Action After 30 Years [66].

De-orbiting or debris mitigation techniques are mostly passive, such as orbital decay or drag sails. These techniques are useful, but not totally effective, as they rely on the spacecraft's functionality at End of Life (EoL). A defunct satellite, in this case, is not guaranteed to have a safe de-orbiting. Between 60% and 70% of LEO satellites comply with the guidelines imposed for post-mission and even less de-orbit within the assigned time frame [5]. Additionally, satellites from higher orbits will eventually enter mid-range LEO after completion of their mission due to slow orbital decay, increasing collision risks. With the orbital population projected to continue growing in the coming decades, ADR is becoming an increasingly urgent priority. Starfixers Inc. aims to mitigate existing threats and enable safe LEO for future science and commercial missions.

1.2 Regulatory and Legal Drivers

On top of the physical collision risk, space debris is rapidly becoming a legal problem. The growing risk of collisions in space has led regulatory bodies around the world to introduce stricter de-orbit requirements, making it an important factor in mission design. Recently, the United Nations Committee on the Peaceful Uses of Outer Space (COPUOS) posed new, voluntary guidelines for the long-term sustainability of outer space, like post-mission disposal within 5 years [76]. Although they are voluntary, they are already enforced in mission planning and national policies.

Even though its enforcement mechanisms are limited, the Inter-Agency Space Debris Coordination Committee provides the global baseline for responsible satellite behaviour, leaving room for national space authorities to take the lead in establishing more binding regulations. This has already been done by several nations and unions, including the United States, the European Union, and Japan. De-orbiting within the 25-year rule, and more recently proposed 5-year de-orbiting guidelines and contracts, all reflect the efforts to increase accountability and control of space debris. States are also liable for damage caused by their space objects, leading to growing financial risks in the absence of ADR. Starfixers Inc.'s service could be utilised by governments to avoid substantial reparation costs.

Insurance is commonly used for space missions, and the insurers increasingly require debris mitigation plans for new missions as a mandatory condition for coverage. For mega-constellations in particular, this demand is growing, effectively enforcing debris mitigation. If operators still want their insurance contracts or access to launch, they must design for the de-orbiting of the mission at EoL. The combination of drivers originating from the legal standpoint, as well as from an insurance point of view, shapes the service Starfixers Inc. must provide. The ability to de-orbit non-operational debris and uncooperative or tumbling satellites for which passive de-orbiting systems are not effective fills the gaps left in debris mitigation plans.

1.3 Customer Division

ADR service demand is not uniform across the entire space industry, but concentrated among a few customer segments with specific operational profiles and economic incentives. Identification and understanding of these incentives are essential for the design of an ADR system that fits seamlessly into the real world.

The previously mentioned mega-constellations are the largest potential customers due to the enormous number of satellites that pose a danger to orbital congestion. The companies behind the constellations are now facing pressure from regulatory and economic sides, as well as possible reputational damage. The pressure is expected to increase further as the issue worsens, possibly leading to enforced de-orbiting regulations in the future. Therefore, it is an economic need to seriously consider using ADR systems such as the one provided by Starfixers Inc. As of now, the satellites in their constellations are low-cost and therefore often lack redundant de-orbiting systems. While they rely on onboard propulsion for de-orbiting, a malfunction might render this impossible, posing a long-term collision risk. Still, they are scaling up the number of satellites, increasing the number of future targets for ADR missions. The usage of the ADR service is a risk reduction, but also a protection of future launch possibilities in LEO.

Governmental space agencies also have legal incentives to take the lead in orbital sustainability. Governmental agencies do not have their own mega-constellations, but have a large number of big satellites, such as rocket stages still floating around in space, most of which do not have any de-orbit systems. Space agencies are currently investing some money into the Research & Development (R&D) of ADR services, including projects like ClearSpace-1. They may have a less price-sensitive approach than commercial entities, but they have to act as a role model, demonstrating transparency, safety and traceability.

Although insurance companies and launch service providers are not direct customers of ADR services, they indirectly influence the market by only insuring or approving launches under certain (sustainability) conditions. As orbital congestion increases, insurers increasingly factor space debris mitigation efforts into risk assessments[93]. This requires that satellite owners must show mitigation measures, making room for ADR missions, possibly with contracts being made before launch to satisfy insurance companies. Table 1.1 categorises the main stakeholders that influence the ADR development and illustrates their different incentives.

For Starfixers Inc., this entails the following: Firstly, for mega-constellations, the ADR frequency can be high, leading to a lower cost per de-orbiting. Then, government agencies have an obligation to act as a role model for sustainability, opening doors for ADR investment. Insurers and launch entities might demand pre-mission ADR planning to guarantee de-orbit. These three segments combined create a significant market gap for ADR missions with high financial opportunities.

Table 1.1: Key Stakeholders in the Space Ecosystem.

Stakeholder Group	**Examples**
Government and Regulatory Bodies	• Space Agencies (e.g., NASA, ESA, JAXA) • International Organisations (e.g., UNOOSA, IADC) • Policy Makers and Legal Experts
Industry and Technology Developers	• Private Aerospace Companies (e.g., Astroscale, ClearSpace) • Scientists and Researchers (e.g., Universities and research institutions) • Insurance Companies
Public and Advocacy Groups	• Environmental Advocates • General Public and Awareness Campaigns
Customers	• Commercial Satellite Operators • Launch Providers • Government Space Agencies • Military Entities • Research Institutions • Insurance Companies

This chain of influence is further clarified in Figure 1.5, displaying how the funding flows between stakeholders. Figure 1.6 illustrates the relation between stakeholder influence and interest in ADR. It is evident that space agencies and major space companies are the ones to target.

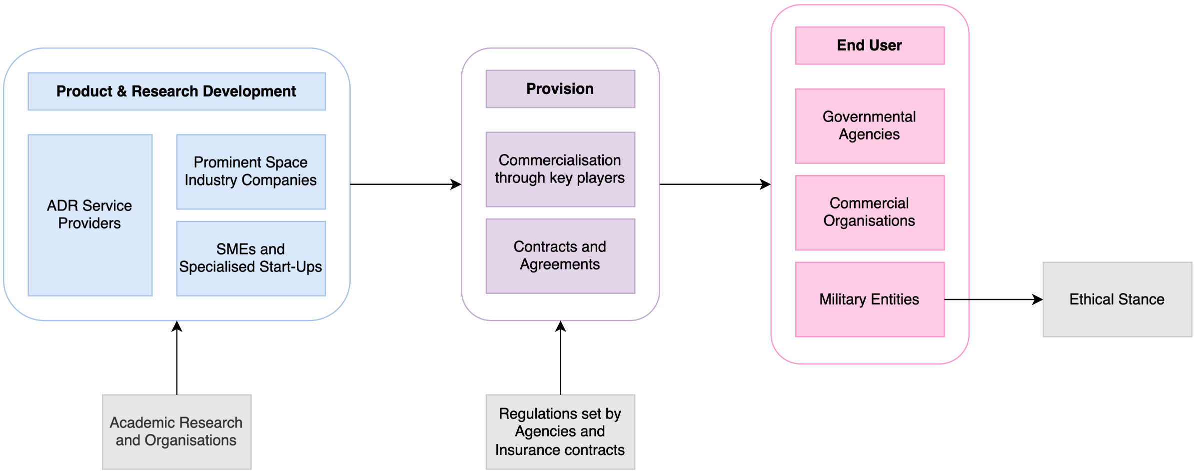

Figure 1.5: ADR Market Stakeholder Analysis.

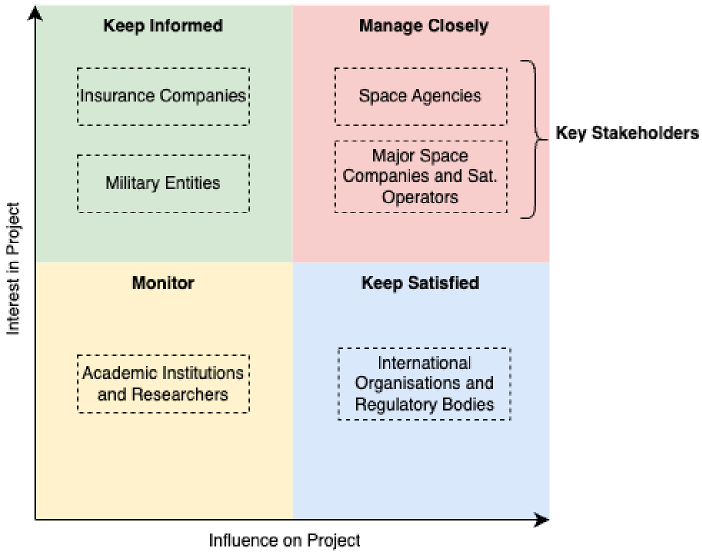

Figure 1.6: Interest-Influence Map of Stakeholders.

1.4 Market Size and Forecast

Figure 1.7 [5]provides context of the lifecycle of the product in a broader style, emphasising the current ADR life cycle stage and the stages to come.

Trend analysis and sizing of the market are essential for system design and strategic positioning. The total addressable market for ADR is defined by the number of defunct or post-mission satellites in LEO. In 2024, there were more than 10 000 satellites in LEO, of which approximately 3 500 were post-mission or defunct [51]. Around 2 500 new satellites are launched into LEO annually, and ESA estimates a total of 60 000 - 80 000 objects to orbit in LEO by 2030, with $5-10\%$ requiring ADR [5]. Removing just five high-risk objects per year significantly improves debris stability[65]. At the moment, a €100 million cost for ten satellites means a tenth of that per individual satellite de-orbiting. However, this amount includes all R&D and other non-recurring costs. After one mission, the subsequent mission cost will be significantly lower. In the meantime, the demand will continue to increase.

---

[5] `eightception.com/characteristics-of-the-product-life-cycle-stages/`

In the past, the market was constrained by technological readiness, but recent projects, like ClearSpace-1, have moved ADR in the commercial direction. Despite these developments, multi-target ADR systems like Starfixers Inc. have not yet reached this level of development. Currently, no adaptable ADR mission has been launched or developed, and even single-target ADR is not yet tested in-orbit. The ADR market size was valued at €1.13 billion in 2024 and it is expected to reach €4.76 billion by 2032, which is an average annual growth of 20%[94]. In 2024 only, entities like ESA, Lockheed Martin and the United States Space Force invested hundreds of millions of euros in ADR startups [94]. The adjacent space tug market is also expected to grow significantly. Some technologies that are being developed there are also of use in the Starfixers Inc. program, such as autonomous navigation and rendezvous. By combining technologies from other markets, the R&D cost and development time for ADR can be substantially reduced.

At the moment, the growth of the market is heavily dependent on investments from governments and large aerospace companies. In a few years, the mega-constellation companies are expected to become the largest customers. Currently, there is a lack of urgency from their side due to high initial costs and insufficient regulation, but governmental entities are aware of the importance of ADR, and regulations are likely to become stricter.

It is important to carefully assess the profitability of ADR according to a 2023 NASA report on the cost and benefit analysis of ADR [97], removing a single satellite from orbit leads to a risk reduction that is worth €3.03 million in the first year, which is a value increasing over time. Since companies will place a strong value on long-term safety and public accountability, a price in the range of €5 million to €10 million is realistic for most critical orbits. By targeting medium-sized, tumbling objects in LEO, Starfixers Inc.'s design is both technically feasible and economically viable. After the first mission, the spacecraft's cost will drop drastically, causing a significant reduction in the cost per debris due to the absence of R&D costs. From Table 12.1, a recurring cost of €60.75 million per spacecraft is extracted, which is a huge drop of €39.25 million in expenses. It is expected that the first mission might lose money, which would be compensated by the subsequent profitable missions and high market share.

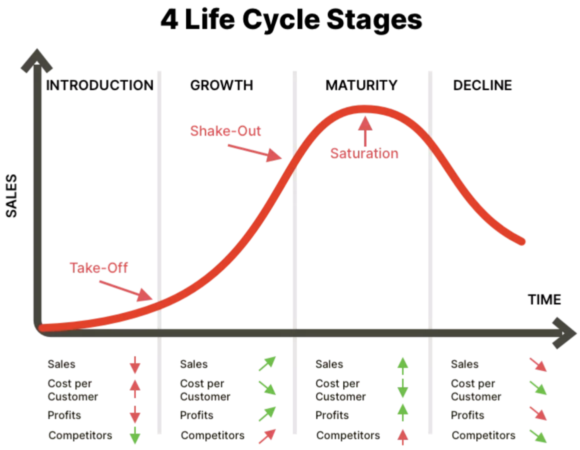

Figure 1.7: Product Life Cycle Stage Diagram.

1.5 Competition

The ADR market is underdeveloped but rapidly expanding, shaped by funding and several startups pioneering the concept. Starfixers Inc. must identify itself as a technically feasible, cost-efficient, and versatile service. The combination of those attributes is something that current startups lack. Most existing missions share two limitations: they are designed for a single target, and the target is cooperative/pre-

prepared. These limitations make them unsuitable for multi-target removal or uncooperative targets. Starfixers Inc., on the other hand, will provide a flexible and adaptable de-orbiting service.

Apart from the fact that the number of targets to de-orbit is larger for Starfixers, Inc., the actual congestion problem is largely due to defunct, uncooperative satellites. Since existing missions do not address this problem, there is a clear opportunity for a mission targeting defunct satellites. Instead of being a demonstrative governmental mission, this is a commercially scalable ADR platform. This scalability results from an approach that is flexible to target mass and altitude, capable of de-orbiting multiple (uncooperative) targets and cost-optimised. Rather than selling one-time missions, it would offer pay-per-removal or subscription-based service to mega-constellation providers, allowing for recurring, steady revenue. The mission is not competing with the demonstrative missions, but is pioneering as the first commercial ADR service provider.

In order to understand how several actors contribute to and depend on ADR services, Figure 1.8 visualises the key interactions between the policy makers, customers and mission enablers within the ADR value chain.

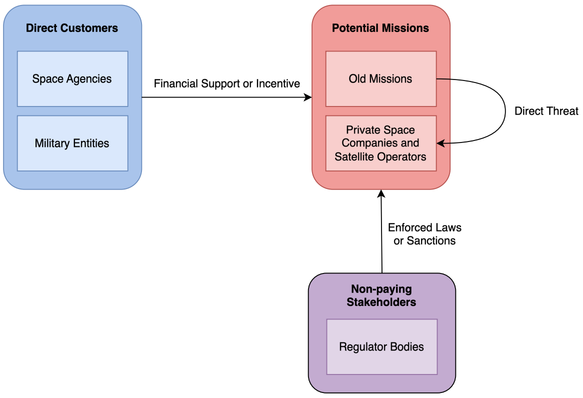

Figure 1.8: Customer Flow Diagram

1.6 Design Drivers from Market Requirements

The most congested altitudes with the highest probability for conjunction events in LEO are in the range from 400 to 1000 km (with peaks between 500 and 800 km), while the objects at that altitude mainly have a mass between 100 and 1000 kg (with peaks between 200 and 700 kg) [29]. This means that the design is defined to operate for targets at 550-630 km altitude with a 250-500 kg mass, capturing a significant part of the ranges. The adaptability of the system is a top priority driving the design, since it opens up many other potential targets. The Starfixers, Inc. is able to cope with both ends of the altitude and mass ranges. The only thing that changes is the amount of fuel that is onboard the spacecraft. For out-of-range targets, such as ten 500kg targets at 900km altitude, de-orbiting is not possible with one unit, but the mission could be adapted to de-orbit less debris. Then, the service price would have to change accordingly.

It is beneficial to be able to remove both predetermined targets, as well as targets for which information is obtained after launch. Therefore, a design with the appropriate detection systems and autonomous navigation is applied to the Starfixers Inc. spacecraft. Beyond removal, the mission could also evolve to support inspection and diagnosis missions and relocation of targets, making it multifunctional in even more ways.

Moreover, cost efficiency will be one of the main aspects driving the design. The affordability of the ADR system will greatly determine the feasibility and scalability of the service in a competitive and rapidly evolving market.

1.7 User Requirements Summary

To translate the market demands into specifications of the system, high-level requirements were formalised while being considerate of the stakeholder feedback. These requirements act as drivers for design, performance, and operation and are displayed in Table 1.2. The requirements naming convention was updated since the Project Plan, according to the requirement discovery tree. [R-SYS-xx] will be used for system requirements and [R-SUB-XXX-xx] for subsystem requirements.

Table 1.2: High-level Customer Requirements for the ADR Mission.

Category	Requirement
Performance	**[R-SYS-05]** The ADR spacecraft shall be capable of de-orbiting at least 10 target satellites from the same orbital altitude and plane within one year.
	[R-SYS-38] The ADR spacecraft shall be capable of de-orbiting a target satellite with a mass between 250–500 kg, operating in a circular LEO at an altitude between 550–630 km.
	[R-SYS-39] The ADR spacecraft shall be capable of de-orbiting uncooperative satellites tumbling at a rate of up to 1 rpm about their primary axis.
Safety and Reliability	**[R-SYS-15]** In the event of a failure, the ADR spacecraft shall de-orbit within 5 years.
	[R-SYS-35] During its operational phase, the ADR spacecraft shall maintain an Accepted Collision Probability Level (ACPL) with trackable debris below 1.0×10^{-4}.
Sustainability	**[R-SYS-12]** The ADR spacecraft shall not generate any additional debris during its operations.
	[R-SYS-14] At the end of its operational lifetime, the ADR spacecraft shall de-orbit within 5 years.
	[R-SYS-18] The ADR spacecraft shall utilise non-toxic propellants.
Engineering Budgets	**[R-SUB-STR-15]** The ADR spacecraft shall fit within the payload fairing of a single launch vehicle.
	[R-SUB-TTC-01] The ADR spacecraft shall communicate with ground operators via the ESA Estrack network.
Cost	**[R-SYS-26]** The total mission cost, including manufacturing, testing, launch, and operations, shall be less than €100 million.
Launch	**[R-SYS-27]** The ADR spacecraft shall be launched before January 1, 2030.

1.8 SWOT Analysis

Using the market analysis described in previous sections, a SWOT analysis can be performed. It is visualised in Table 1.3.

Altogether, the market for ADR is transitioning from demonstrative concepts to commercial removal of targets. With tens of thousands of satellites in LEO in the coming years, regulatory global frameworks will introduce the demand for scalable, cost-effective ADR solutions. Starfixers Inc. has a strategic position to serve this need by aligning its design with the market demands. Multi-target, adaptable, and cost-efficient missions with the possibility to potentially alter the mission objective are what the market demands. By integrating these design drivers into a spacecraft, the Starfixers Inc. team pioneers in the early stage of the ADR era.

Table 1.3: SWOT analysis.

Category	Key Points
Strengths	• **Technical Viability:** Removes at least 10 satellites/year in high-risk LEO, including Starlink range. • **Defined Requirements:** Clear performance metrics (e.g., tumbling targets, ACPL). • **Environmental Sustainability:** Non-toxic propellants, debris-neutral operations (environmental, social and governance, (ESG) appeal). • **Cost-Conscious Design:** €100M cap makes it appealing to agencies/operators. • **Early Mover Advantage:** Can shape future standards and partnerships.
Weaknesses	• **Limited Mission Capacity:** 10/year may not meet demand growth. • **Reliance on Public Sector:** Dependent on regulation or state support. • **Uncertain Economic Viability:** Return On Investment (ROI) range (1:10 to 10:1) poses risk. • **Ethical Constraints:** Military limitations, consent requirement reduces flexibility.
Opportunities	• **Regulatory Momentum:** Rules will mandate Active Debris Removal (ADR). • **Scaling Potential:** Parallel systems or higher removal rates are possible. • **Market Gap:** Inactive satellites and failures in LEO create demand. • **Public-Private Partnerships:** Scope for funding and technical collaboration. • **International Collaboration:** Support from ESA, UNOOSA, etc.
Threats	• **Emerging Competition:** Astroscale, Airbus, ClearSpace may lead. • **Legal Barriers:** Owner consent limits target availability. • **Funding Gaps:** Weak private demand may delay adoption. • **Technological Complexity:** Fast-tumbling or large debris is difficult. • **Reputation Risk:** Collisions or failure could hurt credibility.

2 Mission Concept & Breakdown

This chapter presents the foundation for the Starfixer mission. It begins with a description of the mission need and project objective, followed by a summary of the design trade-off that led to the chosen de-orbiting method. Finally, key mission parameters are discussed and a functional analysis is conducted. The functional breakdown structure and functional flow diagram are presented to guide the spacecraft's system-level design and operations.

2.1 Mission Need and Project Objective

Following the observations made in chapter 1, a mission need statement and project objective were derived. These drive the overall need for Starfixers' mission and the design of the ADR spacecraft ”Starfixer” for a safe and sustainable space environment.

Mission Need Statement

The mission need statement formulates the scientific need or gap in a concise and explicit way. For this mission in particular, the mission need statement is given below:

> ”The growing number of satellites and space debris in Earth's orbit is increasing collision risks and threatening the sustainability of space operations. To preserve a safe and stable orbital environment, there is a pressing need for active debris removal missions capable of targeting multiple objects efficiently.”

Project Objective Statement

The project objective describes the overall, measurable goal for the design of the product aligned with the mission need statement. For this mission, the project objective was stated in the following way:

> ”Design an active debris removal mission to de-orbit a minimum of 10 spacecraft in one year from LEO orbits between 550-630 km within a budget of €100 million, by 10 students in 10 weeks full-time.”

Figure 2.1: Starfixers Mission Patch.

2.2 Trade-off Summary

Before delving into the design of the spacecraft, a trade-off was performed in an earlier report to analyse possible ways to complete the Project Objective mentioned above [14]. This trade-off followed from the early phases of the project, where a design option tree resulted in five feasible solutions to be explored [13]. These are the following: clustering the debris onto a structure to de-orbit them (Clustering), tugging down the debris one by one via a tether after capture using claws or a net (Space Tug), attaching a drag sail or balloon to the each debris to speed up its passive de-orbit (Drag Attachment), attaching a thruster to each debris to allow it to lower its own altitude (Thruster Attachment) and finally Gas Shepherding (Gas Shepherd) which consists of blasting gas onto the debris using the main propulsion unit of the ADR spacecraft to change its speed. In order to select the most promising of these five designs, trade-off criteria were established to ensure all the options were analysed critically in the same manner. The criteria defined for that purpose were: cost including Technology Readiness Level (TRL) to estimate any developments necessary for the design, chance of operation success, debris creation probability and method adaptability for different debris types and orbits. The Operation Success criterion was then subdivided into three sub-criteria: Spacecraft Reliability, which concerns the survivability of physical mission-critical components of the ADR spacecraft throughout operation, ADCS and GN&C Complexity, referring to the operational precision required for the mission, and De-orbit Success, denoting the success rate of the de-orbiting method applied to the target. Each criterion was assigned a weight based on its influence on reaching a successful design, combined with a score for each option and criterion. A weight of 4/18 was assigned to the cost criterion due to the importance of design cost-efficiency in securing market entry and facilitating technology scalability. Adaptability was also considered as a trade-off criterion, due to the importance of handling a broad variety of debris when offering de-orbiting as a service. Despite of its importance, adaptability was deemed less critical for the design choice and was assigned a weight of 2/18. Operation Success and Debris Creation Probability, with given weights of 7/18 and 5/18 respectively, were the criteria with highest weights. As the main mission objective is to increase LEO sustainability, these two criteria should drive the choice of the design the most, maximising operation success and minimising the debris creation probability for that purpose. The design option trade-off is then summarised in Table 2.1:

Table 2.1: Trade-off Table for Payload Options.

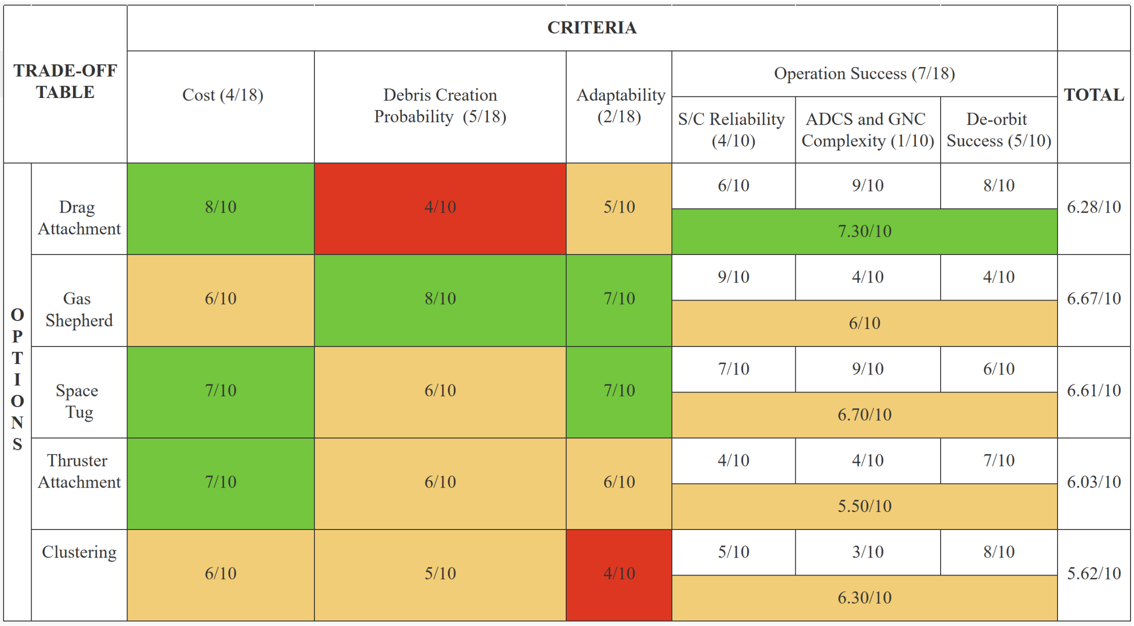

<table>
<tr><td rowspan="3" colspan="2">TRADE-OFF TABLE</td><td colspan="6">CRITERIA</td><td></td></tr>
<tr><td rowspan="2">Cost (4/18)</td><td rowspan="2">Debris Creation Probability (5/18)</td><td rowspan="2">Adaptability (2/18)</td><td colspan="3">Operation Success (7/18)</td><td rowspan="2">TOTAL</td></tr>
<tr><td>S/C Reliability (4/10)</td><td>ADCS and GNC Complexity (1/10)</td><td>De-orbit Success (5/10)</td></tr>
<tr><td rowspan="10">OPTIONS</td><td rowspan="2">Drag Attachment</td><td rowspan="2">8/10</td><td rowspan="2">4/10</td><td rowspan="2">5/10</td><td>6/10</td><td>9/10</td><td>8/10</td><td rowspan="2">6.28/10</td></tr>
<tr><td colspan="3">7.30/10</td></tr>
<tr><td rowspan="2">Gas Shepherd</td><td rowspan="2">6/10</td><td rowspan="2">8/10</td><td rowspan="2">7/10</td><td>9/10</td><td>4/10</td><td>4/10</td><td rowspan="2">6.67/10</td></tr>
<tr><td colspan="3">6/10</td></tr>
<tr><td rowspan="2">Space Tug</td><td rowspan="2">7/10</td><td rowspan="2">6/10</td><td rowspan="2">7/10</td><td>7/10</td><td>9/10</td><td>6/10</td><td rowspan="2">6.61/10</td></tr>
<tr><td colspan="3">6.70/10</td></tr>
<tr><td rowspan="2">Thruster Attachment</td><td rowspan="2">7/10</td><td rowspan="2">6/10</td><td rowspan="2">6/10</td><td>4/10</td><td>4/10</td><td>7/10</td><td rowspan="2">6.03/10</td></tr>
<tr><td colspan="3">5.50/10</td></tr>
<tr><td rowspan="2">Clustering</td><td rowspan="2">6/10</td><td rowspan="2">5/10</td><td rowspan="2">4/10</td><td>5/10</td><td>3/10</td><td>8/10</td><td rowspan="2">5.62/10</td></tr>
<tr><td colspan="3">6.30/10</td></tr>
</table>

Colour-blind accessibility note: Colours in Figure 8.1 represent qualitative performance levels as follows: **Green** = high performance, Yellow = moderate performance, and **Red** = low performance. All values are also presented numerically to ensure accessibility for readers with colour vision deficiencies.

As can be observed in Table 2.1, by grading all the options with respect to each other, their respective drawbacks and advantages were brought to light. After scaling these with the weights of the criteria, it became clear which option reached an overall better score. For example, the Drag Attachment scored relatively high on the cost criteria compared to the Gas Shepherd and Clustering, thanks to the low ΔV required and the high Technology Readiness Level due to proven experiments with drag sails and nets.

For Debris Creation Probability, however, the Drag Sail lost a significant amount of points because of its higher probability to create debris due to the sail's large area. The Gas Shepherd scored 8/10 due to the contactless method of interaction with the debris.

For Adaptability, the Clustering design lost a significant amount of points due to the complexity of docking with varying types of debris and attaching them to a beam. The Gas Shepherd and Space Tug scored a 7/10 on this criterion for their ability to adapt to the debris shape and even the initial debris orbit. It is important to note that the Drag Attachment lost a considerable amount of points on this criterion due to its low adaptability to higher orbits of the target. Drag is highly dependent on altitude and the launch is planned during a solar minimum[6], leading to a significant decrease in drag at LEO and increasing the mission duration.

For the last criterion, Operation Success, the Drag Attachment scored the best because of high reliability of the drag system and low complexity of the ADCS and GN&C for the shooting mechanism. This would require less precision than docking for other options. The Thruster Attachment method scored the lowest on this criterion because of the lower reliability of the system, as the de-orbiting would be dependent on successful docking, attachment and activation of the thrusters. Each element of this method would require highly complex ADCS and GN&C subsystems.

Ultimately, the trade-off led to the selection of Gas Shepherd as the de-orbiting strategy for the mission due to its well-balanced performance on all the selected criteria, offering potential for sustainability and a favourable market positioning. An overview of the operation of this method is described in Section 2.3 in addition to some important assumptions made for the mission design.

2.3 Mission Parameters

The Gas Shepherding method relies on the impingement of a gas plume. Accelerated gas coming from a thruster of the ADR spacecraft hits the debris and partially transfers its momentum. By positioning the ADR spacecraft in front of the debris, this momentum transfer can be utilised to slow down the debris and cause it to change its initial orbit to a lower energy one. Enough momentum has to be transferred to the debris such that its final orbit passes through a higher atmospheric density region and causes passive de-orbiting in under 1 year. When shooting gas at the target debris, it is inevitable that the ADR spacecraft would accelerate itself and move away from the debris. Therefore, multiple rendezvous manoeuvres are required per debris to ensure de-orbiting.

The ten targets will be de-orbited 1-by-1, meaning that the ADR spacecraft will perform a series of momentum transfer manoeuvres with each debris until de-orbited before switching to the next one. This approach simplifies orbital manoeuvring as all of the momentum transfer manoeuvres can be performed at the same spot, at the apogee of the debris orbit. The method is easily adaptable to debris of various masses, altitudes, and tumbling rates in accordance with the requirements described in Section 1.7. However, when considering different sets of targets, the fuel required for de-orbiting, and therefore the sizing of the ADR spacecraft, could differ immensely.

In light of this, the decision was made to focus on designing the ADR spacecraft for a specific selection of targets. Further detailed spacecraft design assumes that all ten targets are Starlink V1 satellites on a circular 600 km altitude orbit at a 53° inclination, 260 kg mass each, and an arbitrary angular phase angle and tumbling rate (within the range specified in **[R-SUB-PAY-02]**). As described in chapter 1, this assumption captures the middle-range targets. Furthermore, Starlink v1 satellites are the most common

---

[6] https://www.swpc.noaa.gov/products/solar-cycle-progression

satellite variant in LEO, making them the primary de-orbiting target. The orbital altitude of the debris was assumed to be 50 km higher than the true altitude (600 km instead of 550 km) in order to achieve a more general design capable of de-orbiting a wider debris range.

2.4 Functional Analysis

With the mission parameters defined, it is imperative to identify the functions that the ADR spacecraft will have to perform during its mission lifetime. In order to effectively model the interactions between functions and create a comprehensive visual summary, useful tools such as the Functional Breakdown Structure and the Functional Flow Diagram are required.

The Functional Breakdown Structure is a hierarchical structure that subdivides each system-level function into smaller functions and then subfunctions, etc. This tool is great for showing dependencies between different functions. It illustrates which functions belong to each level and the parent-child relationship between the levels. The Functional Breakdown Structure is presented in Figure 2.2 and is utilised for identification and hierarchical categorisation of mission functions that are then used to focus design and development of the mission and as a checklist for subsystem performance. This is in particular useful for the design of the command and data handling subsystem that has to tie together the functions performed by various other subsystems.

The Functional Flow Diagram uses the functions identified in the Functional Breakdown Structure and connects them in chronological order. This serves to clearly demonstrate the order in which certain actions have to be performed throughout the mission. It is used to organise the functions in order and develop a detailed operational procedure later on. The development of orbital manoeuvring is greatly facilitated by the diagram. Furthermore, it allows for division of the operation into larger functional blocks that can be used to assess telecommunication and power demands at various operational stages. The Functional Flow Diagram can be seen in Figure 2.3.

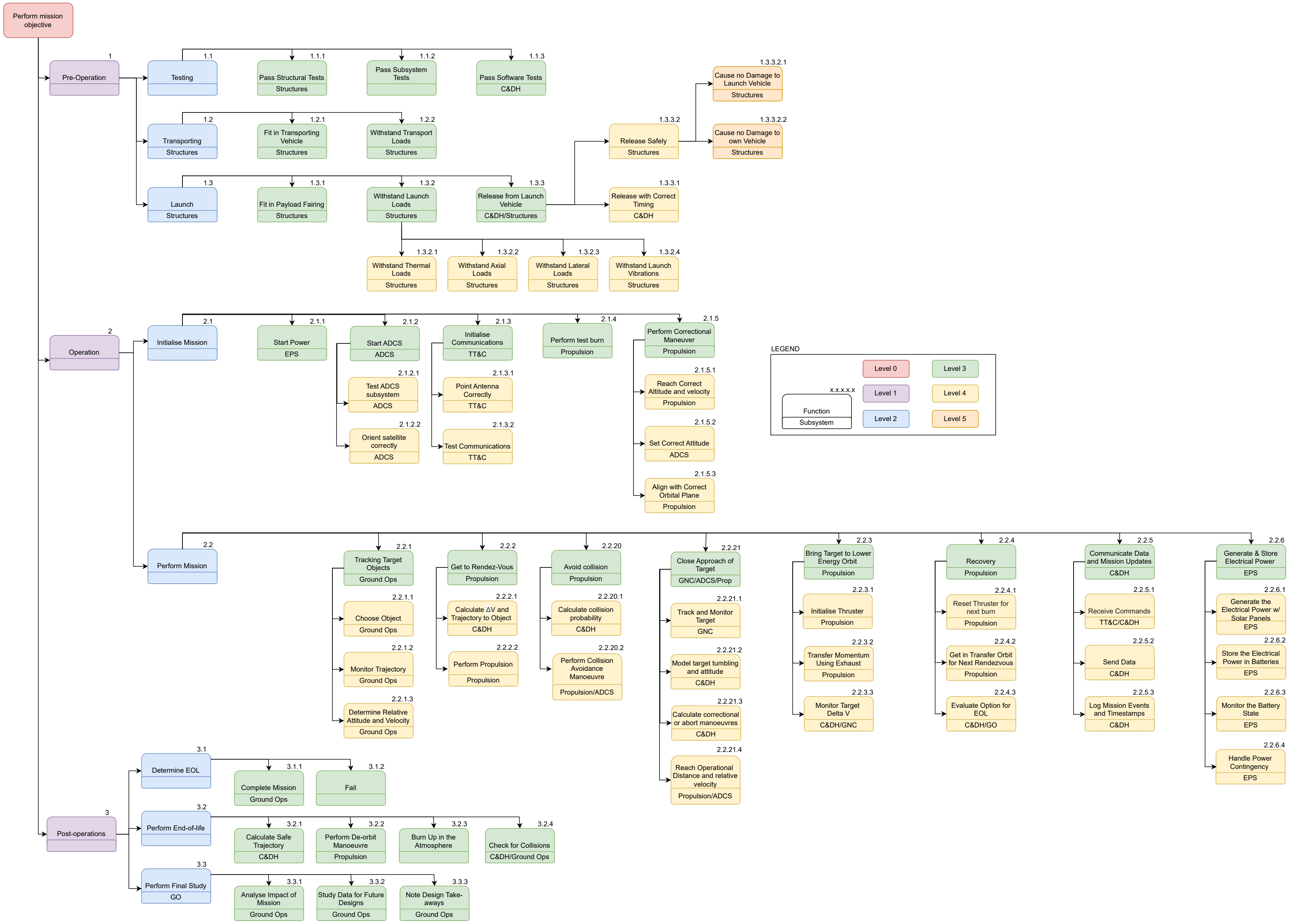

Figure 2.2: Functional Breakdown Structure of the ADR spacecraft.

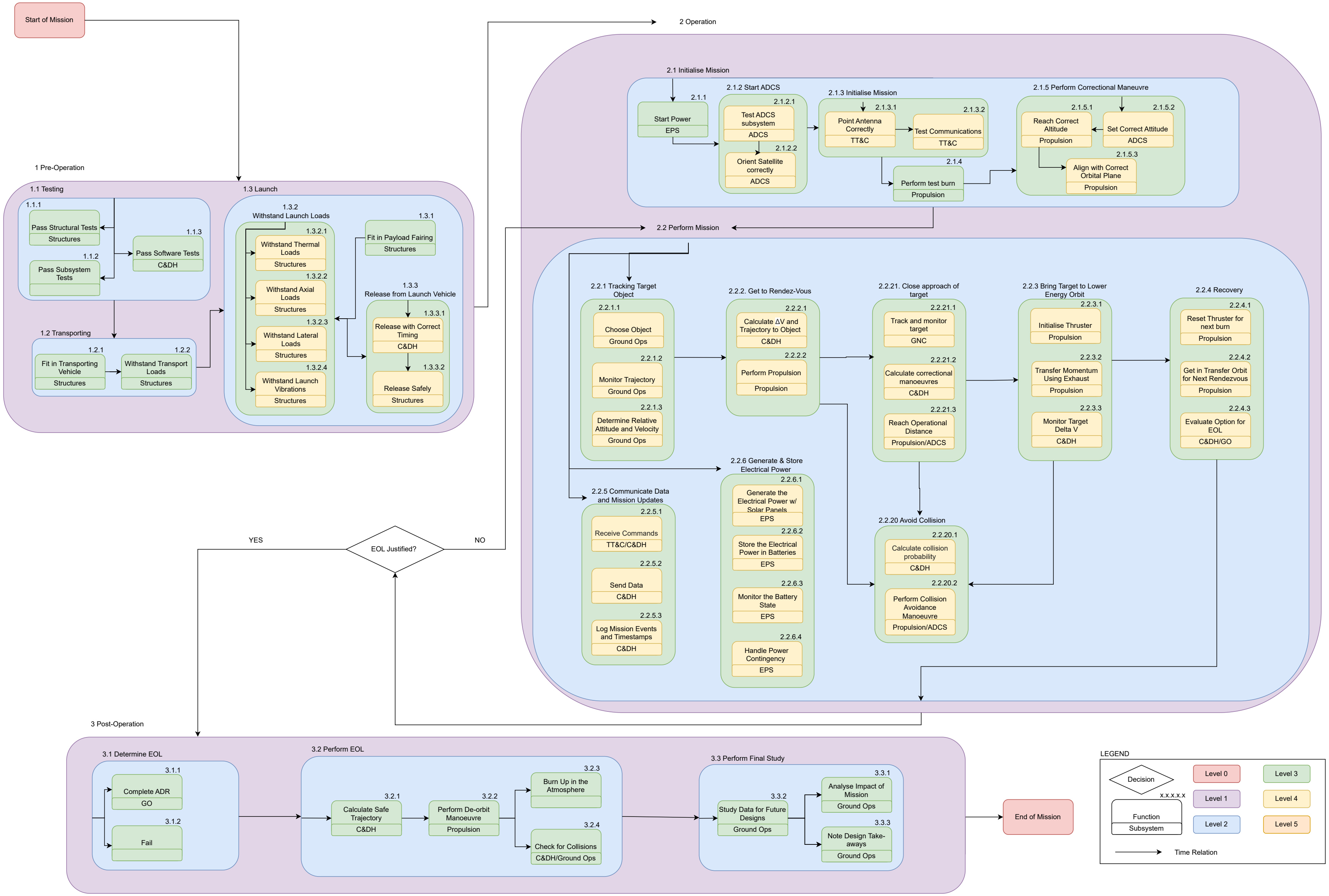

Figure 2.3: Functional Flow Diagram of the ADR spacecraft.

3 Mission Characteristics

After having defined the mission concept, this chapter will discuss at a higher level the mission characteristics, operational flow and system-level modelling of the ADR mission. First, Section 3.1 will discuss the Operations and Logistics, outlining the different mission phases from launch, to orbital phase and disposal. Then, Section 3.2 will discuss the physics of the momentum transfer to the target and the astrodynamics of the operational procedure, including the orbital manoeuvres for rendezvous and transfer to the target. Lastly, Section 3.3 will discuss other important aspects such as drag, tumbling of the target, and collision. Moreover, a generalised model will be presented as a tool to adapt to different kinds of missions.

3.1 Operations and Logistics

The operational and logistic flow of the mission is presented in Figure 3.1. The diagram is divided into seven major mission phases: Pre-launch, Launch, Start-up & Approach of First Target, Observe and Prepare, Perform Momentum Transfer, Safety Check, Outer Orbit and EoL. These phases capture the chronological and functional progression of the mission from ground-based preparation through to spacecraft decommissioning. The yellow boxes indicate tasks executed by the ground station, whereas the white boxes represent operations conducted onboard the spacecraft. This distinction is especially critical in phases where real-time decision-making plays a significant role. For instance, in the 'Safety Check' phase, the ground segment is responsible for computing the collision probability, Pc, and evaluating it against the accepted collision probability level (ACPL), in order to verify compliance with mission-level safety thresholds and regulatory constraints. In contrast, during the 'Perform Momentum Transfer' phase, the spacecraft autonomously determines the safety of the pre-computed manoeuvre using onboard sensors and computational systems, thereby reducing latency and increasing responsiveness in critical proximity operations.

In addition to structuring the mission timeline, the defined phases also serve as a framework for the spacecraft's operational modes. These operational phases: Launch, Startup, Observe, Prepare, De-orbit Operation, Outer Orbit, and EoL are essential for modelling and allocating the spacecraft's power, thermal, and data-handling resources. They provide the basis for estimating subsystem-level requirements and designing the autonomous mode transitions that govern the spacecraft's behaviour throughout the mission. This dual usage of the phases ensures consistency between high-level mission planning and low-level subsystem operation, contributing to a coherent and integrated mission architecture.

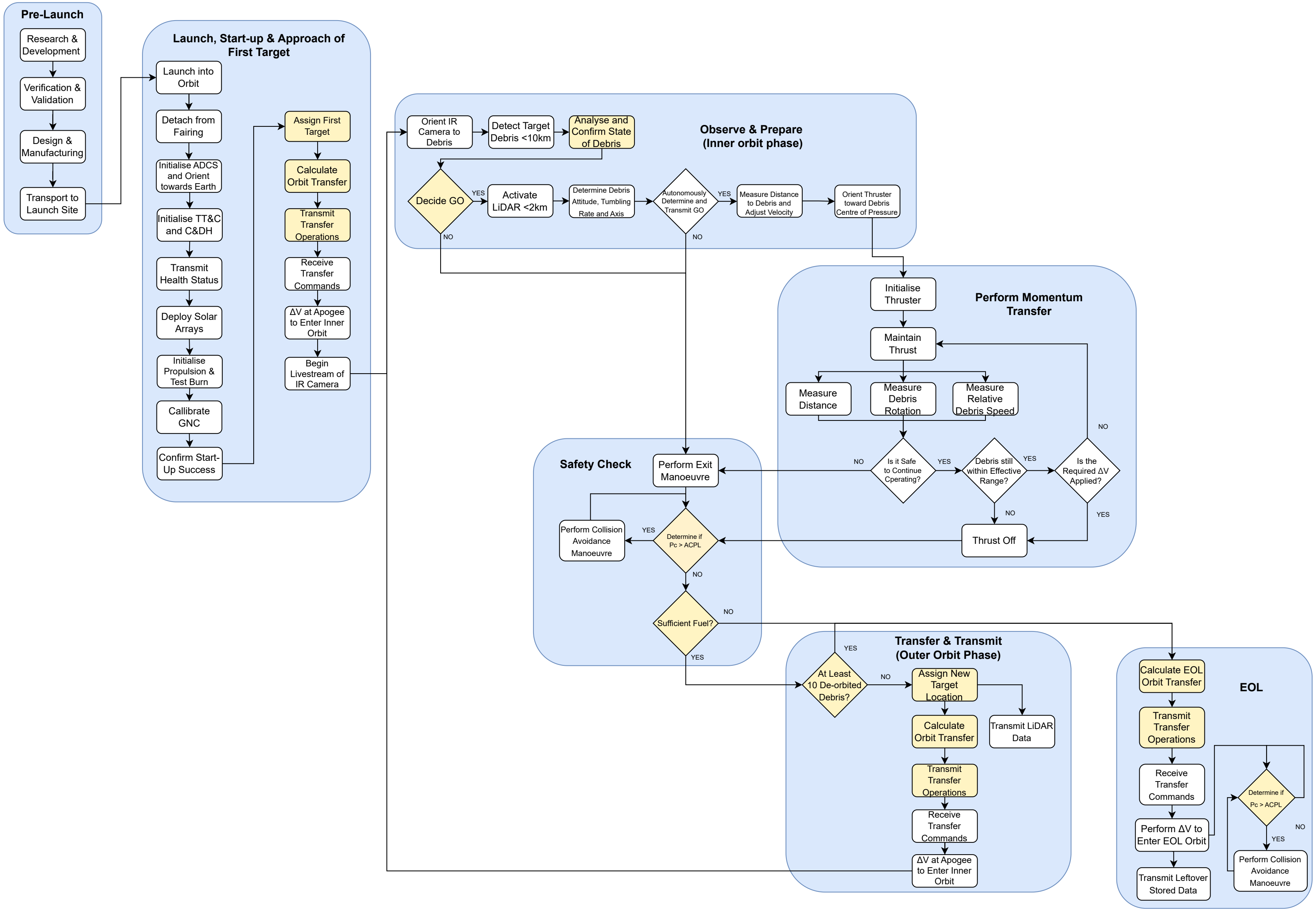

Figure 3.1: Operational and Logistic Flow Diagram of the ADR mission.

3.2 Astrodynamic Characteristics

In this section, all the calculations regarding the astrodynamic characteristics of the ADR spacecraft are presented. In the first subsection, the momentum transfer is analysed, explaining the general de-orbiting method and discussing method-specific values. Next, the target sequencing logic is discussed and chosen between either 1-by-1 or 10-by-10. With the target de-orbiting sequence determined, the different phases of the operational procedure are explained, and the results are presented.

Momentum transfer

This subsection analyses the dynamic interaction between the ADR spacecraft and the debris, focusing on the modelling of relative position and velocity during the manoeuvre, ultimately allowing for finding the required ΔV. After explaining the general momentum transfer calculation, the efficiency, the operating distance, and the initial relative velocity are discussed.

The approach of the ADR satellite with the debris objects is one of the most vital parts of the Starfixers Inc. mission. The dynamics of the approach are delicate and involve characterising the relative velocity and relative position of the two satellites. The derivation of the kinematic equations is done in this subsection, where a generic configuration of the Starfixers Inc. spacecraft is considered. The ADR spacecraft is considered to have two thrusters, one of which is used for acceleration and debris de-orbiting. The other one will be used to brake and get the optimal relative velocity when the debris is approaching to avoid having to rotate 180°, for acquisition of the desired initial relative velocity, and then another 180° to get back in front of the debris with the correct orientation.

To begin with the derivation, a combined Kinematic and Free Body Diagram, along with the used coordinate system, is presented in Figure 3.2:

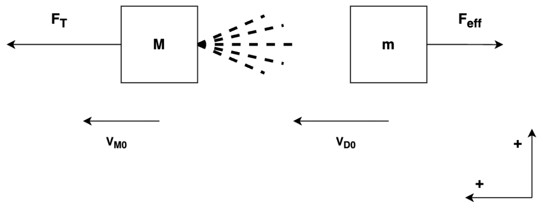

Figure 3.2: Kinematic & Free Body Diagram.

In the above diagram, M represents the mass of the Starfixers Inc. satellite, while m is the mass of the debris object to be de-orbited. Furthermore, V_{M_0} and V_{D_0} display the initial velocities of the ADR satellite and the debris object, respectively. Additionally, F_T is the thrust produced by the ADR satellite when the burn initiates, and F_{eff} is the effective thrust imparted on the debris. The coordinate system, as shown in the figure, is used for sign conventions, and it has to be stated that relative velocity/position is always considered as the relative velocity of the debris with respect to the ADR satellite. Finally, the dashed lines on the right of "M" represent the gas expansion from gas shepherding, and are illustrated for the reader's visual and conceptual aid.

Having established the above, the first step is to express the relative velocity (Equation 3.1).

$$V_r(t) = V_D(t) - V_M(t) \tag{3.1}$$

For which V_{D} is the debris velocity and V_{M} is the ADR satellite velocity. V_{r_0} is defined as $V_{\mathrm{r}}(0)$, or the initial relative velocity of the debris with respect to the ADR satellite. This velocity will be taken into account for each debris encounter.

The velocity of the debris is: $V_D(t) = V_{D_0} - \int_{t_0}^{t} \frac{F_{\text{eff}}}{m}\, d\tau = V_{D_0} - \int_{t_0}^{t} \frac{F_T \cdot \eta(S_r(\tau))}{m}\, d\tau$, where the second term captures the deceleration, and η is the momentum transfer efficiency, a function of S_r (i.e. the relative position between the satellites), which is increasing with decreasing distance to the debris spacecraft.

Moreover, the velocity of the ADR satellite can be expanded to: $V_M(t) = V_{M_0} + \Delta V(t)$, where $\Delta V(t) = I_{sp} \cdot g_0 \cdot \ln\left(\frac{M}{M - \dot{m}_T \cdot t}\right)$, following from the Tsiolkovsky rocket equation, and $\dot{m}_T$ is the mass flow of the expelled gas, g_0 is the standard gravitational acceleration and I_{sp} is the specific impulse of the thruster.

With these expressions, one can formulate an expression for the relative velocity, as seen below in Equation 3.2.

$$V_r(t) = V_{D_0} - \int_{t_0}^{t} \frac{F_T \cdot \eta(S_r(\tau))}{m}\, d\tau - V_{M_0} - I_{sp} \cdot g_0 \cdot \ln\left(\frac{M}{M - \dot{m}_T \cdot t}\right) \tag{3.2}$$

The above expression can be further reduced to Equation 3.3.

$$V_r(t) = V_{r_0} - \int_{t_0}^{t} \frac{F_T \cdot \eta(S_r(\tau))}{m}\, d\tau - I_{\text{sp}} \cdot g_0 \cdot \ln\left(\frac{M}{M - \dot{m}_T \cdot t}\right) \tag{3.3}$$

In order to get an expression for the relative position of the debris with respect to the ADR satellite, one must integrate the above equation with respect to t, yielding Equation 3.4.

$$\begin{aligned} S_r(t) = S_{r_0} + V_{r_0} \cdot t - \int_{t_0}^{t} \int_{t_0}^{t} \frac{F_T \cdot \eta(S_r(\tau))}{m}\, d\tau\, d\tau \\ - I_{sp} \cdot g_0 \cdot \left(\frac{(M - \dot{m}_T \cdot t) \cdot \ln(M - \dot{m}_T \cdot t)}{\dot{m}_T} + \ln(M) \cdot t + t - M \cdot \frac{\ln(M)}{\dot{m}_T} \right) \end{aligned} \tag{3.4}$$

With S_r being the relative position of the two objects as a function of time, S_{r_0} the initial relative position of the objects (right before the burn), and the rest of the parameters follow from the derivations above.

The derived expressions will therefore be used to model the approach of the ADR satellite to the debris object. The assumptions that are used in the expressions, as well as the assumptions used for their derivation, are discussed in the following subsection.

Momentum Transfer Efficiency

The efficiency of the momentum transfer from the spacecraft to the debris depends on the exhaust plume characteristics, the collision between the exhaust and debris, the effective area distribution of the debris, and the distance between debris and spacecraft [12].

Exhaust plume characteristics include the half cone angle of the plume, which essentially determines how much the gas spreads. It also includes the spread of mass along the central axis through the middle of the thruster. Naturally, more mass will be present around this axis than away from it.

The efficiency of a collision between a gas and a solid is characterised by the Accommodation Coefficient (AC). This factor varies a lot for different materials, gas speeds and temperatures. An AC of 0 means no momentum is transferred, 1 means that all momentum is transferred from the gas to the solid [12].

The effective area distribution of the debris depends on its orientation and its tumbling characteristics. The debris will always be de-tumbled in such a way that its effective area is maximised, as shown in Figure 3.3. In the case of de-orbiting a Starlink satellite, the exhaust plume will have to be pointed perpendicularly at the big solar panel.

To compute the efficiency at a certain distance, a numerical model can be created based on an analytical formula, shown in Equation 3.5. The debris will have to be divided into a number of very small parts. For each part, the fraction of mass (compared to what is exhausted from the spacecraft (M_{tot})) impinging onto it can be calculated, yielding m_{flux}. Multiplying this by the cosine of the incidence angle θ and the AC results in the momentum transfer efficiency in the along-track direction of this part. Adding up the efficiencies of each debris part will then result in the total efficiency of the momentum transfer.

$$\eta = \iint_{A_{Debris}} \frac{m_{flux} \cdot \cos(\theta) \cdot AC}{M_{tot}} dA \tag{3.5}$$

The effective area of a Starlink satellite is a 3.1 m by 10.9 m rectangle. It will be assumed that the exhaust mass is distributed in a Gaussian bell-curve with the 2 standard deviation mark at the end of the half cone [45]. This means 95.4 % of the exhausted mass is exhausted within the defined plume. To verify this assumption, it is recommended to test it as well. Plotting the efficiencies with these values with the distance on the x-axis results in Figure 3.3.

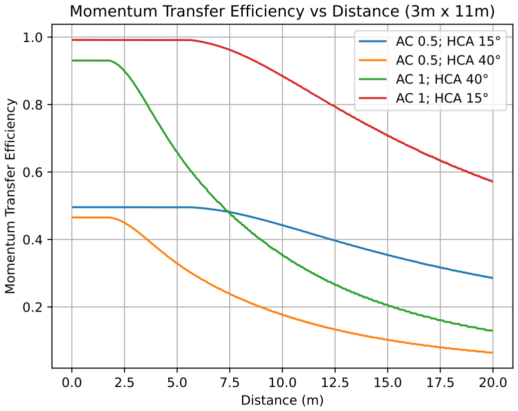

Figure 3.3: Momentum Transfer Efficiency Plotted over Distance, using different ACs and half cone angles (HCA).

For this report, it will be assumed that the accommodation factor between the exhaust and the Starlink debris is 0.5, as values range heavily between 0 and 1[7]. As a recommendation, accommodation factors will need to be tested physically for common materials in spacecraft debris. The assumption is made that the nozzle of the main thruster will be manufactured and tested in such a way that the half cone angle equals 15 degrees. The efficiency stays relatively constant until 6 m (meaning all mass hits the debris) and starts rapidly dropping off at 10 m. The plume, with the active range, is visualised in Figure 3.4.

---

[7] `thermopedia.com/content/286/`

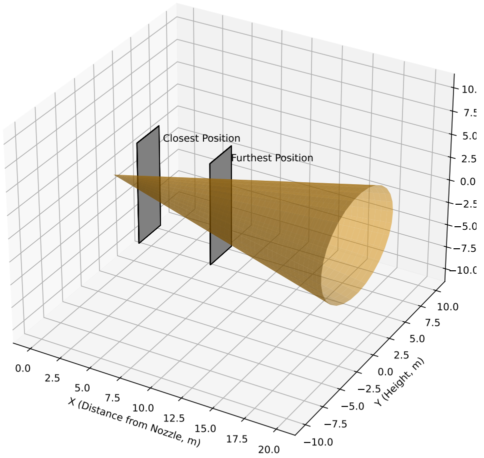

Figure 3.4: Spacecraft Plume with Starlink in its Closest and Furthest Position.

Operating distance

The distance from the debris in which the spacecraft will operate is a variable that can be chosen. The trade-off is mainly done between propellant mass, safety and reliability (amount of rendezvous). The 2 variables that can be chosen are the closest distance range and the furthest distance (where the main thruster will fire and stop firing). Closest distance ranges of 2-3 m, 3-4 m, and 4-5 m were considered, as closer than 2 m will be very unsafe and will not increase efficiency anymore. More than 5 m will lead to an unnecessarily high rendezvous or propellant amount. The furthest distances that will be considered are 4-15 m in intervals of 1 m. All the options are plotted in Figure 3.5 for a 1000 kg wet mass. It is visualised in a scatter plot since the calculations are computationally intensive and cannot be done for all intermediate values.

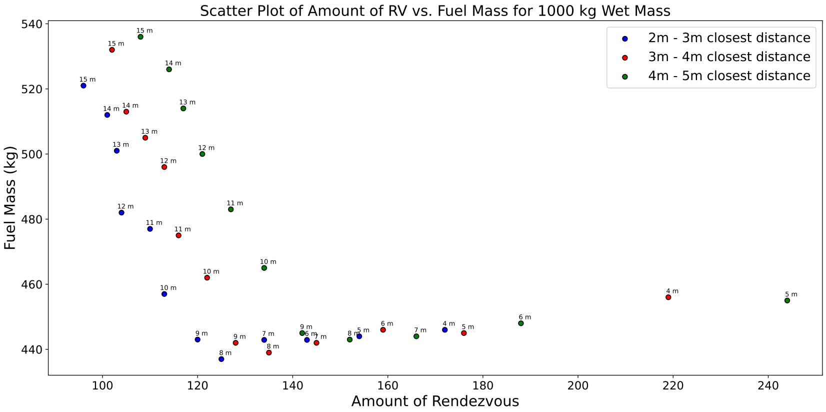

Figure 3.5: Fuel Mass and Amount of Rendezvous for Different Operating Distances.

For an optimal operating distance, a dot on the lower left needs to be chosen, while also taking into account safety. A small increase in propellant mass is justified by a big increase in safety. For this reason, 3-4 m closest distance and 9 m furthest distance are chosen.

Initial Relative Velocity V_{r0}

The optimal initial relative velocity needs to be reached every rendezvous. Initial relative velocity is dictated by the operating distances. It needs to be chosen such that when starting to apply thrust at the furthest operating distance, it will reach the closest operating distance range and then return to the furthest operating distance. There are many relative velocities that will comply with this requirement, so the optimum needs to be found. In this case, optimal relative velocity depends greatly on safety: the lower the better. In case of failure of the thruster, collisions may occur where lower velocities are preferred. To find the optimal relative velocity, values are tested starting from zero and increasing afterwards in small steps. The first value that corresponds to the operating distances is chosen. This value is in the order of magnitude of 4-5 m/s, depending on the mass of the ADR spacecraft at each rendezvous, which is deemed a safe approaching speed.

Target Sequencing Logic

The orbital manoeuvring complexity, the required ΔV, and therefore, fuel mass, highly depend on the approach selected for target sequencing. The most straightforward strategy is to de-orbit targets 1-by-1, which was initially selected. Detailed analysis of the primary option can be seen in the next subsection. However, to guarantee the optimal targeting sequencing logic, one must also assess an alternative method, 10-by-10. 10-by-10 refers to a concept of performing a singular momentum-transferring burn on all ten debris, effectively moving them to the same elliptical orbit and repeating this sequence layer by layer until all the debris reaches the target passive de-orbiting perigee altitude of 381km, which is the maximal altitude for a 260 kg debris to de-orbit in the required time-frame [14],[38].Figure 3.6 depicts a single de-orbiting cycle of the 10-by-10 method.

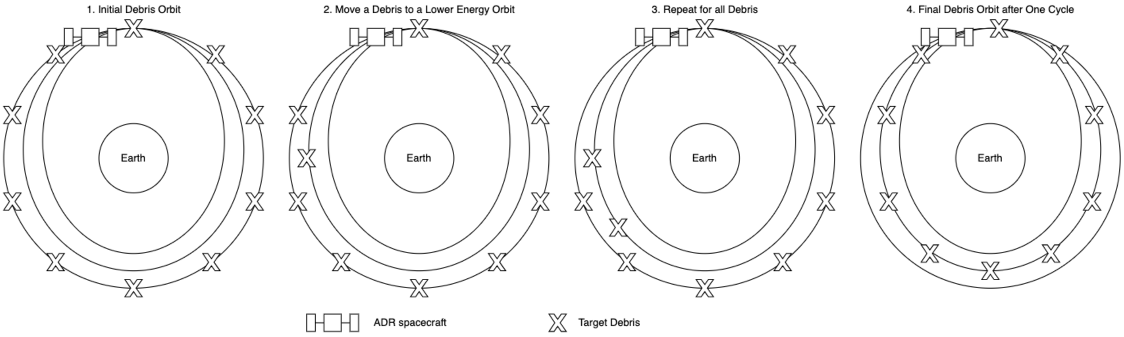

Figure 3.6: Schematic Description of a Single Orbital Cycle of the 10-by-10 Method.

In order to select the best sequencing logic, it is of paramount importance to consider equivalent conditions for both methods to improve the objectivity of the results. For that, it was chosen to assess the alternative 10-by-10 strategy on the standard, simplified target scenario. In that scenario, all targets are Starlink V1 satellites orbiting Earth at 600 km altitude in LEO. The same target mass and altitude allow for a valid comparison of the methods. Furthermore, to evaluate the time-performance of the strategies, all of the targets were assumed to be equally spread through the orbit, leading to a 36-degree phase difference between all consecutive targets at the start of the operation. Also, for orbital time estimation, the orbital period for all orbits was assumed to be equal to that of a circular 600km LEO, which is $\approx$96.5 minutes. This assumption was deemed reasonable as the orbital period for the final debris orbit (i.e. the inner most layer with perigee at 381km altitude) is only $\approx$2 minutes slower. It must be mentioned that it is possible that some hybrid of 1-by-1 and 10-by-10 strategies could be optimal for a specific combination of targets' masses, altitudes, and phase differences. These cases will not be considered at this stage due to the immense computational complexity and sensitivity to initial conditions. As a recommendation, an optimisation algorithm that considers the hybrid options could be created in later stages of the mission design, but it falls outside of the scope of this report.

In order to evaluate the 10-by-10 de-orbit targeting sequence method, and hence assess potential advantages and disadvantages it has compared to 1-by-1 de-orbiting, one has to consider mission constraints. The most significant constraints that exist, following from the user requirements, are mission duration (**[R-SYS-05]**) and mission cost (**[R-SYS-26]**). Naturally, mission duration is directly affected by the operational procedure, meaning that the debris targeting sequence is of utmost importance. Mission cost, although a crucial mission parameter, is influenced by the targeting sequence on a secondary level, as the cost arises from the fuel required to perform the mission, which will increase launch cost, assuming that the bus and other components involved are considered fixed.

Therefore, the feasibility assessment begins with the consideration of the time constraint. As per **[R-SYS-05]**, all debris objects shall be de-orbited within a year from launch. Previous calculations [14] show that a debris object with a perigee altitude of 381km passively de-orbits (i.e. reaches perigee altitude of 100km, where it disintegrates because of atmospheric drag) within 281.93 days from the last momentum transfer manoeuvre on said debris. Based on this, the ADR satellite has (365 - 281.93) = 83.07 ≈ 83 days, to perform all manoeuvres on all debris objects. Assuming an average orbital period of 96.5 minutes at LEO, 83 days is enough time for the completion of ≈1240 orbits around Earth. Including a safety margin to this number, 1200 orbits around Earth is the ”maximum” time allowed for any operation to take place. After this, the debris passively de-orbits while the ADR satellite performs its EoL manoeuvre.

Having established this, the next step is estimating the total number of orbits required to complete the mission through the 10-by-10 approach. The following formula conservatively estimates this number, taking into account all of the major manoeuvres to be performed:

$$X = [N \cdot (f(\Delta\Phi) + 1)] \cdot (N_{Mt} - 1) \tag{3.6}$$

where X is the total amount of orbits (i.e. 1200), $N = 10$ is the number of debris objects to be de-orbited, $N_{Mt} = 33$ is the approximate number of momentum transfer manoeuvres on each debris object (a conservatively large value that was found during preliminary design when constant efficiency was assumed), and $f(\Delta\Phi)$ is the number of orbits needed to time the rendezvous with the debris, when transferring from debris to debris. Essentially, the entire parenthesis that is multiplied by N captures the phase shift to be performed to rendezvous with the next debris, an orbit for correcting for the initial relative velocity between the ADR satellite and the debris, as well as a separate orbit accounting for the post-burn duration until the ADR satellite reaches apogee again (the ”+1” term).

Solving for $f(\Delta\Phi)$ yields that transferring between targets must be done within 2.75 orbits (i.e. 2 orbits), per debris, per rendezvous. If this is not met, then the mission duration requirement is violated, and the mission fails.

The transfer between targets, now, entails two manoeuvres. One accounting for the phase shift of 36° (as per the generic case when all debris is symmetrically positioned around Earth discussed above), and a separate one to account for the V_{r_0} at rendezvous. Naturally, these two manoeuvres have to be performed at the apogee of the orbit such that the rotation of the orbit's line of apsides is avoided, meaning that this already hits the limit of 2 orbits.

To induce a passive phase shift, the ADR satellite needs to change its orbit either to a lower one or a higher one, as ”chasing” the debris object is equivalent to letting the debris ”chase” the Starfixers Inc. spacecraft. When performing this analysis, it was shown that lowering the orbit such that the phase shift after one orbit is 36° is not possible, as the satellite would have to traverse through Earth's surface. Therefore, the satellite needs to enter a higher orbit to achieve this. The calculated perigee and apogee altitude for this higher orbit (to transfer to another debris object at 600 km altitude) is 6971km and 7971km, respectively (with a semi-major axis of 7471km). To make this possible, a manoeuvre of $\Delta V \approx 750$m/s is required. This is a very large value, and considering that this has to be done approximately $10 \cdot 33$ times, it deems the 10-by-10 approach infeasible. Additionally, when considering an improved momentum transfer efficiency, the total number of momentum transfer manoeuvres per debris (M_t) changes from 33 to 11, where 11 is the least possible number of manoeuvres and is not conservative. This leads to a new transfer requirement of 11 orbits when using Equation 3.6, where the majority of the 36-degree shift must be performed in 10 orbits following the logic described above. This leads to significantly better results of only 25m/s per transfer, and the transfer only needs to be performed $10 \cdot 11 = 110$ times, leading to the total ΔV of 2750 m/s, when considering the best efficiency numbers. A Python algorithm was created to calculate the ΔV for non-transfer manoeuvres of the 10-by-10 method, which was found to be around 2570 m/s. Thus, the best-case scenario 10-by-10 requires $\approx$ 5320 m/s of ΔV, which is around double that of 1-by-1 found in Table 3.1, leading to a complete rejection of the method.

Moreover, besides the changes in operational procedure for the 10-by-10 strategy, there are other mission aspects that play an important role. First of all, atmospheric drag and its effect significantly differ between the two de-orbiting approaches. When considering the 10-by-10 approach, all debris objects are moved to the next, lower, orbit, where the ”loop” of manoeuvring restarts, until all debris are de-orbited from the last layer (orbit), in contrary to the 1-by-1 approach, which entails a full de-orbit of one individual debris before moving on to the next one. The effect of drag on this is massive. When one considers that drag starts acting before the debris reaches a perigee of 381km altitude (for its passive de-orbit), the operation becomes way more complex, as unequal drag effects will act on the different debris objects, leading to the change of their orbits. This is why, realistically, the 10-by-10 method results in 10 different orbits and/or orbital planes of the debris as the operation moves on, making the mission way more complex and removing the control that Starfixers Inc. have over the mission. Even though drag also exists in the 1-by-1 scenario, the effects differ. This is because when ”following” each debris closely until it de-orbits, drag acts on the ADR satellite as well, mostly cancelling out its relative effect.

Further aspects that need to be mentioned regard collision probability and sensitivity to initial conditions. Expanding on the former, when moving all debris through 33 (or 11) orbital layers until they de-orbit, the collision risk is exponentially increased, as any miss-timing could have catastrophic consequences. The latter concerns the initial radial position of the debris objects before operations commence, and it is true that, although a generic case of equally spaced debris at 36° increments was considered, any alteration on this could lead to more complex operations and waiting times for passive phase shifting, potentially violating the time constraint of the mission. Finally, for the reasons analysed above, the Starfixers Inc. group discarded the 10-by-10 method and will go forward with the already discussed 1-by-1 approach.

Sequential Operational Procedure

Now that the target de-orbiting sequence was determined, it is possible to delve deeper into the different phases of the operational procedure. Figure 3.7 illustrates all de-orbiting stages for a single target, including repeated rendezvous operations until the transfer to the next piece of debris, which will be discussed in detail in this section.

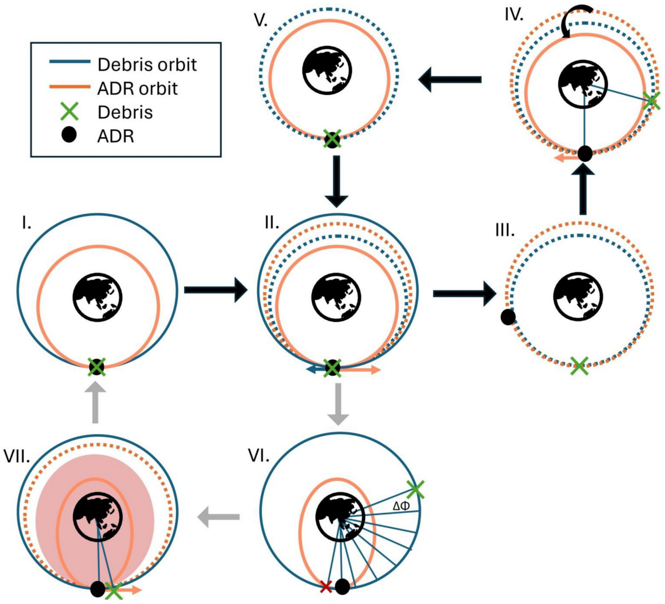

Figure 3.7: Sequential Operational Procedure.

I. In this phase, the ADR spacecraft finds itself in a lower energy orbit than the target, ready to meet at apogee for the momentum transfer with the correct relative velocity.

II. At this stage, the momentum transfer, as explained in Section 3.2, takes place. The ADR spacecraft is propelled to a higher energy orbit than the initial one, while the target debris is decelerated into a lower energy orbit. Since the ADR spacecraft is faster than the target when leaving the rendezvous, its new orbit will always be a higher energy orbit than the new target orbit. The exact new orbit altitudes can be computed using the ΔV of each body and rearranging the vis-viva equation (Equation 3.7), where a_{sm} is the semi-major axis in meters, r the radius at apogee in meters as well, and μ is the standard gravitational parameter in $\mathrm{m}^3\mathrm{s}^{-2}$. After this step, it is required to check if enough ΔV was applied to the debris. If it is the case, no additional rendezvous are required with this target and the ADR spacecraft can go on with phase VI., which will be explained further. Otherwise, additional rendezvous would be required to perform more momentum transfer manoeuvres, and phase III would follow.

$$V = \sqrt{\mu\left(\frac{2}{r} - \frac{1}{a_{sm}}\right)} \tag{3.7}$$

III. After one period in these new orbits, the ADR spacecraft will lag behind on the target due to the difference in orbital period ΔT, where period is computed with Equation 3.8.

$$T_{2\pi} = 2\pi\sqrt{\frac{a_{sm}^3}{\mu}} \tag{3.8}$$

IV. The idea of this phase is to catch up with the same debris in two orbits. As the ADR spacecraft had a longer period for the first orbit, a decelerating ΔV should be applied when the ADR spacecraft reaches its apogee, to propel it to a lower energy orbit. This lower energy orbit should be such that Equation 3.9 is satisfied, were $T_{2\pi,\mathrm{ADR}_1}$ is the ADR spacecraft orbital period of the first orbit, $T_{2\pi,\mathrm{ADR}_2}$ the ADR spacecraft shorter orbital period of the second orbit, and $T_{2\pi,\mathrm{debris}}$ is the constant orbital period of the debris. The exact ΔV can be computed using Equation 3.7 and Equation 3.8.

$$2T_{2\pi,\text{debris}} = T_{2\pi,\text{ADR}_1} + T_{2\pi,\text{ADR}_2} \tag{3.9}$$

V. If the ΔV of step IV. is applied successfully, ADR spacecraft and target should meet again at apogee, where a burn will be performed to get the correct relative velocity. Then the momentum transfer would be reapplied to the same target and phases II. to V. would be repeated.

VI. Once the last momentum transfer has been applied to a debris, the ADR spacecraft will find itself in an orbit with a perigee around 381 km altitude, and will have to meet with the next debris in the initial circular orbit. In this phase, the debris will catch up with a certain $\Delta\phi$ (in degrees) according to Equation 3.10. Once the debris passively arrives at an orbital position, relative to the ADR spacecraft, where another orbit (so another $\Delta\phi$) overshoots the "catching-up" motion, a ΔV will be applied in order to prevent this event.

$$\Delta\phi = \frac{T_{2\pi,ADR} - T_{2\pi,circular}}{T_{2\pi,circular}} \cdot 360^\circ \tag{3.10}$$

VII. In this last phase, a ΔV is applied so that the ADR spacecraft meets with the debris after an integer number of orbits. This ΔV should be such that the debris keeps catching up by an angle smaller than $\Delta\phi$ to minimise the number of orbits while ensuring that the new relative velocity with the debris is smaller than the maximum allowed relative velocity of 8m/s. The red zone in phase VII. represents all of the orbits within this range. Phases I. to VII. are repeated until all debris is de-orbited.

The results in terms of ΔV, mass, and time for the general case defined previously, following this procedure, are presented in Table 3.1. A 10% margin for dry mass is included for contingency reasons, as well as additional fuel mass accounting for the possibility of de-orbiting an extra debris object in case of procedure failure. Both of these margins are included in the 'Dry mass + extra fuel' result. The computational model used for this sequence of operations will later be explained in the 'Optimisation and Method Adaptability' subsection of Section 3.3.

Table 3.1: Results for the General Mission of 10 Satellites at 600 km Altitude.

General case values	
Wet mass	646 kg
Dry mass + extra fuel	294.1 kg
Fuel mass	351.9 kg
ΔV	2586.8 m/s
Number of RDV	153

3.3 Additional Considerations

Given the time constraints of the project, only a selection of mission aspects could be examined in greater detail. Among the areas selected for further evaluation are the influence of atmospheric drag and the possible tumbling behaviour of the debris. Drag behaviour must be assessed to quantify its effect on the required mission ΔV. With regards to tumbling, it could necessitate the development of de-tumbling strategies, causing potential structural integrity issues. Then, collision avoidance manoeuvres, optimisation, and method adaptability are also analysed further in detail.

Drag

To assess whether atmospheric drag has a significant effect on the spacecraft throughout the entire ADR mission and not just during the final de-orbiting phase, a drag model was integrated into the main orbital simulation. This model estimates the spacecraft and debris altitude during each rendezvous and two-orbit phasing manoeuvre, calculates the corresponding atmospheric density, and derives the resulting drag force and velocity loss. By incrementally summing these effects across all mission phases, the simulation provides a total ΔV loss due to drag. This allows for evaluating whether the accumulated loss requires additional propellant or remains negligible within the mission's LEO operational altitude range.

At each rendezvous and two-orbit phasing step, the velocities of both the ADR spacecraft and the debris were used to compute the current semi-major axis via the vis-viva equation, as seen in Equation 3.7. Assuming a fixed apogee of 600 km altitude, this allowed for the derivation of the corresponding perigee radius, and thus the instantaneous orbital altitude, using $r_{\text{per}} = 2a_{sm} - r_{\text{apo}}$ and $h = r_{\text{per}} - R_{\text{Earth}}$. With the altitude known, the atmospheric density at each step was estimated using an exponential model representative of the LEO environment, as seen in Equation 3.11.

$$\rho(h) = \rho_0 \cdot \exp\left(-\frac{h - h_0}{H}\right) \tag{3.11}$$

Here, $\rho_0 = 3.614 \cdot 10^{-13}\ kg/m^3$ is the reference density at 400 km, and H=60km is the scale height. These parameters are consistent with standard atmospheric models for altitudes between 300–600 km. The drag force was then computed for both objects using Equation 3.12.

$$F_{\text{drag}} = \frac{1}{2} \cdot C_d \cdot A \cdot \rho(h) \cdot v^2 \tag{3.12}$$

where $C_d = 2.4$ for the debris and $C_d = 2.2$ for the ADR spacecraft, chosen based on empirical estimates for compact and panel-equipped bodies in free molecular flow regimes.[59] A is the cross-sectional area calculated to be 32.8 m² for the debris and 3 m² for the ADR spacecraft. The resulting acceleration was obtained by dividing the drag force by mass, and the incremental ΔV loss per orbit was estimated using Equation 3.13.

$$\Delta v_{\text{drag}} = a_{\text{drag}} \cdot t_{\text{drag}} \tag{3.13}$$

In this, $t_{\text{drag}} = 2897$s, approximating the time the spacecraft spends in the lower half of its elliptical orbit, where the atmospheric density is significantly higher and drag forces are more pronounced. Although this does not represent the final de-orbiting phase, such elliptical orbits occur frequently during routine two-orbit phasing manoeuvres at LEO altitudes. As a result, the per-orbit impact of drag remains small but persistent throughout the mission.

Each computed drag-induced velocity loss was subtracted from the instantaneous velocity of both the ADR spacecraft and the debris and cumulatively stored in a list. At the end of the simulation, the total additional ΔV required to counteract drag across the entire mission was calculated and found to be approximately 0.1296 m/s, which is negligible relative to the mission's total propellant expenditure. This is visualised in Figure 3.8, which plots the drag-induced ΔV per orbit as a function of altitude across all rendezvous phases. The figure clearly shows that the drag losses grow as altitude decreases, consistent with the exponential increase in atmospheric density and the quadratic dependence of drag on velocity. Each horizontal band in Figure 3.8 corresponds to one debris target, and within each band, the drag grows with successive orbits at lower altitudes. This trend confirms that while drag becomes more significant near the lower end of the operational altitude range, its cumulative effect across the full mission remains minimal. Therefore, drag-induced losses do not require dedicated compensation in the propellant budget.

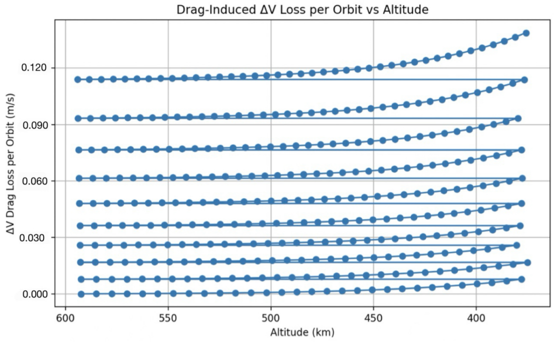

Figure 3.8: Drag-induced Velocity Loss per Orbit as a Function of Altitude.

Tumbling

When a Starlink satellite loses attitude control due to onboard failures or power loss, it gradually begins to tumble in space instead of maintaining a stable orientation. This behaviour is common among defunct satellites; once active stabilisation stops, external forces take over. Starlink satellites, equipped with reaction wheels and magnetorquers, rely on these systems to maintain precise attitude, but without control they are affected by environmental torques such as solar radiation pressure, gravity-gradient forces due to their asymmetrical structure, and weak aerodynamic drag at LEO altitudes of around 600 kilometers [32]. Observations across many retired satellites show that nearly all enter some form of tumbling, and Starlink is no exception. SpaceX defines any rotation exceeding 0.005 radians per second as unstable, equivalent to one full rotation in about 20 minutes [40]. Without active damping, small perturbations accumulate over time, causing the satellite's angular velocity to increase. Defunct Starlink satellites typically tumble with angular velocities between 0.01 and 0.1 radians per second, resulting in rotation periods of 60 to 600 seconds, with no reported cases of extreme spin rates [17, 36].

While there is no direct published data on the exact tumble axis of defunct Starlink V1 satellites, analysis of their design suggests that any arbitrary rotation can be decomposed into rotations around the satellite's principal axes [36]. For simplification, the dominant rotational modes are assumed to align with the principal axes. Due to the asymmetrical mass distribution, with a central bus and an extended solar panel, end-over-end tumbling around the axis perpendicular to the main bus surface, labelled as the Y-axis in Figure 3.9, is expected to be significant. This mode causes the satellite to flip forward in an end-over-end motion. Considering the solar panel has a length of 8.86 meters [30], and that the distance from the satellite to the Starfixers Inc. spacecraft will be as close as two meters at some point, this is critical. A collision between the solar panel and the ADR spacecraft would create additional debris, which is not in compliance with [**R-SYS-12**].

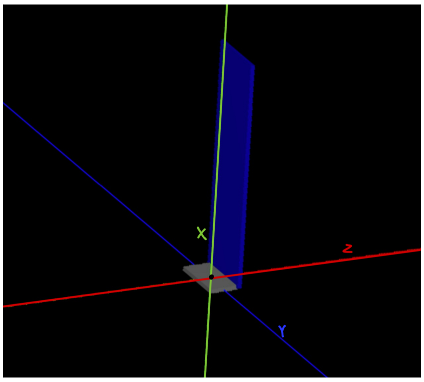

Figure 3.9: Axes of Starlink Satellite.

To tackle this issue, the tumbling behaviour of the Starlink V1 satellite was analysed by modelling its rotational dynamics around the principal axes. The satellite was treated as a rigid body with constant mass and uniform density, which is a standard assumption for intact, non-fragmented spacecraft and is particularly valid for the monolithic structure of the Starlink V1 design. Its principal mass moments of inertia (MMoI) about the X, Y, and Z axes were calculated using the standard formulation for a uniform rectangular prism as seen in Equation 3.14.

$$I_i = \frac{1}{12} m(d_j^2 + d_k^2) \tag{3.14}$$

where m is the mass of the satellite element, and d_j, d_k are the dimensions orthogonal to axis i. The solar panel consists of two parts, the cell-interconnect-coverglass (CIC) and the structural reinforcement. A 2.06 kg/m^2 CIC combined with the structural mass gives a total mass density of approximately $4kg/m^2$ [92]. The solar panel has a $8.86m$ span and a $3.7m$ width, leading to an area and mass of $33m^2$ and $132kg$ respectively. Since the total mass is $260kg$, the bus mass is $128kg$. Now, the centre of mass (CoM) position can be determined, and moments of inertia can be calculated. The CoM position is $(2.32, 0, 0.37)$, so the distance between the CoM of the Starlink V1 components and the global Starlink V1 CoM is known, which is necessary to compute the MMoI. The MMoI around the X-axis and Y-axis were computed in a Python script [8], outputting 807.50 kg/m^2 and 2199.34 $kg \cdot m^2$ respectively.

Although real satellite tumbling involves complex coupled rotational dynamics, any arbitrary angular motion can be decomposed into rotations about the principal axes of inertia through eigenvalue analysis. Therefore, for simplification, the analysis assumes decoupled single-axis rotation, which captures the dominant behaviour and avoids the need for solving the full Euler rotational equations.

To represent a worst-case operational scenario, the initial angular velocity was set to 1 revolution per minute (RPM) as for **[R-SYS-39]**, corresponding to an angular rate of approximately 0.104 radians per second.

Detumbling was modelled by applying an external torque generated by a 465 N spacecraft-mounted thruster, assuming a fixed efficiency of 50%. While the true momentum transfer efficiency varies with distance and plume dispersion, a constant value of 50% was chosen based on the previously derived momentum transfer efficiency model to represent a conservative average for the detumbling phase. The applied torque is expressed in Equation 3.15 as the product of an effective thrust force $F_{\text{effective}}$, accounting for plume efficiency losses, and the lever arm distance r, from the CoM to the point where the thrust acts, perpendicular to the axis of rotation.

$$\tau = F_{\text{effective}} \cdot r \tag{3.15}$$

The lever arm r_i for each rotation axis is defined as the maximum distance of the point of action of $F_{\text{effective}}$ from the global Starlink V1 CoM.

- X-axis spin: The solar array spans $L_x = 8.86\,\text{m}$ in the $+X$ direction, and the CoM is located at $x_{\text{COM}} = 2.32\,\text{m}$. Hence $r_X = L_x - x_{\text{COM}} = 8.86 - 2.32 = 6.54\,\text{m}$.
- Y-axis spin: The bus width is $L_y = 3.7\,\text{m}$, so the furthest edge is half that distance from the CoM: $r_Y = \frac{L_y}{2} = \frac{3.7}{2} = 1.85\,\text{m}$.
- Z-axis spin: The cross-sectional dimension perpendicular to Z is negligible, so thrust-impingement detumble about Z is not practical, so r_Z is omitted.

These represent the maximum theoretical lever arms for torque generation, although practical values may be slightly lower due to plume divergence and targeting inaccuracies, which are conservatively accounted

---

[8] https://github.com/ViktorZupnik/Starfixers/blob/Final-Branch/Orbital%20mechanics%20and%20procedure/Tumbling.py

for by the efficiency factor applied to $F_{\text{effective}}$. Given the torque, the angular acceleration about each axis was determined using Equation 3.16

$$\alpha_i = \frac{\tau}{I_i} \tag{3.16}$$

The satellite's angular velocity was iteratively updated over discrete time steps by applying this angular acceleration. Detumbling was considered achieved once the angular velocity magnitude dropped below a predefined operational threshold of 0.005 rad/s, consistent with SpaceX's definition of an unstable satellite attitude.

Environmental perturbations such as solar radiation pressure, gravity-gradient torques, and atmospheric drag were neglected during this process. This is justified because the characteristic time to detumble (minutes to tens of minutes) is short relative to the timescales over which environmental torques act significantly, and the magnitudes of these perturbations are orders of magnitude smaller than the applied control torque.

In parallel, the cumulative velocity increment (ΔV) expended by the thruster was computed by discretising the total time. t into increments and "looping" Equation 3.17 over those increments. This way, the incremental ΔV values can be determined and then summed up, resulting in the final ΔV induced by de-tumbling operations.

$$\Delta V = \frac{F_{\text{effective}} \cdot t}{m} \tag{3.17}$$

Finally, it is assumed that the Starlink V1 satellite does not undergo structural deformation or fragmentation during the manoeuvre, and that the CoM remains fixed relative to the body frame. This procedure enabled the estimation of the total time and propellant consumption required to safely reduce the satellite's tumbling to acceptable levels. The results are summarised in Table 3.2 and can be seen in Figure 3.10 and Figure 3.11, where it is clear that the X-axis detumble uses about 0.347 m/s in 0.19 s, whereas the Y-axis detumble requires roughly 0.274 m/s over about 0.15 s before the spin falls below the 0.005 rad/s threshold. The nearly perfectly linear slopes reflect the bang–bang law: a constant translational acceleration $F_{\text{effective}}/m$ applied to the Starlink V1 satellite until each ω_i (angular velocity around an i^{th} principal axis of the debris) reaches zero.

Together, these results confirm that a bang–bang pulse about the Y-axis is both faster and lower in ΔV than an equivalent pulse about the X-axis, exactly as expected from the higher angular acceleration α_y versus α_x. This quantifies a clear strategy: always eliminate the higher-inertia spin with larger ΔV and then devote the rest of the ΔV to the lower-inertia spin.

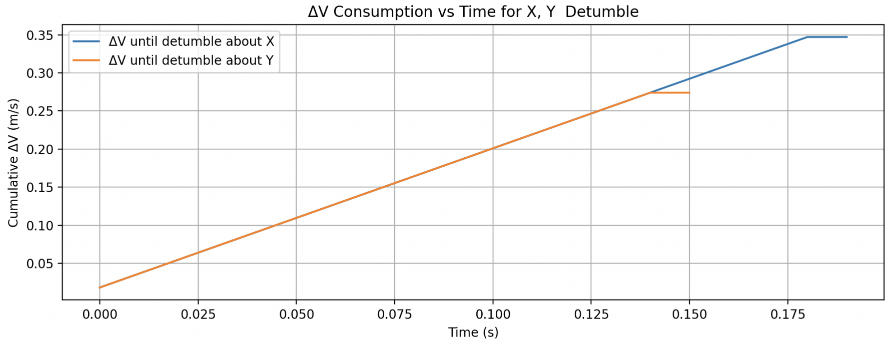

Figure 3.10: Cumulative ΔV Consumption Over Time During Single-axis Detumbling About X and Y.

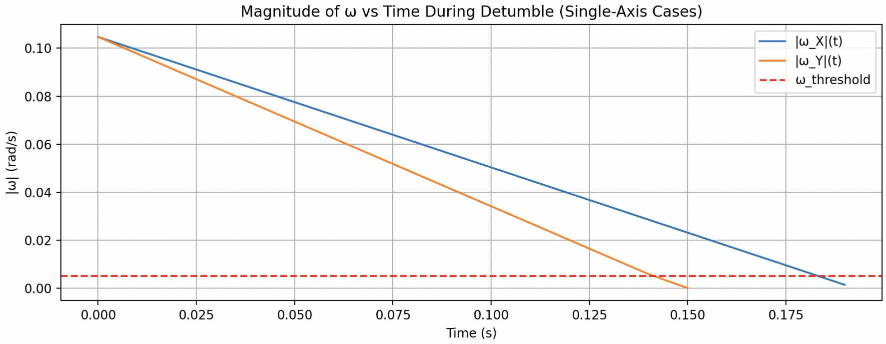

Figure 3.11: Angular Velocity Decay Over Time for Each Axis During Detumbling, Compared to Threshold $\omega_{\text{threshold}}$.

Table 3.2: Detumbling Performance per Axis.

Axis	α [rad/s^2]	t [s]	ΔV [m/s]
X	0.544	0.19	0.347
Y	0.706	0.15	0.274

De-tumbling approach

The principle behind the approach the ADR will take to stabilise the Starlink V1 debris is very straightforward. The thruster that is used to de-orbit the targets is also used to detumble them. Basically, if thrust is not exactly applied through the CoM, a torque will be induced on the target. If located correctly, this can exactly counter the torque that the target was experiencing. A sidenote: torque around the Z-axis can not be countered, since the movement is perpendicular with respect to the thrust vector, i.e. nothing can be done to stop it. On the other hand, for the same reason, the de-orbiting can then still be performed because the solar panel surface will always face the thruster perpendicularly.

Consequently, there are two other axes around which the target can rotate, and the detumbling principles are the same for both cases. Say there are four possible orientations of the spacecraft, A, B, C and D, as in Figure 3.12. Imagine cases A and B, where the target is rotating towards the ADR spacecraft, but not perpendicular yet, and where it is rotating the same way, but it has already been in a perpendicular position. It is easy to see now why rotation around the Z-axis can not be stopped, there would be no surface perpendicular to the ADR spacecraft to stop rotation. For detumbling and de-orbiting, it is not relevant whether the target is facing towards the ADR spacecraft or rotated 180°. Position C and D in Figure 3.12 are like positions A and B, but rotated 180°.

In case A and C, one burst is sufficient to stop the rotation. When timed correctly, and the de-tumbling burn entirely eliminates the debris' spin, the debris' rotational rate can be exactly zero when the solar panel is pointing straight up or straight down, ensuring a perpendicular area for the thruster to start de-orbiting the target. However, in case B and D, if the same action were performed, the rotational velocity would be zero when the solar panel is not pointing straight up or down, so not perpendicular to the ADR spacecraft. To solve this, first, thrust will be applied below the CoM (with below being in the direction of negative X-axis) to accelerate the rotational velocity in a clockwise direction. This means that in the same rendezvous, the orientation of the target will go from B to C or from D to A. Then, when the timing is right and the target satellite is in either position A or C, a second thrust will be expelled, and the rotational velocity will be zero again.

For safety, the distance between target and the ADR spacecraft has to exceed $6.64m$ (the distance between CoM and solar panel top edge) to ensure no extra debris will be created by contact between the two objects. When the target is rotating in an anti-clockwise direction, the same approach is used, but now for both positions B and D, one burst is sufficient, while positions A and C must first be rotated to position B and D. With rotation around the X-axis, the same principle is used. The only difference is that, instead of a thrust burst below or above the CoM, the thrust will be to the left or right of the CoM. The maximum distance from the CoM at which the thrust can be applied is smaller than in the Y-axis-rotation case, because the solar panel width is smaller than its length. However, the MMoI around the X-axis is smaller than around the Y-axis, so this makes it easier to stop the rotation.

The ADCS will make sure that the ADR satellite is able to thrust wherever required, while the gimbal accuracy ensures high certainty on the location of the thrust vector, which, together with the knowledge of rotational velocity ensures that the ADR spacecraft can determine for how long the thrust needs to be applied in order to stop the rotation. This location determines the distance from the CoM and thus the moment arm of the force. If additional control authority or finer tuning is required, the spacecraft can also fire its adverse thruster, which applies torque in the opposite direction, to help decelerate any residual spin or to rapidly reverse the applied torque during a bang–bang detumble sequence, while the ADCS cold gas thrusters can cancel the induced translational motion of the ADR spacecraft.

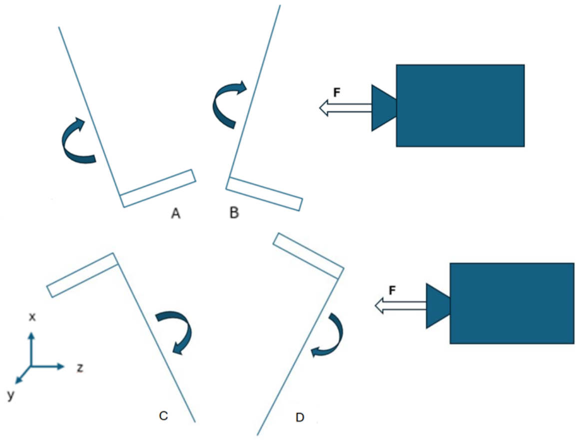

Figure 3.12: Detumbling Approach on The Starlink Satellites.

Structural Integrity of Solar Panels under Thrust

When thrust is applied to the solar panel of the Starlink V1 satellite, the loads induced might break the solar panel structure, something that, again, is not in compliance with [**R-SYS-12**]. To test this, two approaches can be used.

The ADR spacecraft will be applying thrust in a range from 3 to 9 metres, depending on the rotational velocity of the target, at different distances from the CoM. Analysis can be performed on the maximum load that will be induced on the solar panel, and on whether it can withstand this load. This requires a thorough investigation on how the force acting on the solar panel changes with distance and angle of contact. For example, from a distance of 3 metres, a force acting on the very top of the panel has a different effect than from 9 metres acting just above the CoM.

The other approach is to check whether the solar panel structure can handle a force acting perpendicular to the solar panel, from a distance of 2 metres (using one less meter as a safety margin), as illustrated in Figure 3.13. While this is the maximum possible torque, it is not realistic since the thruster will be aligned with the CoM of the target. However, if the structure can cope with this hypothetical maximum load, it can cope with any other situation. This approach is much easier to assess, and thus will be performed first. It is assumed the attachment to the bus is perfect, so it can handle any stress, and no vibrations or oscillations are considered.

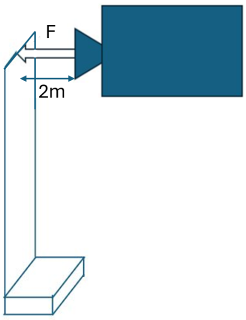

Figure 3.13: Diagram of Worst-case Scenario Detumbling.

Since no material and structural specifications of the solar panel are known, a simple analytical model for worst-case bending stress has to be used. In essence, the situation resembles a cantilever plate under a point load that is supported at its base. However, the base itself is not supported, but has six degrees of freedom. For panel thickness and material, a total of $5mm$ and CFRP-like laminate are assumed. The latter has an elasticity modulus E of approximately 70 GPa. The area moment of inertia (AMoI) around the Y-axis equals

$$I_{A,y} = \frac{bh^3}{12} = \frac{3.7 \cdot 8.86^3}{12} = 214.45m^4, \tag{3.18}$$

where b is the panel width and h is the panel height. For a force of 465N acting on the cantilever beam with a length (height) of 8.86 and a $c = \frac{h}{2} = 0.0025m$ distance from the neutral axis to the outer edge enables the bending stress calculation. The maximum bending moment M_b is the force multiplied by the panel length, i.e. $465 \cdot 8.86 \cdot 0.5 = 2059.95 \approx 2060Nm$ (this accounts for the aforementioned fixed efficiency at 50%). The effective lever arm is taken as the distance from the top of the solar panel to its attachment point on the Starlink V1 bus, i.e. equal to 8.86 m. Consequently, the bending stress is calculated:

$$\sigma = \sigma_{max} = \frac{M_b \cdot c}{I_A} = \frac{2060 \cdot 0.0025}{214.45} = 0.024Pa \tag{3.19}$$

which is well within the CFRP maximum bending stress of around $1500MPa$ [4]. Since bending is dominant, the structural integrity of the Starlink satellite will be maintained during both detumbling and de-orbiting.

Sensor-Driven Initial Characterization

Before initiating detumbling, the ADR spacecraft must characterize the debris motion using onboard sensors. This is essential to target the correct axis and apply controlled torque effectively. In order to do this, the ADR spacecraft must:

- Measure the debris's angular velocity vector $\vec{\omega}_{\text{deb}} = [\omega_x, \omega_y, \omega_z]$ in its principal-axis frame.
- Estimate the orientation of the debris's body axes in inertial space (e.g., via quaternion or rotation matrix).

This is achieved through:

- High-rate imaging or LiDAR to detect feature rotation and angular rate.
- Star-tracker/IMU on the spacecraft to maintain an absolute inertial reference.
- Cross-frame motion tracking to compute $\vec{\omega_{\text{deb}}}$.

Debris typically spins around all three axes $(\omega_x, \omega_y, \omega_z)$. To simplify this, each axis is addressed sequentially:

1. Measure body rates and identify the axis i_1 with the largest $|\omega_i|$.
2. Orient the spacecraft so the thruster plume applies torque perpendicular to axis i_1 at the largest lever arm r_{i_1}.
3. Burn at a point that induces rotation opposite to ω_{i_1}, applying $\tau_{i_1} = F_{\text{effective}} \times r_{i_1}$, until $|\omega_{i_1}| < \omega_{\text{threshold}}$ (e.g. 0.005 rad/s), then shut off.
4. Re-measure ω, identify next axis, i_2, and repeat.
5. Final clean-up on remaining axis i_3.

Collision Avoidance Manoeuvres

In order to comply with **[R-SYS-34]** and **[R-SYS-38]**, a thorough study on collision probability and avoidance manoeuvres has to be carried out:

As the debris flux varies depending on the altitude at which a spacecraft is situated, a discretisation was made for the passive de-orbiting of a 260kg Starlink from an orbit at 600km altitude at apogee and 381km perigee, after the ADR spacecraft performed the last momentum transfer manoeuvre. This discretisation was made using the OSCAR tool from DRAMA [38], using an average area for the Starlink V1 satellite of 19.5577 m^2, calculated using CROC (again, from DRAMA [38]). The segmentation is displayed in Figure 3.14:

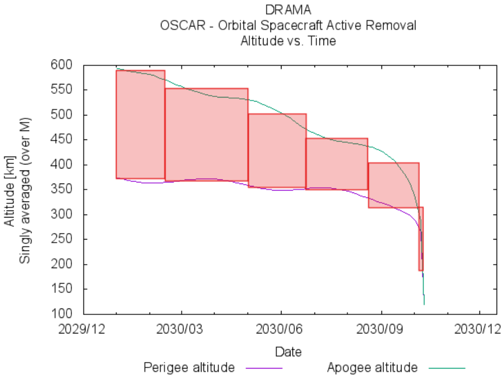

Figure 3.14: Discretised Altitudes for the Debris De-orbiting Phase.

The discretised orbital segments, the debris flux at each of them, and the probability of collision for the debris at each of them, are displayed in Table 3.3:

Table 3.3: Orbital Segments, Flux & Time per Segment and Collision Probability for the De-orbited Debris.

Perigee h [km]	Apogee h [km]	Flux [km^{-2}yr]	Time [months]	Pc ($\cdot 10^{-4}$)
370	585	34.63	1.5	0.847
360	550	30.71	2.5	1.251
350	500	18.24	1.8	0.535
345	450	14.25	1.8	0.418
300	400	6.639	1.5	0.162
180	300	1.503	0.1	0.00245
TOTAL			**9.2**	**3.215**

The same methodology is followed to calculate the collision probability of the ADR spacecraft during its de-orbiting phase, now using an average area of 3 m^2. The orbit segmentation during the ADR spacecraft EoL is shown in Figure 3.15:

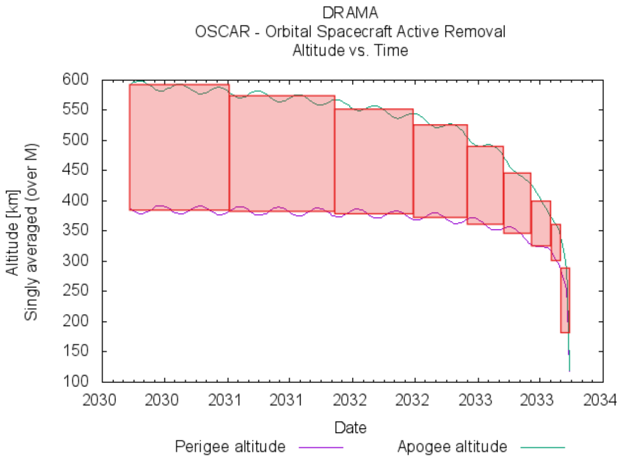

Figure 3.15: Discretised Altitudes for the ADR Spacecraft De-orbiting Phase.

The specific altitudes for each segment, as well as the debris flux, time, and collision probability at each of them, are displayed in Table 3.4

Table 3.4: Orbital Segments, Flux & Time per Segment and Collision Probability for the ADR Spacecraft EoL.

Perigee h [km]	**Apogee h [km]**	**Flux [km^{-2}yr]**	**Time [months]**	**Pc ($\cdot 10^{-4}$)**
385	590	32.72	10	0.818
380	575	36.41	10.3	0.938
375	550	32.56	7.5	0.611
370	525	20.44	5.2	0.266
360	490	17.20	3.5	0.151
350	445	13.29	2.5	0.0831
325	400	7.571	2	0.0379
305	365	7.723	1	0.0193
180	285	1.496	0.8	0.00299
TOTAL			**42.8**	**2.927**

To assess the ADR spacecraft's collision probability, mission orbits with a fixed apogee of 600km and varying perigee altitudes were analysed, as shown in Figure 3.16a. These orbits were then sorted from highest to lowest perigee and discretised as illustrated in Figure 3.14, Figure 3.15, and Figure 3.16b:

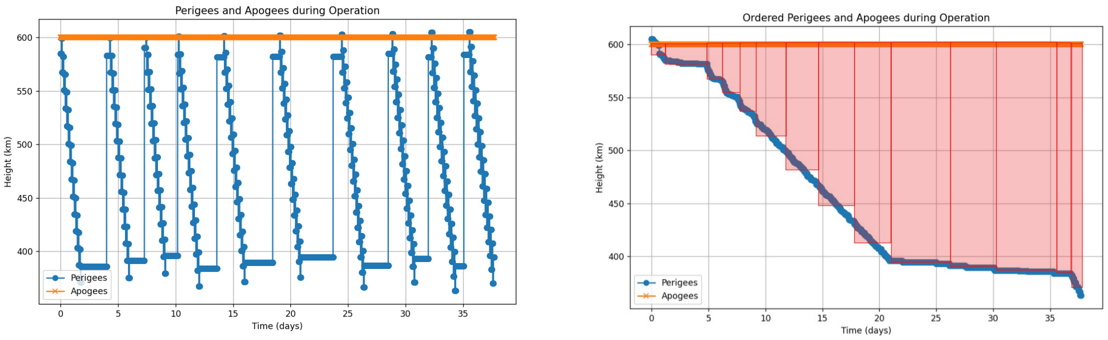

(a) Change in ADR Spacecraft Apogee Altitude.

(b) Discretised Altitudes for the ADR Spacecraft Operational Phase.

Figure 3.16: Change in ADR Spacecraft Apogee Altitude Throughout the Mission, chronological and ordered by magnitude.

The actual numbers for perigee altitude, flux, and time at each orbit, as well as total collision probability during the ADR spacecraft's operation, are shown in Table 3.5:

Table 3.5: Orbital Segments, Flux & Time per Segment and Collision Probability for the ADR Spacecraft's Operational Phase.

Perigee h [km]	Apogee h [km]	Flux [km^{-2}yr]	Time (days)	Pc ($\cdot 10^{-7}$)
590	600	5.5	1.36	0.621
580	600	10.1	3.41	2.83
570	600	16.8	1.59	2.20
555	600	28.1	1.36	3.15
535	600	21.2	1.36	2.38
515	600	17.9	2.73	4.01
480	600	17.1	2.73	3.84
445	600	17.7	3.07	4.46
415	600	13.2	3.07	3.33
395	600	12.1	5.23	5.20
390	600	11.9	4.09	3.99
387	600	11.9	5.11	5.00
385	600	11.8	1.25	1.21
370	600	11.6	1.02	0.976
TOTAL			**37.4**	**43.2**

To assess whether collision avoidance manoeuvres are necessary, an analysis of the compliance on **[R-SYS-34]** and **[R-SYS-38]** is needed. As the collision probability Pc is always lower than the Accepted Collision Probability Level ACPL, for each of the phases, there is no need for performing collision avoidance manoeuvres. The results are summarised in Table 3.6:

Table 3.6: Summary of Pc and ACPL Throughout the Mission.

Phase	Pc	ACPL	Pc<ACPL
Debris passive de-orbiting	$3.22\cdot10^{-4}$	10^{-3}	YES
ADR EoL	$2.93\cdot10^{-4}$	10^{-3}	YES
ADR Operation	$4.32\cdot10^{-6}$	10^{-4}	YES

Optimisation and Method Adaptability

The aim of Starfixers Inc. is to provide a service where clients would pay to get their satellites de-orbit. However, the focus has so far been put only on 10 equal 260kg satellites at 600km of altitude. To be able to reach a wider customer base, the de-orbiting methodology was adapted to de-orbit satellites from 250kg to 500kg and from 550km to 630km in altitude, both following from **[R-SUB-PAY-03]**. Then, one ADR satellite could combine the orders for various clients with different satellites, and minimal changes would have to be made to the original prototype for that purpose.

Additionally, an optimisation code [9] was developed such that for a given set of satellites with different masses, orbital altitudes, and initial orbital angular positions with respect to the ADR spacecraft, the best sequence to follow was calculated to minimise total fuel mass needed. This would then minimise the total cost of the mission, maximising, in turn, the possible benefits of the provided service.

This section will explain how this code works and how Starfixers, Inc. plans to implement it when providing a service. As displayed in Figure 3.17, the code inputs an array of satellites with different orbital altitudes and masses, and placed at different angular positions.

---

[9] `https://tinyurl.com/58kxzt34`

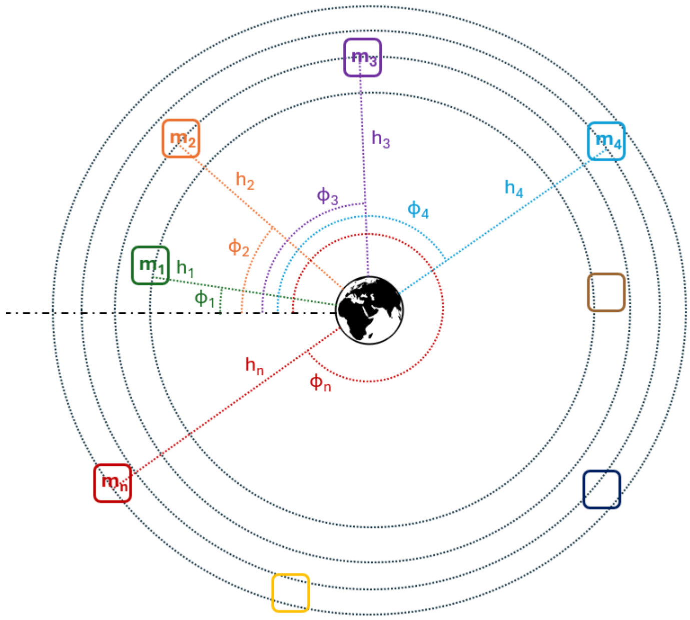

Figure 3.17: Arbitrary Initial Satellite Layout to input.

Next, a similar code to the one developed in [14] is run for every possible de-orbiting sequence, and the sequence resulting in the lowest spent fuel mass is selected as the optimal, as long as the time constraint is satisfied.

The program is summarised in Figure 3.20, and consists of a high-level loop that ensures that after one debris is de-orbited, if not all of them have been de-orbited yet, the ADR spacecraft proceeds with the next one. Inside that loop, another one, shown in Figure 3.19, iterates until the necessary ΔV is transferred to the debris. This ΔV calculation is based on the minimum altitude at which each satellite has to be brought, depending on its mass and initial altitude. Using the OSCAR tool from DRAMA ([38]) and simple orbital mechanics calculations, the minimum perigee altitude (hmin) at which each debris spacecraft should be brought is calculated. This relationship is displayed in Figure 3.18:

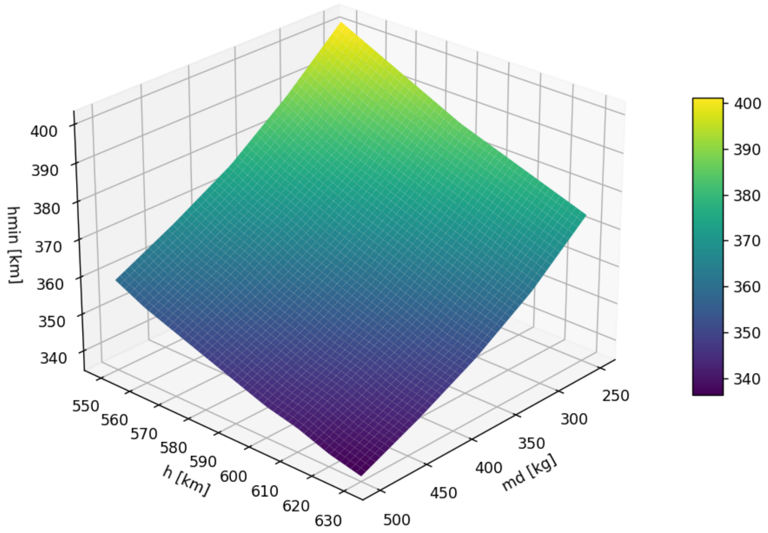

Figure 3.18: Perigee Altitude to Bring Debris of Mass md at Circular Orbit with Altitude h.

The tool starts by picking the first sequence of debris and goes inside the loop in Figure 3.19, where all of the burns for momentum transfer, rendezvous, and transfer are calculated, as well as the propellant mass expenditure and the time spent. Figure 3.20 shows the zoomed-out version and checks whether it is needed to transfer to the next debris. If the de-orbited debris of said sequence was the last one, then the last part of the loop is entered, and the procedure is repeated for the next sequence.

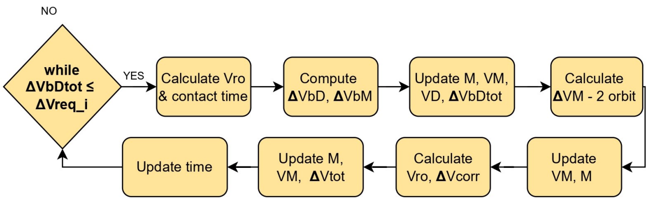

Figure 3.19: Optimisation Code Debris Loop Flowchart.

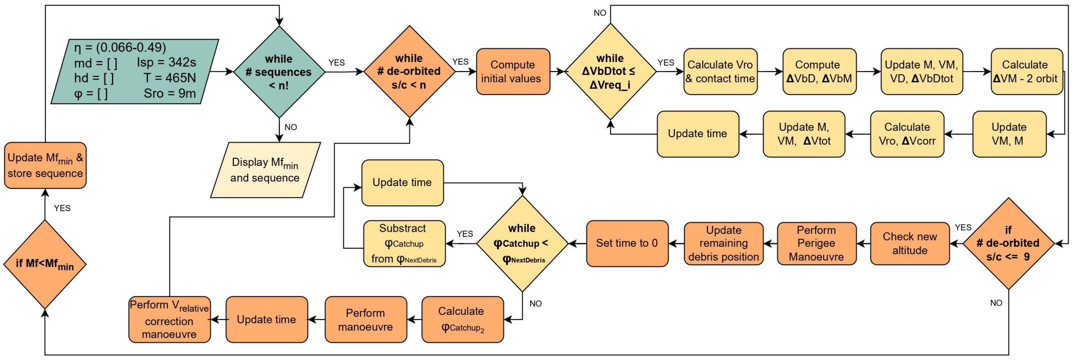

Figure 3.20: Flow Chart of Operational Computations.

In comparison with the general case of 10 debris at the same altitude, where all manoeuvres were performed at apogee, it is important to note that with changing debris altitudes, the transfer manoeuvre to the next debris altitude will have to be performed at the perigee. Then, the apogee of the ADR spacecraft will be raised or lowered to the altitude of the new debris. This perigee manoeuvre increases the apogee altitude and is illustrated in Figure 3.21. Hereafter, the ADR spacecraft can catch up with the next debris as in phases VI. and VII. of Figure 3.7.

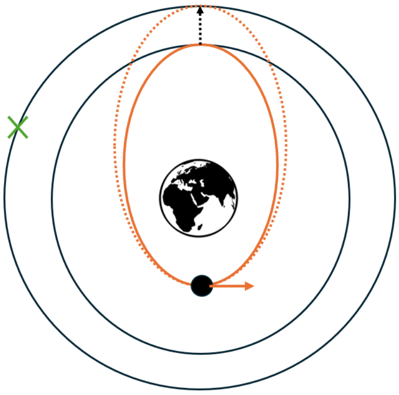

Figure 3.21: Representation of a Manoeuvre at Perigee to Increase Apogee Altitude.

4 Risk and Reliability

This chapter presents the mission architecture and risk assessment framework developed for the Starfixers Inc. debris removal mission, taking into account the chosen design concept. First, Section 4.1 presents technical risk identification and assessment methodology and 26 identified risks. Second, Table 4.3 includes mitigation strategies selected for each of the identified risks and a detailed risk bow-tie diagram for the risk of collision, which was determined to be most critical. Finally, Section 4.3 presents risk maps before and after applying mitigation strategies, depicting the resultant risk reduction.

4.1 Technical Risk Identification

Technical risk is a key factor in space missions, representing the likelihood of system failures that could impact performance, cost, or technical goals. To evaluate its impact, the expected value model is used, quantifying risk based on its probability and potential consequences. The risk factor can then be found by taking the product of Probability and Severity. The consequences of the risk can be assessed and ranked according to Table 4.1 [48].

Table 4.1: Severity and Probability Scale.

Scale	Severity of consequence [S]	Probability [P]
1	Negligible; inconvenience or non-operational impact. No reduction in technical performance.	Very low: < 1%
2	Marginal; degradation of the secondary mission. Minimal to small reduction in technical performance.	Low: 1-10%
3	Moderate; degraded system performance and mission success is questionable. Some reduction in technical performance.	Medium: 10-30%
4	Critical; critical failure that endangers the mission, with considerable reduction in technical performance.	High: 30-50%
5	Catastrophic; mission failure and significant degradation or non-achievement of technical performance.	Very high: > 50%

To assess the overall impact of each risk, the likelihood (P) and severity (S) scores are multiplied, yielding a final risk value (R). Higher R values indicate more critical risks, requiring stronger and more detailed mitigation measures. An overview of the identified technical risks is presented in Table 4.2.

Table 4.2: Risk Identification.

ID	Description	P	S	R
GNC and ADCS Risks				
TR-27	Relative Positioning: Inaccurate relative positioning during close-range operations may lead to collision with debris or failed momentum transfer.	4	4	16
TR-28	GNC adaptation failure: Inability to model or handle debris rotation or mass properties may cause misalignment, loss of control, or collision.	4	5	20
TR-29	Collision Risk: Misaligned gas jet may spin debris unpredictably, risking impact with the spacecraft.	4	5	20
TR-30	Velocity Synchronisation: Discrepancies in matching the spacecraft's velocity with the target can cause collisions or ineffective momentum transfer.	4	4	16

ID	Description	P	S	R
TR-31	Maintaining orientation: Frequent reorientation during close-proximity operations may cause loss of orientation control or mission instability.	3	4	12
TR-32	Attitude control overload: Continuous high demand on sensors and actuators may degrade performance and cause failure during close-proximity operations.	3	4	12
TR-33	Sensor disruption: Optical glints or thermal effects/clouds may interfere with sensor performance.	4	4	16
TR-34	Orbital prediction errors: Inaccuracies in forecasting debris position may lead to failed rendezvous.	2	3	6
TR-35	Communication Loss: Risk of losing communications during critical phase of the mission due to spacecraft reorientation during plume push operation.	2	4	8
TR-36	Telemetry Bandwidth Overruns: High data rate sensors during debris approach may overload available downlink bandwidth.	2	2	4
Power, Propulsion Risks				
TR-37	Fuel Margin Risk: High fuel demand limits margin for error, increasing the risk of mission failure if additional manoeuvres or retries are needed.	3	2	6
TR-38	Thruster Development Risk: Proposed thruster (465 N, Isp = 342 s) is still under development. Risks include qualification, availability, and cost overruns.	4	4	16
TR-39	Thrust Vector Adjustment: Risk of failing to perform constant thrust correction, needed to maintain position and alignment, especially if debris is rotating.	3	4	12
TR-40	Propulsion failure during critical phase: Loss of the main propulsion system during approach or gas jet firing could result in mission failure or collision.	2	5	10
TR-41	Thrust instability: Inconsistent gas pressure or poor flow regulation may cause unsteady thrust output, affecting momentum transfer accuracy.	3	4	12
TR-42	Thermal risk during firing: Continuous or high-frequency thruster use may lead to overheating, damaging sensitive components.	2	3	6
TR-43	Power failure: Electrical loss from battery degradation, distribution faults, or overconsumption may disable critical systems such as comms and propulsion.	2	4	8
TR-44	Mechanical fatigue from thrust cycling: Repeated thruster activation may cause structural fatigue or wear in valves, nozzles, and mounts over time.	3	3	9
Operational and Environmental Risks				
TR-45	Plume behaviour variability: Unpredictable gas plume dynamics in vacuum conditions may reduce control over momentum transfer effectiveness.	4	4	16
TR-46	Poor debris orientation: Targets with minimal or misaligned cross-sectional area may not receive sufficient plume force for de-orbiting.	3	3	9
TR-47	High-relative motion targets: Fast-approaching or rapidly spinning debris may be too unstable or hazardous to engage effectively.	3	4	12
TR-48	Debris heating and damage: Hot exhaust gases may melt or damage debris surfaces, leading to fragmentation or altered behaviour.	2	4	8
TR-49	Mission timeline extension: Additional approach attempts or corrections may significantly extend the overall mission duration and resource use.	2	2	4

4.2 Technical Risk Mitigation

This section summarises the suggested mitigation strategies corresponding to each identified risk listed in Table 4.2. For each risk, Table 4.3 outlines the proposed mitigation actions and contingency plans, all intended to reduce the overall risk level.

Table 4.3: Risk Mitigation and Contingency Strategy.

ID	Mitigation Strategy	P	S	R
	GNC and ADCS Risks			
TR-27	Use high precision LiDAR and optical navigation with real time updates.	2	4	8
TR-28	Use onboard cameras and LiDAR to update the guidance system and align the plume.	3	4	12
TR-29	Use closed-loop control with visual feedback to align plume with debris centre of pressure.	2	4	8
TR-30	Implement Doppler Radar to measure the debris's relative speed and a Kalman filter to combine this with other sensor data, allowing precise velocity matching.	2	2	4
TR-31	Use fast-response reaction wheels and predictive attitude control to adjust the spacecraft's orientation in advance.	2	3	6
TR-32	Add redundancy in sensors and schedule thermal/power loads to avoid continuous overload.	2	3	6
TR-33	Implement multi-sensor fusion with filtering and shielding: use redundant sensors (e.g., star tracker + sun sensor + IMU) combined via an Extended Kalman Filter (EKF), and apply physical baffling or coatings to reduce stray light and thermal shielding to stabilise sensor temperatures.	3	3	9
TR-34	Continuously update position data and refine onboard orbit estimation using sensor fusion to minimise prediction errors and improve navigation accuracy.	1	3	3
TR-35	Use omnidirectional backup antennas and autonomous fallback sequences.	1	3	3
TR-36	Prioritise critical telemetry and compress non-essential data during high-bandwidth phases to maintain communication performance.	1	2	2
	Power, Propulsion Risks			
TR-37	Add 10% propellant margin and optimise manoeuvrer planning.	2	2	4
TR-38	Use a heritage-based design, early supplier engagement, and maintain a qualified backup thruster option.	2	4	10
TR-39	Use closed-loop control with real-time feedback from relative navigation sensors (e.g. LiDAR, cameras) and employ thrust vector control algorithms that adjust dynamically to debris motion.	2	4	8
TR-40	Include a secondary propulsion unit and fault detection with rapid switch-over.	1	5	5
TR-41	Use pressure regulators, real-time sensors and multi-stage flow control combined with in-flight calibration to ensure stable thrust and accurate momentum transfer.	2	4	8
TR-42	Implement active thermal management (e.g., heat sinks, radiators, or thermal straps), enforce duty cycle limits on thruster use, and monitor temperature with onboard sensors to avoid overheating.	1	3	3
TR-43	Design with redundant batteries, implement critical load prioritisation logic, include real-time power monitoring and integrate autonomous power shedding protocols to maintain essential functions during partial or total power failures.	1	4	4
TR-44	Use high-durability materials and components rated for repeated thermal and mechanical stress, and include redundancy in critical thruster elements. Implement thrust scheduling strategies to minimise unnecessary activations, and monitor component health in real time to detect early signs of wear.	2	3	6
	Operational and Environmental Risks			
TR-45	Implement adaptive thrust control algorithms with real-time feedback to adjust to unexpected debris responses during momentum transfer. Use shaped nozzles and maintain a conservative stand-off distance. Perform intensive testing during design phases.	2	4	8
TR-46	During rendezvous, onboard sensors can assess orientation in real-time, allowing adaptive control algorithms to adjust thrust direction or delay engagement. If necessary, small plume pulses can be used to gently reorient debris before the main momentum transfer.	2	2	4

ID	Mitigation and Contingency Strategy	P	S	R
TR-47	Pre-mission debris have to be filtered based on rotation rate and relative velocity thresholds. Include real-time tracking and motion prediction algorithms that can assess stability and abort engagement if conditions exceed safe limits. If possible, controlled plume pulses may be used to gradually slow or stabilise the target before full engagement.	2	2	4
TR-48	Select low temperature gas emissions in design and perform pre-engagement analysis of material properties and thermal response to avoid fragile or heat-sensitive targets. Maintain a sufficient stand-off distance to reduce direct thermal exposure.	1	2	2
TR-49	Optimise trajectory planning and target sequencing to minimise unnecessary manoeuvres. Incorporate buffer margins in time and fuel budgets, and enable autonomous decision-making to reduce delays from repeated approach attempts.	1	2	2

The identified risks and mitigation strategies for the most critical risk are shown in a Risk Bow-Tie Diagram Figure 4.3, where collision is the main shared hazard (in red); causes (turquoise), consequences (blue), preventive controls (white, left), and contingency measures (right) are also illustrated.

4.3 Risk Map

This section summarises the identified technical risks on a risk map based on their probability and severity, as shown in Figure 4.1. Red zones mark the most critical risks needing strong mitigation and contingency plans, orange zones indicate moderate risks, and green zones represent low-priority risks. The updated risk map in Figure 4.2 shows the impact of applied mitigation and contingency measures, using the same colour scheme to reflect revised criticality levels.

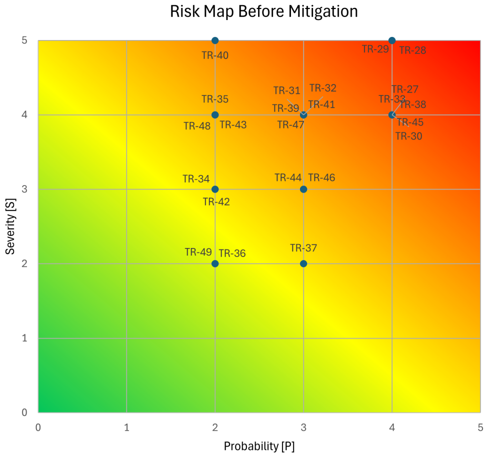

Figure 4.1: Risk Map Before Mitigation.

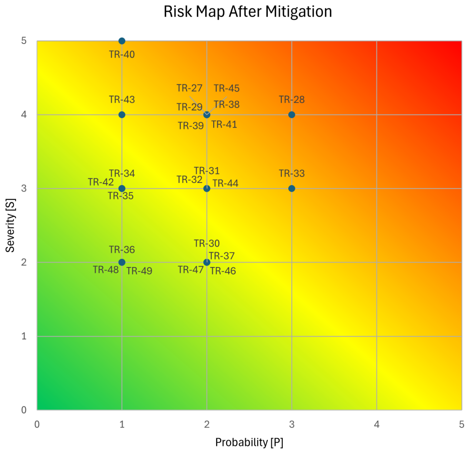

Figure 4.2: Risk Map After Mitigation.

Overall, the identification of technical risks and their corresponding mitigation measures, as illustrated in Figure 4.3, played an integral role in shaping the design and requirements for the mission. Several key risks are directly translated into new design requirements, documented in Section 13.3. By addressing potential failure modes such as sensor degradation, propulsion issues, and communication loss, the team was able to implement targeted design improvements that enhance resilience and ensure mission continuity. Sensor-related risks led to the integration of redundant architectures and higher-frequency data processing, while propulsion and control vulnerabilities led to the adoption of adaptive algorithms and increased propellant margins.

These risk-informed decisions have been embedded into the final system design and will be reflected in the spacecraft subsystems and configuration, ensuring a safer mission.

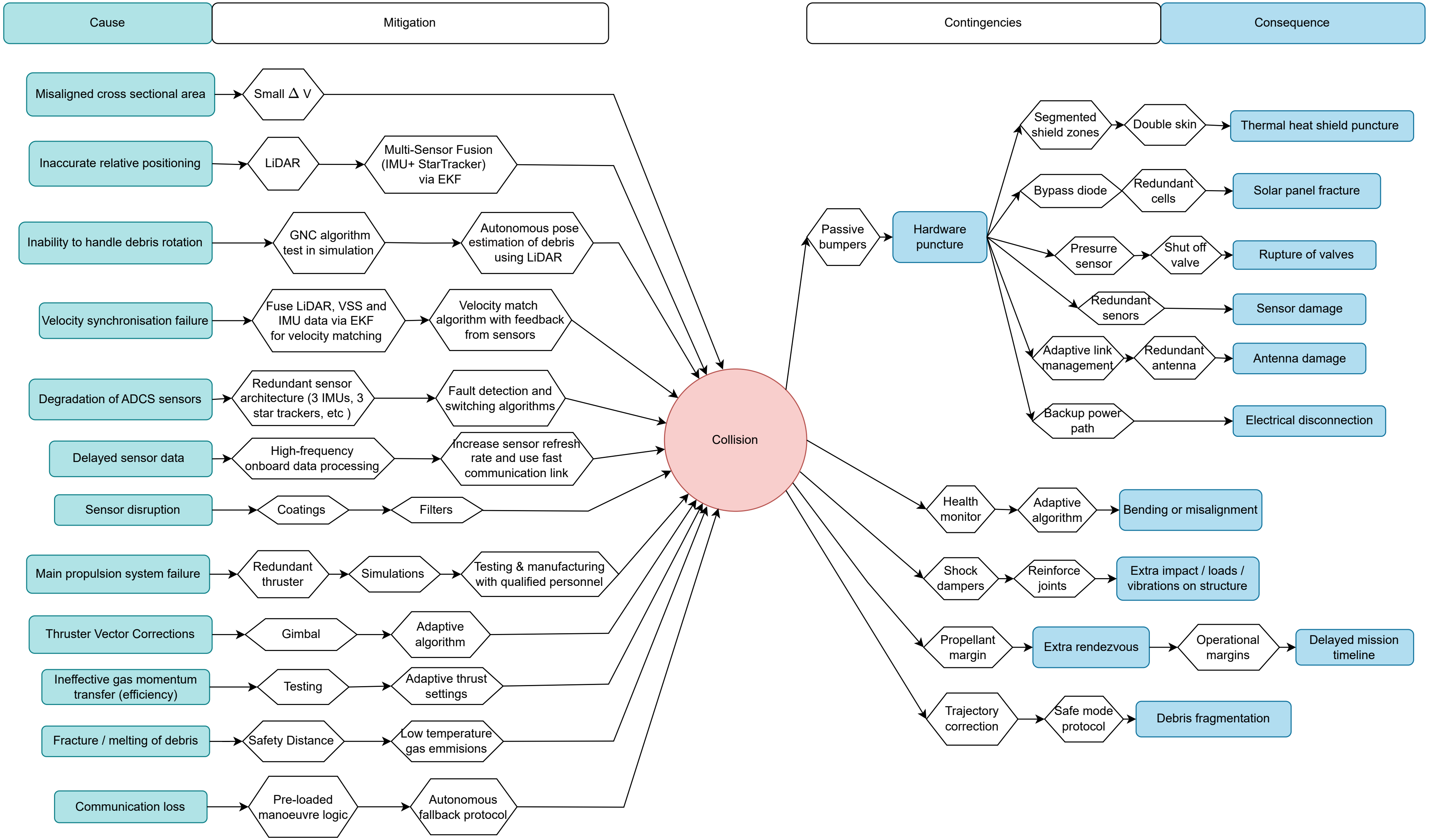

Figure 4.3: Risk Bow-Tie diagram.

5 Guidance Navigation and Control

The Guidance Navigation and Control (GN&C) subsystem is responsible for determining the position of the spacecraft and is closely linked to the Attitude Determination and Control System (ADCS), discussed later in chapter 6. The GN&C shall accurately determine the position and velocity of the spacecraft with respect to Earth, as well as determine the relative motion of the target debris during rendezvous and close-proximity operations. Moreover, the GN&C subsystem enables the observation and documentation of the first in-space application of gas shepherding and active multi-target debris removal.

To ensure GN&C functions as desired and meets all requirements described in Section 13.3, the subsystem will consist of a Global Navigation Satellite System (GNSS) receiver and antennas, infrared cameras and Light Detection and Ranging (LiDAR) sensors. This chapter explores the GN&C components and their adherence to the requirements.

5.1 GNSS

An accurate knowledge of the spacecraft's position is important for various factors, one of which is the mission's sustainability goal to achieve a Platinum Space Sustainability Rating. Orbital State Knowledge is defined as one of the four main criteria for this Sustainability Rating and the highest score is awarded to a mission if it maintains "orbital state knowledge of the object within < 1 km in any direction" [28]. While this imposes a constraint on the required orbital knowledge, a more limiting constraint is imposed by the mission's operational logistics.

To de-orbit 10 satellites, the spacecraft will have more than 170 rendezvous with close proximity operations taking place along the orbit of the debris, within a range of 9 meters. As the positional accuracy of debris tracking is of the order of tens of meters [18], it could pose a problem for rendezvous if the spacecraft's location is inaccurate as well. Each rendezvous manoeuvre would require additional fuel to perform orbit adjustments, worsening the efficiency of the mission.

To overcome this, the spacecraft will make use of Galileo, ESA's Global Navigation Satellite System, for a highly accurate orbit knowledge. Galileo, in 2025, is fully operational with 26 active satellites in a circular orbit at an altitude of 23616km and 56° inclination [10]. Galileo is four times more accurate than GPS and its High Accuracy Service (HAS) can provide a position accuracy on the order of 20cm[11]. The spacecraft will have two Isispace GNSS antenna patches [12], designed for a frequency of 1575MHz, which align with Galileo's HAS signals transmitted in E1B band (1559-1591MHz) at 125 bps [19]. One antenna patch will be placed on a side with a solar array and the other will be placed away from Earth, opposite to the side with antennas for ground communication. These locations offer the most outward exposure, ensuring that the patch antenna's 140° field of view has a high probability of receiving signals from at least four Galileo satellites. The Galileo system is designed so that, on average, six to eight satellites are visible from any point on Earth, with the likelihood of additional satellite visibility increasing at higher orbital altitudes.

The Galileo signals will be processed by SpacePNT's GNSS receiver, NaviLEO. This receiver is compatible for two antenna inputs and Galileo's E1B frequencies [13]. The obtained spacecraft position and orbit

---

[10] `https://www.esa.int/Applications/Satellite_navigation/Galileo/Four_Galileo_satellites`

[11] `https://rb.gy/i4lfz2`

[12] `https://www.isispace.nl/product/gnss-patch-antenna/`

[13] `https://rb.gy/ke9k9q`

determination flows to the C&DH computer, and is later transmitted to Earth for orbit verification.

5.2 Infrared cameras

While the GNSS ensures accurate positional knowledge of the spacecraft, the infrared cameras and LiDAR will provide this knowledge for the debris. The distance between the spacecraft and the debris will vary significantly for each rendezvous due to the two-orbit method. Therefore, before the spacecraft reaches the proximity required for gas shepherding momentum transfer, each GN&C sensor plays a specific role in gathering critical information. The spacecraft will have two infrared Narrow Field of View (NFOV) cameras for long-range imaging and two infrared Wide Field of View (WFOV) cameras for close-range imaging and livestreaming of the momentum transfer operations. There will always be at least one camera active during the repeated operational phases: outer orbit, observe, prepare and de-orbit operation. The specifications of the cameras are presented in Table 5.1. Both these cameras are unaffected by lighting influence from the Sun and were chosen because of their heritage in successful target approach and close proximity rendezvous missions such as Northrop Grumman's Mission Extension Vehicles 1 & 2. Four examples of images taken by the MEV-2 are presented in Figure 5.1.

Table 5.1: Specifications of the Malin Space Science Systems NFOV and WFOV Infrared Cameras [14].

	ECAM-IR3A (NFOV)	**ECAM-IR3A (WFOV)**
FOV (h° x v°)	16°x12°	48°x36°
Operating Range	<10km	<15m
Resolution	640x480 pixels	
Conversion Bit Depth	16 bits	
Frame Rate	12 fps	
Mass	0.525 kg	
Imaging Power	2 W	

The NFOV camera will continuously track the position of the debris within an effective range of 10km, fulfilling requirement **[R-SUB-ADC-01]**. Other than tracking the location of the debris, the NFOV images will be transmitted to Earth and analysed for debris intactness before the operation is cleared to continue. The use of the NFOV camera imposes requirements on the ADCS through the pointing accuracy and slew rate during imaging.

As can be seen in Table 5.1, the ECAM-IR3A NFOV has a 16°x12° FOV for a 640x480 pixel resolution, meaning each pixel is defined by 0.025°x0.025°. With a frame rate of 12fps, each frame is exposed for $1/12 \approx 83.3$ms. If the spacecraft rotates too much within that period, the pixels are smeared out and cause motion blur. An image shift of ≤1 pixel therefore leads to a maximum slew rate of $\omega_{max} = \frac{0.025°}{0.0833s} = 0.3°/s$. Given the camera will continuously track the debris, the spacecraft will always have a slew rate to keep the debris centred in its optical FOV. However, as the orbits of debris and spacecraft only vary slightly throughout the whole mission, the relative velocity of the debris perpendicular to the spacecraft's path shall not be high enough to cause this motion blur. The most important cause of motion blur will therefore be coarse attitude control. To prevent this, the ADCS shall be able to control its slew rate in the order of 0.1°/s and have attitude knowledge better than 0.01°.

The importance of the WFOV camera can be seen by analysing Figure 5.1c and Figure 5.1d. In both images, the distance to the IS-10-02 satellite appears to be rather similar due to the NFOV camera's narrow field of view, while in fact they are taken 85m apart. For the purpose of livestreaming the gas shepherding manoeuvre, the NFOV camera becomes ineffective, and the WFOV camera is activated

---

[14] `https://www.msss.com/files/ECAM-IR3A.pdf`

and livestreamed once the debris is within a range of 15m. Considering the importance of capturing this mission's operations, two NFOV and two WFOV cameras are mounted onboard the spacecraft for redundancy.

(a) NFOV Image of IS-10-02 at 3.2km. **(b)** NFOV Image of IS-10-02 at 1.5km.

(c) NFOV Image of IS-10-02 at 100m. **(d)** WFOV Image of IS-10-02 at 15m.

Figure 5.1: Four Images of MEV-2's Target Satellite (IS-10-02) During Pre-docking Approach [80]

5.3 LiDAR

After accurately positioning the spacecraft in the desired rendezvous orbit, tracking the debris and analysing its intactness with the infrared cameras, the spacecraft shall perform its momentum transfer manoeuvre. Each rendezvous, the thruster is activated and its exhaust plume slows down the debris to further lower its orbit as described in Section 3.2. The success of each manoeuvre is dependent on the accuracy of the thruster's plume having contact with the debris; thus, naturally, requirements follow from this. To ensure this accuracy, the spacecraft will have an RVS3000-3D Light Detection and Ranging (LiDAR) sensor on board from Jena-Optronik. Due to the crucial role of the LiDAR for the mission's success, a second LiDAR sensor will be on board for redundancy. One of these will be active during the prepare and de-orbit operational phase. First, the requirements will be described, after which the functioning of the LiDAR is discussed.

The efficiency of the plume's momentum transfer is dictated by the spacecraft's distance to the debris, the plume's expansion and therefore the effective contact area with the debris. As a result, the debris shall have a relative approach velocity of less than 10m/s, and the thruster is activated once the debris is within 9m distance, such that it shall not be closer than 3m. This operation sequence is highly dynamic and requires accurate knowledge of the debris's distance, relative approach velocity and attitude. Turning on the thruster further away than 9m decreases both plume efficiency and contact time, while turning on the thruster closer than 9m increases the chance of collision.

Considering the final converged dry and wet mass of the spacecraft, a sensitivity analysis was conducted to evaluate the impact of inaccurate thruster activation. Specifically, the analysis investigated scenarios in which the thruster is consistently triggered too early due to mismeasurement of the relative distance or approach velocity. If the thruster is activated too late, the available margin before a potential collision is only 3 meters, posing a significant risk to the spacecraft.

Table 5.2 presents the results of activating the thruster at distances greater than the nominal 9 meters. As discussed in Section 3.2, the efficiency of momentum transfer via the thruster plume decreases with increasing distance, leading to a rise in both fuel consumption and the number of required rendezvous to de-orbit 10 targets. While early activation results in lower efficiency, it poses far less risk than late activation, which could result in a collision with the debris.

Table 5.2: Effect of Thruster Activation Distance on the Number of Rendezvous and Required Fuel Mass to De-orbit 10 Targets.

Distance [m]	No. rendezvous	Fuel mass [kg]
9	153	351
10	153	356
11	153	363
12	154	367
13	157	375
14	159	381

Other than distance, an important factor for momentum transfer efficiency is that the plume is directed at the right point. If misaligned too much, the plume area might fall off the sides of the debris, decreasing the effective area. Preventing this requires precise attitude knowledge, pointing accuracy and relative debris attitude knowledge to align the thruster with the centre of pressure. Figure 5.2 presents the effect of thruster misalignment on the efficiency over distance and ultimately the required fuel to de-orbit 10 targets.

For thruster activation at 9m distance, if the thruster is misaligned by 6°, the debris is still de-orbited in the same number of rendezvous. However, over 20kg of additional fuel is required to achieve the same goal. The NFOV camera already requires a high pointing accuracy and therefore attitude knowledge, so correctly pointing the thruster should not have offsets of that severity. However, the same misalignment problem could occur if the thruster is thought to be pointed correctly, but the calculation of the centre of pressure is off. For the same severity, at 6° and a debris distance of 9m, the horizontal offset would be 0.95m. To fully overcome this problem, the GN&C shall be able to correctly know the centre of pressure with an accuracy of ± 0.1m at a distance of 9m.

Determining the centre of pressure requires complete knowledge of the orientation of the debris and its structure while moving through space. A LiDAR sensor, specifically Jena-Optronik's RVS3000-3D, shall be able to obtain this knowledge and level of accuracy of the debris and meet requirements **[R-SUB-ADC-02]**, **[R-SUB-ADC-03]**, **[R-SUB-ADC-13]**, **[R-SUB-ADC-14]** and **[R-SUB-ADC-18]**. By emitting and receiving light, the LiDAR creates a 3D point cloud of the collected data. This point cloud is overlaid with a known CAD model of the target debris to accurately determine its attitude and locate the centre of pressure. Jena Optronik's LiDAR has a successful heritage in space: it was used on Northrop Grumman's MEV 1 & 2, where it was used for attitude determination and guidance while docking the MEV to a functioning satellite. In addition, it was used to guide docking during the ATV5 ISS supply mission. In a meeting between Starfixers, Inc. and Jena-Optronik, Jena-Optronik stated that although the operations of the Starfixers mission are significantly more dynamic and high-velocity than previous uses, it is possible for the LiDAR to function well if it is combined with the infrared cameras through sensor collaboration. The infrared cameras could namely provide prior knowledge of the debris orientation

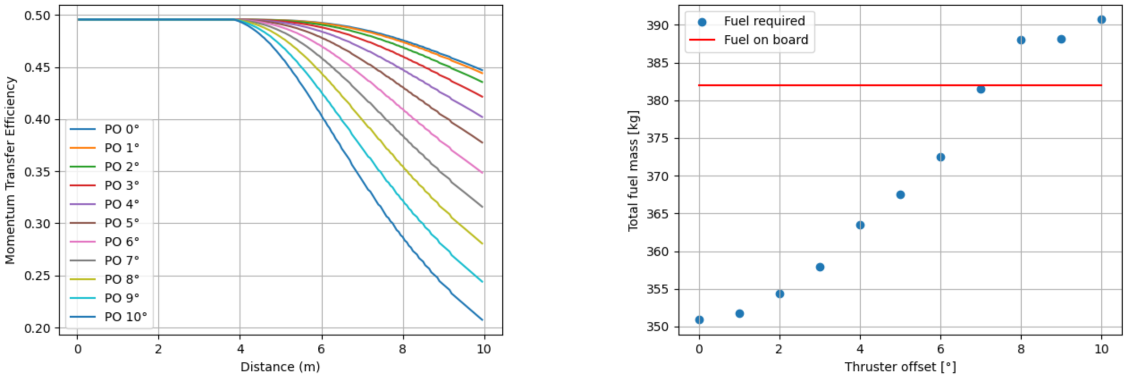

(a) Momentum Transfer Efficiency Over Distance Due to Plume Offset (PO), at AC = 0.5 and HCA = 15 degrees.

(b) Effect of Thruster/Plume Offset on the Required Fuel to De-orbit 10 Targets.

Figure 5.2: The Effect of Inaccurate Momentum Transfer.

before the system can start correctly overlaying the point clouds with the CAD model. However, due to the time it takes for a single scan and processing, the LiDAR can only measure the attitude of targets with an angular velocity of up to max 5°/s. Other than that, the LiDAR is flexible and can alter its FOV from 1°x1° to 40°x40°. To ensure the target is always within FOV, the ADCS must have a pointing accuracy better than 0.5°.

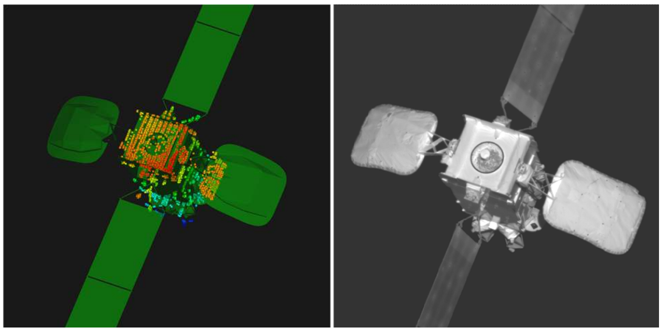

Figure 5.3: LIDAR Point Cloud of IS-10-02 Target With 6 Degree of Freedom Model Overlay at 60 m. The Infrared Image of the Same Time Reference Is Added for Comparison [80].

The placement of the LiDAR and infrared cameras can be seen in Figure 5.4, the GNSS receiver and antennas are not visible in this image.

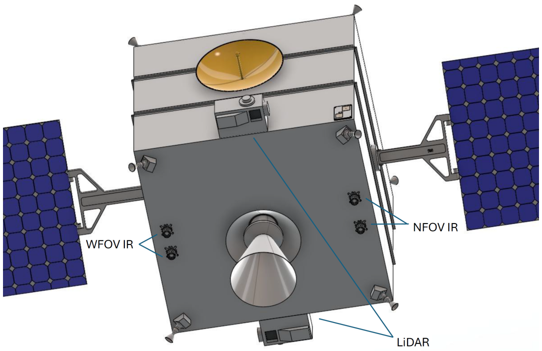

Figure 5.4: Location of LiDAR and Infrared Cameras on the Side With the Main Thruster.

6 Attitude Determination and Control System

The ADCS ensures that the spacecraft maintains the correct orientation throughout all its mission phases. It works closely with the GN&C subsystem to guarantee accurate attitude knowledge of the spacecraft and a sufficiently high pointing accuracy. This chapter discusses the ADCS sensors, actuators and how the system fulfils the requirements imposed by GN&C.

6.1 Sensors

The sensors in the ADCS provide the spacecraft with accurate and reliable attitude knowledge across all mission phases. High-precision sensors such as star trackers ensure the required knowledge for a high pointing accuracy. The inertial measurement units (IMU) provide continuity during dynamic operations and sun sensors offer redundancy and can support safe-mode operations when other sensors are inactive. Together, they enable continuous, accurate attitude estimation aligned with the GN&C requirements.

Star Trackers

From the GN&C subsystem, the spacecraft is required to have an attitude knowledge of better than 0.01°. To achieve this accuracy, two Rocketlab ST-16RT2 star trackers[15] will be part of the ADCS. The ST-16RT2 reliably has a 5 arcsecond ($\approx 0.0014^\circ$) accuracy, which satisfies **[R-SUB-ADC-09]**. Moreover, Rocketlab's star tracker has a heritage of over 160 units sent into orbit. The small baffle is chosen for this mission because there is no need for even higher accuracy with a larger baffle. Even though the risk of radiation influences is little for star trackers for short operational missions in LEO, two star trackers will be on board in separate non-earth facing faces in case one of the trackers is blinded by the sun.

Inertial Measurement Unit

Two space-grade Stim377H IMUs from Safran[16] are included in the ADCS, one for redundancy. Each IMU consists of three accelerometers, gyros and inclinometers to provide angular rate and linear acceleration measurements. These are critical for attitude propagation during star tracker dropouts and during dynamic phases like the momentum transfer manoeuvres. The Stim377H has demonstrated flight heritage and is suitable for precise attitude estimation in collaboration with the star trackers.

Sun Sensor

As an additional reserve for the star trackers, four NewSpace Systems AquilaH01 sun sensors will be distributed on the spacecraft to provide full sky coverage. This sun sensor is small, lightweight, cheap and especially reliable. They have been proven to last >5 years in LEO and are currently baselined on 5 constellations[17].

6.2 Actuators

Accurate sensors and attitude knowledge is only half of the ADCS subsystem. With information given from the sensors, two types of actuators will be on board to actually control the attitude of the spacecraft.

---

[15] `https://rocketlabcorp.com/assets/Uploads/ST-16RT2-Datasheet-v4.1.pdf`

[16] `https://safran-navigation-timing.com/solution/inertial-measurement-units/`

[17] `https://shorturl.at/qkVfZ`

Reaction Wheels

The reaction wheels provide attitude control of the spacecraft for multiple purposes. It has to be able to perform fine slews and adjustments for precise pointing, as well as perform larger slews to drastically change the attitude of the spacecraft. Initially, the mission plan was to have a single main thruster that would apply all ΔV needs. Combined with the two-orbit operational procedure, this led to the reaction wheels having to rotate the spacecraft 180° and back mere moments before the momentum transfer took place. This would allow the thruster to apply very small ΔV to match the calculated relative approach velocity. This demanded very powerful reaction wheels, while unnecessarily inducing a risk for collisions, hence a second thruster was placed on the opposite side of the main thruster. This would allow for small ΔV adjustments without high demands for ADCS.

The critical design case for the reaction wheels is being able to rotate the spacecraft 90° within 100s, so the adverse thruster can perform an exit manoeuvre in case the main thruster fails when the spacecraft is already in place for rendezvous. To prevent catastrophic collision, the spacecraft will rotate over its axis with the least MMoI and use the adverse thruster to reach a safe distance of at least 10m. In case the adverse thruster fails as well, the cold gas thrusters can be used to perform this exit manoeuvre.

The reaction wheels each have to be capable of storing the momentum caused by this exit manoeuvre, which is calculated using Equation 6.1 below:

$$H_{\text{exit}} = \omega_{\text{exit}} \cdot I = \frac{2\theta}{t} \cdot I \tag{6.1}$$

where H_{exit} is the required momentum storage in each reaction wheel in Nms, ω_{exit} is the required slew rate in rad/s, θ is the required rotation in rad, t is the time in s in which the rotation has to be done and I is the lowest MMoI of the spacecraft. This results in a required momentum storage of 0.694 Nms for each exit manoeuvre.

The required torque to be able to perform such a rotation is calculated using the following:

$$\tau = I \cdot \alpha = I \cdot \frac{2\theta}{t^2} \tag{6.2}$$

where τ is the required torque in Nm and α is the angular acceleration in rad/s^2. For the critical case of requirement **[R-SUB-ADC-05]**, the reaction wheel have to be able to sustain a torque of 0.03Nm.

To satisfy the conditions of the exit manoeuvre and meet requirements **[R-SUB-ADC-05]** and **[R-SUB-ADC-16]** while providing fine actuator control for pointing precision, the spacecraft will have four Libra6[18] reaction wheels in pyramid configuration around its centre of gravity. This allows for three-axis actuator coverage, even in case one reaction wheel becomes saturated or fails. The Libra6 reaction wheels have a total momentum storage of 7.83Nms (5000rpm) per wheel, which prevents early saturation of the actuators, while also having a high speed control accuracy of ±0.14rpm and a peak torque of 0.31Nm. This high speed control accuracy meets requirements **[R-SUB-ADC-07]** and **[R-SUB-ADC-17]**.

Cold Gas Thrusters

In addition to the reaction wheels, the spacecraft will also have eight Gaseous Nitrogen (GN_2) thrusters. Gaseous nitrogen is used for sustainability purposes: it is a non-toxic propellant and is widely available. Moreover, it requires no combustion and is commonly used for small thrusters in ADCS subsystems. The cold gas thrusters will have three functions: to desaturate the reaction wheels, to make translational movements during rendezvous and to serve as final backup to perform the exit manoeuvre. The

---

[18] `https://shorturl.at/Cx7nt`

configuration of the cold gas thrusters on the corners of the spacecraft is visible in Figure 6.1, where they have a 45° inclination and are aligned such that their vector does not align with the centre of gravity of the spacecraft. This allows the thrusters to provide translational and rotational displacements, depending on which pairs of thrusters are activated. Given that the cold gas thrusters were already required for translational movements, they also bear the responsibility for wheel desaturation to avoid having additional magnetorquers to serve that purpose.

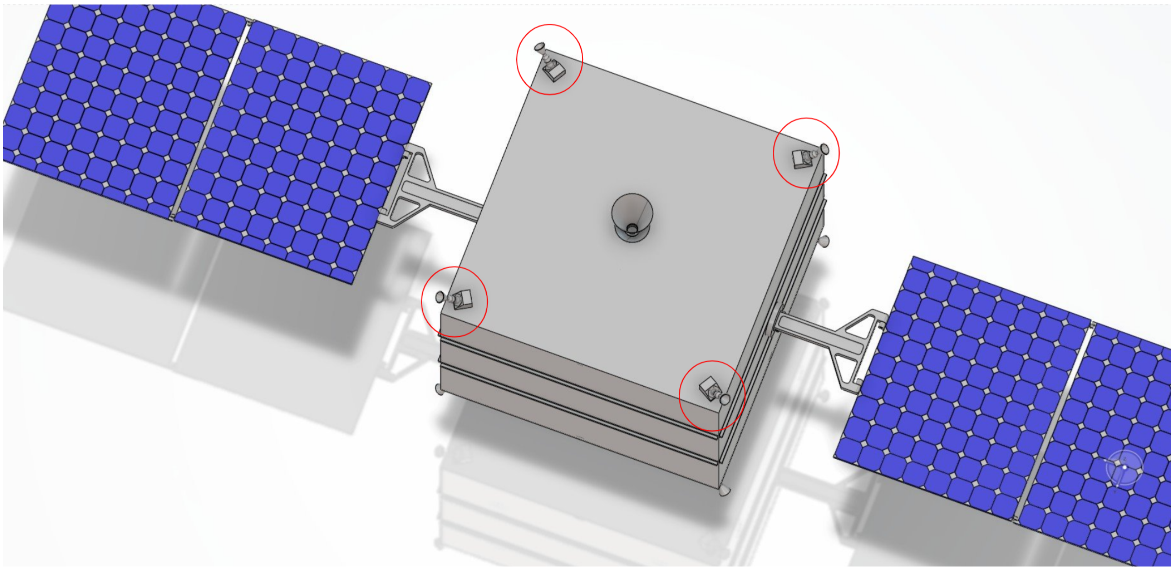

Figure 6.1: Placement and Orientation of the Cold Gas Thrusters on the Corners of the Spacecraft, as Seen From the Side Opposing the Main Thruster.

Moog's 58E163A model thruster will be used for its high specific impulse of 70s for GN_2 and compatibility with a pressure of 90 bar[19]. This significantly reduces the gas tank size compared to other thrusters with higher thrust values, but operating at lower pressures and with lower specific impulses. To size the volume of required gas, it is necessary to look at the full desaturation of a single wheel.

The total coupled torque caused by a pair of thrusters is defined as:

$$\tau_t = F \cdot d \tag{6.3}$$

where τ_t is the torque in Nm, F the thrust of a single thruster in N and d the arm between the thrusters in m. With the Moog 58E163A model's thrust of 0.9N and a distance of 1m (length of spacecraft, elaborated upon further in chapter 11), creates a moment of 0.9Nm thus to fully desaturate a single wheel it would take $\frac{7.83Nms}{0.9Nm} = 8.7s$.

The mass flow can be calculated using the equation:

$$\dot{m} = \frac{F_T}{v_e} = \frac{F_T}{I_{sp} \cdot g_0} \tag{6.4}$$

where $\dot{m}$ is the mass flow in kg/s, F_T the applied thrust in N, v_e the exhaust velocity of the gas leaving the thruster in m/s, I_{sp} the specific impulse in s and g_0 the standard gravitation acceleration of 9.80655 m/s^2. Applying $F_T = 1.8N$ and $I_{sp} = 70s$ in Equation 6.4 results in a mass flow of 0.00262 kg/s. Thus, for a full desaturation of a single reaction wheel, 22.8g of GN_2 is used in a burn time of 8.7s. A single cold

---

[19] `https://shorturl.at/aDijJ`

gas thruster performing the exit manoeuvre to 10m of distance, in case of both bi-propellant thrusters failing, requires 23.8g of GN_2.

It is difficult to predict the exact number of desaturations that will have to be performed during the mission or the amount of gas required for small translational manoeuvres. From the mission operations and logistics, it can be concluded that saturation build-up will be relatively slow due to the short period of operation and the main use of the reaction wheels being to provide accurate pointing. While a more in-depth quantisation of the required gas is recommended for the next design phase, a conservative number of 250g is chosen to ensure sufficient onboard propellant.

The required volume of GN_2 can be calculated using the ideal gas law:

$$v_{GN_2} = \frac{mRT}{M_m p} \tag{6.5}$$

where v_{GN_2} is the volume in m^3, m is the mass of the gas in kg, R is the universal gas constant of 8.314 J/molK, M_m is the molar mass of nitrogen (28.02g/mol) and p is the pressure at which the gas is stored in Pa. For 250g of GN_2 stored at 293.15K and 90 bar, a total volume of 2.42L is required. To store this, a single 2.5L spherical tank will be used. The nitrogen tank will be made from Aluminium 2219-T87 due to its high strength-to-weight ratio and heritage in space missions [16]. The characteristics of the fuel tank are calculated with a safety factor of 2 to ensure the hoop stress does not exceed the material's yield stress σ_Y:

$$\sigma_{hoop} = \frac{pr}{2t_w} \tag{6.6}$$

where σ_{hoop} is the hoop stress for spheres in MPa, p is the pressure of the tank in Pa, r is the radius in m and t_w is the wall thickness in m. The characteristics of the tank are presented in Table 6.1.

Table 6.1: Characteristics of the GN_2 Fuel Tank.

Parameter	Values
σ_Y	395 MPa
σ_{hoop} at 90bar	189 MPa
Radius	84 mm
Wall thickness	2 mm
Volume	2.5 L
Tank mass	0.63 kg

7 Propulsion

In this chapter, the propulsion subsystem's design is presented. The propulsion subsystem is of utmost importance as it allows the spacecraft to accelerate and decelerate. In Section 7.1, the thruster and its propellant are chosen. In Section 7.2, the propellant tanks containing both oxidiser and fuel are sized and in Section 7.3 the gimbal of the propulsion system is chosen. Section 7.4 shows an overview of the propulsion subsystem components, with an architecture diagram.

7.1 Thruster and Propellant

The most vital parts of the propulsion subsystem are the thrusters. They provide ΔV to the spacecraft to perform the necessary manoeuvres and the de-orbit operations. As of **[R-SUB-PRO-09]**, and **[R-SUB-PRO-14]**, the thrusters shall use non-toxic propellants and a specific impulse of at least 330s. First, the main thruster is chosen. Then the use of an adverse thruster is researched and justified. Lastly, the properties of the propellant are listed.

Main Thruster

According to **[R-SUB-PRO-01]**, the main thruster shall have a thrust of at least 400N. A thruster designed by researchers at the University of Padova uses a combination of H_2O_2 and kerosene as propellant [11], which is both green and non-toxic. Additionally, the thruster under research provides a thrust of 465 N and a specific impulse of 342 s, thus complying with all the previously stated requirements. No mass of the thruster was provided, so an estimation was done using the mass of another bi-propellant thruster of 450 N. The BT-4 rocket engine by IHI Aerospace has a total mass of 4.0 kg, which will be multiplied by 1.5 to be conservative[20]. Thus, the thruster by the Padova University will be estimated at 6.0 kg.

In Section 3.2, the assumption was made that the main thruster will have to be redesigned in such a way that it complies with **[R-SUB-PRO-15]**. The propulsion subsystem shall have a plume expansion half-cone angle of under 15 degrees for the main thruster. This could be achieved by narrowing the thruster nozzle or by using an aerospike nozzle. As a recommendation, research will have to be done on how to reduce this angle as much as possible to ensure more efficient momentum transfer. The thruster is shown in Figure 7.1.

Adverse Thruster

One of the options considered to improve and simplify the orbital manoeuvring of the mission was to make use of an additional thruster placed opposite the main spacecraft thruster. The idea is to turn on both thrusters simultaneously to lower the net thrust and acceleration of the ADR spacecraft itself. This lower acceleration of the spacecraft increases the contact time with the target, allowing for fewer orbital manoeuvres and a potential lower total fuel requirement and time, compared to not having the adverse thruster. The idea was heavily inspired by the ion beam shepherding technology [9]. In order to assess the adverse thrust concept, a Python algorithm was created that calculates the total fuel required for the mission for a range of adverse thrust values. Figure 7.2 depicts the output of the algorithm when run for a spacecraft with an initial mass of 2000kg. As can be seen, using an adverse thruster to prolong contact time with the target is highly inefficient in terms of fuel. It was demonstrated that adverse thrust may allow for minimal operational time improvement at the cost of significantly more fuel.

---

[20] `https://www.satcatalog.com/component/bt-4/`

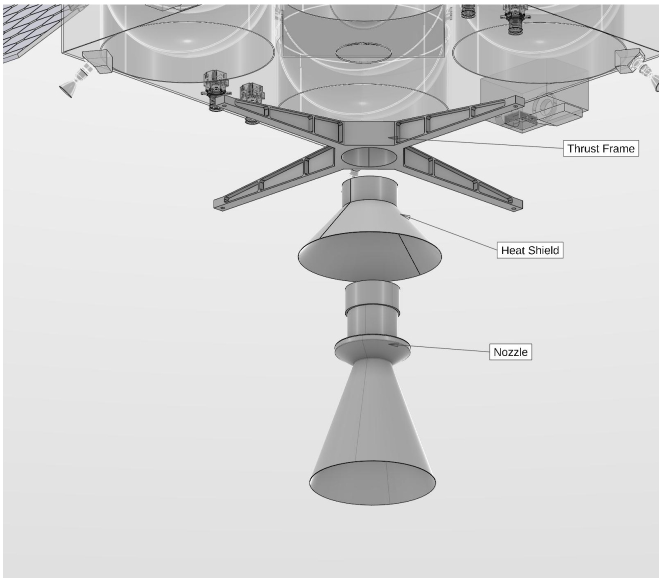

Figure 7.1: Exploded View of the Thruster Assembly.

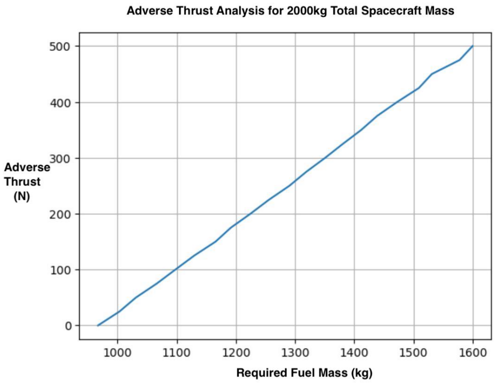

Figure 7.2: Adverse Thruster Sensibility Analysis.

These results led to the rejection of the idea. However, the use of a small adverse thruster was deemed necessary to make small velocity adjustments, improve safety and relieve ADCS from performing a 180-degree spin manoeuvre in close proximity to the target debris as described in chapter 6. In order to make use of the existing fuel infrastructure of the spacecraft, the adverse thruster will be a downsized version of the main thruster. As the main thruster is going to be developed for the mission using the design proposed by Padova University [11, 20], developing a smaller version using the same design and oxidiser/fuel (O/F) combination will not add much additional cost or complexity. An assumption is made that it will be possible to achieve a specific impulse equal to or comparable to the 342-second impulse of the main thruster. With this assumption, the fuel consumption of the mission would not be affected as the thrusters would never be activated simultaneously, and providing manoeuvring ΔV requires the same fuel mass investment for thrusters of equal I_{sp}. Therefore, the only additional mass is the mass of the adverse thruster itself and the corresponding plumbing. The adverse thruster does not partake in momentum transfer and does not need to have high thrust. Complying with **[R-SUB-PRO-37]**, a 50N thruster will be used as a balance between mass and thrust. Thrusters of around 50N weigh between

0.5[21] and 2.1[22] kg, thus the mass of the adverse thruster was preliminarily estimated to be 1.5 kilograms with additional plumbing of 5 kg.

Propellant

Both the main and the adverse thruster use a combination of highly stabilised H_2O_2 and RP-1 kerosene, both non-toxic. The O/F ratio of the thruster designed by the University of Padova is 6.5 [11]. This means that for every kg of kerosene, there will be 6.5 kg of oxidiser. The oxidiser H_2O_2 has a very high density of 1450 kg/m^3 [23], which makes it very volume efficient. High test peroxide costs €4/kg[24]. The RP-1 kerosene has a relatively low density of 796.6 kg/m^3 at 300 K, making the propellant combination less volume efficient [3]. The spacecraft temperature will stay between 278.1-312.8 K as defined in Section 11.6, so the density will often be even higher in reality. This means the value of 796.6 kg/m^3 is generally conservative. RP-1 kerosene costs only €2.3/kg[25].

7.2 Propellant Tanks

This section explains the design and sizing of the propellant tanks, with a focus on ensuring sufficient volume for the chosen propellants. A brief structural analysis will also be performed to verify that the tanks can withstand internal pressures without failure.

Common Bulkhead Tank Design

In Section 7.1 it was decided to use RP1 as fuel and H_2O_2 as oxidiser of the spacecraft. They have to be separated by either loading them into different tanks or by using a common bulkhead tank. The common bulkhead tank separates the fuel and the oxidiser within one tank by using a third hemispherical cap on the inside. Common bulkhead tanks benefit from the fact that the propellant mass is distributed better and that the dry mass decreases since only 3 hemispherical caps are needed instead of 4 for the separate tanks [98]. Figure 7.3 shows the inside of the tank that will be used on the spacecraft. The small red compartment will be filled with fuel, and the big grey compartment will be used for the oxidiser. Taking into account the mass densities and O/F ratio from Section 7.1, this leads to a volume fraction of 78/22 for oxidiser and fuel, respectively.

Figure 7.3: Inside of the Common Bulkhead Tank Used on the Spacecraft.

Propellant mass

Using the astrodynamic characteristics written in Section 3.2, the ΔV of the spacecraft can be calculated using the Python script, and a value of 2587 m/s for 10 pieces of debris is found. For a more conservative

---

[21] `https://satsearch.co/products/rafael-45n-thruster`

[22] `https://satsearch.co/products/ecaps-50n-hpgp-thruster`

[23] `https://gestis.dguv.de/data?name=002430`

[24] `https://www.htphub.com/`

[25] `https://spaceinsider.tech/2023/06/13/how-much-does-rocket-fuel-cost/`

figure, it will be assumed that 11 pieces of debris will have to be de-orbited instead of 10 (≈ 10% margin). This leads to a ΔV of 2941 m/s. The I_{sp} was defined in Section 7.1 to be 342 s, and the gravitational constant g_0 is defined as 9.80665 m/s^2. Using the Tsiolkovsky equation, Equation 7.1, the propellant mass can then be found.

$$\Delta V = I_{sp} g_0 \ln \frac{m_{dry} + m_{prop}}{m_{dry}} \tag{7.1}$$

It is important to note that the dry mass and the propellant mass depend on each other. A higher propellant mass leads to bigger propellant tanks and a bigger/stronger structure, which in turn leads to a higher propellant mass, which is an effect known as the snowball effect. This keeps on repeating until the values converge at some point. Thus, the calculation of the dry and propellant mass have been iterated and after convergence, a propellant mass of 381.9 kg is found.

Capacity

In Section 11.1, it is decided to use four propellant tanks. This is mainly due to the fact that a big part of the spacecraft volume will be taken up by the propellant tanks. In order to have efficient attitude control, the reaction wheels of the ADCS subsystem have to be placed in the center of gravity. Splitting up the tank volume into four tanks will thus leave the required space in the middle.

Using the propellant properties from Section 7.1 and the propellant mass of 381.9 kg, the total capacity of the tanks can be found with Equation 7.2. A total tank capacity of 292.2 L was found, with ≈73.0 L capacity per tank.

$$v_{\text{cap}} = \frac{O/F}{O/F+1}\frac{m_{\text{prop}}}{\rho_{\text{ox}}} + \frac{1}{O/F+1}\frac{m_{\text{prop}}}{\rho_{\text{fuel}}} \tag{7.2}$$

Dimensions

In this subsection, the final dimensions of each tank will be computed. The capacity of the tank is not equal to the volume since some space will be used for pressurant gas. From the capacity of 73 L, the tank volume can be found using a linear relationship from statistics. 8 other propellant tanks were researched on its capacity and outer volume, arriving at the graph in Figure 7.4[26]. The data point used in this mission is indicated as well, leading to a tank volume of 93.6 L.

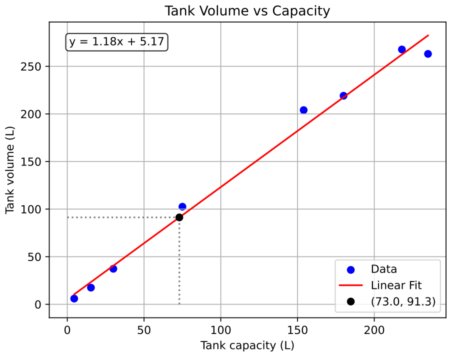

Figure 7.4: Statistical Relation Between the Capacity and the Volume of Spacecraft Propellant Tanks.

A capsule-shaped propellant tank will be assumed, as this is both strong and efficient in terms of mass

---

[26] `https://satsearch.co/products/categories/satellite/orbit-determination-and-control/propellant-tank`

capacity. This shape still has one free parameter that can be chosen for a certain volume, namely the diameter/height ratio. Since a somewhat cubical spacecraft shape is desired for low mass moments of inertia and the tanks will be placed close to each other, a diameter/height ratio of 0.5 is chosen. Section 11.1 contains more information on what this configuration will look like. With all the necessary parameters defined, the diameter and height can be computed: 0.412 m in diameter and 0.823 m in height.

Thickness and Material

The thickness of the propellant tanks is chosen as 3 mm, based on other propellant tanks available on the market. Because the strength of aluminium will suffice, Al 7075-T6 is used to manufacture the propellant tanks. This material has a lower density of 2810 kg/m^3 than titanium alloys, but still a high yield strength of 503 MPa[27]. To ensure proper flow of the propellant to the thrusters, the tanks will be pressurised with helium to pressure p = 30 bar or 3 MPa. This will induce a hoop and a longitudinal stress, calculated with Equation 7.3. r denotes the radius of the tanks, and t_w denotes the wall thickness. The tank design will be analysed to ensure the tank can handle these stresses.

$$\sigma_{\text{hoop}} = \frac{pr}{t_w}, \qquad \sigma_{\text{long}} = \frac{pr}{2t_w} \tag{7.3}$$

This results in a hoop stress of 205.8 MPa and a longitudinal stress of 102.9 MPa. The maximum of this is 2.44 times lower than the yield strength of the aluminium alloy, so essentially a safety factor of 2.44 is applied. Using these dimensions, the tanks (without attachments) have a mass of 8.97 kg per tank or 35.9 kg for all four tanks.

7.3 Gimbal

The main thruster will need bi-directional thrust vector control, allowing for a range of at least 10 degrees in all directions. This is dictated by **[R-SUB-PRO-36]**. The most logical way to allow for this is by putting the thruster on a gimbal. The Model-T 24-28V gimbal by Moog complies with these requirements[28]. It was initially designed to mount electrical propulsion but has also been used for NTO/MMH bi-propellant combinations.

7.4 Overview and Architecture

Table 7.1 shows the mass, power and cost budget of the propulsion subsystem for each component.[29] Figure 7.5 shows the interactions between the components of the propulsion subsystem. Green arrows resemble electrical wires, and black arrows resemble pipes for the gas or liquid to run through.

Table 7.1: Budgeting of the Mass, Power and Cost of the Propulsion Subsystem.

Component	Amount	Total Mass [kg]	Total Cost [k €]	Total Power [W]
Tank (with attachments)	4	62.8	13.188	0
Plumbing and Valves	1	22	50	30
Gimbal	1	5	100	15
Main Thruster	1	6.0	1000	0
Adverse Thruster	1	1.5	300	0
Kerosene RP1	63.9 L	50.9	0.025	0
H2O2	228.3 L	331.0	1.364	0
Total	**N/A**	**479.2**	**1464.5**	**45**

---

[27] `https://asm.matweb.com/search/specificmaterial.asp?bassnum=ma7075t6`

[28] `https://www.moog.com/products/space-mechanisms/gimbals`

[29] `https://shorturl.at/KxJOJ`

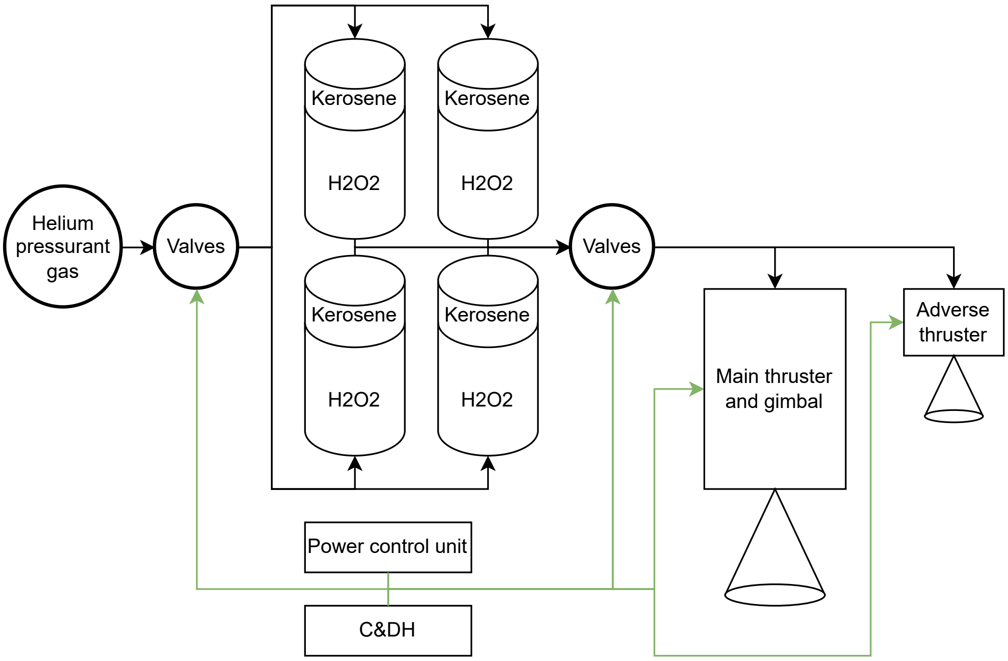

Figure 7.5: Architecture Diagram of the Propulsion Subsystem.

8 Electrical Power Subsystem

In this chapter, the electrical power subsystem or EPS, is designed. The EPS provides power to all the other subsystems during the mission. In Section 8.1, the power budget per mission phase is determined. In Section 8.2, the components are chosen, taking into account the EPS requirements. In Section 8.3, the battery pack and the solar panels are sized accordingly. Section 8.4 shows an overview of the EPS design, including the electrical block diagram.

8.1 Mission Phases and Power Budgeting

During the mission, there are multiple phases in which different components and subsystems are active. This was calculated by allocating to each component an active time fraction of a certain phase. Then, by looking up or calculating the idle and active power of each component, the power budget can be created. This is defined as a requirement and verified in Table 13.11. Additionally, it is important to know the running time for each mode (per operational orbit when applicable): 1000 s for launch, 1200 s for startup, 800 s for observe, 1200 s for prepare, 6 s for de-orbit, 3655 s for outer orbit. The EoL mission phase will continue until disintegration after the mission, so there is no running time for this phase.

Figure 8.1 and Figure 8.2 show the non-repeated and the repeated mission phases, respectively. It is important to note that for EoL, the timestamps are not accurate, as it will continue onwards for a very long time. To add to this, only the worst-case orbit scenario of the repeated phases is provided, which will be repeated 10 times during the mission. Between two separate repeated phases, there might be some ”empty orbits” of just the outer orbit mission phase. The repeated phases mark within the dotted lines refers to the repeated phases in the second figure.

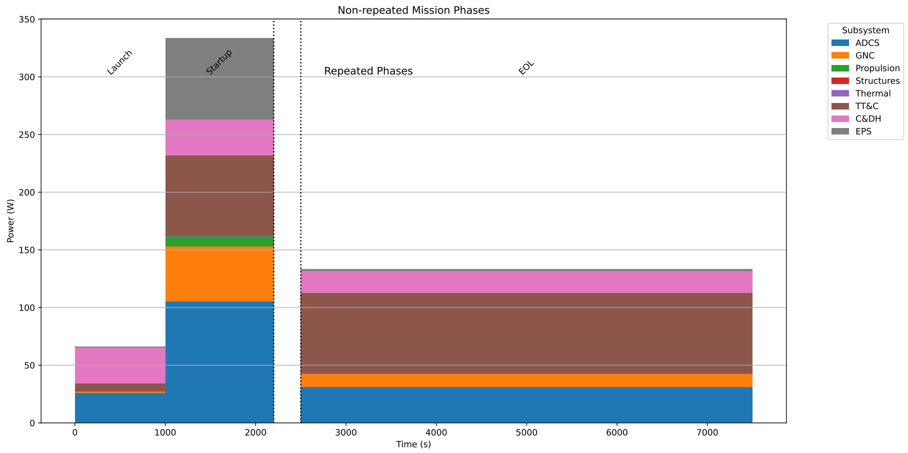

Figure 8.1: Required Power During the Non-repeated Phase.

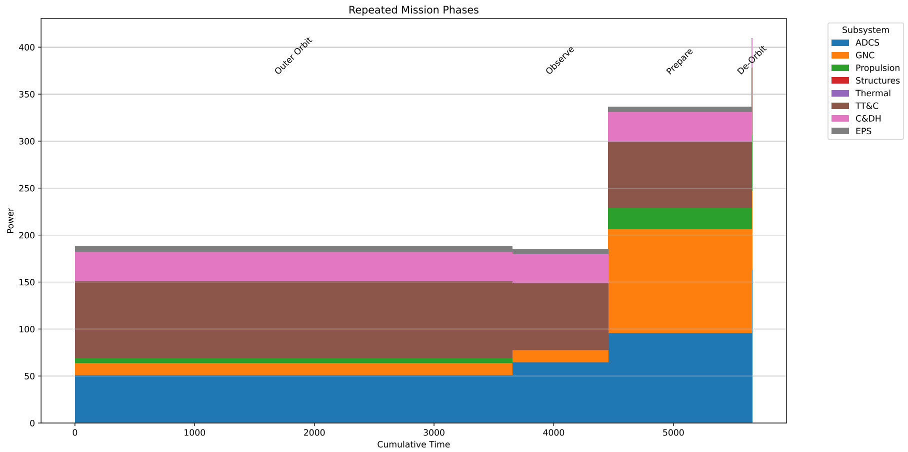

Figure 8.2: Required Power During the Repeated Phase.

8.2 Components and Configuration

In this section, the required components of the EPS, along with their configuration, will be chosen. These consist of the solar cells, maximum power point trackers (MPPT), power control unit (PCU) and the batteries.

Batteries

The spacecraft components will run at voltages between 3.3 V and 28 V as per **[R-SUB-EPS-18]**, so a nominal battery voltage of at least 28 V will be chosen. Due to its discharge efficiency, energy density, reliability and cycle life, Li-ion 18500 Rechargeable Cells are chosen from Batteryspace[30]. Their nominal voltage is 3.7 V, so using 8 cells in series results in 29.6 V. Hence, they will be placed in an array of a multiple of 8 cells by x cells, where x is defined in Section 8.3.

PCU

The PCU (or PMU) of the spacecraft will be chosen such that requirements **[R-SUB-EPS-11]**, **[R-SUB-EPS-12]**, and **[R-SUB-EPS-18]** are fulfilled. The PCU-110 by Berlin Space Technologies is a very versatile and adaptable PCU. It is able to handle power regulation, power switching, DC/DC conversion and contains safety features[31]. With some optional adaptations, it can output voltages anywhere between 1.8 V and 28 V, complying with the requirement. The solar power input voltage can be anywhere between 20 V - 25 V DC.

Solar Cell

In order to generate power on the spacecraft in LEO, solar cells are used. The solar cells are not inside the spacecraft, so it is very important to choose LEO-graded solar panels to ensure thermal and radiation damage prevention or protection. They will not be able to be protected by any structure, nor will they be heated or cooled. For easy extendability, the small 32% Quadruple Junction GaAs Solar Cell 4G32C[32] of Azurspace was chosen. This company is known for its very reliable solar cells, also offering high efficiencies.

Each solar cell has an output voltage of 2.9 V. The PCU accepts voltage anywhere between 20 V and 25 V, which can be achieved by putting 8 solar cells in series, resulting in a voltage of 23.2 V. This means each solar panel will be an array of a multiple of 8 cells by x cells where x will be determined in

---

[30] `https://www.batteryspace.com/aaaaaseriesli-ioncells.aspx`

[31] `https://satsearch.co/products/berlin-space-tech-pcu-110`

[32] `https://www.azurspace.com/index.php/en/products/products-space/space-solar-cells`

Section 8.3.

MPPT

The EPS also needs a maximum power point tracker to maximise the power output of the solar panels. This function is performed by the PPT-650 from AgilSpace[33]. The power is transferred from the solar cells via wires and connectors to the maximum power point trackers, which are specifically designed to handle variable power sources like solar arrays. They sample the cell output and apply the proper resistance (load) to obtain maximum power [95]. The PPT-650 can handle a maximum of 650 W, which should be plenty for both solar panels. However, for redundancy and to be conservative, two PPT-650 will be put on the spacecraft, one for each panel.

8.3 Sizing

In this section, the sizing of the battery pack and solar panels is carried out based on the spacecraft's power requirements. Additionally, the corresponding mass of each component is calculated to support system-level mass budgeting and integration planning.

Battery Pack

There are two important cases when the spacecraft needs a battery: during startup and during eclipse. Necessary capacity will be calculated for both such that the battery can be sized for the most constraining case.

During startup, the spacecraft should not rely on the solar panels being able to perform all initiation operations. To be conservative, it will be assumed that all power during the launch and startup will be provided by the batteries. To calculate the total energy used, the first two bars from Figure 8.1 can be integrated, resulting in a total energy of 466 kJ.

During an eclipse, the solar cells cannot generate any power, and thus, a battery pack of sufficient size is necessary. As of requirement **[R-SUB-EPS-08]**, the battery pack shall store enough energy for the spacecraft to support one outer orbit - observe - prepare - operation cycle during eclipse. With this requirement, the necessary amount of batteries can be calculated.

First, the eclipse time needs to be calculated, which is dependent on the altitude, inclination and solar longitude. The inclination was determined to be 53°. In terms of eclipse, the worst case will be found by using the lowest operational altitude the spacecraft: 381 km. As a simplification, this orbit will be considered circular since its eccentricity is only 0.016. This greatly reduces computational difficulty when using a Python script. Plotting the eclipse time for solar longitude, renders Figure 8.3a, showing a worst-case eclipse time of 2170 s at solar longitude of 126.8 and 233.2 degrees. Figure 8.3b shows the orbit for this worst-case scenario.

---

[33] `https://satsearch.co/products/agil-space-ppt-650-solar-peak-power-tracker-sppt`

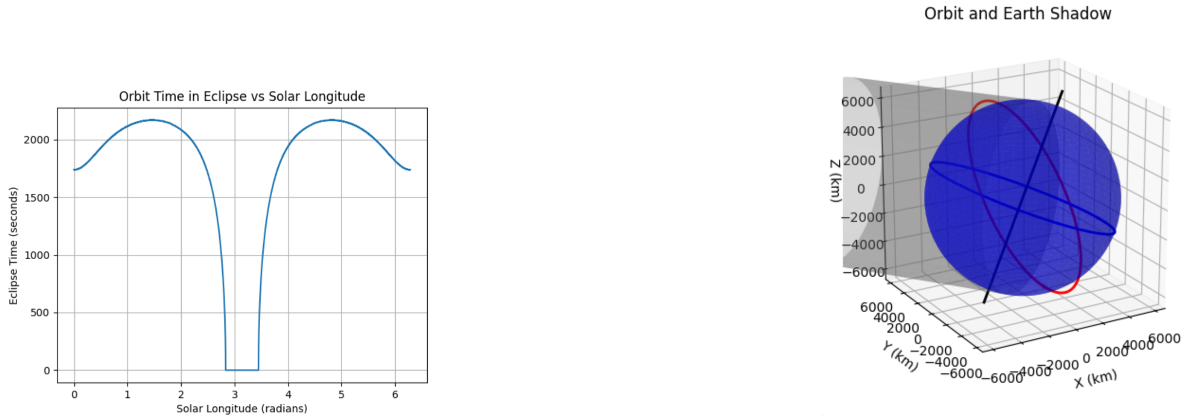

(a) Graph Showing Eclipse Time per Orbit for All Solar Longitudes.

(b) Eclipse Worst Case Orbit (red) Around the Earth, Equator (blue) Indicated for Clarity.

Figure 8.3: Eclipse of the Spacecraft.

From the eclipse time of 2170 s and the mission phases, the time for each phase in eclipse can be calculated. Using their corresponding power, the energy per phase and total energy can also be calculated. This is tabulated in Table 8.1.

Table 8.1: Time, Power and Energy for each Mission Phase in Eclipse.

Mission Phase	Time [s]	Average Power [W]	Energy [J]
Outer Orbit	164	187.7	30 785
Observe	800	185.5	148 370
Prepare	1200	336.4	403 660
De-orbit operation	6	409.9	2459
Total	**2170**	**269.7**	**585 274**

The total of 585 kJ is higher than that of the launch and startup phase, so the eclipse is the more constraining case. Of course, all batteries and wires have losses. The energy retrieved after a charge will always be less than what was put in. Parasitic reactions that occur within the electrochemistry of the battery prevent the efficiency from reaching 100 percent[34]. Using a very conservative coulombic and energy efficiency of 0.95 for both, the energy retrieved from the batteries in eclipse will equal 180 Wh.

An important parameter of the batteries is their capacity after a certain number of cycles. It is estimated that the spacecraft will do about 500 orbits within its operational life. However, the batteries will not be discharged fully each cycle, or not at all when looking at Figure 8.3a. It is very difficult to put an exact number on the amount of full discharges, so 300 will be chosen. The Li-ion 18500 battery has 80% capacity at 300 cycles. The depth-of-discharge of Li-ion batteries is about 85 percent[35], but to be conservative with the capacity after 300 cycles, 80% is chosen. An additional 10% margin from the contingency planning is added. This results in a minimum battery capacity of 310 Wh at launch. Using the properties and configuration from Section 8.2, a total amount of 56 batteries is found in an 8x7 array, having an actual capacity of 332 Wh. The total mass is 2.02 kg.

---

[34] `https://batteryuniversity.com/article/bu-808c-coulombic-and-energy-efficiency-with-the-battery`

[35] `www.energysage.com/energy-storage/depth-of-discharge/`

Solar Panels

As of requirement **[R-SUB-EPS-09]**, the EPS solar panels shall generate at least 648 kJ in one daylight cycle to charge the batteries after an eclipse operation. One daylight cycle will take 3491 s in the worst-case scenario. The battery energy spent during the eclipse was calculated previously to be 180 Wh. Hence, the solar panels will charge the batteries in addition to providing power to the subsystems as required by requirement **[R-SUB-EPS-17]**. Again, the worst-case scenario, where a full de-orbiting operation cycle is happening while charging the batteries, will be assumed. To calculate the power and energy of the phases, the values of Table 8.1 can be reused with some minor changes. Its result is tabulated in Table 8.2.

Table 8.2: Time, Power and Energy for each Mission Phase in Daylight Cycle.

Mission Phase	Time [s]	Average Power [W]	Energy [J]
Charge batteries	3491	187.2	648503
Outer Orbit	1485	187.7	278754
Observe	800	185.5	148370
Prepare	1200	336.4	403660
De-orbit operation	6	409.9	2459
Total	**3491**	**424.4**	**1481746**

The total energy that needs to be generated each daylight cycle is thus equal to 1 481 746 J. The solar panels will be active 3491 s, resulting in the required generated power of 424.4 W during daylight, which is indicated in the table. At maximum degradation, the solar cells have an efficiency η_{sc} of 20.1 percent[36]. Requirement **[R-SUB-EPS-16]** together with the ADCS star tracker and sun sensors ensure that the solar incidence angle θ will be at most 15 degrees. With a solar constant J_s of 1367 W/m^2 [15] and a margin of 10% (safety factor SF of 1.1), a minimum solar cell area A_{sc} of 1.76 m^2 is found, using Equation 8.1.

$$A_{sc} = \frac{SF \cdot P}{J_s \eta_{sc} \cos\theta}, \tag{8.1}$$

With P being the generated power. Each solar cell has a total area $3.2 \cdot 10^{-3} m^2$ but an effective area of $3.018 \cdot 10^{-3} m^2$, resulting in a minimum of 583 cells. Due to the chosen configuration in Section 8.2, the solar panels will have 608 cells in total, so 304 each. This is done in a 16x19 array with dimensions 0.76m x 1.28m. With a mass of 2.6 g per cell, the total solar array mass is 1.58 kg.

8.4 Overview

Table 8.3 tabulates an overview of the components of the electrical power subsystem with their mass and cost. In Figure 8.4, the electrical block diagram is visualised. The Electrical Block Diagram shows the electrical equipment of the product or system and its mutual relations and interactions. The solar cells generate electrical power, which is processed using Maximum Power Point Tracking (MPPT) to optimise efficiency. Next, the power will be converted (DC/DC) and regulated by the PCU-110. Additionally, the PCU handles charging and discharging of the batteries. The power can then be distributed by the PCU to all the separate subsystems and their corresponding components. There will also be a connection between the C&DH and TT&C to receive and handle commands, which can then be transmitted to the PCU. As a result, the PCU and C&DH subsystem will work in close parallel.

---

[36] `https://www.azurspace.com/index.php/en/products/products-space/space-solar-cells`

Table 8.3: Budgeting of the Mass and Cost of the EPS.

Component	Amount	Total Mass [kg]	Total Cost [k €]
Solar Cells	608	1.58	156.864
Batteries	56	2.02	0.383
PCU	1	1.08	127.2
MPPT	2	1.00	390.0
Wiring	1	2.5	0.159
Total	**N/A**	**8.18**	**674.6**

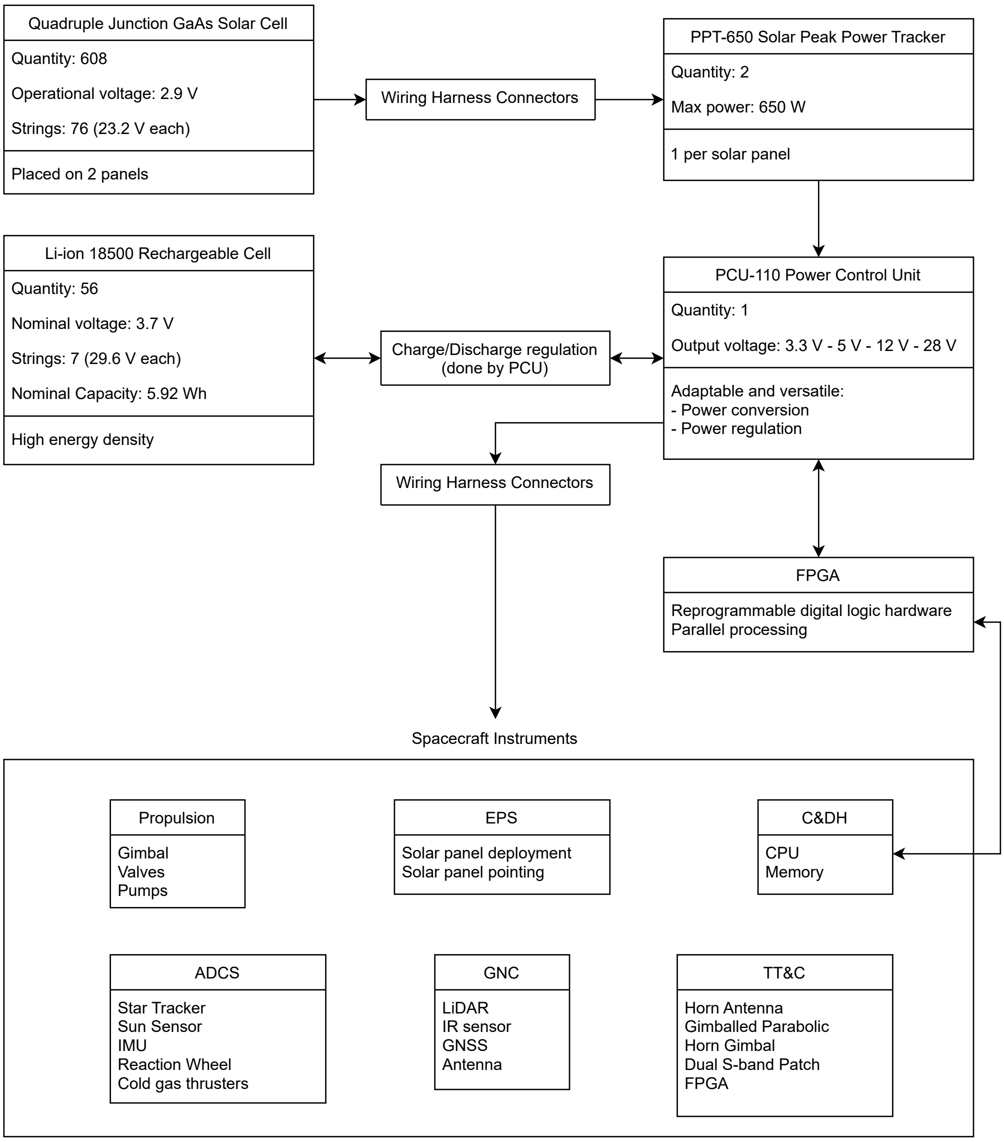

Figure 8.4: Electrical Block Diagram of the Spacecraft.

9 Telemetry, Tracking and Command

Having established the mission and its operations, this chapter explores the communication needs of the spacecraft in order to build the telemetry, tracking and command (TT&C) subsystem. This begins with an analysis of ground station coverage in Section 9.1, from which antennas are selected in Section 9.2 and together these are used in the link budget to ensure the communication architecture can accommodate the required data rates shown in Section 9.3. Finally, a discussion regarding on board equipment is expressed in Section 9.4 upon which the communication flow is shown in Section 9.5.

9.1 Ground Stations

The first step in designing the spacecraft's communication architecture is selecting appropriate ground stations for the mission. This selection is based on three main criteria: (1) coverage compatibility with a 600km orbit at 53° inclination, (2) support for S-band and either Ka- or X-band frequencies in line with NASA recommendations and past mission practices, and (3) compliance with requirement **[R-SUB-TTC-01]** [37]. To evaluate and refine orbital coverage, stations from ESA's core and cooperative ground network were assessed for frequency band compatibility. Their geographical distribution is shown in Figure 9.1a, and the results of the frequency band assessment are summarised in Table 9.1.

(a) Map Showing Locations of ESA Tracking (Estrack) Stations as of 2017.[38]

(b) Screenshot of Matlab Satellite Viewer.

Figure 9.1: Comparison of ESA Ground Stations and Satellite Tracking Interface.

Table 9.1: Ground Station Frequency Band Support with Sources.

Station	S-band	X-band	Ka-band	Source
ESA Core Network				
Kourou	Available	Available	Not available	[37]
Kiruna	Available	Available	Not available	[37]
Redu	Available	Not available	Available	[34]
Cebreros (DS)	Available	Available	Available	[37]

Continued on next page

---

[37] `https://www.nasa.gov/smallsat-institute/sst-soa/soa-communications/`

Table 9.1 – continued from previous page

Station	S-band	X-band	Ka-band	Source
New Norcia (DS)	Available	Available	Available	[37]
Santa Maria	Available	Available	Not available	[37]
Malargüe (DS)	Available	Available	Available	[37]
Cooperative Network				
Poker Flat	Available	Not available	Not available	[37]
Goldstone (DSN)	Available	Available	Available	[71]
Madrid (DSN)	Available	Available	Available	[71]
Weilheim (DLR)	Available	Available	Unknown	[42]
Esrange (SSC)	Available	Available	Not available	[96]
Hartebeesthoek	Available	Available	Not available	[85]
Malindi	Available	Available	Not available	[37]
Kerguelen	Available	Not available	Not available	[37]
Usuda (JAXA)	Available	Available	Available	[61]
Masuda (JAXA)	Available	Available	Available	[61]
Canberra (DSN)	Available	Available	Available	[71]

In order to analyse the coverage provided by the compatible ground stations mentioned above, the built-in MATLAB aeroSATCOM function was used with the orbital parameters defined as 600km altitude circular orbit at 53° inclination. The various station locations were defined by longitude and latitude and it was run for a 24 hour simulation. This led to the visual interaction between ground stations and the spacecraft shown in Figure 9.1b where it is communicating with Kourou. The program also outputs the start and end of contact times with all the stations for each orbit. They are compiled in Table 9.2, which displays contact time with X-band compatible stations.

Table 9.2: Contact Time Per Orbit With Totals Excluding Overlap.

Orbit	GS	Contact Time (s)	Orbit	GS	Contact Time (s)
1	Santa Maria	600	2	Goldstone	600
1	Cebreros	600	2	Santa Maria	600
1	Madrid	600	2	Cebreros	720
1	Weilheim	720	2	Madrid	720
1	Kiruna	480	2	Weilheim	660
1	Esrange	480	2	Malindi	720
1	Malindi	120	2	New Norcia	360
1	New Norcia	600	2	Canberra	600
1	Canberra	480	2		
Total Contact Time (s)		**2220**	**Total Contact Time (s)**		**3240**
3	Goldstone	720	4	Goldstone	600
3	Santa Maria	720	4	Poker Flat	300
3	Cebreros	720	4	Santa Maria	660
3	Madrid	720	4	Cebreros	120

Continued on next page

Orbit	GS	Contact Time (s)	Orbit	GS	Contact Time (s)
3	Weilheim	360	4	Madrid	120
3	Malindi	540	4	Hartebeesthoek	660
3	Hartebeesthoek	720	4	New Norcia	660
3	New Norcia	360	4	Canberra	660
3	Canberra	720	4		
Total Contact Time (s)		**3420**	**Total Contact Time (s)**		**2880**
5	Poker Flat	540	6	Goldstone	720
5	Goldstone	480	6	Santa Maria	600
5	Kourou	540	6	Cebreros	660
5	Hartebeesthoek	240	6	Madrid	600
Total Contact Time (s)		**2220**	**Total Contact Time (s)**		**2580**
7	Hartebeesthoek	360	8	Goldstone	720
7	Santa Maria	540	8	Poker Flat	720
7	Cebreros	540	8	Santa Maria	720
7	Madrid	720	8	Cebreros	720
7	Weilheim	720	8	Madrid	720
7	Malindi	0	8	Weilheim	720
7			8	Malindi	720
7			8	New Norcia	720
Total Contact Time (s)		**2880**	**Total Contact Time (s)**		**3600**
9	Goldstone	360	10	Goldstone	600
9	Santa Maria	360	10	Santa Maria	480
9	Cebreros	480	10	Cebreros	0
9	Madrid	480	10	Madrid	0
9	Weilheim	720	10	Weilheim	0
9	Malindi	0	10	Malindi	0
Total Contact Time (s)		**2400**	**Total Contact Time (s)**		**1080**
11	Goldstone	540	12	Goldstone	720
11	Santa Maria	360	12	Santa Maria	720
11	Cebreros	480	12	Cebreros	720
11	Madrid	0	12	Madrid	720
Total Contact Time (s)		**1380**	**Total Contact Time (s)**		**2880**
13	Goldstone	720	14	Goldstone	540
13	Santa Maria	720	14	Santa Maria	600
13	Cebreros	720	14	Cebreros	600
13	Madrid	660	14	Madrid	600
13	Weilheim	0	14	Weilheim	0
13	Malindi	0	14	Malindi	0
Total Contact Time (s)		**3720**	**Total Contact Time (s)**		**2340**
15	Goldstone	720			
15	Santa Maria	720			
15	Cebreros	720			
15	Madrid	300			
Total Contact Time (s)		**2460**			

From Table 9.2, it can be observed that contact is made every orbit with the use of multiple stations compatible with S and X band frequencies as previously mentioned. Therefore, telemetry and command can take place every orbit, as well as the LiDAR data dumping between each rendezvous. In order to find the limiting contact time and by extension data rate, it shall be assumed the LiDAR data is to be dumped in one go using one ground station. Therefore, the orbit with the shortest maximum contact time is 540s in orbits 5 and 11.

Concerning the infrared livestream, ground station contact is not constant throughout the day as they do not cover the span of the globe. Therefore, there are two possibilities to ensure contact during the uncovered times. With current operations, the momentum transfer can happen above an uncovered point in orbit which in turn requires the use of relay satellites to maintain contact. This could entail high costs and additional communication equipment. Another option would be to set the rendezvous to be above ground stations as much as possible. For various orbits, contact can be made with the Santa Maria ground station, so the spacecraft could be set to perform momentum transfers in those moments. This would require an iteration of operations for windows of non-operation when contact is not possible, possibly creating delay in reaching targets compared to the ideal two-orbit strategy. Additional fuel, mass and costs would trickle from this solution. A trade-off between these two options must be analysed in the following design phases by contacting suitable relaying services and inquiring their costs and collaboration possibilities. For the sake of the following analysis, it will be assumed that X-band is used and operations are adapted accordingly. If this were to change, the method for link budget would remain, while antenna type and architecture may slightly vary.

9.2 On-board Antennas

The antennas can already be selected based on band type chosen in Section 9.1.

Telemetry and command functions will operate through a shared dual S-band patch antenna, such as the model provided by IQ Spacecom [39]. This antenna is compact, lightweight, and supports simultaneous transmission and reception over standard S-band frequencies (1995–2185 MHz), making it well-suited to small satellite platforms.

For both the LiDAR data dump and the real-time infrared camera livestream, each requiring high data throughput during short ground station passes, the KaPDA-Gimbal from Tendeg LLC was selected[40]. This deployable, high gain antenna supports both X-band and Ka-band operation and integrates a two axis gimballed pointing system for precise beam steering. Although capable of Ka-band transmission, current mission operations assume the use of X-band, taking advantage of its broader ground segment support and atmospheric robustness. The gimballed system ensures stable, high gain directional links throughout each pass, maximising data transfer efficiency for both burst-mode LiDAR dumps and continuous infrared video streams.

9.3 Link Budget Method

In order to construct a link budget, the operations shown in Figure 3.1 must be considered. The communication can be split into three parts:

- The command uplink, for reception of orders from the ground requiring a wide beam, low complexity antenna.
- The health and fuel level downlink, which also needs wide coverage as it is unknown where on Earth this data will be received.
- The limiting payload data downlink, whether for live stream or dumping purposes.

The link budgets for the satellite communication system were developed using a reverse link budget approach. This method begins with a required signal-to-noise ratio (SNR) at the receiver and works backward to determine the necessary transmission power and antenna gains. The methodology follows standard practices in satellite communication system design [68, 79].

1. Data rate estimation: For standard telemetry and command links, typical data rates for LEO satellites were used [41]. For payloads such as the infrared camera, the required data rate was computed as:

---

[39] `https://www.iq-spacecom.com/shop/s-band-dual-patch-antenna1995-2185-mhz`

[40] `https://www.satnow.com/products/satellite-antennas/tendeg-llc/126-1372-kapda-gimbal`

[41] `https://www.nasa.gov/smallsat-institute/sst-soa/ground-data-systems-and-mission-operations/?utm.com`

$$DR = D \cdot N_p \cdot FR \tag{9.1}$$

where DR is the data rate in bits per second, D is the pixel depth in bits, N_p is the number of pixels per frame (image resolution), and FR is the frame rate in frames per second. The infrared camera stream was assumed to be subject to lossy compression, which is typical in space applications to reduce bandwidth requirements, particularly using standards such as JPEG2000 or CCSDS 122.0-B-1 [88]. For the LiDAR, the data rate is found based on operational and contact time:

$$DR_{\text{downlink}} = \frac{DR_{\text{recorded}} \times t_{\text{recorded}}}{t_{\text{min. contact}}} = \frac{\text{LiDAR data stored}}{t_{\text{min. contact}}} \tag{9.2}$$

with the assumption of one contact window per orbit to dump all the data.

2. Modulation and target SNR: Each communication link was assigned a modulation scheme appropriate for its data rate and robustness. For example:
   - Binary Phase Shift Keying (BPSK) requires approximately 9 dB SNR
   - Quadrature Phase Shift Keying (QPSK) requires approximately 11 dB SNR

   An additional 3 dB margin was added to account for implementation and environmental losses, resulting in typical target SNRs of 12 to 14 dB.
3. Bandwidth estimation: Given the modulation scheme and the pulse shaping filter, the minimum required channel bandwidth B can be approximated using:

$$B = R_s(1 + \alpha_{ro}) \tag{9.3}$$

where R_s is the symbol rate in symbols per second, and α_{ro} is the roll-off factor due to filtering. For many practical systems, α_{ro} is typically 0.35. The symbol rate depends on the modulation order M and the data rate DR:

$$DR_s = \frac{DR}{\log_2 M} \tag{9.4}$$

Thus, the bandwidth in terms of data rate and modulation order is:

$$B = \frac{R}{\log_2 M}(1 + \alpha_{ro}) \tag{9.5}$$

4. Received power: The required received power P_{rx} was computed using:

$$P_{\text{rx}} = N + \text{SNR}_{\text{target}} \tag{9.6}$$

where N is the noise power in dBW, computed as:

$$N = 10 \log_{10}(kT_{\text{sys}}B) \tag{9.7}$$

with $k = 1.38 \times 10^{-23}$ J/K (Boltzmann constant), T_{sys} the system noise temperature in kelvin, and B the bandwidth in hertz.

5. EIRP calculation: The required equivalent isotropically radiated power (EIRP) was calculated as:

$$\text{EIRP} = P_{\text{rx}} + L_{\text{fs}} + L_{\text{other}} - G_{\text{rx}} \tag{9.8}$$

where L_{fs} is the free-space path loss, L_{other} accounts for additional losses (e.g., atmospheric, polarization), and G_{rx} is the receiver antenna gain.

The free-space path loss in decibels can be calculated, assuming distance in kilometres and frequency in gigahertz, by:

$$L_{\text{fs}} = 20 \log_{10}(d) + 20 \log_{10}(f) + 92.45 \tag{9.9}$$

where d_{km} is the slant range between the satellite and the ground station in kilometres, f_{GHz} is the operating frequency in gigahertz, and 92.45 is a constant derived from the speed of light and unit conversions.

For a typical low Earth orbit at 600 km altitude and 53° inclination, the worst-case slant range when the satellite is near the horizon can be approximated at around 2,500 km. This value was used in the FSPL calculation to ensure a conservative link budget.

6. Transmit power: The transmit power P_{tx} required to meet the EIRP was then calculated by:

$$P_{\mathrm{tx}} = \mathrm{EIRP} - G_{\mathrm{tx}} \tag{9.10}$$

where G_{tx} is the transmitter antenna gain.

7. Verification and adjustment: These values were iterated with realistic parameters for antennas and transceivers:
   - Compliance with transmitter power budgets and size constraints
   - Use of available S-band or X-band hardware
   - Sufficient SNR during realistic contact durations

This process resulted in the following link budget shown in Table 9.3

Table 9.3: Link Budget Results.

Parameter	**Telemetry DL**	**IR Payload DL**	**LiDAR Dump**	**Command UL**
Band	S-band	X-band	X-band	S-band
Data Rate [bps]	9 600	5 000 000	1 155 556	9 600
Modulation	BPSK	QPSK	QPSK	BPSK
Filtering	0.35	0.35	0.35	0.35
Bandwidth [Hz]	11 500	3 375 000	780 000	12 960
TX Gain [dB]	5.00	45.00	45.00	35.00
TX Power [dBW]	-19.00	-35.54	-41.90	-19.00
RX Gain [dB]	35.00	45.00	45.00	5.00
Path Loss [dB]	160.00	168.00	168.00	160.00
Other Loss [dB]	3.00	3.00	3.00	3.00
Tsys [K]	500.00	600.00	600.00	500.00
Noise Figure [dB]	4.00	4.00	4.00	4.00
Noise Power [dBW]	-161.00	-135.54	-141.90	-161.00
Received Power [dBW]	-146.00	-120.54	-126.90	-146.00
SNR Target [dB]	15.00	15.00	15.00	15.00

The link budget analysis confirms that all communication links achieve the specified SNR target of 15 dB. This outcome is expected, as the system was designed from the required SNR, ensuring each link nominally satisfies its performance criteria. The S-band links are appropriately dimensioned for low-rate, robust communication, making efficient use of bandwidth and power. In the X-band payload downlinks, intended for high-throughput data transmission, the IR livestream operates at a higher data rate and wider bandwidth, but benefits from a slightly stronger received power level. In contrast, the LiDAR dump downlink, while still meeting its SNR requirement, operates closer to the margin due to its narrower bandwidth and lower received power. This suggests that, of the two, the LiDAR link is marginally more constrained. Nevertheless, both remain within acceptable limits, indicating a well-balanced and purpose-fit communications architecture.

9.4 On-board Equipment

The TT&C subsystem will be implemented using a dedicated Field-Programmable Gate Array (FPGA) designed to perform all essential radio functions required for both S-band and X-band communication links. This FPGA will replace multiple discrete hardware components traditionally found in TT&C transceiver subsystems, such as separate modulators, demodulators, forward error correction encoders and decoders, digital signal processors and filtering units. Typically distributed across specialised ASICs or mixed-signal devices, these functions will be consolidated into a single reconfigurable platform.

The FPGA will handle modulation and demodulation of radio frequency signals, advanced forward error correction algorithms (e.g., Low-Density Parity-Check or Turbo codes), and pulse shaping filters such as root-raised cosine to control bandwidth and minimise inter-symbol interference. In addition, it will manage data framing, synchronisation, timing recovery, and protocol control to ensure robust link layer operation. High-speed digital interfaces will enable seamless data exchange with onboard payload and telemetry processors, while integrated control logic will provide configuration management and system status monitoring.

By integrating these functions within one FPGA, the design streamlines hardware architecture, reduces power consumption, and improves system reliability by minimising inter-component connections. The inherent flexibility of the FPGA also allows for adaptation of modulation schemes, coding rates, and data handling protocols through firmware updates, supporting evolving mission requirements without hardware changes. Ultimately, this approach replaces the conventional multi-chip TT&C transceiver assembly with a highly integrated, power-efficient, and adaptable digital solution.

9.5 Communication Block Diagram

Figure 9.2 shows the communication block diagram, representing the flow of signals and data between the communication systems of the spacecraft and the ground station.

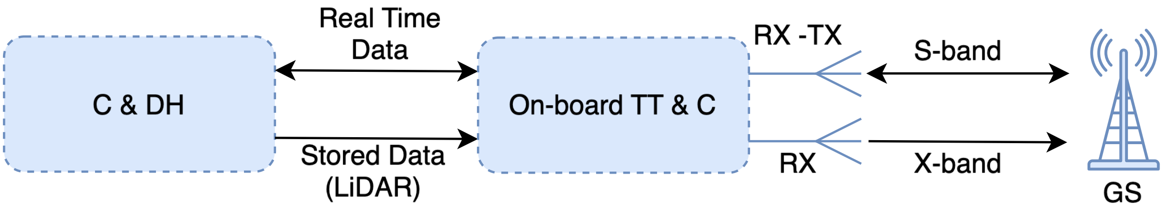

Figure 9.2: Communication Flow Diagram.

10 Command and Data Handling

This chapter is dedicated to the detailed design of the Command and Data Handling (C&DH) subsystem for the ADR satellite. The focus lies both on defining the C&DH subsystem's interface with the rest of the satellite and on developing its internal architecture. The discussion begins in Section 10.1, where the system-level interface is established, including the selection of an appropriate computer network architecture and the mapping of information and command flows across subsystems. The analysis then shifts inward in Section 10.2, where each critical module of the C&DH is examined and collectively integrated into a dedicated hardware block diagram capturing their interconnections. Following this, specific components are selected and preliminary estimates for mass, power consumption and cost are provided. The chapter concludes with a brief note on software considerations and the rationale for omitting detailed software design.

10.1 System-Level Interface with C&DH

This section defines how the Command and Data Handling (C&DH) subsystem interfaces with the rest of the spacecraft, both physically and logically. It begins by comparing different Computer Network Architectures (CNA). Then, the flow of information and commands between subsystems is addressed. Finally, a System-level Data Handling Block Diagram is presented in order to illustrate the resulting communication logic, the placement of processing units, and the overall structure of subsystem interactions within the satellite.

Computer Network Architecture

Before diving into the detailed design of the C&DH subsystem for the ADR satellite, it is crucial that the interface of all other subsystems with the C&DH is clearly defined. This hierarchical design method allows for the identification of the components needed for the C&DH subsystem itself, leading to a more accurate design.

The first aspect to be considered is the CNA, i.e. how subsystems will communicate with one another. This entails the definition of information and command flow within the subsystems, leading to a detailed System-Level Data Handling Block Diagram to be presented at the end of this section.

In the determination of a specific CNA, Starfixers Inc. considered three different options:

- Centralised (Star) Architecture
- Ring Architecture
- Bus Architecture

A very basic overview of the above configurations is depicted in Figure 10.1, as presented in a lecture by KiboCUBE Academy[42].

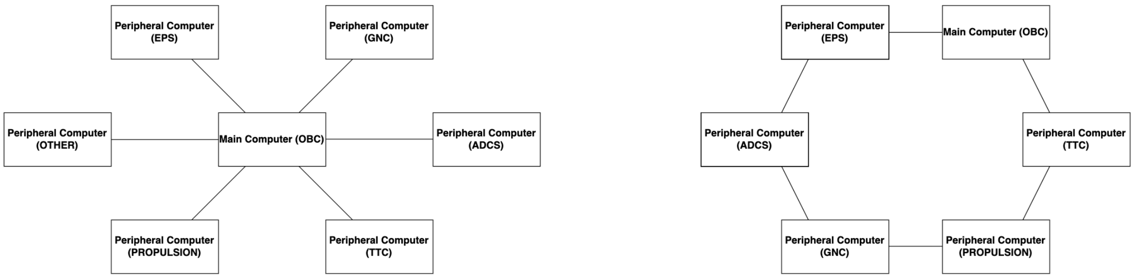

A) Centralised (Star) Architecture

B) Ring Architecture

---

[42] `https://shorturl.at/dEKDt`

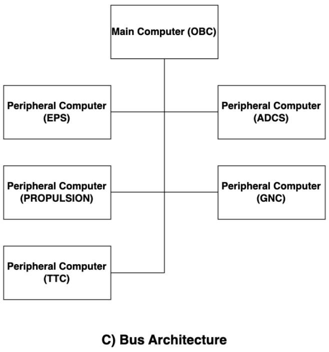

Figure 10.1: Different Computer Network Architectures.

A Star Architecture entails direct connection of the main computer to the other subsystems, and hence is considered to provide high system integrity as unit failure has less influence on the overall satellite performance compared to a more convoluted design. However, due to this Point-to-Point (P2P) connection manner, a larger wiring harness is needed, which in turn increases the mass of the satellite, as well as the free space captured inside the structure of the ADR.

The Ring Architecture, on the other hand, requires less wiring while also allowing for the easy addition of a new node to the system. Nevertheless, because in this configuration information flows through many nodes until it arrives at the intended one, there is a huge influence of unit failure. For instance, referring to Figure 10.1, if the peripheral computer of the TT&C subsystem fails, then a message from the main computer to the Propulsion subsystem either cannot get there, assuming that the command/information flow flows clockwise, or takes longer to arrive to the Propulsion subsystem, in case the flow can go both ways.

Finally, the Bus Architecture carries the same advantages as the Ring Architecture, i.e. it requires less wiring harness than the Star Architecture, while it is also relatively easy to add a new node to the system. However, this configuration is interface-sensitive, meaning that all subsystems must adhere to a shared communication protocol and timing. Any mismatch or failure in one unit's interface (e.g. due to noise, timing conflicts, or protocol violation) can disrupt or even halt communication on the entire bus.

Having established the above, one must now perform a trade-off on these three configurations. Instead of a conventional trade-off analysis using weighted criteria, however, a few high-level considerations about the ADR mission and the current system design allow for the straightforward selection of one CNA among the three options. These considerations include the complexity of the operational procedure, as well as the satellite's dry mass margins.

First, the operational procedure, as discussed in chapter 3, involves critical, time-sensitive tasks such as real-time image capture and transmission during debris rendezvous, autonomous decision-making under tight temporal constraints, and constant monitoring of satellite health. Such complexity demands a communication architecture with minimal latency, deterministic behaviour, and efficient fault isolation. These requirements favour a centralised system where all subsystems directly interface with the main On-Board Computer (OBC), minimising the risk of cascading failures and simplifying debugging and control logic.

Second, while both the Ring and Bus architectures present clear advantages in terms of reduced harness mass and easier node integration, the ADR mission is not constrained by mass. As established in the system-level mass budget, the current dry mass of the satellite remains significantly below the allowable limit derived from the cost user requirement. Hence, the additional wiring mass introduced by a Star Architecture is acceptable, especially considering the operational reliability and fault containment it provides.

Therefore, based on the above rationale, the Centralised (Star) Architecture is selected as the most appropriate Computer Network Architecture for the ADR satellite. This configuration ensures that all subsystems are directly managed by the OBC, simplifying integration, ensuring data reliability, and supporting the mission's operational complexity.

Information and Command Flow

Following the selection of the CNA, the next step prior to constructing the System-Level Data Handling Block Diagram is to define how the C&DH subsystem will interface with the remaining subsystems. This leads to another design decision: whether to adopt a) a single main computer (hosted within the C&DH OBC module), or b) a central main computer supplemented by distributed peripheral computers located within other subsystems.

This trade-off applies exclusively to active subsystems, which are defined as those that either perform onboard processing or store and handle mission data. Passive subsystems, such as Structures and Thermal Control, are excluded from this discussion, as they do not perform active operations or interface digitally with the C&DH subsystem. It is worth noting that, while thermal subsystems in some missions may collect data such as temperature or radiation levels, in this specific spacecraft design, the system is engineered to survive the full range of thermal and radiation extremes without requiring active regulation, as discussed in chapter 11. However, temperature, among other readings, of critical components will still be taken at the subsystem level and transmitted to the C&DH's Health Monitoring Unit to support system diagnostics and fault detection.

Given the complexity of the ADR mission, Starfixers, Inc. has opted for the architecture involving distributed peripheral computers embedded within key active subsystems. While a single centralised OBC may offer certain integration and testing advantages, it would require an extremely intricate software stack, capable of simultaneously managing propulsion sequences, attitude manoeuvres, real-time navigation decisions, and high-speed data transmission. Housing all this logic in a single processing unit would lead to convoluted algorithmic dependencies and increased latency, which are unacceptable for real-time control.

Instead, placing dedicated FPGAs within each critical subsystem, namely Propulsion, ADCS, GN&C, TT&C, and EPS, supports a modular architecture where each unit handles its own specialised operations. This not only simplifies the main OBC's role (which becomes more supervisory in nature) but also reduces overall software complexity and supports faster, parallel execution. Moreover, fault detection and isolation become more straightforward, as anomalies can be traced more easily to their originating subsystem. Finally, such an approach enhances scalability and future-proofing, allowing individual subsystem firmware to be updated or reconfigured with minimal disruption to the rest of the system. Therefore, referring to Figure 10.1, the boxes named "Peripheral Computer" resemble the FPGA associated with each subsystem.

For clarity, an FPGA is a type of integrated circuit that can be reconfigured after manufacturing to perform custom logic functions. Unlike fixed-function microcontrollers or processors, FPGAs consist of a matrix of programmable logic blocks and reconfigurable interconnects, allowing for the implementation of hardware-level parallelism tailored to the specific needs of each subsystem. This makes them highly suitable for tasks requiring deterministic timing, low-latency processing, and high reliability, particularly in space systems. In the context of the ADR mission, FPGAs will be used as dedicated control units within the aforementioned subsystems, executing time-critical algorithms and handling subsystem-level decision-making independently of the main OBC [43]. The exact logic architecture and internal state machines for each FPGA will be defined in later stages of the design process, once the full set of mission-specific operational requirements and software routines has been finalised.

Data Handling Block Diagram

Now that the System-level interface with the C&DH subsystem has been defined, the satellite System-level Data Handling Block Diagram can be created, explaining the information and command flow logic within the subsystems. This is depicted in Figure 10.2.

---

[43] `https://shorturl.at/Gitua`

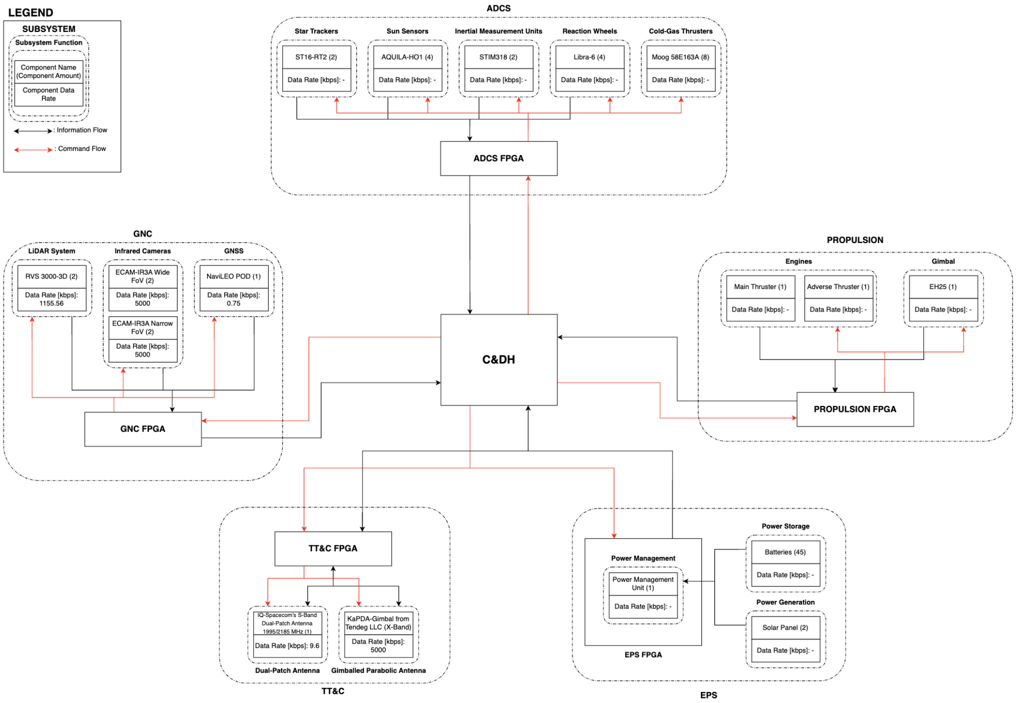

Figure 10.2: System-Level Data Handling Block Diagram.

As can be observed in the above block diagram, the interface between the C&DH subsystem of the ADR satellite and the rest of the subsystems is straightforward. The relationship between C&DH and all other subsystems, except for the TT&C subsystem, is the following: C&DH receives information through the FPGA unit of each of the subsystems and then sends commands to those subsystems accordingly. In the case of the TT&C subsystem, the only thing that changes is that the information flow is bidirectional. This is because instead of the C&DH just commanding the TT&C FPGA, it has to pass information through it in case of data transmission.

Final Note on Subsystems Integration with C&DH

As a final note, it has to be mentioned that the System-Level Data Handling Block Diagram reflects a high-reliability architecture in which every subsystem is governed by a dedicated FPGA, enabling direct and deterministic P2P connections across the satellite. This design approach, while resilient and highly flexible, inevitably leads to an overengineered system. FPGAs offer the advantage of reconfigurability, allowing the system to be adapted more easily in case mission parameters evolve. For instance, if the orbital characteristics or mass distribution of target debris change, the FPGAs governing subsystems that have to adapt to the new parameters can be easily updated. However, this flexibility comes at the cost of increased design complexity and development effort, as FPGA-based logic must be custom-built and thoroughly validated. Consequently, during later stages of the design process, this architecture is expected to be optimised. Specifically, some subsystem FPGAs will likely be replaced by commercially available microcontrollers that still meet mission requirements but reduce implementation effort, cost, and potential development risk. This hybrid approach preserves design adaptability where needed while streamlining the overall system.

10.2 Detailed C&DH Design

Moving on from the design of the global ADR interface to the detailed design of the C&DH subsystem is like taking Figure 10.2 and zooming in on the central block labelled ”C&DH”. The first aspect that this section addresses is the modules that the ADR spacecraft’s C&DH subsystem consists of, along with their role. After these have been defined, a hardware block diagram of the specific subsystem is shown, while the specific equipment used for each component of the C&DH’s modules is determined. This is followed by a preliminary estimation of the mass, power, and cost of the C&DH subsystem. Lastly, the software logic of the C&DH subsystem is discussed.

C&DH Subsystem Modules

The Command and Data Handling (C&DH) subsystem is composed of the following key modules:

- On-Board Computer
- Data Storage Unit
- Health Monitoring Unit
- Command Receiver
- Telemetry Transmitter

Within the C&DH design, each of these components fulfils a unique and crucial function. They serve as the foundation for spacecraft decision-making and control. Each module's design must be treated meticulously and precisely because of its vital role in facilitating autonomous operation, defect detection, data management, and communication with ground systems. Each component's internal logic and function are broken down in detail in the following subsections.

On-Board Computer (OBC)

The satellite's core processing unit is called the On-Board Computer. It is in charge of processing mission and housekeeping data, managing subsystem coordination, running the flight software, and making crucial decisions in real time or according to predetermined logic. Deterministic task scheduling, priority-based execution, and quick interrupt management are made possible by the Real-Time Operating System (RTOS) that the OBC normally runs.

The OBC also hosts Fault Detection, Isolation, and Recovery (FDIR) algorithms, which guarantee that the spacecraft can react to anomalies without requiring rapid ground involvement. These include watchdog mechanisms, exception handling routines, and error counters. Decision-making algorithms, such as mode switching (e.g., from ”Observe” to ”Prepare” mode), are embedded within the OBC software.

Lastly, in radiation-prone environments, Single-Event Upsets (SEUs) can corrupt memory or processing tasks. To mitigate this, the OBC implements Error Correction Codes (ECC) on both instruction and data memory, allowing the correction of single-bit errors and detection of multi-bit errors, thereby increasing reliability.

Data Storage Unit

Both volatile and non-volatile memory resources that are necessary for mission operations are provided by the data storage unit. Real-time telemetry caching, buffering, and short-term processing are all done with volatile memory, like RAM. Solid-state disks (SSDs) and other non-volatile memory are used to store command history, housekeeping logs, and payload/mission data for downlink during ground station passes.

Strong data storage is essential for both telemetry persistence in the event of communication delays and science missions carrying large payloads. While specific memory technologies (such as NAND Flash and SRAM) are covered in the CDH Equipment and Characteristics subsection, it is crucial to remember that read/write speeds, endurance, and radiation tolerance must all be taken into account when choosing memory that fits the operational profile of the satellite.

Health Monitoring Unit (HMU)

The Health Monitoring Unit is dedicated to supervising the overall status and safety of the satellite's subsystems. It integrates watchdog timers that monitor the OBC and other critical modules, automatically resetting components in the event of a hang or failure. It also includes current limit detectors and radiation counters that track system conditions and anomalies.

Error detection circuits flag threshold violations and interface with the OBC for possible corrective action. The HMU is designed to act autonomously where needed but also provides regular status reports to the OBC and, by extension, to the ground through the telemetry channel. Its tight integration with the rest of the C&DH ensures rapid fault response and contributes to the spacecraft's overall fault-tolerance strategy.

Command Receiver (CR) and Telemetry Transmitter (TT)

Although traditionally treated as distinct modules, the CR and TT are closely related to the TT&C subsystem and can be logically grouped. In the proposed architecture (i.e. hybrid FPGA - Main Computer configuration within the C&DH), both functions are managed by a single FPGA-based interface module, which streamlines handling of uplinked commands and downlinked telemetry by centralising timing and signal processing functions.

The CR handles the decoding of uplinked signals, extracting binary command data and relaying it to the OBC through a defined command interpretation interface. This interface filters, prioritises, and verifies commands before execution, ensuring the integrity of received instructions.

The TT collects data from the OBC and other subsystems, formats it into structured frames, and manages its storage and transmission through a prioritisation buffer. This allows high-importance telemetry (e.g. fault indicators) to be prioritised over routine data when bandwidth is limited.

By consolidating these functions onto an FPGA, board complexity is reduced, power consumption is lowered, and timing precision is increased, while the modularity in software interfaces is maintained. This integration also supports future flexibility in protocol or standard upgrades via reprogramming.

Further Considerations

An important architectural decision in the design of the C&DH subsystem involves the choice of component interconnection scheme. After evaluating common standards such as PC-104 stacking and Backplane architectures, a P2P interface scheme is selected for this satellite. P2P connections provide dedicated communication lines between modules, minimising bus contention and reducing the risk of bottlenecks during time-critical operations. Most importantly, they enhance data integrity and electromagnetic compatibility, which are both essential in the harsh and noisy environment of space. While PC-104 offers a compact and modular solution, its shared bus can introduce latency and increase complexity in debugging or fault isolation. Given the relatively small number of C&DH modules and the need for predictable performance and high fault tolerance, the P2P approach provides a cleaner, more straightforward electrical interface tailored to the mission's reliability and responsiveness requirements.

C&DH Hardware Block Diagram

Having established all relevant information about the C&DH subsystem, a hardware block diagram dedicated explicitly to the C&DH is provided in Figure 10.3, where each module is clearly illustrated along with its functional connections, highlighting the internal structure of the subsystem.

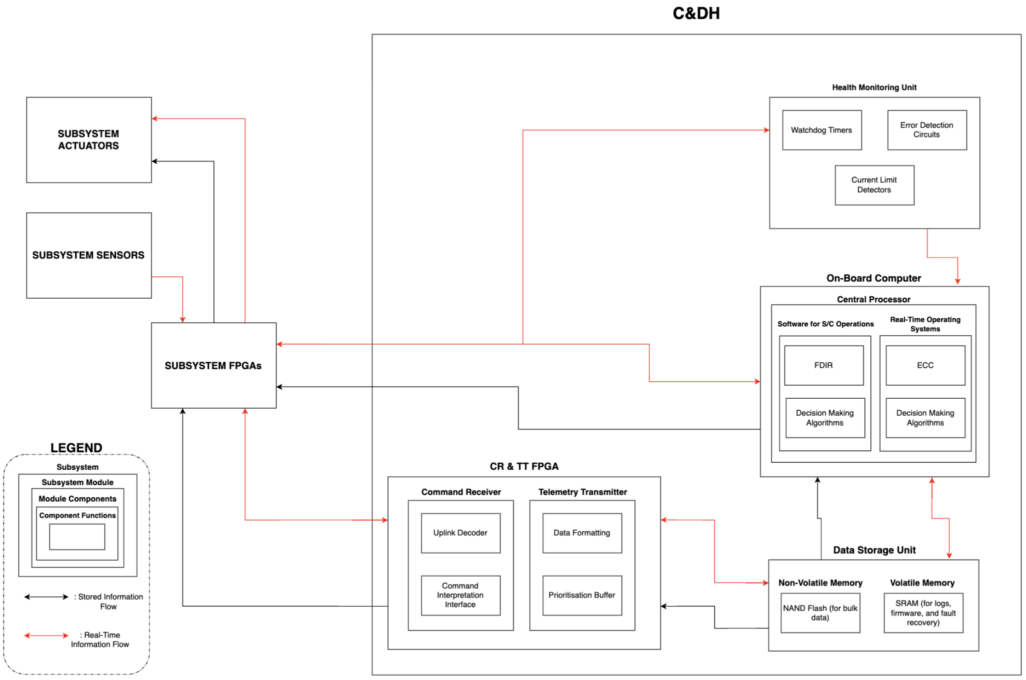

Figure 10.3: C&DH Subsystem Hardware Block Diagram.

As can be deduced from Figure 10.3, the C&DH hardware block diagram outlines the internal flow of information between key subsystem modules. Subsystem FPGAs interface with sensors and actuators, relaying real-time and stored data to the OBC, which runs FDIR, decision-making algorithms, and an RTOS with ECC, which, besides continuously checking for software malfunctions, is also responsible for flagging and correcting SEUs. The HMU provides real-time subsystem-level fault detection to the OBC. Commands from the ground are processed by the CR, while the TT formats telemetry for downlink. All data is routed through the Data Storage Unit, consisting of non-volatile NAND Flash for bulk data and SRAM for logs and recovery. Note that specifically for the Data Storage Unit, the type of equipment, i.e. NAND Flash and SRAM, have already been chosen. Justification for these follows in the next subsection, where equipment for the C&DH is selected. The architecture ensures reliable, fault-tolerant operation through P2P communication.

Following from that, an important consideration about Figure 10.3, which is not addressed purely in the diagram, is the electrical signalling standard that will be used within the C&DH subsystem. In implementing P2P communication across the C&DH subsystem, a suitable electrical signalling standard is essential to ensure signal integrity, low power consumption, and compatibility with space-grade electronics. Three common options are LVDS (Low Voltage Differential Signalling), M-LVDS (Multipoint LVDS), and PECL (Positive Emitter Coupled Logic). PECL offers very high-speed operation but requires a higher voltage supply and is more susceptible to noise, making it less ideal for low-power space systems. M-LVDS is designed for multipoint bus configurations, which are not aligned with the ADR's strict P2P architecture. LVDS, on the other hand, is optimised for high-speed, low-voltage (3.3V) differential signalling between two nodes, offering excellent noise immunity and low electromagnetic interference (EMI) [44]. Given our emphasis on P2P integrity, fault isolation, and minimal power draw, LVDS is selected as the signal transmission method for the internal data lines of the C&DH subsystem.

C&DH Equipment and Characteristics

With the architecture and constituent modules of the C&DH subsystem defined, the next step involves selecting specific equipment to implement the design. Equipment selection is carried out at both the module and component levels, depending on the availability and relevance of commercial off-the-shelf (COTS) products. For instance, in the case of the OBC, the central processor (CPU) will be selected from existing commercial options that satisfy the functional and performance requirements of the mission. Conversely, for modules such as the HMU, a fully integrated COTS solution will be selected without delving into the component level (e.g., watchdog timers, current limit detectors). In general, detailed component selection is only performed for critical elements such as the CPU and memory units (volatile and non-volatile). Additionally, the LVDS interfaces between subsystems (mentioned earlier in this chapter) will also be selected. As for the FPGAs, given their fully customisable nature and their presence across all subsystems, they will be developed and integrated in-house. Accordingly, mass, power, and cost estimates for FPGAs will be derived from historical mission data and statistical references.

It has to be noted that the component selection follows a bottom-up approach, beginning with the identification of specific equipment for individual components where applicable (e.g. within the OBC and Data Storage Unit), and subsequently progressing to the selection of complete subsystem modules (e.g. HMU).

Data Storage Unit

It is important to begin the component selection by considering the Data Storage Unit. This is because the CPU partially depends on the (non-)volatile memory units, and therefore, this will allow a better flow/logic in component selection. For the Data Storage Unit, the type of SSD and RAM has already been defined in Figure 10.3, as a NAND Flash for the non-volatile memory and an SRAM for the volatile memory unit.

The types of memory are as such because of various reasons. Initially, the NAND Flash is a type of SSD that offers high storage density while having a low power consumption (especially important considering that dissipated heat has to be minimised in order to maintain acceptable temperature levels inside the satellite) [45]. Moreover, NAND Flash cards are mature and space-proven, having been used in multiple space missions, while also existing in radiation-tolerant or radiation-hardened versions, which is also an important factor.

Regarding the SRAM (Static-RAM), the most important aspect considered is radiation tolerance. Since the RAM unit is responsible for successfully storing data for real-time operations, SEUs have to be minimised, if not entirely eliminated. An SRAM unit is designed specifically for that, i.e. it exhibits high radiation immunity due to its design,

---

[44] `https://www.taitien.com/wp-content/uploads/2015/12/AP20100820-PECL-and-LVDS.pdf`

[45] `https://www.techtarget.com/searchstorage/definition/NAND-flash-memory`

architecture, and operating principles. Furthermore, an SRAM provides very fast read/write speeds, making it excellent for real-time operations, logs, and buffer telemetry before transmission [46].

Having justified the selection of these specific types of memory units, one must now consider the amount of memory space needed for each unit. In order to do so, the most crucial aspects governing the required memory space have to be identified, again for each unit. Starting with the Non-Volatile Memory (NAND Flash), the data stored in this unit consists of:

- Software (including redundancy)
- Housekeeping Data
- Command logs
- Other subsystem logs
- LiDAR data

The satellite's flight software and its redundancy backups are obviously housed in the Non-Volatile Memory. For a mission of this complexity, and assuming an RTOS with FDIR, image-processing capabilities, and communication stacks, an estimated 400MB should be reserved for software storage. Moreover, command logs, which include both executed and queued commands, are minimal in size. Based on expected uplink rates and command complexity, a conservative estimate of 3MB should suffice. In addition, Housekeeping data is expected to be around 12.5MB per day, but since downlink happens every day, the required space is also 12.5MB as they will be overwritten after transmission.

The subsystem logs, such as those from the GN&C and ADCS modules, include time-stamped position, velocity, attitude, and control signals. These are typically stored at lower data rates with compressed formats and require approximately 150MB/day. Assuming a buffer of 1-2 orbits before downlink, an estimate of 150MB is adequate.

Finally, the most significant data type stored in NAND Flash is that from the LiDAR sensor. While this will eventually be downlinked to Earth, it cannot pass only through volatile memory due to timing constraints and potential disruption of real-time operations, such as infrared livestreaming. As such, LiDAR data is stored in NAND Flash temporarily. However, LiDAR data transmission is expected to occur every 1–2 orbits, allowing the overwriting of older data once it has been downlinked. Thus, the required NAND Flash capacity for LiDAR is capped at the size generated in a single rendezvous.

During one rendezvous, the LiDAR unit gathers data at a rate of 144.44 KBps over approximately 1206s, yielding 174.2MB of data per encounter. Summing all the above, the total required NAND Flash capacity is roughly 739.7 MB. Adding a margin of ≈100%, a 1.5GB NAND Flash card is expected to accommodate the satellite's needs.

The chosen NAND Flash is the 8GB NAND Flash by 3Dplus [47]. Even though its density is much higher than the one required for the ADR satellite, it is a very reliable, space-qualified, radiation-tolerant product that fits this mission perfectly. Additionally, the NAND Flash ensures compliance with **R-SUB-CDH-10**. The extra storage space can be used for other data types or simply left empty. The only thing that is affected by the extra density is the cost of the product, but considering the $100M budget, the cost of an SSD card is of little importance.

Moving on to the Volatile Memory (SRAM), the approach for ”sizing” it and selecting a specific product is quite different. This is because all data passes through the SRAM before any operation takes place. For example, LiDAR data will be transmitted not in real-time (and therefore has to be stored in the NAND Flash as explained earlier), but still passes through the SRAM before downlink. On the other hand, the data from the infrared cameras, which has to be livestreamed, is captured by the GN&C and then immediately moved to the SRAM for transmission (i.e. it does not pass through the NAND Flash at all). Therefore, one crucial parameter for a RAM unit, besides its working memory (for OBC operations), is the buffer size. The SRAM memory space is governed by these two parameters.

Before discussing the SRAM buffer size, one must estimate the total amount of data that has to be stored in the SRAM at once (again, for OBC operations). This data consists of the real-time operating software, function call stacks, local variables, intermediate processing storage, etc. The total estimate for the size of the SRAM working memory is ≈10MB. This value is deduced by scaling up the already existing SRAM unit by Endurosat [48], used by

---

[46] `https://www.techtarget.com/whatis/definition/SRAM-static-random-access-memory`

[47] `https://www.3d-plus.com/products/space-radiation-tolerant-nand-flash/`

[48] `https://www.endurosat.com/products/onboard-computer/`

Cubesats, based on the Starfixers mission complexity.

The estimation of the buffer size follows a different path, as it is primarily dictated by the TT&C and GN&C subsystems. This is because the GN&C captures data from different instruments, namely the LiDAR, IR camera, and GNSS, at different data rates. Then the TT&C subsystem has to transmit this data at a rate that accommodates the reception data rates and prevents buffer overflow. Counter-intuitively, the antennas used for the transmission of this data play no role in the buffer size, as the transmission data rate is governed by the dedicated TT&C FPGA (or microcontroller), which modulates the signal itself. The data flow for signal transmission, where signals (data) are received either from the TT&C or the GN&C subsystems, is depicted in Figure 10.4.

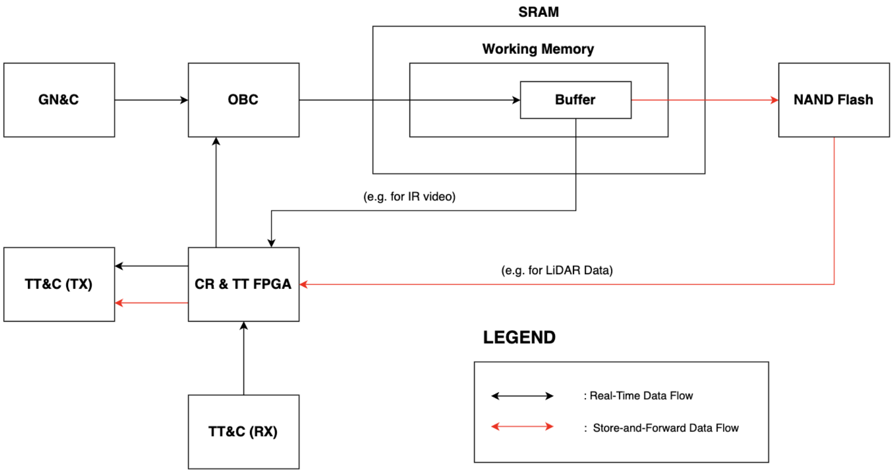

Figure 10.4: RX/TX Data Flow.

There is a moment in the ADR operation when the C&DH subsystem will be receiving data from all: IR camera, LiDAR sensor, and GNSS, at the rates of: 0.625 MBps, 144.444 KBps, and 0.094 KBps, respectively. What this entails is that a total of ≈0.77 Mbps will be flowing through the SRAM buffer at this moment. Therefore, an appropriate buffer size must be selected in order to ensure that buffer overflow, and hence data loss, because of software bugs or overlapping subsystem activity, will not occur. As a rule of thumb, the buffer size can be estimated as:

$$BS \geq DR_{\max} \cdot L_{s,\max} \tag{10.1}$$

where BS is the buffer size, DR_{MAX} is the maximum data rate through the buffer, and $L_{\max}$ is the maximum acceptable latency. Setting the $L_{s,\max}$ to 1 s, this leads to a buffer size of at least 0.77 MB. Adding a margin, an appropriate buffer size would be 1 MB.

Therefore, the most optimal SRAM for the ADR satellite would have a total size of ≈11 MB (where 1 MB is dedicated to the buffer). For this reason, the SRAM selected is the 16 MB SRAM, again by 3Dplus [49]. This SRAM is space-qualified and radiation-tolerant (and hence compliant with **R-SUB-CDH-11** and **R-SUB-CDH-12**), and is therefore the optimal option for the Starfixers Inc. group.

Central Processor

Following the selection of equipment for the Data Storage Unit is the selection of a CPU. The chosen CPU follows from the OBC-15 On-Board Computer by AgilSpace, which will be the ADR OBC, and is the TSC695FL (ERC32) (Sparc V7 Architecture) [50]. This CPU (OBC) is compatible with the 16MB SRAM unit, as well as the 3.3V LVDS requirement, and is an FPGA-based reconfigurable OBC that allows for mission parameter updates if needed.

---

[49] `https://www.3d-plus.com/products/space-radiation-tolerant-sram-memory/`

[50] `https://satsearch.co/products/agil-space-obc-15-on-board-computer`

Furthermore, the fact that it is an FPGA-based OBC enables the integration of the CR & TT (FPGA) module to the OBC, and therefore a separate module for command/telemetry applications does not need to be implemented. This equipment is a high-performance piece of technology that is space-qualified.

The only downside is that it does not support LVDS interfaces, which are essential to the ADR satellite. This problem can be solved by incorporating Bridge Integrated Circuits that convert the electrical and protocol layers. Further details on these parts are out of the scope of this report, and this is therefore not discussed further.

Finally, it has to be noted that the selected OBC, once set-up and integrated to the ADR spacecraft, will be compliant with **R-SUB-CDH-01** and **R-SUB-CDH-02**.

HMU

The HMU selected for the ADR satellite is the ”Spacecraft monitoring system” by Micro-Cameras & Space Exploration SA (MCSE) [51]. It provides antenna deployment monitoring, solar panels deployment monitoring, health checks, anomaly investigation, and failure assessment. These are all critical for the ADR satellite, and therefore, this component is deemed appropriate for the Starfixers Inc. mission.

LVDS Interfaces

Finally, the LVDS interfaces will be provided by 3Dplus, and they will specifically be the ”Driver and Receiver” Space Qualified Dual drivers and Dual receiver with individual enables LVDS interfaces [52]. They are also radiation-tolerant and therefore prove to be suitable for the ADR mission.

Component Characteristics

The characteristics of the above selected components are summarised in Table 10.1.

Table 10.1: C&DH Component Characteristics.

Component	**Amount**	**Mass [kg]**	**Power [W]**	**Cost [€]**	**Operating Temperature Range [°C]**
3Dplus 8GB NAND Flash	1	-	-	-	-55 to 125
3Dplus 16MB SRAM	1	-	-	-	-55 to 125
3Dplus LVDS Interfaces	5	-	-	-	-55 to 125
AgilSpace OBC-15	1	1.5	7.5	-	-20 to 70 (operating) -40 to 85 (non-operating)
MCSE Spacecraft Monitoring System	1	-	-	-	-
Subsystem FPGAs	-	-	-	-	-55 to 125

As can be seen in Table 10.1, most cells are left blank. This is because the specifications of the above components are, unfortunately, not publicly available. Therefore, the C&DH mass, power, and cost will be estimated through literature about past missions with a similar mission profile. However, one thing that is abundantly clear through Table 10.1 is that the operating temperature for the C&DH subsystem, dictated by the OBC unit, is -20 to 70 °C.

Moving on to past ADR mission literature, research yielded the following results, based on ESA’s research paper on Active Debris Removal through expanding foam applications [67]:

- $m_{\text{CDH}} = 3.4\% \cdot m_{\text{dry}} = 3.4\% \cdot 239.9 = 8.16\text{kg}$
- $P_{\text{CDH}} = 5\% \cdot P_{\text{TOTAL}} = 5\% \cdot 434.35 = 21.72\text{W}$

Of course, when estimating the mass and power of subsystems through this method, an iterative process is needed until convergence of the final dry mass and total power. This is because the C&DH subsystem is already considered

---

[51] `https://satsearch.co/products/mcse-spacecraft-monitoring-system`

[52] `https://www.3d-plus.com/products/lvds-space-radiation-tolerant-interfaces/`

a part of the dry mass and total power. In the bullet list above, the values used for the Starfixers' ADR's m_{dry} and P_{TOTAL} are conservative estimates already including safety margins.

As final values, the C&DH subsystem is deemed to have the following characteristics:

- m_{CDH} = 9kg
- P_{CDH} = 31W (it depends on the operational mode, but it acquires this value as maximum)

As these values reduce the aforementioned iterative process and convergence of the final dry mass and total power is achieved.

As for the cost of the C&DH subsystem, it comprises two main parts: the component cost and the FPGA development and integration cost. The component cost is estimated to be ≈ €50k, based on the parts used (although this is really an arbitrary number). Furthermore, the development and design of the FPGA modules, which will be done in-house, cannot really be estimated at this design stage. However, it is not expected to exceed €15-20k per module. Therefore, taking a worst-case scenario into account, the total estimated cost for the C&DH subsystem is ≈ €150k, although it is subject to refinement moving forward.

C&DH Software Design

The design approach adopted for the C&DH subsystem followed a top-down methodology, beginning with the selection of an appropriate CNA, continuing with the definition of subsystem interfaces (e.g. via FPGAs), and concluding with a detailed Hardware Block Diagram that illustrates the internal flow of data and commands. The final step in the design of the C&DH subsystem is developing the software that governs the entire ADR operation. This entails the implementation of decision-making algorithms, system logic, and fault-handling software. Such tasks typically require the specialised expertise of computer scientists/engineers or electronic engineers, and therefore are deemed to be out of the scope of this report. In practice, these professionals would be responsible for coding and validating the software stack in accordance with system-level requirements. Hence, the detailed software design is intentionally omitted from this document.

11 Structures and Thermal Design

The structures subsystem is one of the most fundamental aspects of any spacecraft. The goal of structures is to provide mounting and support for all other subsystems while also serving as a passive thermal regulator, radiation protection, and debris shielding. The subsystem includes several components, among which are the spacecraft bus with fuel tanks, all internal load-carrying components, and attachment points of other subsystems such as the solar panel unfolding mechanism and supports, sensor and thruster attachments, antenna supports, and internal mounting spots for ADCS, C&DH, etc. This chapter begins with the configuration of the tanks under Section 11.1, followed by the limit loads determined according to the launcher and the material selection in Section 11.2. Subsequently, the compliance with these loads will be analysed in Section 11.3 and Section 11.4. The chapter will conclude with an overview of solar array attachment and the thermal and radiation protection measures in Section 11.5, Section 11.6 and Section 11.7.

11.1 Tank Configuration

To begin designing the structures subsystem for the ADR mission, the general bus layout has to be first selected. Due to the absence of a traditional payload and the high fuel capacity of the mission, it was decided to utilise internal fuel tanks as supports for the bus. Three main design concepts for the bus layout were proposed and can be seen in Figure 11.1. The first layout option involves a cube with a spherical fuel tank in the middle. The second option is a rectangular prism bus with four pill-shaped fuel tanks at its corners. Finally, the third layout is a cylindrical bus body with two pill-shaped/spherical fuel tanks. It must be acknowledged that, regardless of the layout choice, the tanks have to be custom-designed and manufactured due to the unusual bi-propellant choice, as no commercially available tanks of the required capacity exist.

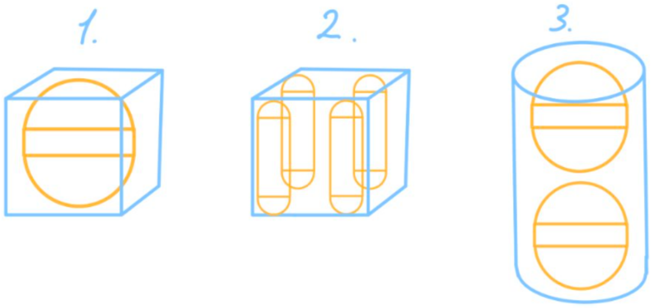

Figure 11.1: Bus Layout Options.

In order to choose a single layout, it was decided to perform a trade-off by comparing the six layout parameters that were deemed most crucial for the choice. The trade-off criteria include: manufacturing complexity, mass-symmetry for ADCS placement, strength, solar panel attachment complexity, sensor attachment complexity, and mass. Each criterion had a weight assigned to it based on its importance for the mission. The weights are as follows: strength - $\frac{7}{28}$, ADCS symmetry - $\frac{6}{28}$, mass - $\frac{5}{28}$, solar panel attachment complexity - $\frac{4}{28}$, manufacturing - $\frac{3}{28}$, and sensor attachment complexity - $\frac{3}{28}$. Strength and ADCS symmetry received the highest weights as these parameters directly influence the reliability of the mission, affecting the probability of creating additional debris and hence mission sustainability. Following them are mass and solar panel attachment complexity, which greatly affect the cost of the mission and thus are important to maximise the RoI of Starfixers Inc. Finally, manufacturing and sensor attachment complexity were given the lowest weights due to their relatively lower influence on reliability and cost.

In Table 11.1 are displayed the trade-off scores out of 10 that were given per criterion for each of the layout options. In the table, L1, L2, and L3 represent layouts corresponding to the numbering in Figure 11.1. The criteria names are also shortened, where ”ADCS Symmetry” stands for mass-symmetry for ADCS placement, ”Solar Panel” stands for solar panel attachment complexity, ”Sensor” stands for sensor attachment complexity, and ”Production” stands for manufacturing complexity. Scores 8-10 (green) signify excellent performance, 5-7 (yellow) stand for sufficient performance, and 1-4 (red) indicate problematic performance.

Table 11.1: Bus Layout Trade-off. Colour-blind Note: Criteria Scores 8–10 are Green, 5–7 Yellow, and 1–4 Red.

	Strength $\frac{7}{28}$	**ADCS Symmetry** $\frac{6}{28}$	**Mass** $\frac{5}{28}$	**Solar Panel** $\frac{4}{28}$	**Production** $\frac{3}{28}$	**Sensor** $\frac{3}{28}$	**Total**
L1	8	3	8	8	8	9	7.04
L2	7	8	6	8	7	9	**7.39**
L3	8	6	7	4	6	7	6.5

From Table 11.1 one can see that option one performs incredibly well on all criteria aside from the ADCS symmetry. This comes from the inability to place ADCS anywhere close to the centre of mass of the configuration. As for the third layout option, it performs decently well on most criteria but generally loses to the other options, especially on the attachment of solar panels and sensors. Thus, the second layout option is concluded to be the most optimal. It scores well on all criteria without any major downsides and has the highest total score of 7.39.

In order to obtain the dimensions of the bus, the required free space within the spacecraft needs to be determined. The second layout option L2 was chosen such that the reaction wheels could be placed in the middle. As most of the other internal components are relatively small and can be freely placed anywhere in the interior of the spacecraft, the reaction wheel assembly will be the most critical factor for the free space. In the worst case volume-wise, the four reaction wheels will be placed in a square. In reality, they will be placed in a pyramid shape, for which the dimensions are hard to estimate. With a reaction wheel thickness of 100 mm and a diameter of 206 mm, it will take up a square of 406 mm by 406 mm. To provide space for wiring and plumbing in between, a square of 420 mm by 420 mm will be left between the propellant tanks. Figure 11.2a shows a top view of the propellant; the orange square represents the 420x420 mm^2 free space to place the reaction wheels. The total dimensions of this layout, and thus the dimensions of the spacecraft inside components, are 1000x1000x823 mm^3.

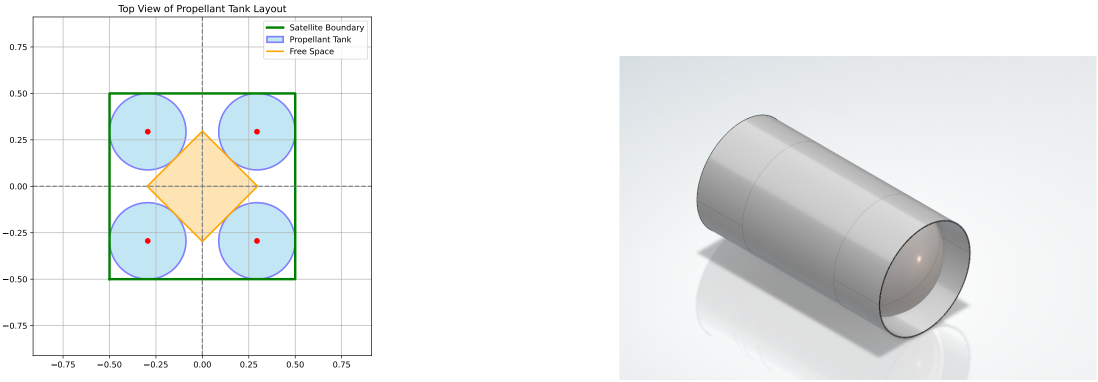

(a) Layout of the Propellant Tanks With the Free Space Indicated.

(b) Propellant Tank With Cylindrical Extensions.

Figure 11.2: Propellant Tank Layout Option Considered in the Design Process.

11.2 Limit Loads Identification and Material Selection

Having established the general layout of the spacecraft’s bus, the design stage can begin, which must ensure that the ADR spacecraft can sustain all of the loads through the mission from transporting to the launch site until its EoL. Most of the critical load cases happen during the launch, making the launcher selection crucial for the structural design of the spacecraft. The Falcon 9 launch vehicle has been chosen for the mission due to its low cost per launched kilogram and reusability of its booster stage, which makes it one of the most sustainable and cost-effective large launch vehicles. The maximum potential loads from spacecraft assembly to EoL are shown in Table 11.2[53].

Table 11.2: Maximum Spacecraft Lifetime Experienced Loads.

Undeployed Configuration	Construction Loads		Ngb
	Transportation Loads		
	Vehicle Vibrations		~1 [Hz]
	Launch Loads	Fuel Burnout and Trajectory Flight	
		Axial Thruster Vibrations	<35 [Hz]
		Lateral Thruster Vibrations	<10 [Hz]
		Axial Sine Vibrations	<100 [Hz], 1[g]
		Lateral Sine Vibrations	<100 [Hz], 1[g]
		Acoustic Vibrations	<10000 [Hz], OASPL 131.4 [dB]
		Random Vibrations	<2000 [Hz], GRMS 5.13 [$\frac{g^2}{Hz}$]
		Axial Acceleration	8.5 [g]
		Lateral Acceleration	3 [g]
		1st Stage Separation	
		Separation Shock	Ngb
		Spacecraft Separation	
		Separation Shock	Ngb
Deployed Configuration	**In Flight Loads**	Transfer Flight and Orbit Insertion	
		Bi-propellant thruster	465 [N]
		Mission Life	
		Bi-propellant thruster	465 [N]
		Disturbance Torques	~0.1 [Nm]
Other Loads		Internal Pressure	Ngb
		Unexpected Shocks	Ngb
		Thermal Loads	TBD

In Table 11.2 ”Ngb” represents negligible loads, and ”TBD” stands for ”To Be Determined” as thermal loads strongly depend on the thermal control subsystem.

Fuel tanks occupy the majority of the bus volume, and at launch, their mass with fuel is substantially above 50 % of the total launch mass. In order to utilise the fuel tanks better, it was decided that with minor modifications, they could serve as load-carrying support pillars for the bus. In order to effectively distribute axial loads through the tanks and provide better support, cylindrical extensions were designed that go on top of the tanks’ outer caps and attach to the bus walls, effectively turning the tanks into cylindrical axial pillars. Figure 11.2b demonstrates the tank design with the cylindrical extensions.

Due to the presence of atomic oxygen at LEO, using composites for the structure is restricted [54]. Thus, for the material selection, two common aerospace metal options were considered: Ti6Al4V alloy and Al7075-T6 alloy. Both materials have a high strength-to-density ratio and a long space heritage[55].

---

[53] `https://www.spacex.com/media/falcon-users-guide-2025-03-14.pdf`

[54] `https://ntrs.nasa.gov/citations/19950021215`

[55] `https://ntrs.nasa.gov/citations/19720022809`

Table 11.3: Material Properties of Common Space Alloys.

Material	ρ **[kg/m^3]**	**E [GPa]**	$\sigma_{ultimate}$ **[MPa]**	σ_y **[MPa]**	**Cost [€/m^3]**	**Manufacturability**
Ti6Al4V	4430	113.8	950	880	9 641 325	Acceptable
Al7075-T6	2810	71.7	572	503	588 225	Excellent

From Table 11.3 one can see that both alloys display excellent mechanical properties and that while Ti6Al4V[56][57] is stronger, it is also proportionally heavier than Al7075-T6 [58][59]. However, the substantially higher cost of the titanium alloy and the excellent manufacturability of the aluminium alloy lead to the selection of aluminium as the primary bus material. Moreover, aluminium is a more sustainable material due to its abundance and easy recycling. Furthermore, in order to decrease thermal expansion loads and allow for easier welding of the assembly parts, the fuel tanks and cylindrical tank extensions will be manufactured using the same AL7075-T6 alloy.

11.3 Static and Dynamic Loads

For static loads, a conservative load envelope of the Falcon 9's User's Guide [91] was used, resulting in the loads in Table 11.2. In order to conservatively estimate the static load experienced by the bus panels and evaluate design compliance with **[R-SUB-STR-1,2,3,4,24,25]**, the highest load scenario was considered. For the axial static load, the considered point was the bottom of the side plates, right before the bottom plate. At this point at launch, the structure carries the load of the entire ADR spacecraft with fuel along with all of the internal components, excluding only the bottom panel and thruster that is attached to it, giving M_{axial}. The static load was estimated using the standard formula in Equation 11.1.

$$\sigma_{\text{static}_{\text{axial}}} = \frac{M_{b,\text{axial}} \cdot a_{\text{axial}}}{A_{\text{axial}}} \tag{11.1}$$

$a_{\text{axial}} = 8.5g$ following the launcher guide, and A_{axial} is the total cross-sectional area that carries the load. The analysis was repeated following the same logic for static lateral load. However, two cases were considered based on different adaptor attachment methods. For the case where the side walls are clamped, the stress was calculated at the side of the panel and considered all of the mass, excluding the side bus panel, using Equation 11.2

$$\sigma_{\text{static}_{\text{lateral1}}} = \frac{M_{b,\text{lateral}} \cdot a_{\text{lateral}}}{A_{\text{lateral}}} \tag{11.2}$$

$a_{\text{lateral}} = 3g$ following the launcher guide, and A_{lateral} is the total cross-sectional area that carries the load. In the second case taken into account only the bottom side is clamped, which would induce bending of the whole structure, with critical stress of the walls and tanks at the bottom plate. The worst-case conservative estimate of $M_{b,\text{axial}}$ consisted of two fuel tanks, the mass of 5 of the spacecraft panels, as well as 3 rods, 10 stiffeners and other subsystems carried by the spacecraft. This stress was computed using Equation 11.3, with L being the height of the structure, c the distance to the neutral axis and I_A the AMoI.

$$\sigma_{\text{static}_{\text{lateral2}}} = \frac{M_{b,\text{axial}} \cdot a_{\text{lateral}} \cdot L \cdot c}{I_A} \tag{11.3}$$

The resultant static stresses can be seen in Table 11.4. The axial stress is relatively low; this is due to the large load-carrying area in the axial direction, as all four tanks act as pillars and carry a large fraction of the load. The lateral static stress is unnoticeably higher than axial despite a much lower lateral acceleration. This is because tanks are unable to support the structure laterally, leading to a significantly lower load-carrying area in the lateral direction. Also, due to symmetry of the structure, the load in both lateral directions is approximately equal and is described by the value in Table 11.4. Moreover, the unclamped side walls case seems to be critical in terms of static stresses.

---

[56] `https://asm.matweb.com/search/specificmaterial.asp?bassnum=mtp641`

[57] `https://shorturl.at/BdLz4`

[58] `https://asm.matweb.com/search/specificmaterial.asp?bassnum=ma7075t6`

[59] `https://shorturl.at/KxJ0J`

To effectively model the dynamic loads experienced by the spacecraft's structure, it is important to use a valid and conservative simulation model. The design of the payload fairing is outside of the scope of this report, and therefore, the structure will be modelled as if it is rigidly clamped to the launch vehicle. During launch, the payload fairing acts as a damping system for the spacecraft, making this assumption conservative. The dynamic model used is shown in Figure 11.3. As it can be seen, the load-carrying components are modelled as springs, making the spacecraft behave as a single-degree-of-freedom system. Looking at Figure 11.3, it can be observed that for the axial direction, bus panels and fuel tanks are springs attached in parallel. It is assumed that all springs deflect equally, leading to an assumption that the top plate of the bus is infinitely rigid and does not deform significantly under the launch loads. For the lateral direction, the walls and support rods are modelled as parallel springs, and the same assumption is made that the top plate (top relatively to the load direction) is infinitely rigid. It must be mentioned that the reasoning for the introduction of rods and their sizing is described in Section 11.4. Also, any stiffeners are accounted for in the bus panel springs; the design and reasoning for stiffener use is also developed in Section 11.4.

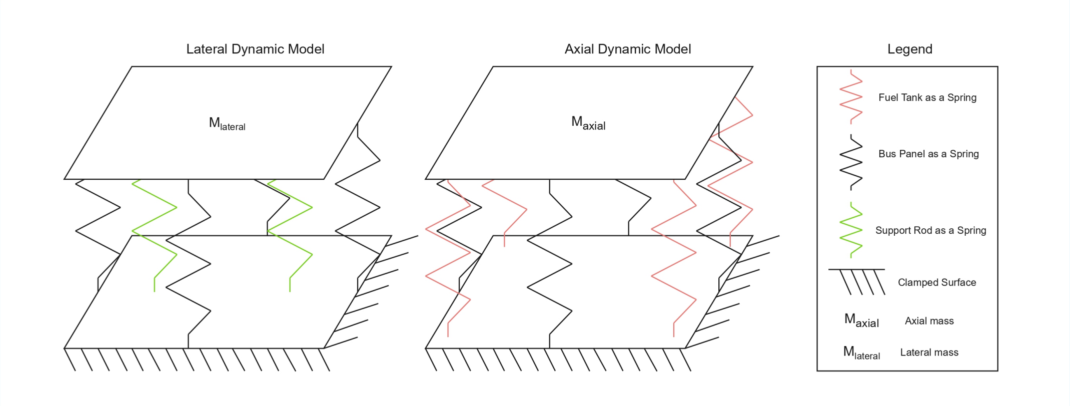

Figure 11.3: Structural Dynamic Model.

To proceed with dynamic load modelling, it is essential to calculate the stiffness of the components that are modelled as springs. The general formula for the axial stiffness of a component is described in Equation 11.4[60]

$$k = \frac{A \cdot E}{L} \tag{11.4}$$

where k is the stiffness, A is the cross-sectional area, E is the elastic modulus of the material, and L is the length. Equation 11.4 is simplified for constant elastic modulus and cross-sectional area of an object. It is valid to utilise this equation here as the material is constant for the entire spacecraft's structure, and the cross-section is generally constant for each component. For rectangular bus panels, the stiffness is calculated using Equation 11.5

$$k_{\text{panel}} = \frac{W_{\text{panel}} t_w E}{L_{\text{panel}}} \tag{11.5}$$

where W_{panel} is the panel's width, t_w is the wall thickness of the panel, E is the elastic modulus of Al7075-T6, and L_{panel} is the panel's length. The stiffness of stiffeners and rods is calculated in Section 11.4. The fuel tanks are essentially cylindrical pillars; therefore, their stiffness can be calculated using Equation 11.6.

$$k_{\text{tanks}} = 4\frac{\pi(r_{\text{tank}}^2 - (r_{\text{tank}} - t_{w,\text{tank}})^2)}{L_{\text{tank}}} \tag{11.6}$$

where 4 is the number of tanks, r_{tank} is the outer radius of a tank, $t_{w,\text{tank}}$ is the tank wall thickness, and L_{tank} is the tank's height. Due to the parallel nature of the springs, the total stiffness for both axial and lateral directions can be calculated as $k_{\text{total}} = \Sigma k_{\text{component}}$. This leads to 2.38 and 0.972 $\frac{GN}{m}$ for axial and lateral stiffness, respectively. As mentioned before, the axial stiffness is predictably much higher than the lateral stiffness due to the effect of the fuel tanks. Having obtained the stiffnesses, it becomes possible to model the response of the system to

---

[60] `https://shorturl.at/9icV8`

forcing vibrations. The angular frequency of the structure in both directions can be calculated as described in Equation 11.7.

$$\omega = \sqrt{\frac{k_{\text{total}}}{M}} \tag{11.7}$$

In this equation, M is the oscillating mass as depicted in Figure 11.3, M_{axial} or $M_{b,\text{lateral}}$ for each loading case respectively. In the real world, the mass is not concentrated on top of the "springs" (panels, tanks, etc.) but rather distributed along their length. To keep the calculations conservative, it will be assumed that the oscillating mass is equal to the axial and lateral masses used for static stress analysis, and that all of the mass is on top of the springs. This is an extremely conservative assumption that leads to a drastic overestimation of the dynamic stresses; therefore, no safety factor will be used for the analysis. Like previously mentioned in the static loads discussion, the case for unclamped side walls was also taken into account. The stiffness of walls and tanks was computed using Equation 11.8 and the forcing function was applied to the axial dynamic model of Figure 11.3.

$$K = \frac{3 \cdot E \cdot I}{L^3} \tag{11.8}$$

Following the vibrational loads described in Falcon 9's User's Guide [91], sine vibrations, acoustic vibration and random vibrations were analysed. Random vibrations were identified as the most critical dynamic load case due to the large equivalent acceleration of GRMS = 5.13g, which stands for "gravitational root mean square" value. The largest load due to vibration occurs at a 925 Hz frequency. The dynamic loading of the system was modelled with a driving force $F = 5.13Mg$. Where g is the gravitational acceleration and M is the oscillating mass for each specific loading case. The system's response was modelled using a Python script[61] and taking into account a 1% damping ratio as suggested by ESA[62]. Damping allows for the simulation of the dissipation of the vibrations over time. The resultant oscillations can be seen in Figure 11.4.

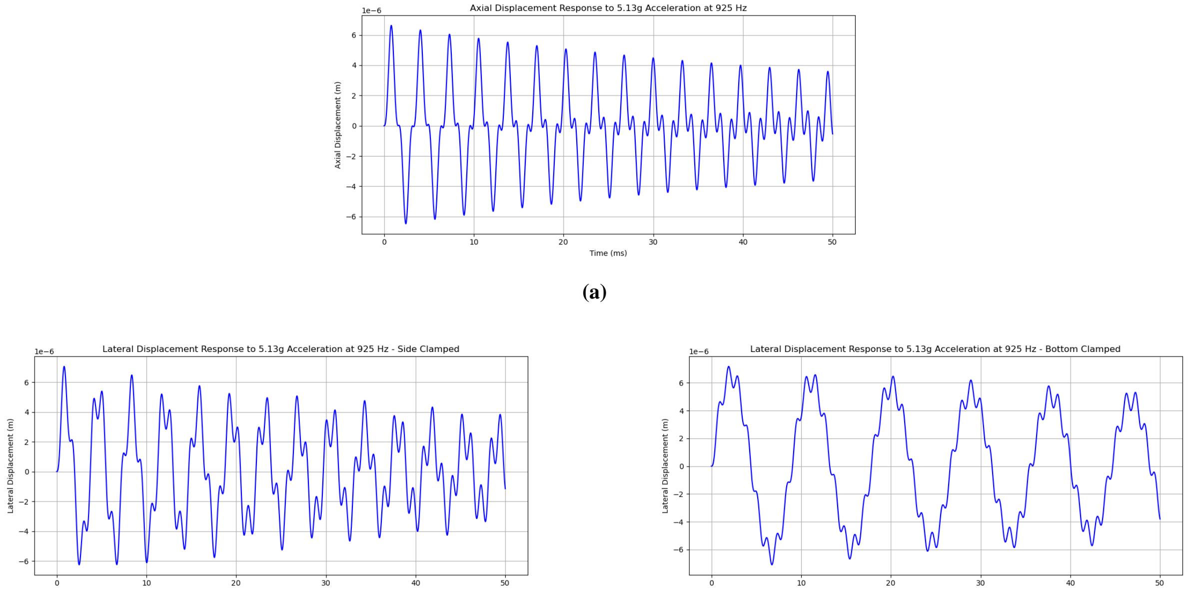

(a)

(b)

(c)

Figure 11.4: Comparison of Structural Responses Under Dynamic Loads un Different Directions and Boundary Conditions.

From Figure 11.4, one can see that the response is stable and does not exceed 10^{-5}m in amplitude. By taking the largest amplitude peaks in Figure 11.4, one can calculate the limit internal stress that arises from the dynamic loads using the standard stress-strain relationship[63]. Where strain is $\varepsilon_{\max} = \frac{\Delta l_{\max}}{l}$ with $\Delta l_{\max}$ being the maximum

---

[61] `https://github.com/ViktorZupnik/Starfixers/blob/Final-Branch/Structures%20and%20Thermal%20Subsystem/Load_analysis.py`, Starfixers Inc. GitHub Repository

[62] `https://shorturl.at/oTeV4`

[63] `https://shorturl.at/itmdm`

deflection, and l being the element's initial length. Then, the stress is found as $\sigma_{\max_{\text{dynamic}}} = \varepsilon_{\max} E$. The values for the limit dynamic stresses can be seen in Table 11.4.

Table 11.4: Limit Static and Dynamic Stresses of the Structure in Axial and Lateral Directions.

Direction	Limit Static Stress [kPa]	Limit Dynamic Stress [kPa]
Axial Direction	609	577
Lateral Direction – Sides Clamped	875	505
Lateral Direction – Bottom Clamped	17 224	1 144

11.4 Buckling and Bending

Following the launch load analysis, failure under buckling was assessed to evaluate the structural integrity of the design and compliance with **[R-SUB-STR-20]** and **[R-SUB-STR-21]**. The bare walls and tanks were evaluated separately using Equation 11.9 and Equation 11.10 for buckling stress, where $t_{w,\text{wall}}$ and $t_{w,\text{tank}}$ are wall and tank thickness, b effective sheet width, r_{tank} tank radius, C buckling coefficient, in this case 4 due to the fixed boundaries on both sides, SF the safety factor of 1.1 and v the Poisson ratio of 0.334. For a 3 mm aluminium sheet, the buckling stress was found to be 2.15 MPa for top and bottom walls and 3.15 MPa for sidewalls. Although the sum of static and dynamic loads does not exceed the critical buckling stress, buckling could still occur, as this failure mode is highly sensitive to material imperfections and deformation. Therefore, the integration of stiffening elements was implemented to guarantee structural integrity.

$$\sigma_{buckling-wall} = \frac{1}{SF} \cdot C \cdot \frac{\pi^2 \cdot E}{12 \cdot (1 - v^2)} \cdot \left(\frac{t_{w,wall}}{b}\right)^2 \tag{11.9}$$

$$\sigma_{buckling-pipe} = \frac{0.605 \cdot E \cdot t_{tank}}{r_{tank}} \tag{11.10}$$

For the lateral loading case, omega stiffeners were chosen to reinforce the walls by reducing the effective panel width and thus improving the buckling resistance. The crippling stress of the stiffener was computed using Equation 11.11 for every part of the omega stringer represented by Figure 11.5 and then taking a weighted average with Equation 11.12, where σ_y is the yield stress, α and n material specific constants and A_i the area of individual parts.

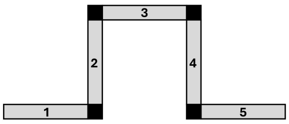

Figure 11.5: Schematic Representation of Omega Stringer.

$$\frac{\sigma_{crippling}}{\sigma_y} = \alpha \left[\frac{C}{\sigma_y} \cdot \frac{\pi^2 E}{12(1 - v^2)} \left(\frac{t}{b}\right)^2\right]^{1-n} \tag{11.11}$$

$$\sigma = \frac{\sum \sigma_{\text{crippling}_i} A_i}{\sum A_i} \tag{11.12}$$

Using these formulas, two stiffeners were added on every side wall, and two were added on top and bottom walls, forming a cross to support both lateral directions. This layout is displayed in Figure 15.1. The dimensions, crippling stress and buckling stress of the new sheet are summarised in Table 11.5. It is important to note that the stiffeners on the sidewall will be placed outside of the main cube, since inside they would have to be interrupted by the tank structures. On the top and bottom walls, however, the stringers will be placed inside, as these walls will support the thrusters, shown as well in Figure 15.1.

Table 11.5: Summary of Stiffener Properties and Effects.

Stiffener Dimensions [mm]		$A_{\textbf{stiff}}$ **[mm^2]**	$\sigma_{\textbf{stiff}}$ **[MPa]**	$\sigma_{\textbf{buckling}_{\textbf{side}}}$ **[MPa]**	$\sigma_{\textbf{buckling}_{\textbf{top-bottom}}}$ **[MPa]**
t_{stiff}	$b_{1,2,3,4,5}$	50	597.40	64.15	28.52
1	10				

For the axial loading case, the tanks themselves were considered internal stiffeners due to their rigid connection to the walls, as can be seen in Figure 11.6. Under compression, these connections reduce the effective sheet width and will thus increase the buckling capacity of the side walls. These calculations showed a drastic increase in buckling resistance of the sheet, providing the desired safety margin. This reduction in effective sheet width also allows for compliance with the high compressive stress induced on the side walls due to the critical lateral loading case discussed before. For both the lateral and axial loading cases, it is important to keep in mind the conservativeness of the calculations performed under Section 11.3, meaning that the stresses estimated in that section were overestimations of real-life stresses to account for unforeseen loading cases and magnitudes.

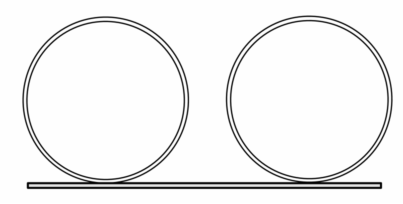

Figure 11.6: Propellant Tanks Acting as Circular Stiffeners.

Lastly, the bending of the tanks under uniform lateral loading was explored as specified in **[R-SUB-STR-22]**, as it is undesired to have large bending deflections of these structures. To redistribute the bending loads, small rods were added between all the tanks to interconnect them, which will restrain relative motion and act as a load distributor and enhance structural coherence by simultaneously serving as attachment points for other subsystems. The updated structure with rods and stiffeners can be seen in Figure 15.1. The images show an opening on the top and bottom wall for the thruster attachment. This component will be load-bearing and will replace the existing stiffeners without compromising the overall structural integrity. Finally, the lateral and axial stresses and displacements were recomputed by updating the mass and stiffnesses due to these extra components, reducing the maximal displacements.

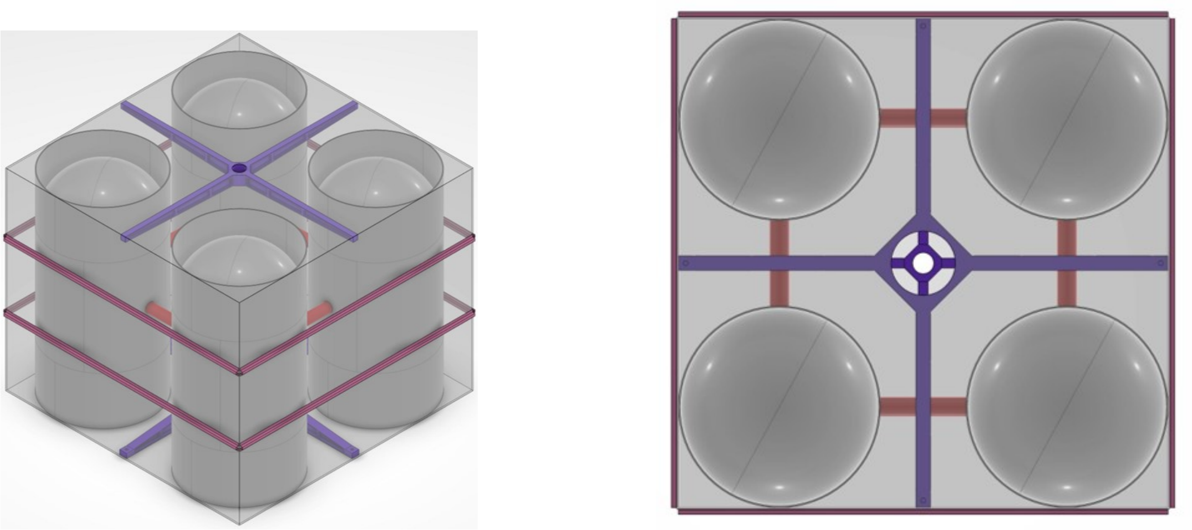

Figure 11.7: Structural Layout.

11.5 Solar array attachment

One of the most critical parts of a spacecraft is the attachment mechanism of the solar panels to the spacecraft. It needs to be lightweight, sustain loads and vibrations during launch and operation, keep the array folded inside the payload fairing during launch, and be able to orient the solar panels towards the sun at any moment during the mission, among many others.

To fulfil all of these functions, the company SpaceTech GmbH Immenstaad (STI) designed the solar panel deployment mechanism [64] displayed in Figure 11.8a, including a yoke connecting the panel to the spacecraft, with a rotating hinge, performed by the Solar Array Drive Assembly (SADA) and the STI deployment mechanisms.

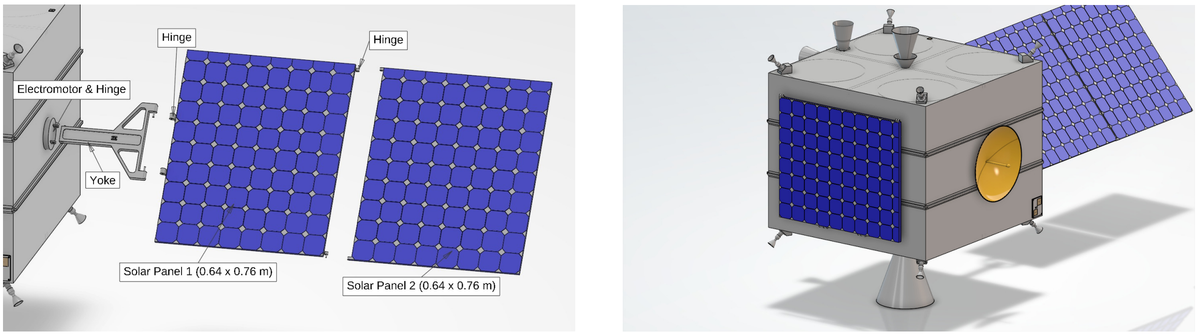

(a) Exploded View of Integrated STI Solar Arrays.

(b) Folded Solar Panel Configuration.

Figure 11.8: Solar Array Configuration and Folding.

According to STI[64], the mechanical components of the mechanism weigh between 3 and 6kg per m^2 of solar array and have a reliability higher than 0.9999. Over 300 solar arrays have been deployed in orbit with a 100% success rate. The operational temperature range is adapted to each specific mission. Additionally, the mechanism can withstand acoustic vibrations up to 148dB and mechanical vibrations up to 20g along any axis, significantly exceeding the loads experienced by the spacecraft, which reach a maximum of 131.4dB for acoustic loads, 8.5g for axial loads and 3g for lateral loads as shown in Table 11.2.

Taking the worst-case mass of 6kg/m^2, and given that the solar array will have an area of $\approx 2\ \text{m}^2$, the total structural mass of the solar array attachment will be around 12kg.

---

[64] `https://spacetech-i.com/fileadmin/user_upload/Equipment/Solar_Arrays/STI-DS-03-20229-191_Datasheet_SolarArrays_2023-11-9_web.pdf`

11.6 Thermal Subsystem

The thermal subsystem is required to maintain the temperatures inside the spacecraft within acceptable bounds for all components to work and not exceed their operating limits as per **[R-SUB-THE-01]**, while being mass and power-efficient. This can be done by using active or passive thermal systems. For this project, a passive system would be preferred due to its simplicity, reliability, mass efficiency, and low power consumption, leading to a higher mission sustainability and overall lower cost.

Thermal equilibrium of the spacecraft in a vacuum is affected by heat transfer through radiation. The sources to be taken into account are solar radiation $\dot{Q}_{\text{sun}}$, reflection of solar radiation by the Earth or albedo effect $\dot{Q}_{\text{albedo}}$, Earth infrared radiation $\dot{Q}_{\text{Earth}}$, heat emitted by the spacecraft $\dot{Q}_{\text{emitted}}$ and internal heat $\dot{Q}_{\text{internal}}$. Equation 11.13 summarises the sources of heat absorption and emission of the spacecraft leading to the net heat flow.

$$\dot{Q}_{\text{net}} = \dot{Q}_{\text{albedo}} + \dot{Q}_{\text{sun}} + \dot{Q}_{\text{Earth}} + \dot{Q}_{\text{internal}} - \dot{Q}_{\text{emitted}} \tag{11.13}$$

$\dot{Q}_{\text{sun}}$ is computed using Equation 11.14, where J_s is the solar intensity of 1361 W/m^2 at 1 AU according to [47], A_s the exposed area and α_s the absorptivity of the outer surface.

$$\dot{Q}_{\text{sun}} = \alpha_s \cdot J_s \cdot A_s \tag{11.14}$$

Part of this solar radiation is reflected by Earth and computed by Equation 11.15 where A_e is the Earth's exposed area and a[65]the percentage that is reflected. The field view factor f is defined by R_E Earth radius and R orbital radius:

$$\dot{Q}_{\text{albedo}} = \alpha_s \cdot J_s \cdot a \cdot A_e \cdot f, \qquad f = \frac{1 - \sqrt{1 - \left(\frac{R_E}{R}\right)^2}}{2} \tag{11.15}$$

For Earth infrared radiation, Equation 11.16 is used with J_{IR} as 237 W/m^2.[66]

Finally, the emitted heat flux can be computed using Equation 11.17, where ϵ_s is the emissivity of the outer layer, σ the Boltzmann constant and A_{emitted} the total emitting area.

$$\dot{Q}_{\text{IR}} = \alpha_s \cdot J_{\text{IR}} \cdot A_e \cdot f \tag{11.16}$$

$$\dot{Q}_{\text{emitted}} = \epsilon_s \cdot \sigma \cdot T^4 \cdot A_{\text{emitted}} \tag{11.17}$$

Based on these equations, the thermal equilibrium temperatures of the spacecraft can be computed at eclipse and in sunlight to solve for $\dot{Q}_{\text{net}}$ equals zero, ensuring the spacecraft is not heating up or cooling down. Solving for these two scenarios, however, would imply a steady state scenario where the spacecraft actually reaches and stabilises at these temperatures, which will not happen due to the short orbital periods. Constant change between the sunlit area and the eclipse will keep the temperatures in a substantially tighter range. Although, to remain conservative, these equations were still solved and the equilibrium temperatures were computed for different values of α_s and ϵ_s for differently treated aluminium types according to [50] and [63], and are displayed in Table 11.6. For the temperatures in eclipse only $\dot{Q}_{\text{emitted}}$, $\dot{Q}_{\text{Earth}}$ and $\dot{Q}_{\text{internal}}$ are considered.

Table 11.6: Equilibrium Temperatures for Different Aluminium Coefficients of Absorptivity and Emission.

Aluminium Type	***Black Anodized***		***Buffed***		***Lightly Oxidized***		***Standard***		***High Emittance***	
Coefficients $\alpha_s \mid \epsilon_s$	0.65	0.82	0.16	0.03	0.20	0.15	0.35	0.79	0.27	0.82
T$_{\text{Eclipse}}$ [K]	131.71		301.17		201.40		132.95		131.71	
T$_{\text{Sunlight}}$ [K]	248.12		421.97		294.43		218.10		204.54	

These ranges clearly indicate that some thermal control is needed; however, since these values are not too extreme, passive thermal control will be sufficient. Multi-layer Insulation (MLI) was chosen as the primary source of

---

[65] `https://earthobservatory.nasa.gov/images/84499/measuring-earths-albedo`

[66] `https://www.spenvis.oma.be/help/background/illumination/illumination.html#infra`

thermal control. MLI consists of multiple layers alternating between low-emissivity materials and empty spaces to reduce conduction as well as minimise absorption and internal heat emission. In this design, the outer layer will be assumed to be made of aluminised Kapton, which offers a balance between a low absorptivity coefficient of 0.14 and emissivity of 0.09 ([52, 100]). The MLI will be made of 20 layers for which a reasonable heat transfer coefficient, U_{MLI}, has a value of 0.5 W/m^{2}K based on approximations according to [52]. This low coefficient will limit the temperature fluctuations inside the spacecraft, leading to a quasi-isolated system. Based on Equation 11.18, the temperature on the outer layer would range from 264.8K to 326.1K, and it would remain between 278.1K and 312.8K on the inner side of the cube, with $\dot{Q}_{\text{internal}}$ taken as 127 W or 50 % of the power used by the components inside the bus during the most intensive phase.

$$T_{\text{inner}} = T_{\text{outer}} \pm \frac{\dot{Q}_{\text{internal}}}{U_{\text{MLI}} \cdot A_{\text{e}}} \tag{11.18}$$

This approach remains mass and power efficient while ensuring thermal survival of all subsystems. This justifies the decision not to perform transient analysis; however, for further design, this time-dependent thermal analysis could be performed, also taking into account heat conduction paths and heat flows inside the spacecraft. Also, due to a relatively low temperature range inside the spacecraft and consistent material use, the structural thermal loads were calculated to be negligible for the design. Finally, MLI has to cover all six sides of the spacecraft, the cost and mass of a 20-layer MLI for the ADR spacecraft was conservatively extrapolated using a market-available CubeSat MLI [67] to be around 6 kg and 45000 euros.

11.7 Radiation

The radiation in LEO makes it a critical design element to take into account. However, radiation has an increasingly negative effect, particularly for long missions, which will not be the case for Starfixers. The yearly radiation rate varies significantly depending on the inclination and altitude. For a 1mm aluminium sheet at an inclination of 60 degrees and 600 km altitude, the rate is 1500 rad/year according to [60]. For a mission time of 2 months, this would thus be 125 rad/month, complying with **[R-SUB-STR-08]**. However, this estimate is extremely conservative since the radiation coming through will be significantly lower due to the spacecraft's 3mm wall thickness and the MLI coverage on all surfaces. Therefore, radiation is not expected to be critical for this mission and will thus not require any additional radiation shielding.

---

[67] `https://satsearch.co/products/squid3-space-cubesat-mli`

12 Mission Budget

The following chapter explores various aspects of the mission's budget. It begins with Section 12.1, where mass, power and cost budgets for the subsystems are compiled using their chosen components to obtain a preliminary launch cost. Subsequently, resource allocation is discussed in Section 12.2, including the cost breakdown structure of the mission and post-DSE activities. Finally, ROI is explored in Section 12.3 to assess profitability.

12.1 Total Budget

Having finished the detailed design of Starfixers Inc.'s ADR subsystems, one can now compile mass, cost, and power data. Figure 12.1 highlights the subtotal mass, cost, and power per subsystem, as well as the global totals. Building this table is vital, as a clear overview of these parameters supports further design iterations.

Looking at Figure 12.1, only hardware components are included, excluding development and manufacturing costs, except for the propulsion unit, where in-house thruster development and manufacturing are estimated at €1M (main thruster) and €300k (adverse thruster), based on a 4-month effort as shown in Figure 14.4.

The reasoning behind those values follows from the fact that the development and manufacturing of the two thrusters is completed in a span of 4 months, as shown in Figure 14.4. A team of 20 engineers working on the main thruster, each earning an average salary of €150k per year, results in the thruster costing €1M. Since the adverse thruster is a downscaled version of the main thruster, i.e. they have the same characteristics and specific impulse, the development of it is expected to be significantly less expensive, as the design and documentation will already be more or less complete. Therefore, the adverse thruster only needs to be manufactured, besides minor details that might change in its development, and is evaluated at €300k.

Moreover, some values in Figure 12.1 are left blank due to unavailable public data, but subtotals are filled using conservative estimates from literature and Space Mission Analysis and Design (SMAD) [59]. The bottom of Figure 12.1 shows total mass, cost, and power (both raw and with a margin). It has to be noted that the margin considered for the dry mass is 10%, whereas the margin considered for the wet mass is already included in the total fuel mass value (total fuel mass accounts for 11 debris satellites to be de-orbited instead of 10), and therefore is a summation of the dry mass (with the margin) and the total fuel mass. The launch cost using the Falcon 9 launcher (2416/kg launched) is derived from the final wet mass (with margin), yielding a total hardware plus launch cost of ≈ €6.1M, which is well within the €100M budget set by **[R-SYS-26]**. This excludes satellite development, Manufacturing, Assembly and Integration (MAI) activities, operations, and mission/flight software development.

Given that the MAI (and thus AIT) phase spans two years (see Section 14.2), an estimated average salary of €150k per person per year implies that a team of approximately 80–85 engineers would correspond to the €25M allocated to "AIT & GSE" in Figure 12.2a. While this figure is not based on a detailed cost model, it represents a reasonable estimate and validates the assumed 25% share of the total mission budget.

The "Ground Segment & Operations", in Figure 12.2a, is evaluated at 10% per Michel van Pelt, Head of Cost Engineering at ESA, as discussed in Section 12.2. Finally, the software development is valued at 15% of the mission budget (so €15M), and with hardware amounting to ≈€5M, this results in the "Equipment and Onboard Software" marking a 20% of the mission budget, as shown in Figure 12.2a.

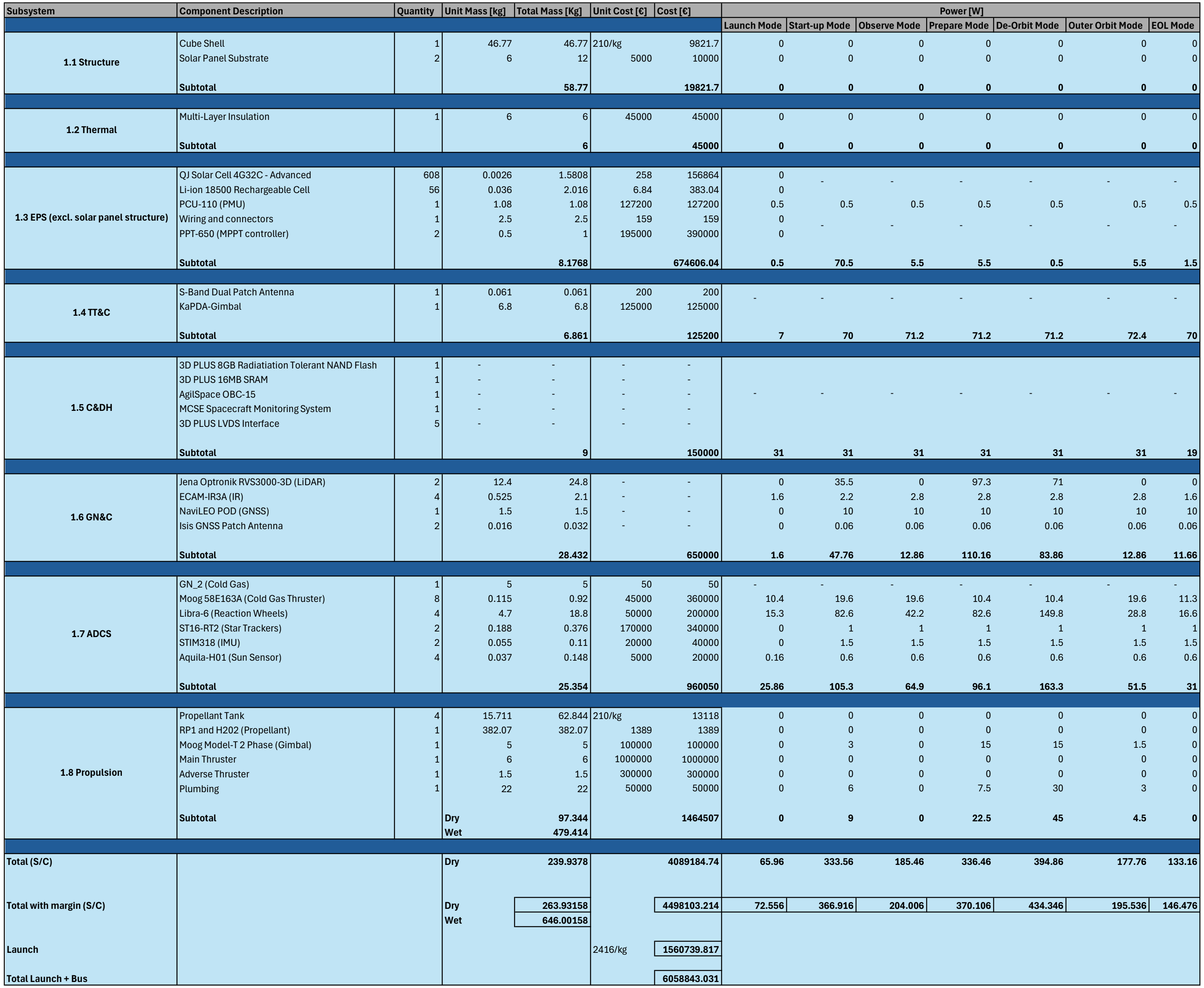

Subsystem	Component Description	Quantity	Unit Mass [kg]	Total Mass [Kg]	Unit Cost [€]	Cost [€]	Power [W]						
							Launch Mode	Start-up Mode	Observe Mode	Prepare Mode	De-Orbit Mode	Outer Orbit Mode	EOL Mode
1.1 Structure	Cube Shell	1	46.77	46.77	210/kg	9821.7	0	0	0	0	0	0	0
	Solar Panel Substrate	2	6	12	5000	10000	0	0	0	0	0	0	0
	Subtotal			**58.77**		**19821.7**	**0**	**0**	**0**	**0**	**0**	**0**	**0**
1.2 Thermal	Multi-Layer Insulation	1	6	6	45000	45000	0	0	0	0	0	0	0
	Subtotal			**6**		**45000**	**0**	**0**	**0**	**0**	**0**	**0**	**0**
1.3 EPS (excl. solar panel structure)	QJ Solar Cell 4G32C - Advanced	608	0.0026	1.5808	258	156864	0	-	-	-	-	-	-
	Li-ion 18500 Rechargeable Cell	56	0.036	2.016	6.84	383.04	0						
	PCU-110 (PMU)	1	1.08	1.08	127200	127200	0.5	0.5	0.5	0.5	0.5	0.5	0.5
	Wiring and connectors	1	2.5	2.5	159	159	0	-	-	-	-	-	-
	PPT-650 (MPPT controller)	2	0.5	1	195000	390000	0						
	Subtotal			**8.1768**		**674606.04**	**0.5**	**70.5**	**5.5**	**5.5**	**0.5**	**5.5**	**1.5**
1.4 TT&C	S-Band Dual Patch Antenna	1	0.061	0.061	200	200	-	-	-	-	-	-	-
	KaPDA-Gimbal	1	6.8	6.8	125000	125000							
	Subtotal			**6.861**		**125200**	**7**	**70**	**71.2**	**71.2**	**71.2**	**72.4**	**70**
1.5 C&DH	3D PLUS 8GB Radiatiation Tolerant NAND Flash	1	-	-	-	-	-	-	-	-	-	-	-
	3D PLUS 16MB SRAM	1	-	-	-	-							
	AgilSpace OBC-15	1	-	-	-	-							
	MCSE Spacecraft Monitoring System	1	-	-	-	-							
	3D PLUS LVDS Interface	5	-	-	-	-							
	Subtotal			**9**		**150000**	**31**	**31**	**31**	**31**	**31**	**31**	**19**
1.6 GN&C	Jena Optronik RVS3000-3D (LiDAR)	2	12.4	24.8	-	-	0	35.5	0	97.3	71	0	0
	ECAM-IR3A (IR)	4	0.525	2.1	-	-	1.6	2.2	2.8	2.8	2.8	2.8	1.6
	NaviLEO POD (GNSS)	1	1.5	1.5	-	-	0	10	10	10	10	10	10
	Isis GNSS Patch Antenna	2	0.016	0.032	-	-	0	0.06	0.06	0.06	0.06	0.06	0.06
	Subtotal			**28.432**		**650000**	**1.6**	**47.76**	**12.86**	**110.16**	**83.86**	**12.86**	**11.66**
1.7 ADCS	GN_2 (Cold Gas)	1	5	5	50	50	-	-	-	-	-	-	-
	Moog 58E163A (Cold Gas Thruster)	8	0.115	0.92	45000	360000	10.4	19.6	19.6	10.4	10.4	19.6	11.3
	Libra-6 (Reaction Wheels)	4	4.7	18.8	50000	200000	15.3	82.6	42.2	82.6	149.8	28.8	16.6
	ST16-RT2 (Star Trackers)	2	0.188	0.376	170000	340000	0	1	1	1	1	1	1
	STIM318 (IMU)	2	0.055	0.11	20000	40000	0	1.5	1.5	1.5	1.5	1.5	1.5
	Aquila-H01 (Sun Sensor)	4	0.037	0.148	5000	20000	0.16	0.6	0.6	0.6	0.6	0.6	0.6
	Subtotal			**25.354**		**960050**	**25.86**	**105.3**	**64.9**	**96.1**	**163.3**	**51.5**	**31**
1.8 Propulsion	Propellant Tank	4	15.711	62.844	210/kg	13118	0	0	0	0	0	0	0
	RP1 and H202 (Propellant)	1	382.07	382.07	1389	1389	0	0	0	0	0	0	0
	Moog Model-T 2 Phase (Gimbal)	1	5	5	100000	100000	0	3	0	15	15	1.5	0
	Main Thruster	1	6	6	1000000	1000000	0	0	0	0	0	0	0
	Adverse Thruster	1	1.5	1.5	300000	300000	0	0	0	0	0	0	0
	Plumbing	1	22	22	50000	50000	0	6	0	7.5	30	3	0
	Subtotal		**Dry**	**97.344**		**1464507**	**0**	**9**	**0**	**22.5**	**45**	**4.5**	**0**
			Wet	**479.414**									
Total (S/C)			**Dry**	**239.9378**		**4089184.74**	**65.96**	**333.56**	**185.46**	**336.46**	**394.86**	**177.76**	**133.16**
Total with margin (S/C)			**Dry**	**263.93158**		**4498103.214**	**72.556**	**366.916**	**204.006**	**370.106**	**434.346**	**195.536**	**146.476**
			Wet	**646.00158**									
Launch					2416/kg	**1560739.817**							
Total Launch + Bus						**6058843.031**							

Figure 12.1: Final Hardware Mass, Cost, and Power Budgets.

12.2 Resource Allocation

According to Michel van Pelt, a first-order cost in terms of percentage of the total cost breakdown for a mission of this size and type (excluding launch) can be described using Figure 12.2a.

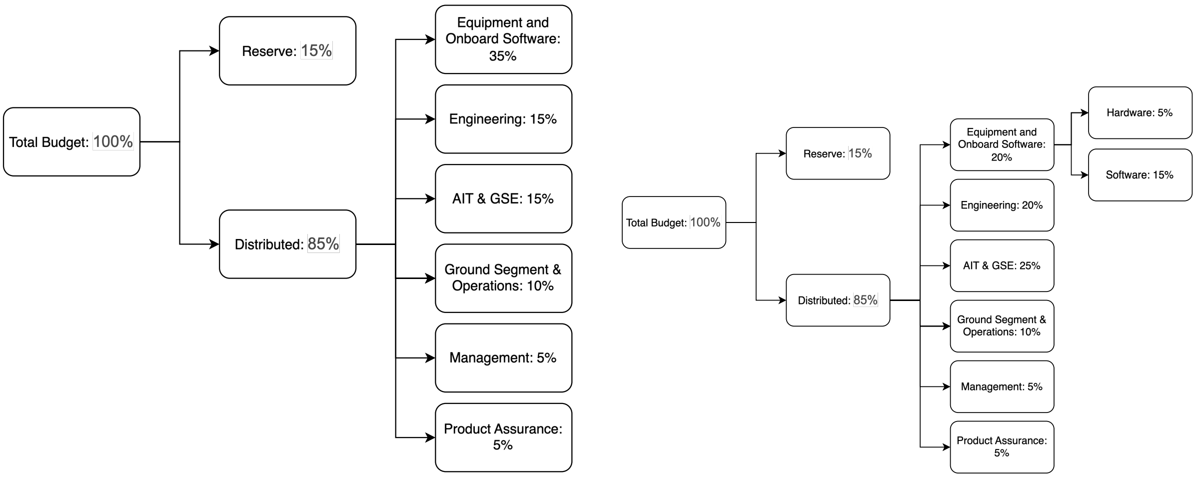

(a) CBS Structure - Theoretical LEO distribution **(b)** CBS Structure - Adapted for Starfixers

Figure 12.2: Comparison of Cost Breakdown Structures.

This preliminary budget allocation also follows recommendations made by SMAD [59] and is expected to vary slightly in reality. Equipment and onboard software refer to all the spacecraft hardware and software. Management includes all the resources needed for staff organisation and coordination, the product assurance refers to all the activities aimed at ensuring mission reliability and quality, including testing, quality control, and compliance with standards and safety protocols. Engineering covers all system and subsystem-level design, analysis, technical support, and documentation throughout the project. AIT and GSE encompass the physical integration, system-level testing, and development of supporting infrastructure on the ground. Ground segment and operations cover the cost of establishing and maintaining mission control, data handling, and long-term operational support. The distributed total represents the core, directly estimated costs, while the reserve accounts for contingency funding to handle unforeseen technical, schedule, or cost risks throughout the development lifecycle. It can be observed that the 35% allocation for equipment and onboard software within the €100 million budget does not align with the total hardware costs outlined in Section 12.1. This discrepancy may be partly attributed to the absence of a payload, which typically represents a significant fraction of spacecraft costs. Additionally, the cost estimations of custom-made components, such as the thruster and various FPGAs, could be underestimated, as well as incomplete definitions of plumbing and electrical interfaces that could contribute to the mismatch. In line with Section 12.1, it is therefore provisionally assumed that hardware accounts for 4-5% of the budget and software for 15-16%.

A larger-than-usual share of the budget has been allocated to AIT, GSE, and engineering activities. This is primarily due to the development of a mission-specific thruster and the added complexity of sensor fusion, which demands additional integration and testing efforts. Furthermore, the inclusion of livestreamed operations introduces unique engineering and testing requirements that are not typical for standard missions. Finally, a significant portion of the AIT & GSE budget is allocated to the development of a scaled-down version of the Starfixers mission. This version will act as a demonstration mission where a CubeSat replica of the Starfixers' spacecraft will perform on-orbit momentum transfer. This is further analysed in chapter 14.

These budget estimates will be further refined with guidance from experienced professionals and validated using tools such as the ESA Costing Software, enabling a more accurate and comprehensive cost assessment as the design matures.

12.3 Return On Investment & Operational Profit

Before addressing profitability or Return On Investment (ROI), it is essential to distinguish between non-recurring costs (associated with development) and recurring costs (linked to production and operations). The current mission, with a total budget of €100 million, includes both categories and is assumed to be funded by a governmental agency such as ESA, similar to the backing that ClearSpace-1 received as a proof of concept.

Although the financial ROI for this first-of-its-kind mission is expected to be zero, the technological and operational ROI is anticipated to be high, with critical advancements in propulsion, sensor integration, and live operations. Moreover, emphasis has been placed throughout the design on the feasibility and scalability of the service in such a competitive market. Once validated, the service can be scaled through subsequent missions with only recurring costs, enabling a significantly higher financial return.

At present, there is no established commercial market for ADR and therefore no existing market price. In effect, this places the mission in a quasi-monopolistic position, allowing Starfixers to set its own price point, at least initially, and be the market leader. This early-mover advantage enables strategic pricing based on cost recovery and target ROI, rather than competing with existing providers. As regulatory frameworks evolve and competitors enter the field, this pricing strategy will naturally need to be revisited and adapted.

Given the urgent demand for ADR to ensure the sustainability of space operations, it is reasonable to assume that regulatory pressure will create a viable and possibly mandatory market for such services. In this context, Starfixers Inc. will be positioned as a commercial, service-based offering, and the following section will proceed to:

1. Define a target ROI,
2. Determine recurring costs,
3. Establish an initial pricing strategy aligned with those objectives.

Considering the high upfront investment and the novelty of the ADR sector, setting a target ROI of 20–30% is both ambitious and justifiable for a first-in-market space service. This figure aligns with typical ROI expectations in the space industry for high-risk, high-capital ventures, particularly where there is potential for regulatory-driven demand. According to OECD and ESA reports on space sector financing, commercial satellite operators and new space ventures generally target ROIs in the 15–30% range, depending on risk level, scalability, and competitive pressure [39, 75]. Provided the absence of established competitors, Starfixers Inc. can aim for the upper end of this range while maintaining flexibility as the market matures. This ROI is not solely financial, but it also reflects returns in market positioning, technological lead, and influence on policy development. It should be noted that in this early phase, pricing can be structured to balance long-term adoption incentives with cost recovery and innovation reinvestment, allowing for adaptation as demand and competition evolve.

The cost of the mission was dissected based on Figure 12.2b, combined with Table 20-9 from the ”Cost Estimating Relationships” chapter of SMAD [59]. The weights per subsystem and recurring/non-recurring ratios were kept as given, however, as previously mentioned in Section 12.2, hardware, software, engineering and AIT budgets were redistributed to match the peculiar needs of this unconventional mission. This resulted in Table 12.1, finding a non-recurring cost of around 40%, and recurring costs of 60% per mission or €60 million of the €100 million budget.

For the current mission design, the objective is to de-orbit 10 defunct spacecraft classified as space debris. With a recurring mission cost of €60 million, this results in a unit cost of €6 million per de-orbit service (so per debris de-orbiting), in order to break even. To achieve the target ROI of 20%, the market price must be set at €7.2 million, as shown in Equation 12.1.

$$ROI = \frac{\text{Price} - \text{Cost}}{\text{Cost}} \tag{12.1}$$

Currently, pricing is determined by Starfixers, whose profitability depends heavily on the timely implementation of regulatory frameworks requiring satellite operators to remove defunct assets. As the market evolves, the optimal price point may need to be adjusted to maximise returns. With increased mission frequency, scaling up to a larger ADR spacecraft could become viable, potentially reducing unit costs. Another development path involves integrating on-orbit servicing capabilities, such as refuelling of the ADR spacecraft, to extend mission duration and enhance operational flexibility. By adopting either of these strategies, the cost per de-orbit service could be significantly reduced, allowing Starfixers to remain competitive if new entrants emerge or simply to improve future profitability. The predicted cost decrease and profit increase are shown in Figure 12.3 below, where the first 2030 mission is shown with no profit and a 10 million euro unit cost and progresses based on the target ROI and recommendations.

Table 12.1: Distributed Mission Cost Breakdown with Recurring and Non-Recurring Allocations. Note: AIT, Program Level (Management and Systems Engineering), GSE, LOOS (Launch and On-Orbit Support).

Subsystem/Activity	Distributed Cost [%]	Non-Recurring [%]	Recurring [%)]
Hardware Bus Total	**5.00**	**60**	**40**
2.1 Structure	0.92	70	30
2.2 Thermal	0.10	50	50
2.3 EPS	1.17	62	38
2.4a TT&C	0.63	71	29
2.4b C&DH	0.86	71	29
2.5 ADCS	0.92	37	63
2.6 Propulsion	0.42	50	50
Software	**15.00**	**75**	**25**
Support	**65.00**	**35**	**65**
3.0 IA&T	15.00	0	100
4.0 Program Level	30.00	50	50
5.0 GSE	10.00	100	0
6.0 LOOS	10.00	0	100
Subtotal	**85.00**	**39.25**	**45.75**
Reserve	**15.00**	**0.00**	**100.00**
Total	**100.00**	**39.25**	**60.75**

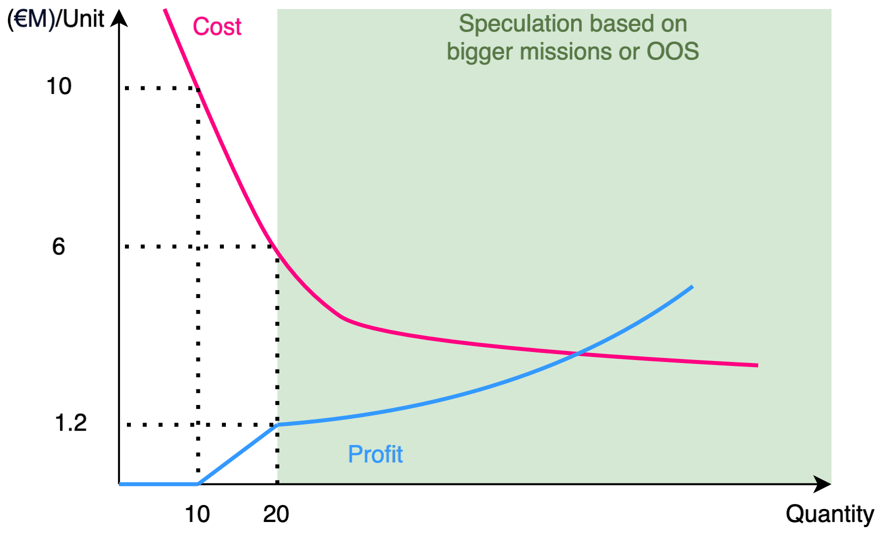

Figure 12.3: Prediction of Cost and Profit.

13 Design Assessment

Having established the design of the mission and spacecraft, one must asses the results. This chapter presents an evaluation of various aspects of the final mission design. First, in Section 13.1, the sustainability of the design and production methods is evaluated. Second, in Section 13.2, the Space Sustainability Rating of the mission is obtained following the official procedure in order to quantify the mission's impact on the orbital environment. Third, Section 13.3 presents the compliance matrix for system-level requirements and the verification plan for all of the requirements. Then, Section 13.4 presents verification of the most relevant Python scripts used for the design. After that, Section 13.5 presents the validation of the efficiency model and the validation plan. Finally, in Section 13.6, sensitivity analysis of the most relevant mission aspects is presented, showing the design's sensitivity to mission-level changes.

13.1 Sustainable Design and Production Methods

Considering sustainability in the design process is essential in the era of peak global energy consumption and rising carbon emissions. It is not sufficient to focus solely on sustainable manufacturing; environmental impact must also be addressed during a product's operational life and at its end-of-life. A multifaceted approach to sustainability must be used for the long-term well-being and prosperity of humanity. The most important sustainability aspects considered for the Starfixers Inc. mission are outlined below: manufacturing, launch and propellant usage, and design for safe disposal.

Manufacturing

Manufacturing is a core element of the mission, determining the structure, materials, and environmental footprint of the ADR mission. Three core manufacturing-related aspects are considered: material selection, structural design, and production methods.

In terms of materials, the use of rare and resource-intensive components is minimised. As mentioned in chapter 11, the spacecraft bus is made of aluminium as well as its stiffeners. The structural design is kept modular and clean. The spacecraft is constructed from large, integrated assemblies rather than multiple riveted parts, which reduces the risk of fragmentation in the event of failure. A one-piece metallic bus casing is preferred to further limit the number of potential debris-generating interfaces.

Moreover, toxic surface coatings are avoided in favour of space-qualified materials such as aluminium with Kapton-based MLI coatings, which were chosen as they offer both thermal performance and material stability without introducing hazardous substances. Additionally, the manufacturing approach seeks to minimise energy-intensive machining techniques where possible, favouring efficient fabrication processes to reduce material waste and carbon footprint. Methods with higher energy efficiency and lower material waste are prioritised instead.

Although a full Life Cycle Assessment (LCA) has not yet been performed, the design has been guided by life cycle thinking. Environmental impact is considered from the early design stages, especially in terms of material choice, propulsion systems, and end-of-life planning. A full LCA is planned for the detailed mission design phase and aims to quantitatively asses mission's environmental impact.

Launch and Propellant Usage

Launch and in-orbit propulsion often represent the most environmentally impactful aspects of a space mission. In response, Starfixers Inc. adopts several mitigation strategies focused on launcher selection and propellant choice.

Requirement **[R-SUB-STR-15]** ensures that the spacecraft fits within a single launch vehicle, minimising emissions associated with multiple deployments. Furthermore, a Falcon 9 launcher with a reusable booster is chosen to reduce waste and carbon emissions[68].

When selecting a launch provider, non-toxic propellants and lower greenhouse gas profiles are preferred. While the launch vehicle propellant is largely outside the mission's direct control, it remains a consideration in procurement and sustainability assessments [69].

For the ADR spacecraft itself, requirement **[R-SYS-18]** states the use of non-toxic propellants across all propulsion systems. The main propulsion relies on a bi-propellant combination of high-test peroxide and RP-1 kerosene, which are both non-toxic propellants. For attitude control, the spacecraft uses cold gas thrusters with an inert, non-toxic propellant- nitrogen, further reducing environmental and operational hazards. These choices align with the mission's sustainability goals of minimising toxic emissions and ensuring safer on-ground assembly and in-orbit operation.

Design for Safe Disposal

In support of orbital sustainability, the spacecraft is designed with end-of-life de-orbiting in mind. Structural and propulsive elements ensure the vehicle can execute a controlled re-entry well within five years of mission end, with nominal timelines under two years. This is achieved even in the event of fuel depletion, meeting and exceeding international post-mission disposal guidelines.

A more comprehensive analysis of the mission's debris removal role, collision risk management, and post-mission procedures is presented in Section 13.2, as part of the Space Sustainability Rating (SSR) evaluation below.

13.2 Space Sustainability Rating

Following the initial design phase of the Starfixers Inc. mission, driven by high-level sustainability objectives and qualitative decision making, this section marks a shift towards a more structured and quantitative analysis of the mission's environmental performance. While the earlier assessment established guiding principles such as debris mitigation, low-impact material selection, and emissions reduction, the current focus is on evaluating how well the mission adheres to recognised sustainability standards using measurable criteria.

The SSR is adopted to assess the mission's sustainability. SSR is developed by leading space agencies and companies such as ESA and Eutelsat to offer a standardised method to quantify a mission's impact on the orbital environment. While most sustainability efforts are subjective, the SSR relies on the mission's technical data and operational plan to produce a clear sustainability score and identify possible improvements.

By employing SSR Starfixers Inc. commits to transparency and accountability of its sustainability efforts. This approach also facilitates benchmarking against other missions and adherence to emerging international best practices in responsible space operations.

This section is therefore dedicated to reviewing the Starfixers Inc. mission design against each of the six SSR modules: Mission Index, Detectability, Identification & Trackability, Collision Avoidance Capability, Data Sharing, Design and Operation Standards, and Use of External Services. A requirement, **[R-SYS-30]**, has been added specifying that the mission must achieve at least a Silver sustainability rating according to the SSR framework. Therefore, this section analyses the mission design in detail against the SSR modules to evaluate compliance with this mandate. Additionally, multiple system-level sustainability requirements naturally drive the design towards sustainability targets.

The ultimate objective is to provide an evidence-based sustainable mission, supporting the goal of achieving a measurable SSR that reflects both the environmental and operational responsibility of the design.

---

[68] `https://www.spacex.com/media/environmental_assessment_falcon9.pdf`

[69] `https://shorturl.at/7Ryo8`

SSR scoring system

The SSR is an internationally recognised framework developed to assess the environmental and operational sustainability of space missions quantitatively [33]. It evaluates missions across six key modules: Mission Index (MI), Detectability, Identification & Trackability (DIT), Collision Avoidance Capability (COLA), Data Sharing, Application of Design and Operation Standards (ADOS), and Use of External Services, to provide a comprehensive sustainability score. The rating system ranges from Bronze to Platinum, reflecting progressively higher levels of sustainable mission design and operation. The SSR enables transparent benchmarking and promotes best practices within the space industry by providing measurable criteria rather than qualitative promises.

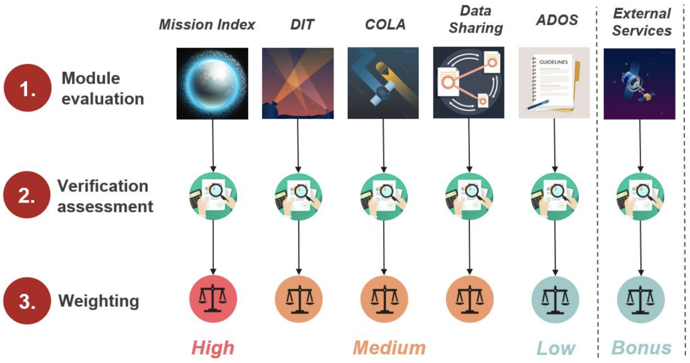

Figure 13.1: SSR Weighting Scheme [33].

Although the SSR does not disclose the exact weighting of its evaluation criteria, an indicative distribution is shared, as shown in Figure 13.1. Based on this figure, approximate weights have been inferred in order to construct a scoring matrix that yields a final overall sustainability score. The bonus module for External Services was excluded from the main calculation, as it does not contribute to the primary rating tier and will be evaluated separately. The remaining contributing modules were scored as follows:

- **MI:** High — 7/20
- **DIT:** Medium — 4/20
- **COLA:** Medium — 4/20
- **Data Sharing:** Medium — 4/20
- **ADOS:** Low — 1/20

Mission Index

The MI evaluates the long-term impact of a space mission on the orbital environment by quantifying the residual risk it poses after its operational lifetime. It considers factors such as orbital altitude, mass, cross-sectional area, mission duration, and the effectiveness of post-mission disposal strategies. The collision index can be found using Equation 13.1:

$$I_c = p_c \times e_c \tag{13.1}$$

where p_c is the collision probability, which can be quantified using ESA's MASTER software, and e_c follows from NASA's Environmental Consequences of Orbital Breakups (ECOB). They are visualised in Figure 13.2. e_c quantifies the severity of the potential fragmentations in terms of the increase in the collision probability for operational satellites using the NASA break-up model to simulate the fragmentation. As explained in Section 3.3, the operational probability of collision is of 4.32×10^{-6} for a duration of t_{op} = 1.19 months with active avoidance measures whereas for the EoL phase it amounts to 2.93×10^{-4} with a total time of t_{EoL} = 42.8 months. The severity of the collision can be quantified using Figure 13.2a below, where one can observe that given the highest altitude considered is 600km at 53° of altitude, $e_c \approx 0.1 \times 10^{-2}$. Overall, this results in a MI of $I_{op} = 4.32 \times 10^{-8}$

and $I_{EoL} = 2.93 \times 10^{-6}$. Although SSR does not disclose how the MI converts to a score, Figure 13.2b displays the top 5 payloads with the highest collision indices which are of the order of 2 $\times 10^{-2}$ or several orders of magnitude larger suggesting a lower collision risk and good score for Starfixers.

However, it is important to note that the MI currently does not account for the unique contributions of ADR missions. These missions, by design, aim to increase the long-term orbital capacity by removing defunct objects from orbit. In contrast, the MI as applied in [64] is structured around missions that reduce orbital capacity, occupying space for their operational lifetime and only removing themselves at end-of-life. This creates an apparent contradiction: applying the current MI methodology to an ADR mission targeting a congested region would yield a worse score, despite the mission's objective being to increase orbital sustainability in that very region.

Given this limitation, a purely quantitative assessment based on the current formulation may misrepresent the benefit of ADR missions. As such, a qualitative argument can be made in favour of a high MI score, grounded in the mission's potential to enhance orbital capacity. A more comprehensive approach might involve developing an adapted methodology that accounts for both the transient risks posed by the ADR spacecraft itself (e.g., during rendezvous) and the long-term benefit of de-orbiting multiple debris objects. This would require balancing short-term collision probability with the net gain in orbital carrying capacity, possibly incorporating probabilities for successful removals and the mitigation of future fragmentation risk.

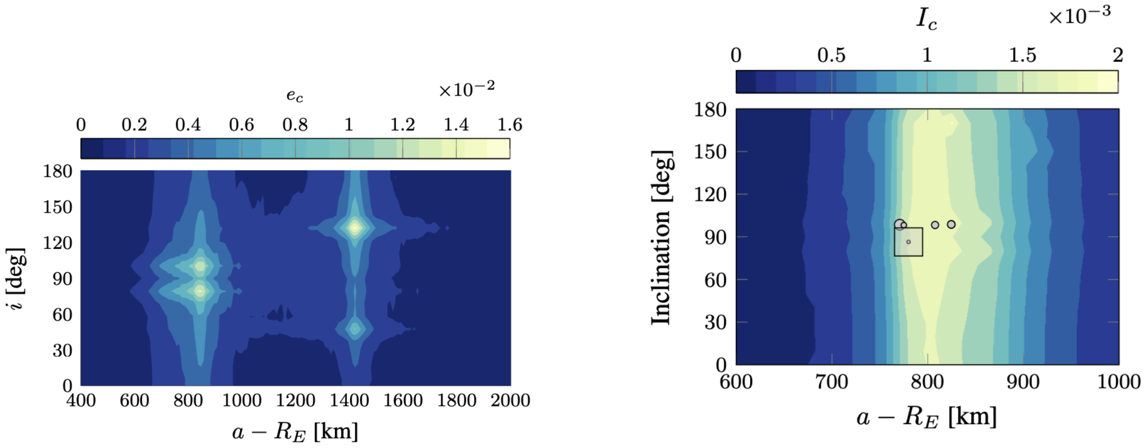

(a) Term e_c for Different Orbital Parameters.

(b) Collision Index for Different Orbital Parameters.

Figure 13.2: Comparison of ECOB Fragmentation and Collision Index [64].

Detectability, Identification & Trackability (DIT)

The DIT module assesses the spacecraft's observability, identification, and trackability by external systems throughout its mission, supporting Space Situational Awareness (SSA) and reducing risks of misidentification or loss of custody. The DIT score is the average of three components:

$$S_{\text{DIT}} = \frac{S_{\text{Detectability}} + S_{\text{Trackability}} + S_{\text{Identification}}}{3} \tag{13.2}$$

Detectability evaluates detection likelihood by ground-based radar and optical sensors. Optical detectability is benchmarked against a limiting magnitude of 15, achievable by typical 0.3–0.5 m telescopes [33]. The spacecraft's size, reflective surfaces, and 600 km orbit yield a visual magnitude brighter than 13, surpassing this threshold. Radar detectability is confirmed with an estimated radar cross-section above 0.3 m^2, detectable by networks like the U.S. SSN and ESA's GRAVES [62, 6]. Both optical and radar components receive full scores: $S_{\text{Detectability}} = 1.0$.

Trackability measures orbital predictability using standard optical and radar tracking. Based on Two-Line Element (TLE) analysis from over 3,200 satellites, scoring uses average pass duration, orbital coverage, and pass interval. For this mission, average pass duration (620 s) and interval (<1.5 h) exceed top thresholds (scoring 1.0 each), while average orbital coverage (19%) scores 0.25. Weighted equally, the trackability score is:

$$S_{\text{Trackability}} = \frac{1 + 0.25 + 1}{3} = 0.75 \tag{13.3}$$

Identification credit is awarded for timely and transparent spacecraft tracking and data sharing. The operator ensures custody within hours of deployment, uses ESA and public SSA databases, and commits to sharing photometric and radiometric data, satisfying the highest questionnaire criteria: $S_{\text{Identification}} = 1.0$.

The final DIT score is:

$$S_{\text{DIT}} = \frac{1.0 + 0.75 + 1.0}{3} = 0.916 \tag{13.4}$$

This reflects strong compliance with best practices in detection, identification, and tracking, supporting mission sustainability and space traffic management.

Collision Avoidance

COLA is a crucial operational capability for any spacecraft, ensuring the safety and sustainability of the mission. It includes precise orbital position knowledge, effective coordination with space operators, and collision avoidance capabilities. Reliable orbit determination and validated positional error allow timely collision predictions, while communication protocols ensure swift coordination in potential collision cases.

The accuracy of COLA measurement directly impacts mission safety and contributes to minimising the risk of generating space debris, supporting the overall objective of responsible in-space operation. SSR provides a matrix as shown below, where the criteria reached by Starfixers have been highlighted in green. SSR provides the following scoring guidance for the COLA matrix:

> *"Entities can receive credit for any box where they satisfy all criteria contained in the box. If an operator is able to fulfil multiple boxes in a single row, those point values are added. During the scoring process, the total number of points earned by the entity is divided by the total possible points. The normalised point total is an input to the full SSR calculation."* [33]

The matrix provided by SSR for COLA has been analysed with regards to Starfixers' mission in Figure 13.3 below, which results in a total score of 0.911 for COLA, reflecting collision avoidance measures being highly able due to the nature of the mission that approaches debris.

Figure 13.3: COLA Grading Matrix by SSR.

Operator Action	No Score	Low Score (2 points)	Medium Score (3 points)	High Score (4 points)	Source/Reasonning
Orbital State Knowledge (during normal operations)	Rely on a third party public SSA provider for state information (e.g., space-track.org TLE)	Operator maintained orbital position state knowledge of object [*]	Maintain orbital state knowledge of object to < 10 km in any directionUpdate orbit determination for the operated satellite when a manoeuvre or other event induces a change to its orbit that would cause the operator's state estimation to be worse than the required orbital state knowledgeCharacterize/validate covariance of your orbit determination	Maintain orbital state knowledge of object to within < 1 km in any directionUpdate orbit determination for the operated satellite when a manoeuvre or other event induces a change to its orbit that would cause the operator's state estimation to be worse than the required orbital state knowledgeCharacterize/validate covariance of your orbit determination	GNSS, star trackers, sun trackers, IMU are all used to conduct operations to be accurate within meters
Collision Avoidance: Availability to Coordinate	Not able to coordinate	Able to coordinate in response to emergencies (but not necessarily on a routine basis)	Able to coordinate during set hours per day	Has a system for routine conjunction assessment and capability to respond to concerns 24 hours per day via human or computer system capable of supporting near-immediate coordination and reaction for urgent issues	Communication at least once per orbit (under 100 minutes) where commands and telemtry are exchanged
Collision Avoidance: Capability to Coordinate	Operator has no dedicated process for conjunction screening, assessment, or mitigationThe operator may be unable to or chose not to ever manoeuvre in response to conjunctions	Has the capability to be contacted in case of close approach or another high-risk event. Operator regularly screens orbits and planned manoeuvres against public catalogues and/or information from SSA sharing organizations and/or third-party SSA providers	Operator is capable of interpreting conjunction data messages and other common formats, to determine risk and generate/screen mitigating manoeuvres. Operator has a system for automated routine conjunction. assessment	Has documented procedures for collision screening, assessment, and mitigationRegularly screens operational spacecraft and planned manoeuvres against SSA sharing organization catalogue	Within mission goal to share the operations, consistent communication and updates to be publically shared
Collision Avoidance: manoeuvre capability	No maneuver capabilities	Any maneuver capabilities (including differential drag)	Reaction (at least Δv=1 cm/s) within 6 orbital revolutions	Reaction (at least Δv=1 cm/s) within 1 orbital revolution	Highly capable ADCS due to delicate operations
BONUS: Maintaining orbital state knowledge after end of normal operations		Maintain orbital state knowledge until spacecraft is placed into a graveyard orbit or is disposed of through atmospheric re-entry	Maintain orbital state knowledge to 10 km until spacecraft is placed into a graveyard orbit or is disposed of through atmospheric re-entry	Maintain orbital state knowledge to 1 km until spacecraft is placed into a graveyard orbit or is disposed of through atmospheric re-entry	Planned EOL graveyard orbit and planned communication until then.

Data Sharing

Data sharing is a critical component of space sustainability, enabling collaboration and improved situational awareness among space entities. While the design and standardisation of data sharing protocols for missions of this nature is still evolving, this mission represents a pioneering step as the first of its kind to openly embrace comprehensive data transparency.

Uniquely, the mission is committed to going public on all fronts, including livestreaming mission activities and actively sharing real-time data for scientific research and broader community engagement. By openly providing telemetry, tracking information, and operational insights, it sets a precedent for collaborative space operations and responsible stewardship.

This openness supports independent V&V efforts and encourages the development of better data-sharing practices across the industry. While formalised scoring matrices for data sharing remain under development, this mission's willingness to share data widely is reflected in Starfixers assigning itself a perfect score of 1 currently. Of course, should the mission become commercialised with clients, the terms of data sharing will need to be reconsidered. However, for this inaugural mission, wide and transparent data sharing is paramount.

Such transparency directly contributes to enhanced SSA, risk mitigation, and fosters trust among space operators, advancing the collective goal of a safer and more sustainable orbital environment [33].

Application of Design and Operation Standards

As part of the ADOS evaluation, the mission underwent a detailed assessment based on a sustainability-focused questionnaire. This questionnaire addresses critical factors such as debris release, explosion risk mitigation, passivation, disposal orbits, and international registration compliance.

By conservatively completing this questionnaire, the mission achieves a total normalised ADOS score of approximately 0.63 as detailed in Table 13.1. This reflects strong performance in key areas such as the use of the most sustainable available launcher (Falcon 9), direct controlled de-orbiting of the spacecraft, and adherence to international registration protocols.

However, certain areas could be improved. In particular, the explosion probability should be calculated, and the debris size that could be potentially generated during operation should be analysed in detail. Due to the lack of analysis, these criteria were assigned a zero, lowering the overall score.

Further efforts to quantify and mitigate these risks are expected to improve the mission's sustainability and increase the ADOS score. The iterative assessment approach highlights the commitment to continuous improvement.

Table 13.1: ADOS Questionnaire Responses and Scoring.

Question	**Answer**	**Score**
Does your spacecraft or launcher release debris in orbit?	Although it is not expected, further analysis is needed to confirm.	0/1
To what level do you minimise the probability of explosion (x) during operation?	Strong mitigation applied, but no current analysis	0/1
Are your spacecraft and launch vehicle passivated after operation?	Spacecraft: Direct controlled de-orbit; Launch Vehicle: Passivated only	Spacecraft: 2/2; Launch Vehicle: 1/2
Does your spacecraft and launch vehicle upper stage use a disposal orbit after the end of operations?	Spacecraft: Direct controlled de-orbit; Launch Vehicle: Stable disposal orbit	Spacecraft: 2/2; Launch Vehicle: 1/2
Does your launching state commit to registering your payload with the UN Register of Objects Launched into Outer Space?	Yes	1/1

Total SSR with Bonus

Finally, after a thorough evaluation of each aspect of the SSR, including the MI, Data Sharing practices, COLA, DIT, and ADOS, an overall sustainability score can be calculated for the mission. As shown in Table 13.2, the weighted combination of these criteria results in a final score of 0.88, earning a Platinum rating, the highest distinction in the SSR system, going significantly beyond [**REQ-SYS-31**]. While this rating reflects excellent adherence to best practices and a strong commitment to responsible space operations, it must be noted that some components of the SSR methodology do not fully capture the complexities of innovative mission types such as ADR. Nonetheless, the high marks in data sharing and collision avoidance reflect a proactive approach to transparency and risk reduction.

Table 13.2: SSR Criteria and Weighted Scores.

Criteria	Weight	Score	Weighted Score
MI	0.35	0.800	0.2800
DIT	0.20	0.916	0.1832
COLA	0.20	0.911	0.1822
Data Sharing	0.20	1.000	0.2000
ADOS	0.05	0.636	0.0318
Total	**1.00**	**–**	**0.8772**

Beyond the standard score, the SSR also awards bonus stars for additional sustainability measures. Of the four possible bonuses, three relate to accommodating on-orbit servicing capabilities; an aspect that has not yet been integrated into the Starfixers design. This does not imply that such capabilities are excluded or unattainable; for example, refuelling may become relevant both commercially and operationally in the future. However, at this design stage, it is premature for Starfixers Inc. to commit to these features.

One bonus criterion concerns the compliance with the 25-year de-orbit rule. Starfixers surpasses this requirement with a stricter standard, defined by **[R-SYS-14]**, enforcing de-orbiting within 5 years. Current mission operation enables de-orbiting in under 4 years, even with full fuel depletion during operation.

Given this strong compliance, combined with the mission's fundamental focus on space sustainability and ADR capabilities, it is estimated that Starfixers Inc. merits one bonus star. Although being an ADR mission is not explicitly covered by existing bonus criteria, these points are intended to recognise extra efforts, efforts that Starfixers demonstrably fulfils.

13.3 Requirements Verification

In this section, the requirements verification is discussed. First, the user requirements that were given at the start of the mission, as well as the system requirements, are displayed. Then, all subsystem requirements are tabulated per subsystem. Per requirement, the verification method is chosen, and the expected compliance is noted as well for the user requirements. The last subsection presents a general plan on how these verification methods will be implemented. It is important to note that some identifiers are missing in the tables, since some requirements were removed after the past report [14]. Additionally, new requirements were added.

User and System Requirements.

The requirements compiled in Table 13.3 represent the system-level outcomes derived from the broader user requirements. Each requirement is clearly identified with its unique ID and is organised into logical categories: Performance, Operation, Sustainability, Legal Constraints and Regulations, and User Constraints. This follows the same structure established in the Requirements Discovery Tree (RDT). This organisation ensures traceability and facilitates further design, verification, and validation processes throughout the development lifecycle. Compliance of the mission with system-level requirements has to be carefully verified in accordance with internationally established verification standards for space missions. According to NASA[70], ”Verification is a formal process, using the method of test, analysis, inspection or demonstration, to confirm that a system and its associated hardware and software components satisfy all specified requirements.” Table 13.3 shows the system requirements and the verification method. The method is selected based on feasibility, cost and effectiveness. The verification methods include Testing (T), Inspection (I), Demonstration (D) and Analysis (A).

For instance, the use of non-toxic propellants can be verified through inspection and does not require any further analysis or testing. Survival during launch, however, cannot be simply inspected or demonstrated; adequate testing is not feasible due to financial constraints, leaving analysis as the most suitable method. A similar method selection approach was used for all system requirements. In addition to the verification method, the expected compliance is added to the last column, with red text implying non-compliance with the requirement.

Table 13.3: System requirements and Compliance for ADR satellite.

Requirement ID	**System Requirement**	**Method**	**Compliant?**
PERFORMANCE			
R-SYS-01	The ADR satellite shall determine the position and attitude of the target debris with an autonomy level of 4.	D	YES
R-SYS-02	The ADR satellite shall be able to approach the target to perform the mission.	D	YES
R-SYS-03	The ADR satellite shall be able to aim for the target to perform the mission.	D	YES
R-SYS-04	The ADR satellite shall be able to de-orbit the target.	D	YES
R-SYS-05	The ADR satellite shall be able to de-orbit at least 10 target satellites from the same orbit altitude and orbit plane in one year.	A	YES, 10 debris with 11th as margin
R-SYS-30	The spacecraft shall have a reliability of at least 95%.	A	NO, 90%
R-SYS-37	The spacecraft de-orbiting operation shall have a success rate of at least 95%.	A,T	TBD
R-SYS-38	The ADR spacecraft shall be capable of de-orbit a target satellite with a mass between 250–500 kg, operating in a circular LEO at an altitude between 550-630 km.	A	YES
OPERATION			
R-SYS-06	The ADR satellite shall be able to survive launch loads without any damage to its structure or payload.	A	YES
R-SYS-07	The ADR satellite shall be able to maintain its activity related to commands and communications throughout its operational life.	T	YES
R-SYS-08	The ADR satellite shall be able to survive thermal loads without any damage to its structure or instruments.	T	YES
R-SYS-09	The ADR satellite shall be able to maintain its orbit during its operational life.	A	YES
R-SYS-10	The ADR satellite shall be able to resist radiation without any significant damage to its structure and instruments.	T	YES
R-SYS-11	The ADR satellite shall not require any maintenance during its operational life of at least 1 year.	A	YES
R-SYS-31	The ADR satellite shall be able to operate within the LEO environmental conditions.	T	YES

---

[70] `https://www.nasa.gov/reference/5-3-product-verification/`

Requirement ID	System Requirement	Method	Compliant?
R-SYS-32	The spacecraft shall survive and remain fully functional when exposed to the expected LEO plasma environment.	T	YES
R-SYS-33	The spacecraft shall deliver sufficient power to sustain the seven modes: launch, startup, observe, prepare, operation, outer orbit and EoL during their operational time.	A	YES
R-SYS-36	The ADR mission shall have a combined Operation Success[71]rate of at least 92.5%.	A,T	TBD
R-SYS-39	The ADR spacecraft shall be capable of de-orbiting uncooperative satellites tumbling at a rate of up to 1 rpm about their principal axis.	A	YES, 1 rpm
SUSTAINABILITY			
R-SYS-12	The ADR spacecraft shall not generate any additional debris during its operations.	A	YES
R-SYS-14	The ADR satellite shall de-orbit within 5 years after EoL.	A	YES, within 3.6 years
R-SYS-15	The ADR satellite shall be able to perform its EoL de-orbit after failure within 5 years.	D	YES
R-SYS-17	Mission information shall be logged and made available publicly in compliance with international norms.	I	YES
R-SYS-18	The ADR satellite shall use non-toxic propellants.	I	YES
R-SYS-20	Transport packing shall be re-usable or recyclable (>80% by volume).	I	YES
R-SYS-21	Production of components exceeding 10 kg shall be localised to minimise intercontinental shipments and avoid reliance on air transport.	D	YES
R-SYS-40	The mission shall achieve at least a silver score in the sustainability index.	A	YES, platinum
R-SYS-34	During its de-orbiting phase, the debris and the ADR spacecraft shall maintain an ACPL below $1.0 \cdot 10^{-3}$ with trackable space objects larger than 1 cm.	A	YES, $3.22 \cdot 10^{-4}$
R-SYS-35	During its operational phase, the ADR shall maintain an ACPL below $1.0 \cdot 10^{-4}$ with space objects larger than 1 cm.	A	YES, $4.32 \cdot 10^{-6}$
LEGAL CONSTRAINTS AND REGULATIONS			
R-SYS-23	The mission shall be performed according to international space regulations and laws.	I	YES
R-SYS-24	The mission shall be performed according to Earth regulations and laws.	I	YES
R-SYS-25	The launch shall be conducted in accordance with the regulations of the country from which it is carried out.	I	YES
USER CONSTRAINTS			
R-SYS-26	The total mission cost, including manufacturing, testing, launch, and operations, shall be less than €100 million.	A	YES, €85 million
R-SYS-27	The ADR satellite shall be launched before 1 January 2030.	I	YES, end of 2029

---

[71] The same definition for Operation Succes was used as defined in Section 2.2

Subsystem Requirements.

From the system requirements, subsystem requirements were generated in the RDT and tabulated per subsystem. Table 13.5, Table 13.6, Table 13.7, Table 13.8, Table 13.9, Table 13.10 and Table 13.11 show these requirements for the ADCS, GN&C, Propulsion, C&DH, TT&C, Thermal, Structural and Electrical subsystem respectively. The approach for subsystem requirement verification is the same as for system requirements. A fitting verification method is chosen for each requirement from test, analysis, demonstration, and inspection.

Table 13.4: ADCS Subsystem Requirements.

Requirement ID	Subsystem Requirement	Method
R-SUB-ADC-05	The ADCS shall be able to rotate the spacecraft 90° on a single axis within 100 seconds.	D
R-SUB-ADC-07	The ADCS shall have a pointing accuracy better than ±0.5° (3σ) for a continuous duration of 300 seconds.	A
R-SUB-ADC-09	The ADCS shall have an attitude knowledge accuracy better than ±0.01° (3σ).	A
R-SUB-ADC-16	The ADCS shall be able to perform an exit manoeuvre of 10 metres within 200 seconds in the event of a thruster failure.	T
R-SUB-ADC-17	The ADCS shall be able to control its slew rate with an accuracy better than 0.1 deg/s (3σ).	A

Table 13.5: GN&C Subsystem Requirements.

Requirement ID	Subsystem Requirement	Method
R-SUB-ADC-01	The GN&C subsystem shall detect the target's presence within a range of 10 kilometres.	T
R-SUB-ADC-02	The GN&C subsystem shall know the relative position of the target with an accuracy better than ±0.1 metres at ranges up to 9 meters.	T
R-SUB-ADC-03	The GN&C subsystem shall track the relative attitude of the target with an accuracy better than ±5° (3σ) at ranges up to 1500 metres.	T
R-SUB-ADC-13	The GN&C subsystem shall be able to measure the relative velocity of the target with an accuracy of ±0.1 m/s (3σ) at ranges up to 9 metres.	T
R-SUB-ADC-14	The GN&C subsystem shall be able to measure the relative angular velocity of targets rotating up to 1 rpm.	A
R-SUB-ADC-18	The GN&C subsystem shall be able to determine the dynamic motion of the target while it is moving at a relative speed of up to 10 m/s.	T

Table 13.6: Propulsion Subsystem Requirements

Requirement ID	Subsystem Requirement	Method
R-SUB-ADC-06	The Propulsion subsystem shall ensure the satellite can maintain controlled positioning within 3-9m range from the debris with a positional accuracy of 10cm.	D
R-SUB-PRO-03	The propulsion subsystem shall be able to change orbital velocity by more than ±5 m/s while maintaining the spacecraft's orbital attitude	A
R-SUB-PRO-06	The propulsion subsystem shall avoid any additional space debris creation during the EoL manoeuvre.	A
R-SUB-PRO-09	The propulsion subsystem shall not make use of any toxic propellants.	I

Continued on next page

Requirement ID	Subsystem Requirement	Method
R-SUB-PRO-15	The propulsion subsystem shall have a specific impulse of more than 330 seconds	T
R-SUB-PRO-16	The propulsion subsystem shall have a plume expansion half-cone angle of under 15 degrees for the main thruster	T
R-SUB-PRO-17	The propulsion subsystem shall allow for bi-directional thrust vector control with a more than 10 degrees range in all directions.	T
R-SUB-PRO-18	The adverse thruster of the propulsion subsystem shall provide thrust of at least 50N.	T
R-SUB-PRO-19	The main thruster of the propulsion subsystem shall provide thrust of at least 400N.	T
R-SUB-PRO-20	The propulsion subsystem shall have a total burn-time of above 1000 seconds	T

Table 13.7: C&DH Subsystem Requirements.

Requirement ID	Subsystem Requirement	Method
R-SUB-CDH-01	The C&DH subsystem shall be able to communicate system status updates with the Ground Segment.	T
R-SUB-CDH-02	The C&DH subsystem shall be able to decode and verify incoming commands from the Ground Station.	T
R-SUB-CDH-03	All manoeuvres shall be logged and shared with international space traffic coordination bodies (e.g., ESA, CSpOC).	I
R-SUB-CDH-08	All manoeuvres shall be planned with international space traffic coordination bodies (e.g., ESA, CSpOC).	D
R-SUB-CDH-10	The C&DH subsystem shall be able to store LiDAR readings/imagery in Non-Volatile Memory.	D
R-SUB-CDH-11	The C&DH subsystem shall include a RAM buffer capable of supporting real-time transmission of infrared video, without loss of information due to buffer overflow.	T
R-SUB-CDH-12	The C&DH subsystem shall be able to correct Single Event Upsets (SEU's).	T

Table 13.8: TT&C Subsystem Requirements.

Requirement ID	Subsystem Requirement	Method
R-SUB-TTC-01	The ADR satellite shall communicate with ground operators via the ESA Estrack network.	D
R-SUB-TTC-04	Tracking and mission telemetry data shall be openly shared in compliance with international norms to support collaborative space sustainability.	D
R-SUB-TTC-11	The TT&C subsystem shall enable data of size 0.186GB to be downlinked once every two orbits.	T
R-SUB-TTC-12	The TT&C subsystem shall enable 76.8KB of data to be uplinked once every two orbits.	T
R-SUB-TTC-13	The TT&C subsystem shall be able to downlink 0.625MBps of data in real-time during operations.	T
R-SUB-TTC-14	The link budget shall have a margin of at least 3 dB.	A

Table 13.9: Thermal Subsystem Requirements.

Requirement ID	Subsystem Requirement	Method
R-SUB-THE-01	The thermal subsystem shall maintain the ADR satellite's components within their own operational temperature range.	A
R-SUB-THE-04	The thermal subsystem shall ensure component survival during all mission phases, including eclipse, safe mode, and launch environments.	A
R-SUB-THE-06	The thermal subsystem shall ensure component survival during temperature swings before and after eclipse.	T

Table 13.10: Structures Subsystem Requirements.

Requirement ID	Subsystem Requirement	Method
R-SUB-STR-01	The structures subsystem shall survive the longitudinal launch loads of up to 8.5 g.	T
R-SUB-STR-02	The structures subsystem shall survive the lateral launch loads of up to 3 g.	T
R-SUB-STR-03	The structures subsystem shall survive the longitudinal vibrations during launch from 5 Hz to 100 Hz and amplitudes of 1 g.	T
R-SUB-STR-04	The structures subsystem shall survive the lateral vibrations during launch from 5 Hz to 100 Hz and amplitudes of 1 g.	T
R-SUB-STR-08	The structures subsystem shall provide sufficient passive shielding to protect sensitive subsystems such that the internal radiation intensity does not exceed 1500 rad/year.	A
R-SUB-STR-10	The structures subsystem shall not be produced using toxic surface coating.	D
R-SUB-STR-11	The structures subsystem shall be produced using sustainably sourced materials.	I
R-SUB-STR-13	The structures subsystem shall ensure no damage is caused to the ADR satellite at deployment from the launch vehicle.	A
R-SUB-STR-15	The ADR spacecraft shall fit within the payload fairing of a single launch vehicle.	D
R-SUB-STR-16	The structures subsystem shall fit in a single transporting ground vehicle on Earth (e.g., truck).	D
R-SUB-STR-20	The structures subsystem shall sustain the axial buckling loads at launch.	A, T
R-SUB-STR-21	The structures subsystem shall sustain the lateral buckling loads at launch.	A, T
R-SUB-STR-22	The structures subsystem shall sustain bending loads induced during the launch.	A, T
R-SUB-STR-23	The structures subsystem shall provide mounting for the other subsystems.	D
R-SUB-STR-24	The structures subsystem shall survive acoustic loads during launch from 31.5 Hz to 10000 Hz with an overall sound pressure level of 137.9 dB.	T
R-SUB-STR-25	The structures subsystem shall survive random vibration loads during launch from 20 Hz to 2000 Hz with root mean square acceleration of 5.13 g.	T

Table 13.11: EPS Subsystem Requirements.

Requirement ID	Subsystem Requirement	Method
R-SUB-EPS-07	The EPS shall maintain all spacecraft surface potentials within ±50 V of the ambient plasma to prevent electrostatic discharge events.	T

Continued on next page

Table 13.11 – continued from previous page

Requirement ID	Subsystem Requirement	Method
R-SUB-EPS-08	The EPS batteries shall discharge 648 kJ to support one outer orbit – observe – prepare – operation cycle during eclipse, at the end of the mission.	T
R-SUB-EPS-09	The EPS solar panels shall generate at least 648 kJ in one daylight cycle.	T
R-SUB-EPS-11	The EPS shall provide regulated power within ±5% of nominal voltage levels to all spacecraft subsystems.	T
R-SUB-EPS-12	The EPS shall include overvoltage and overcurrent protection for all critical power buses.	D
R-SUB-EPS-13	The EPS shall provide at least one redundant power path for each subsystem.	A
R-SUB-EPS-15	The EPS shall provide telemetry data for battery state-of-charge, voltage, current and temperature.	D
R-SUB-EPS-16	The EPS shall point the solar panels such that the solar incidence angle is no larger than 15 degrees at any time.	T
R-SUB-EPS-17	The EPS shall provide the subsystems sufficient average power during a certain mission phase with their corresponding magnitude in Table 13.12.	A
R-SUB-EPS-18	The EPS shall provide the different subsystem components with set voltages ranging between 3.3 V and 28 V.	D

Table 13.12: Power Requirements per Subsystem per Mission Phase in Watts.

	Launch	Startup	Observe	Prepare	De-Orbit Op	Outer Orbit	EoL
ADCS	25.9	105.3	64.9	96.1	163.3	51.5	31.1
GNC	1.6	47.8	12.9	110.1	83.9	12.9	11.7
Propulsion	0.0	9.0	0.0	22.5	60.0	4.5	0.0
Structures	0.0	0.0	0.0	0.0	0.0	0.0	0.0
Thermal	0.0	0.0	0.0	0.0	0.0	0.0	0.0
TT&C	7.0	70.0	71.2	71.2	71.2	82.4	70.0
C&DH	31.0	31.0	31.0	31.0	31.0	31.0	19.0
EPS	0.5	70.5	5.5	5.5	0.5	5.5	1.5

Verification Plan

This subsection contains a general plan on how to verify the user, system and subsystem requirements per verification method. They can be applied for each requirement but will have to be specified in more depth every time.

Testing

Testing will be conducted on both subsystem and system levels to verify functional and performance requirements under simulated operational conditions. Environmental tests (i.e. vibrations, vacuum, radiation) will ensure the spacecraft endures launch and orbit conditions. Functional tests will verify the operating capabilities of ADCS, propulsion, GNC, communications systems and other subsystems. Lastly, ground-based vacuum tests will simulate a full debris momentum transfer operation. All test procedures will follow industry standards.

Inspection

Inspection of the requirements focuses primarily on compliance with legal, regulatory and sustainability requirements. All mission documentation will be reviewed to verify adherence to international space regulations and national laws relevant to the orbital operations that will be performed. Inspections from a third party will ensure that the mission complies with regulations of the country of production and launch. The use of non-toxic propellants will be confirmed through supplier documentation and chemical safety assessments. Inspection will also verify that mission data is logged and made publicly available in accordance with transparency and sustainability standards. Additionally, timeline compliance such as the requirement to launch before 1 January 2030 will be verified by using project schedules and milestone reviews.

Demonstration
Demonstration will be used to verify system capabilities through observable, functional performance in realistic conditions. This includes verifying the spacecraft's ability to navigate, align, and operate near the target debris, as well as execute the de-orbiting manoeuvre. The functional subsystem requirements will be demonstrated individually and within integrated simulations. Mission autonomy, safety protocols and compliance with space traffic coordination procedures will be shown in simulated operational scenarios. Demonstration will also support verification of sustainability elements, such as local production practices and modular structural integration.

Analysis
Analysis is and will be used to verify performance, margins and compliance where direct testing is impractical or not financially viable. Thermal, structural and orbital simulations will verify the performance across worst-case scenarios of the ADR satellite. Computational tools like Python, MATLAB, GMAT and DRAMA will have to be used for modelling and simulation. Reliability analysis will assess mission lifetime and redundancy. Mass and power budgets will be confirmed against the requirements with Excel.

13.4 Code Verification

In order to analyse certain aspects of the active debris removal satellite, Python code was written to model interactions and mechanics. This code on operational procedure, efficiency and load analysis was verified and can be accessed through the Starfixers Inc. GitHub Repository. This procedure will be explained in the next subsections, and the results are tabulated in the corresponding tables.

Momentum Transfer Efficiency Code

The momentum transfer efficiency code (efficiency.py) was verified by first proofreading the code. This was done by someone who did not write the code. During proofreading, all the possible mistakes were eliminated and changed to the correct code. Afterwards, multiple boundary case variables were tested, which are noted below in Table 13.13.

Table 13.13: Test Summary for Momentum Transfer Code Verification.

Test ID	Component/Function	Action	Pass/ Fail	Tool and Comments
1.1	**calculate_efficiency_rect()**	Check zero efficiency at zero debris size	Pass	Visual check by changing area to zero and looking at graph
1.2	**calculate_efficiency_rect()**	Check constant efficiency for different distances at infinite debris size	Pass	Visual check by changing area to 10^6 m^2 and looking at graph
2.1	**calculate_efficiency_rect()**	Check zero efficiency at infinite plume expansion	Pass	Visual check by setting half cone angle at 90 degrees and looking at graph
2.2	**calculate_efficiency_rect()**	Check constant efficiency for no plume expansion	Pass	Visual check by setting half cone angle at 0 degrees and looking at graph
3.1	**calculate_efficiency_rect()**	Check zero efficiency at very high distance and non-infinity debris size	Pass	Visual check by looking at graph and seeing whether it converges to zero

Test ID	Component/Function	Action	Pass/ Fail	Tool and Comments
3.2	**calculate_efficiency_rect()**	Check constant efficiency for infinitesimal distance and different plume expansion	Pass	Visual check by plotting different half cone angles and zooming in to near zero values
4	**General Operation**	Proofreading the code	Pass	Manual check by going through each line and checking whether the right code is written

Operational Procedure Code

Since the momentum transfer code was verified, a constant value of $\eta = 0.2$ will be assumed to verify the other functions of the operational procedure code (General_case_orbital.py). First, the functions used in the code are verified, then the general procedure is verified. These tests can be run through Unit_testing_general.py.

Table 13.14: Test Summary for Component Validation.

Test ID	Component/Function	Action	Pass/ Fail	Tool and Comments
1	**Optvro()**	Check correct calculation of needed relative velocity	Pass	Assert with random input using DESMOS
2	**sr()**	Check relative distance as a function of time	Pass	Assert with random input using DESMOS
3.1	**TimeUnderdistm()**	Check time under a certain relative distance	Pass	Assert with random input using DESMOS
3.2	**TimeUnderdistm()**	Check no time is returned if the distance is not crossed	Pass	Assert $t = 0$
4.1	**calculate_DV_debris()**	Check ΔV applied to debris	Pass	Assert with hand calculation
4.2	**calculate_DV_debris()**	Check no momentum transfer if `TimeUnderdistm()` is none	Pass	Assert $\Delta V = 0$
4.3	**calculate_DV_debris()**	Check no momentum transfer if $\eta = 0$	Pass	Assert $\Delta V = 0$
5.1	**twoorbit()**	Check value for semi-major axis	Pass	Assert with online tool [72]
5.2	**twoorbit()**	Check value for orbital period	Pass	Assert with online tool [72]
5.3	**twoorbit()**	Check sign of ΔV if $V_{\text{debris}} < V_{\text{ADR}}$	Pass	Assert $\Delta V > 0$ for rendezvous
6.1	**General Operation**	Check for mass decrease after each manoeuvre	Pass	Assert $M_i < M_{i-1}$
6.2	**General Operation**	Check mass never drops below M_{dry}	Pass	Assert $M_i > M_{\text{dry}}$
6.3	**General Operation**	Check perigee altitude never goes below 380 km	Pass	Assert $a_m < 6861.5$ km
6.4	**General Operation**	Check ΔV signs	Pass	Assert $\Delta V > 0$

In addition, Figure 3.16a, showing the perigees and apogees altitudes of the ADR throughout the mission, is used as a verification tool for the operational procedure, that is, that the Operational Procedure Code follows the same sequential operation as displayed in Figure 3.7.

Load Analysis code

Table 13.15 summarises the tests that were performed on the load analysis code (Load_analysis.py), containing the results of the static and dynamic loading analysis. The tests can be run using Unit_testing_structures.py.

Table 13.15: Test Summary for Structural Analysis Code Verification.

Test ID	Component/Function	Action	Pass/ Fail	Tool and Comments
1	**bending_stress_at_x()**	Check bending displacement at fixed end is 0	Pass	Assert displacement == 0
2	**omega_stringer()**	Check buckling stress is the same if stiffener thickness is zero	Pass	Assert buckling stress is bare wall buckling stress
3	**pipe_stringer()**	Check effective sheet width barely changes with small tanks	Pass	Assert no significant change in buckling stress
4.1	**Dynamic load simulation**	Check for higher amplitude if higher g enforced on the system	Pass	Assert $max_{\text{displacement1}} < max_{\text{displacement2}}$
4.2	**Dynamic load simulation**	Check response for changing forcing frequency	Pass	Visual check on plots
4.3	**Dynamic load simulation**	Check response for changing damping coefficient	Pass	Visual check on plots

13.5 Validation

During validation, engineers ensure that the right product was built for the given objective. This is often done by comparing it with other missions, building prototypes or by demonstration. In the first subsection, the momentum transfer efficiency model was validated by comparing it with the literature. In the second subsection, a spacecraft validation plan is written. Due to the limited scope of the project, the complete spacecraft can not be validated yet, but a plan has been devised on how to do it with resource constraints.

Momentum Transfer Efficiency Model

A very important parameter when modelling the performance of the spacecraft is the momentum transfer efficiency. Hence, it is imperative to validate the model by comparing it to the literature. This was done by using the same input parameters as the paper written on space debris orbit modification using chemical propulsion shepherding by T. Peters [12]. The space debris frontal shape was set to a rectangle of 0.4 m by 0.4 m. The tested half cone angles were 15 degrees and 40 degrees, both for half and for full specularity. This is done by decreasing the AC. Figure 13.5a shows the momentum transfer efficiency that was used in the ESA paper. Figure 13.5b shows the efficiency that was used for the spacecraft model of this report. It can be seen that graphs of the 15-degree half-cone angle match up almost perfectly. Those of 40 degrees are a bit lower than in the paper, but still follow the same shape. Since a 15-degree half-cone angle is used, the efficiency model can be considered validated.

---

[72] `https://www.calctree.com/templates/orbits`

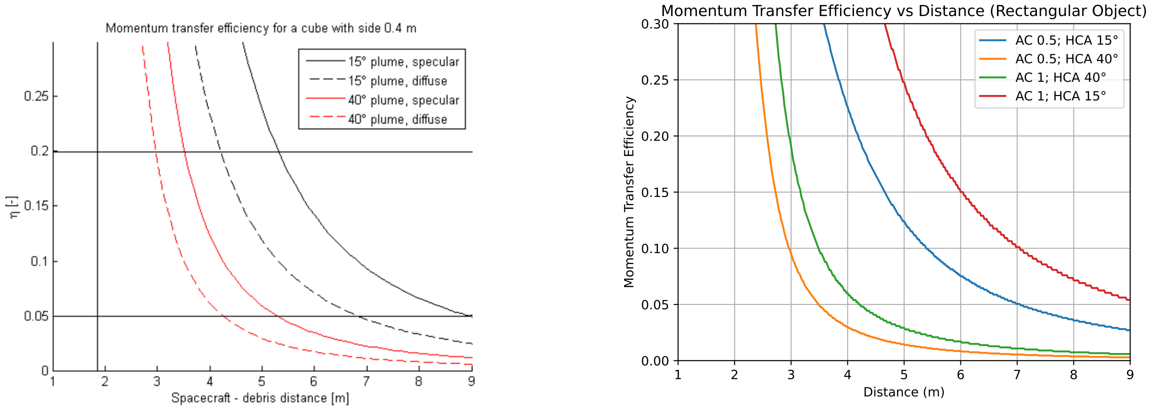

(a) Momentum Transfer Efficiency as a Function of Distance by Peters T. [12]

(b) Momentum Transfer Efficiency as a Function of Distance for a Rectangle of 0.4 m × 0.4 m According to the Model.

Figure 13.5: Validation of Efficiency Models.

Spacecraft Validation

In conceptual design, it is not possible to validate the complete spacecraft already. However, it is possible to propose a high-level validation plan. This will contain the recommended steps that have to be taken to ensure that the spacecraft is built for the right purpose. It is proposed to launch a separate demonstrator mission with a prototype to demonstrate the feasibility of the plume impingement method that the Starfixers satellite will use. This mission would involve 2 smaller CubeSats with similar relative masses and dimensions as the Starfixers and the Starlink satellites. The mission would aim to validate the momentum transfer method, attitude and controllability effects of the manoeuvres in a microgravity environment. Additional validation steps may include Finite Element Method structural simulation, computational fluid dynamics simulations to model the plume behaviour, testing of thruster control systems, and ground-based vacuum chamber experiments to validate the interaction dynamics. Together, these steps would provide a solid foundation for validation of the conceptual design before progressing to full-scale development.

13.6 Sensitivity Analysis

One of the key characteristics of the ADR spacecraft is its scalability. It is very important for having future economic benefit that the ADR can be easily and cheaply adapted. This section explores the extent to which the spacecraft should be changed to do so. In particular, the section will analyse the design sensitivity to debris mass and orbit, time constraints, number of targets and ACPL. Other, more specific sensivity studies have been conducted during subsystem design, such as GN&C (chapter 5) and Propulsion (chapter 7). These are included in those chapters as they were driving the design of the specific subsystem.

Target debris

Requirement [R-SUB-PAY-03] defines target altitudes of 550–630km and debris masses of 250–500kg. Using Figure 3.18, the corresponding perigee altitudes were calculated, as shown in Table 13.16.

Table 13.16: ADR Spacecraft Mass and ΔV to Apply for Each Debris for Various Debris Combinations, the Spacecraft Designed in This Report is Indicated in Bold.

Debris combination (mass [kg], altitude [km])	ADR mass [kg]	Delta V applied per debris [m/s]
250kg, 550km	407	41.12
260kg, 600km	**646**	**60.58**
500kg, 550km	732	53.26
250kg, 630km	756	70.57
500kg, 630km	1082	81.35

Time constraint

One of the driving requirements of the ADR design has been **[R-SYS-05]**. The time constraint of 1 year and the number of debris to de-orbit has greatly affected the current ADR design, but these could be altered depending on the mission and clients. To explore how it could affect the design, various cases were considered, ranging from half a year mission time to 4 years, where the debris de-orbits on its own without need for an ADR mission. The results are summarised in Table 13.17:

Table 13.17: Change of **[R-SYS-05]** Results Summary, Unchanged Case in Bold.

Mission duration requirement [years]	De-orbit time [months]	Perigee final altitude [km]	ΔV transferred to each debris [m/s]	ADR mass [kg]
0.5	2.7	320	77.31	820
1	**10.2**	**381**	**60.58**	**646**
2	22	440	44.02	410
3	34	505	25.98	260
4	46	600	0	0

Number of debris

Again, for the case of de-orbiting Starlink satellites at 600km altitude within one year, the results displayed in Table 13.18 are obtained for the change in mass ADR due to the change in the number of debris to de-orbit:

Table 13.18: Sensitivity Analysis on Debris Number Results, Original Number in Bold.

#Debris	ADR mass [kg]	Operation time [days]
2	200	7.37
5	330	18.01
7	450	27.56
10	**646**	**37.42**
15	1130	58.28
20	1920	65.43

ACPL

Another change that should be taken into account is imposing a higher restriction on the requirements of ACPL, **[R-SYS-34]** and **[R-SYS-38]**, as regulation in this area is likely to become more stringent in the coming years. Using the results from Table 3.6, the collision probability during operation is $4.32 \cdot 10^{-6}$, however, companies such as Starlink are beginning to aim for an ACPL during operation of 10^{-6} [89], so it is probable that such a number will become a standard to be fulfilled. In addition, the expected increase in debris population will increase the collision probability as well. For this reason, collision avoidance manoeuvres will likely have to be analysed in detail for the operation, which has not been done for this report as **[R-SYS-38]** was fulfilled. The ADR spacecraft during EoL satisfies **[R-SYS-34]** by a factor of 3, so if the ACPL for EoL was reduced by a significant amount due to stricter regulations, or if debris population grew considerably, **[R-SYS-34]** may not be fulfilled. Then, more complex collision avoidance manoeuvres would have to be carried out by the ADR. The effect of stricter ACPL for the debris is not considered, as the selected de-orbiting approach does not alter the debris area and therefore, the mission has no effect on the debris's ACPL during operation.

14 Future Development

This chapter explains key elements critical to the successful future development of the ADR satellite. Section 14.1 presents the RAMS characteristics, detailing the system's reliability, availability, maintainability and safety considerations. Section 14.2 describes the Manufacturing, Assembly, and Integration Plan, focusing on the processes and strategies necessary to build and assemble the satellite components. Section 14.3 and Section 14.4 explain the post-DSE Gantt chart and the Project Design and Development Logic, providing insight into the approach taken to guide the satellite's technical development after this project.

14.1 RAMS Characteristics

This chapter discusses the RAMS (Reliability, Availability, Maintainability, and Safety) analysis of the Starfixers satellite. It begins with reliability, assessing the likelihood that the spacecraft will complete its mission without failure. Subsystems are analysed using failure rate models, with special focus on mission-critical areas such as propulsion, GNC, and ADCS. Maintainability is then addressed, highlighting the system's ability to detect, isolate, and recover from faults autonomously, as in-orbit servicing is not possible. Availability is evaluated by combining reliability and maintainability to ensure the spacecraft remains functional when needed. Finally, safety is discussed through hazard identification and mitigation strategies that ensure spacecraft integrity, mission success, and environmental protection throughout all phases of the mission.

Reliability

Reliability is defined as the probability that a system performs its intended function without failure under stated conditions for a specified period [48]. For the Starfixers mission, this means successfully performing ten ADR operations over a one-year mission. The mission-level reliability requirements relevant to this analysis are **[R-SYS-30]**.

To verify compliance, the reliability of each subsystem is modelled using the exponential failure law, assuming a constant failure rate throughout the mission. This assumption is valid for space missions within their operational life, where wear-out failures are minimal. The exponential model is described in Equation 14.1, where λ is the failure rate and t is time in years [48].

$$R(t) = e^{-\lambda t} \tag{14.1}$$

For the analysis, the spacecraft is modelled as a system with some subsystems in series and others in parallel. This makes use of Equation 14.2 for series, where the failure of any single subsystem results in overall mission failure.

$$R_{\text{total}} = \prod_{i=1}^{n} R_i \tag{14.2}$$

Additionally, when modelled as parallel due to redundancy, the system reliability is calculated using Equation 14.3.

$$R = 1 - \prod_{i=1}^{n} (1 - R_i) \tag{14.3}$$

This methodology was applied at the subsystem level, beginning with the propulsion subsystem, which was analyzed in full detail as seen in Figure 14.1. The propulsion system was broken down into five major functional branches: the gimbal, main thruster, tanks system, adverse thruster, and feed system. These were modelled in series, meaning all must function for successful detumbling and debris deorbiting.

Each subsystem block was further decomposed into components and, where applicable, subcomponents. Component reliability values were calculated from mean time between failures (MTBF) available in manufacturer datasheets and literature. For each component, the failure rate was calculated as $\lambda = \frac{1}{\text{MTBF}}$, and the 37-day or 888-hour long mission reliability was calculated using Equation 14.1.

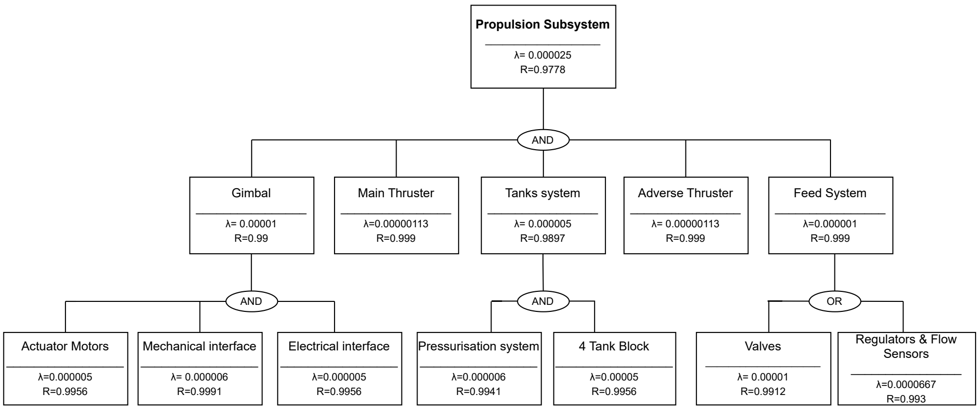

Figure 14.1: Propulsion Subsystem Reliability Tree.

Looking deeper into this, for the gimbal, it was modelled as a combination of actuator motors, a mechanical interface, and an electrical interface, all in series. Each subcomponent had its own MTBF based on typical values for space-rated electromechanical parts, [23][70] and their combined reliability over 888 hours was approximately $R_{\text{gimbal}} = 0.99$.

The main and adverse thrusters, although still under development, are assumed to be designed, qualified, and verified to achieve a high reliability target of $R = 0.999$, corresponding to a failure rate of approximately $\lambda \approx 1.13 \times 10^{-6}$ failures/hour. This level of reliability is essential given the propulsion system's critical role in detumbling and deorbiting. Similar performance has been demonstrated in previous missions such as PRISMA and BIROS, where precise thrust execution and system resilience were mission-enabling [10, 25].

The tank system was modelled as a series of two critical elements: the pressurisation system and the 4-tank block. Since both are necessary to deliver usable propellant, they were modelled in series. The pressurisation system, comprising regulators and valves, was assigned a MTBF of 150,000 hours [72] leading to a reliability of $R = 0.9941$. The tank block, consisting of four tanks, was similarly modelled with a MTBF of 200,000 hours, [101] and a reliability of $R = 0.9956$. Combined, this gave a tank subsystem reliability of $R_{\text{tanks}} = 0.9897$.

The feed system was modelled with an OR gate between two functionally independent paths: one using isolation valves and the other using a regulator and flow sensor path. This configuration assumes that either path is sufficient to allow minimal thrusting in degraded mode [81]. The valve branch had a reliability of R = 0.9912 and the sensor branch R = 0.993 [31]. The resulting feed system reliability was calculated using Equation 14.3 and found to be R = 0.9999.

Multiplying all five top-level component reliabilities in series: $R_{\text{propulsion}} = 0.99 \times 0.999 \times 0.9897 \times 0.999 \times 0.9999 = 0.9778$. This result reflects a realistic and justified subsystem reliability for a short-duration ADR mission with moderate redundancy and robust heritage components.

The same modelling process was applied to the remaining spacecraft subsystems. While not represented visually through fault trees like it was done for the propulsion subsystem, these calculations were performed in a similar fashion resulting in the reliability values as summarised in Table 14.1.

Subsystem	Reliability (1-year)
GNC	0.9908
ADCS	0.9892
TT&C	0.9878
C&DH	0.9810
EPS	0.9862
Propulsion	0.9798
Structures and Thermal	0.9880

Table 14.1: Subsystem Reliability Allocation for One-year Mission Duration.

The GN&C subsystem was modelled using realistic assumptions for heritage components and available datasheet values. The lidar system was modelled with two Jena Optronik RVS3000-3D units in parallel, each assumed to have a MTBF of 50,000 hours [43], resulting in a 37-day reliability of $R = 0.9824$ per unit and a combined OR-reliability of $R = 0.9997$. The infrared camera, based on the ECAM-IR3A model, was considered more susceptible to radiation and thermal effects and was thus assigned a conservative MTBF of 40,000 hours [82], with four units in parallel yielding a system-level reliability of $R = 0.9999$. The GNSS receiver (NaviLEO POD), considered a single point of failure, was modelled with a MTBF of 100,000 hours [90], giving a reliability of $R = 0.9912$. The passive GNSS patch antennas (ISIS) were modelled as two redundant units in parallel, each with a MTBF of 200,000 hours [58], yielding a combined reliability of $R = 0.9998$. Taken together, these components give the GN&C subsystem an overall series reliability of $R_{\text{GNC}} \approx 0.9908$, in line with expected values for short-duration missions where limited redundancy is feasible.

The ADCS subsystem was modelled with a combination of actuators and sensors with partial redundancy. The cold gas actuation system included eight Moog 58E163A thrusters, each with a MTBF of 200,000 hours [53]. Assuming at least three functioning thrusters are sufficient for full-axis control, the system was modelled as a 3-out-of-8 configuration, yielding a reliability of $R = 0.9999$ over 37 days. Reaction wheel actuation was handled by four Sinclair Interplanetary Libra-6 units, each with a conservative MTBF of 60,000 hours [55], modelled using a 2-out-of-4 configuration that tolerated one failure and gave a system-level reliability of $R = 0.9999$. The star tracker system used two ST16-RT2 units, each assumed to have a MTBF of 80,000 hours [83], and modelled in parallel, resulting in a combined reliability of $R = 0.9998$. The inertial measurement unit was modelled using two STIM318 high-grade MEMS IMUs with MTBFs of 100,000 hours [26], resulting in $R = 0.9992$. The Aquila-H01 sun sensors, with four units and a MTBF of 150,000 hours each [24], were modelled in parallel, resulting in a reliability of $R = 0.9999$. These values collectively yielded an overall ADCS subsystem reliability of $R_{\text{ADCS}} \approx 0.9892$.

The TT&C subsystem comprises two key components: a single S-band dual patch antenna and a KaPDA-Gimbal system for directional communication. Both are single points of failure and therefore modelled in series. The S-band antenna, being passive and space-proven, was assigned a MTBF of 250,000 hours [57], resulting in a 37-day reliability of 0.9965. The KaPDA-Gimbal, a more complex electromechanical unit involving moving parts, was assigned a MTBF of 100,000 hours [59], yielding a reliability of 0.9912. TT&C subsystem reliability was thus calculated as: $R_{\text{TT\&C}} = 0.9965 \times 0.9912 = 0.9878$.

The command and data handling (C&DH) subsystem consists of five essential electronic components, all modelled in series due to their critical roles in maintaining onboard control, data processing, and telemetry communication. The radiation-tolerant NAND flash was assigned a MTBF of 500,000 hours [1], giving a 37-day reliability of 0.9982, while the SRAM was modelled with 400,000 hours [2] ($R = 0.9978$). The onboard computer, based on the OBC-15, was assigned 300,000 hours [7] ($R = 0.9971$), and the MCSE monitoring electronics 250,000 hours [69] ($R = 0.9965$). Finally, five LVDS interfaces were included with a MTBF of 500,000 hours each [1], resulting in a combined reliability of $R = 0.9911$. The overall subsystem reliability was $R_{\text{C\&DH}} = 0.9982 \times 0.9978 \times 0.9971 \times 0.9965 \times 0.9911 = 0.9810$.

The electrical power subsystem (EPS) consists of QJ 4G32C solar cells, Li-ion 18500 battery cells, a PCU-110 power control unit, wiring harness, and two 650 MPPT peak power trackers. Partial redundancy was assumed for the energy sources, requiring only 304 out of 608 solar cells and 28 out of 56 batteries to operate nominally. Based on manufacturer data, the solar cells were assigned a MTBF of 250,000 hours [84], giving a 37-day reliability of $R = 0.9999$, while the batteries were modelled with 100,000 hours [77] ($R = 0.9975$). The PCU-110, handling energy conversion and distribution, was assigned a MTBF of 150,000 hours [56] ($R = 0.9941$), and the wiring 200,000 hours [49] ($R = 0.9956$). The MPPT controllers, arranged in an OR configuration, were each given 150,000 hours MTBF [95], resulting in $R = 0.99996$. The total subsystem reliability for the 37-day mission is thus: $R_{\text{EPS}} = 0.99999 \times 0.9975 \times 0.9941 \times 0.9956 \times 0.99996 = 0.9862$.

The Structures and Thermal subsystem includes the CubeShell structure, solar panel substrate, and multi-layer insulation (MLI). As all components are passive and non-electronic, they were assumed to possess high inherent reliability. The CubeShell and substrate were each assigned mean times between failure (MTBF) exceeding 500,000 hours [87, 46], based on the use of aerospace-grade aluminium alloys. In contrast, the MLI, exposed to thermal cycling and atomic oxygen, was modelled with a MTBF of 100,000 hours [44]. All elements were modelled in series, resulting in 37-day reliabilities of $R_{\text{structure}} = 0.997$ and $R_{\text{thermal}} = 0.991$, giving an overall reliability of $R_{\text{Structures+Thermal}} = 0.997 \times 0.991 = 0.988$.This value is consistent with the passive nature of the design and reflects the minor degradation expected in thermal performance during a short-duration mission.

Substituting these values into the series model yields an initial system-level reliability of 90.5%, as seen in Equation 14.4.

$$R_{\text{total}} = 0.9908 \times 0.9892 \times 0.9878 \times 0.9810 \times 0.9862 \times 0.9798 \times 0.9880 = 0.905 \tag{14.4}$$

Although the calculated overall spacecraft reliability of $R_{\text{total}} = 0.905$ falls below the target threshold of 95%, it is well-aligned with industry norms for short-duration active debris removal missions. Comparable CubeSat and small-satellite missions with durations under three months frequently report system-level reliabilities between 85–92% [59, 41], particularly when full system redundancy is limited by constraints on budget, integration time, and complexity. Achieving a higher reliability value would require substantial additional investment in redundant hardware and radiation-hardened components, increasing design complexity and imposing stricter development requirements. The current reliability reflects a deliberate and realistic trade-off between performance and affordability with critical subsystems such as ADCS, EPS, and GNC already including targeted redundancy, ensuring fault tolerance. As such, the design offers an efficient solution that aligns with expectations for first-generation ADR missions and provides a high probability of mission success within the given budget.

Maintainability

Maintainability is the ability of a system to be restored to full functionality with minimal time, cost, and effort. For Starfixers, a non-serviceable spacecraft, maintainability must be inherently embedded in the system architecture, through pre-launch precautions and autonomous in-mission fault handling. Since traditional servicing is infeasible, Starfixers applies two forms of maintainability: preventive (pre-launch) and corrective (onboard), as displayed in Figure 14.2.

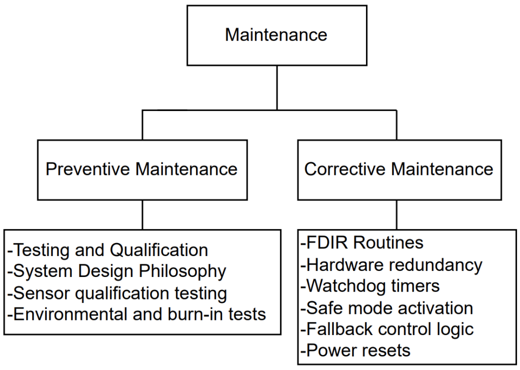

Figure 14.2: Maintenance Policies.

Preventive maintenance is aimed at reducing the likelihood of failures before they occur [48]. This is achieved through rigorous environmental testing, such as thermal-vacuum, vibration, and shock qualification, to ensure that all components can withstand the harsh conditions of launch and space [59]. Additional procedures like burn-in screening are employed to detect early-life failures, while electrical and thermal derating strategies are applied to reduce component stress and extend operational lifetimes. To further increase system reliability, components with high MTBF were selected for all critical subsystems [27]. The spacecraft architecture also prioritises fault isolation, enabling localised failures without affecting overall mission functionality. Redundancy and margin sizing are strategically implemented in several subsystems such as the GNC and EPS, reducing the reliance on post-failure interventions.

Corrective maintenance is managed entirely by onboard systems through autonomous FDIR routines [59]. These continuously monitor performance, detect anomalies, and initiate predefined corrective actions. Watchdog timers are used to identify software hangs and trigger safe power resets, while safe-mode procedures ensure the spacecraft enters a low-power, stable state when serious faults are detected. In degraded scenarios, fallback logic enables the reassignment of functionality, such as switching to backup sensors or alternate control paths, ensuring continued operation. Redundancy is leveraged not only for fault tolerance but also for automatic recovery, allowing the spacecraft to respond quickly and independently to unforeseen events.

Although Starfixers does not have a formal maintainability requirement, the one-year autonomous profile imposes strict constraints: uninterrupted functionality and immediate fault recovery. As a result, subsystem-specific design features were introduced, such as modular electronics, dual-core C&DH processors with autonomous reboot logic, and GNC sensor fusion using triple-redundant LiDAR, VSS, IMU, and GNSS.

To evaluate the effectiveness of the maintainability strategy implemented in Starfixers, subsystem-level metrics were conceptually applied. These include Mean Time to Repair (MTTR), Mean Down Time (MDT), and Mean Time Between Maintenance (MTBM). Since Starfixers is a fully autonomous spacecraft with no logistics or human intervention post-launch, MTTR is governed by internal response times, typically seconds to a few minutes, while MDT is considered equal to MTTR. [48]. The table below summarises the estimated MTTR and conceptually assigned MTBM values per subsystem, highlighting the spacecraft's readiness for continuous operation over the mission duration.

Table 14.2: Estimated MTTR and MTBM Values by Subsystem.

Subsystem	MTTR (hrs)	MTBM (hrs)
GNC	0.01	5000
ADCS	0.02	4000
TT&C	0.05	3500
C&DH	0.02	4000
Power	0	6000
Propulsion	0.03	4200

The Mean Time To Repair (MTTR) and Mean Time Between Maintenance (MTBM) values shown in Table 14.2 were estimated based on the architecture and fault management strategy of each subsystem. For the GNC subsystem, a MTTR of 0.01 hours (36 seconds) is assumed, reflecting the near-instantaneous response enabled by redundant sensors and onboard sensor fusion algorithms [22, 48]. Its relatively low exposure to mechanical wear or harsh thermal cycling justifies a MTBM of 5000 hours, in line with ESA CubeSat GNC hardware reports [41]. The ADCS has a MTTR of 0.02 hours, which accounts for rapid reconfiguration via fallback logic, such as reaction wheel isolation or magnetorquer activation, common in modern small satellite ADCS systems [59].Given its continuous use and exposure to external torques, a MTBM of 4000 hours is considered realistic. For TT&C, which relies on fallback links and reconnection protocols; the assumed MTTR of 0.05 hours reflects the expected delay in re-establishing a link using automated fallback protocols. With limited duty cycles and simple operation modes, a MTBM of 3500 hours is realistic for commercial space-rated transceivers [99]. The C&DH system employs dual-core redundancy with watchdog-driven reboot routines. Upon detection of an anomaly, control is switched or restored autonomously within approximately 2 minutes, resulting in a MTTR of 0.02 hours. Based on redundancy in logic and heritage on-board computers like the OBC-15, a MTBM of 4000 hours was assumed [78, 8]. The power subsystem was designed with high-reliability margining, derated components, and passive design, enabling it to operate without expected need for repair. Thus, its MTTR was set to zero, and the MTBM estimated at 6000 hours so that it is consistent with proven reliability of the EPS architectures [86]. For the propulsion system, a

MTTR of 0.03 hours was assumed, reflecting the time for automatic fault detection and switchover between main and adverse thruster paths or gimbals [48, 54]. The MTBM of 4200 hours reflects accumulated firing cycles over the mission, based on thruster cycle life data from missions such as DLR's BIROS [10]. Finally, structural and thermal subsystems, being passive and non-repairable in orbit, were assigned a MTTR equal to the mission duration (8760 hours). Their MTBM was likewise set to 8760 hours, reflecting that no active maintenance is expected during the mission lifetime.

These values demonstrate the maintainability and fault resilience engineered into each subsystem, supporting Starfixers' autonomous mission objectives and maximizing system availability over its full operational lifetime.

Availability

Availability is defined as the probability that a system is functioning and ready to perform its intended task when required.[48] For the autonomous one-year Starfixers mission, availability is a critical performance measure. It reflects the combined influence of how often a system fails (reliability) and how quickly it recovers (maintainability), and is thus a direct result of both.

While three forms of availability exist: Inherent (A_i), Achieved (A_a), and Operational (A_o) they converge in this context, since Starfixers performs no in-orbit scheduled maintenance and faces no logistic delays. Availability is therefore computed using the simplified expression $A = \frac{\text{MTBM}}{\text{MTBM+MTTR}}$.This equation mirrors the more common reliability-based form $A = \frac{\text{MTBF}}{\text{MTBF+MTTR}}$, since in autonomous systems without repair intervention, MTBF and Mean Time To Failure are equivalent, and MTBM ≈ MTBF.[48]

Using the subsystem MTTR and MTBM values previously defined, availability was calculated and summarised in Table 14.3.

Table 14.3: Estimated Availability per Subsystem.

Subsystem	**Availability** A
GN&C	0.9999
ADCS	0.9999
TT&C	0.9985
C&DH	0.9999
Power	1.000
Propulsion	0.9999
Structures and Thermal	0.406

These values confirm that Starfixers maintains extremely high availability across all mission-critical systems. The only exception is the structural/thermal subsystem, which is non-recoverable upon failure. However, given its low risk of failure and criticality-driven design margins, its impact on total system availability remains contained.

In conclusion, Starfixers achieves continuous functional availability through integrated reliability and autonomous maintainability. With no external repair possible, the system's ability to sustain operation with minimal downtime is both essential and validated by subsystem-level performance metrics.

Safety

Safety in the Starfixers mission is defined as the absence of hazards that may compromise spacecraft integrity, mission success, nearby orbital assets, or the surrounding environment.[48] Due to the autonomous and uncrewed nature of the spacecraft, combined with the complexity of close-proximity operations, safety must be addressed from both a design and operational perspective.

Initial system-level risks were identified using the Bow-Tie risk diagram Figure 4.3, which outlines failure pathways, from initiating causes to consequences, while mapping out preventive and recovery barriers. These risks were further refined using RAMS methodologies to support a robust safety architecture [48]:

- **Failure Modes, Effects and Criticality Analysis** was applied to components and subsystems such as propulsion and GNC. Each potential failure mode was assessed for likelihood and severity, and corresponding mitigation strategies were identified. This analysis enabled the design of redundancy paths or fallback logic to prevent mission compromise.

- **Common Mode and Common Cause Analysis** ensured that redundant systems, such as IMU, LiDAR, and VSS, cannot be simultaneously disabled by shared vulnerabilities like thermal exposure, or bus failure. Countermeasures include spatial separation, power decoupling, and shielding.
- **Operational Hazard Analysis** addressed critical mission phases like rendezvous and detumbling. The system was analysed for vulnerable transitions where re-initialization protocols, must be triggered to prevent the fault from building up.

To illustrate the application of this framework, Figure 14.3 presents a mitigation chain for a representative hazard: debris misalignment. The event sequence progresses through uncontrolled tumble and plume impingement, which may lead to structural damage and ultimately mission failure. Each row represents a fault propagation stage, while the right-hand side shows the corresponding preventive or corrective interventions:

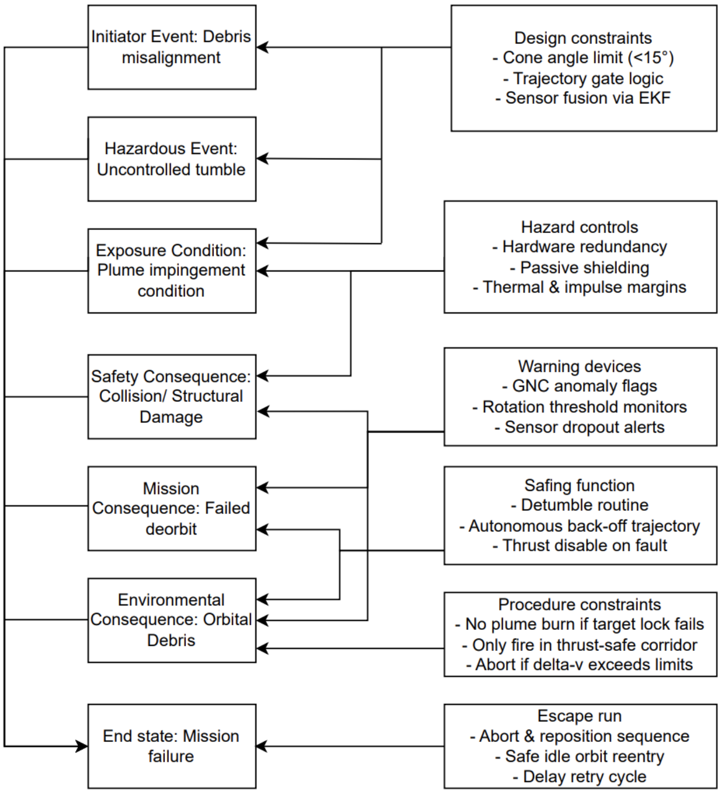

Figure 14.3: Hazard Mitigation Sequence With Intervention Points Across the RAMS Chain.

- **Initiator Event: Debris misalignment**
  Mitigation: Design constraints — half cone angle limits ($< 15°$), trajectory gate logic, and sensor fusion via Extended Kalman Filtering (EKF) ensure proper targeting and entry conditions.
- **Hazardous Event: Uncontrolled tumble**
  Mitigation: Hazard controls — incorporation of hardware redundancy, thermal and impulse margin sizing, and passive shielding to contain failure propagation.
- **Exposure Condition: Plume impingement risk**
  Mitigation: Procedure constraints of plume firing permitted only within thrust-safe corridors and aborted if delta-v or pointing constraints are violated.
- **Safety Consequence: Structural damage or collision**
  Mitigation: Warning devices such as GNC anomaly flags, angular velocity monitors, and sensor dropout detection systems provide early alerts for critical conditions.

- **Mission Consequence: Failed deorbit**
  Mitigation: Safing functions which are automatic routines that a spacecraft executes when a fault is detected, include automatic detumbling routines, back-off trajectories, and thrust disablement routines, restoring system safety and prevent damage escalation.
- **Environmental Consequence: Uncaptured debris**
  Mitigation: Final procedure constraints ensure that only properly aligned burns occur, avoiding plume release into unstable configurations.
- **End State: Mission failure**
  Mitigation: Escape logic including safe idle orbit repositioning, abort manoeuvres, and retry sequencing allow mission continuity under degraded conditions.

This structured logic is not limited to a single hazard. Similar chains are under development for other top-level risks identified in the Bow-Tie analysis, tailored to specific mission phases and subsystems, ensuring multi-layer protection throughout the mission.

In summary, safety in Starfixers is achieved through the integration of design-level protections, operational constraints, autonomous fallback mechanisms, and system-wide redundancy. RAMS methodologies allow the spacecraft to handle anomalies effectively, ensuring safe execution of the mission under uncertain and dynamic conditions.

14.2 Manufacturing, Assembly, and Integration Plan

The MAI Plan outlines the sequence of activities necessary to produce, assemble, and integrate the ADR satellite system. The ADR satellite features a combination of COTS components, such as the OBC, in-house manufactured components/subsystems, such as the Propulsion module and structural frame, and finally custom components that are still outsourced, like the FPGAs mentioned in chapter 10. Proper classification of those components, along with an explanation on the strategy of their procurement, is discussed in the next subsection. This is followed by an analysis of the assembly and integration phases (accompanied by a MAI Timeline Diagram). Finally, a note on the scalability of this production is made.

Component Classification & Procurement Strategy

As mentioned in the introduction of this chapter, proper categorisation of the satellite's components is necessary in order to streamline procurement and scheduling. There are three component classes considered: a) COTS Components, b) Outsourced Custom Components, and c) In-House Manufactured Components. The classification is shown below.

a) Commercial-Off-The-Shelf Components

The COTS components include most of the ADR satellite's components (around 70% of the total equipment). For brevity, a detailed list of those components will be omitted. However, referring back to Figure 10.2, which illustrates all on-board equipment, and then further to Figure 10.3, which shows the C&DH components, all equipment shown besides the subsystems' FPGAs, the Main and Adverse Thrusters, and the structure of the satellite's bus (excluding the solar panels), are considered COTS.

b) Outsourced Custom Components

Moving on to the outsourced custom parts, these include the following: subsystem FPGAs, fuel tanks, solar panels, and finally, the bus structure. As a note on the bus structure, the aluminium sheets that it will be made out of are going to be outsourced, but the assembly of the structure will be done in-house. The manufacturers for all of the outsourced components will be chosen in later design stages, and will be provided with all necessary documentation/specifications for the fabrication of said parts by the Starfixers Inc. group.

c) In-House Manufactured Components

Finally, the only in-house manufactured components of the ADR satellite are the two thrusters. As the design and specifications needed for those thrusters, derived from (sub)system and user requirements, are very intricate (for example, they need to have the same specific impulse, etc.), it was decided that the entire production process of the thrusters will be done in-house.

Assembly & Integration Phases

Once all required components are procured or manufactured, the assembly and integration of the satellite system begins. This process is broken down into distinct phases, some of which can be executed in parallel, while others depend on prior steps due to critical-path constraints. The activities are scheduled based on expected procurement/manufacturing times and subsystem interdependencies, and are illustrated in Figure 14.4 in the next subsection.

Component Testing & Verification Strategy

Prior to the commencement of subsystem assembly, all components undergo testing to ensure their operability and compliance with interfacing and environmental requirements. For COTS and outsourced custom components—such as FPGAs, fuel tanks, solar panels, and the aluminium structure sheets—basic functional and acceptance testing is carried out upon delivery. These components are assumed to have already undergone full V&V procedures by their respective suppliers.

The two in-house manufactured thrusters, however, are subject to a more rigorous V&V process executed by the Starfixers Inc. team. Given their critical role in the mission and their custom-built nature, this process includes detailed performance verification (e.g., specific impulse, thrust vector accuracy) and validation against system-level design requirements.

Following component-level testing, V&V continues at higher integration levels. Subsystem-level V&V takes place after individual subsystems are assembled and includes interface checks, functional testing, and thermal assessments. Finally, once all subsystems are integrated into the main structure, a full-system V&V campaign is executed, including end-to-end mission scenario testing. The timing and structure of this testing strategy are reflected in the MAI Timeline Diagram in Figure 14.4, with component testing scheduled to begin in **Month 2**.

MAI Timeline

The following timeline summarises the MAI activities leading to a flight-ready satellite. Tasks are grouped according to their potential for parallel execution and arranged to respect logical dependencies across subsystems.

- **Months 1–6: Procurement and Manufacturing Phase**
  All COTS components are ordered, and fabrication of in-house components (such as propulsion components and structural frame) begins in parallel. Furthermore, component testing takes place as soon as components are received at the assembly site.
- **Months 7–12: Subsystem Assembly & Validation Phase**
  Individual subsystems (e.g., TT&C, C&DH, ADCS, Propulsion, EPS) are assembled and verified independently. Subsystem-level V&V is performed in this window.
- **Months 13–17: Sub-Assembly Integration & V&V Phase**
  Sub-assemblies are built and thoroughly tested (V&V).
- **Months 18–21: Platform Integration Phase**
  All subsystems are mechanically and electrically integrated into the satellite bus. Cable harnessing, interface bonding, and structural mounting take place.
- **Months 22–24: Final System-level Validation Phase**
  The integrated satellite undergoes full-system V&V. This includes inter-subsystem communication checks, power routing verification, and environmental testing (thermal vacuum, vibration, etc.).

The above activities are depicted in Figure 14.4.

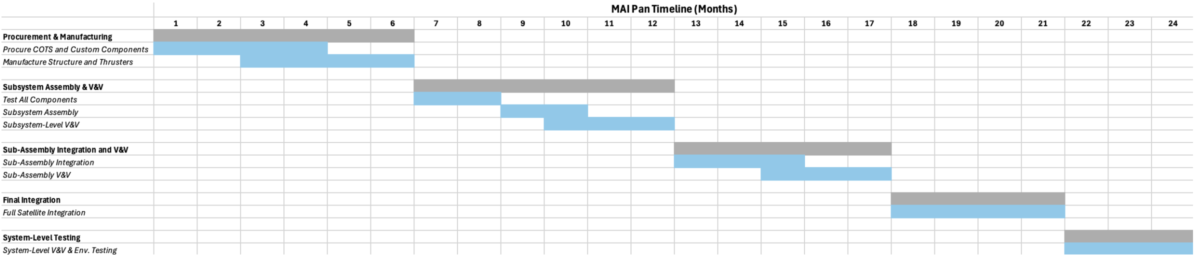

Figure 14.4: MAI Timeline.

As it can be seen, the Gantt chart begins with the procurement of the components. It has to be mentioned that the ordering of those components starts before month 1 in Figure 14.4, and after approval of the final design and specifications (i.e. ”mission is a go”). This is because the production and delivery time of the parts, dictated by the manufacturers but also influenced by new laws, changes in regulations, and the political situation at the country of assembly and integration, cannot be precisely determined. Therefore, the parts will be ordered as early as possible to prevent, or at least minimise the impact of, delays in the MAI process.

Note on Scalability

The MAI process described above is designed primarily for the production of one prototype, but it can be reasonably scaled up to a small series of satellites if required. To enable this, procurement timelines can be compressed by placing bulk orders in advance, specialised jigs and fixtures can be introduced to streamline in-house manufacturing, and a production line approach can be adopted to allow specialised teams to perform tasks in parallel. Furthermore, standardised components, well-documented procedures, and a modular architecture help shorten delivery timelines, simplify training of personnel, and maintain consistent quality across all units. Nevertheless, scaling must account for supplier capabilities, available facilities, and human resources to avoid constraints and ensure a smooth production flow.

Demonstration Mission

The CubeSat demonstration mission will be performed within the Testing & Validation segment of Figure 14.5, which begins in 2028. The demonstration is used as the final in-orbit operational test for the method. The cost of this demonstration is preliminarily estimated at 500 000 euros as the ADR CubeSat is required to have propulsion, ADCS, an infrared camera and a communication module, while the target CubeSat only needs a tracking module, making it very cheap[73]. The cost is included AIT & GSE budget shown in Figure 12.2b. In case the demonstration mission reveals design weaknesses, such as lower-than-expected momentum transfer efficiency, further modifications will be introduced to the thruster nozzle to reach the required efficiency. The main ADR spacecraft will not be assembled until the end of testing, allowing for structural modifications and additional fuel requirements that may be identified through the demonstration mission.

14.3 Post-DSE Gantt Chart

Following this final design report, some guidelines can be made for the future of the project. The timeline for tasks to be completed until launch and their interdependencies are shown below in Figure 14.5, this gives a general overview for which teams of specialised engineers shall create their own subtasks and project management tools to complete them.

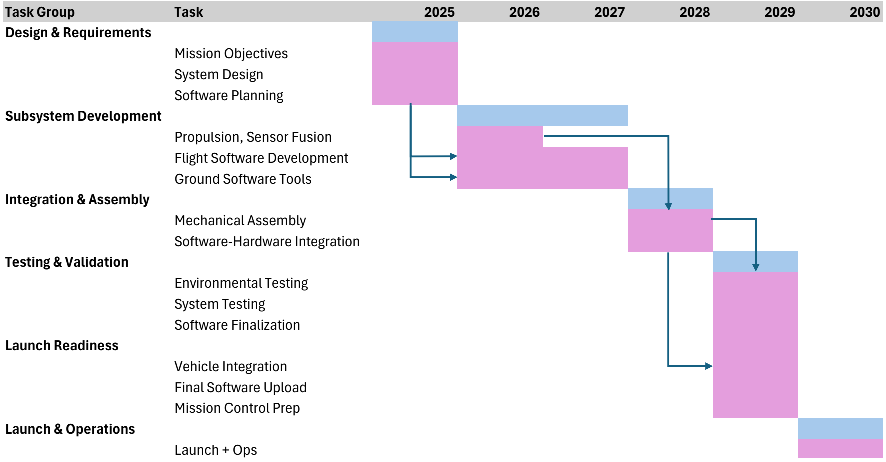

Figure 14.5: Post DSE Project Gantt Chart.

---

[73] `https://nanoavionics.com/blog/how-much-do-cubesats-and-smallsats-cost/`

14.4 Project Design and Development Logic

Figure 14.6 shows the project design and development logic diagram of the Starfixers satellite. It is divided into different phases, each with its sub-activities. The arrows depict a chronological order, where the MAI and V&V phases are run mostly in parallel.

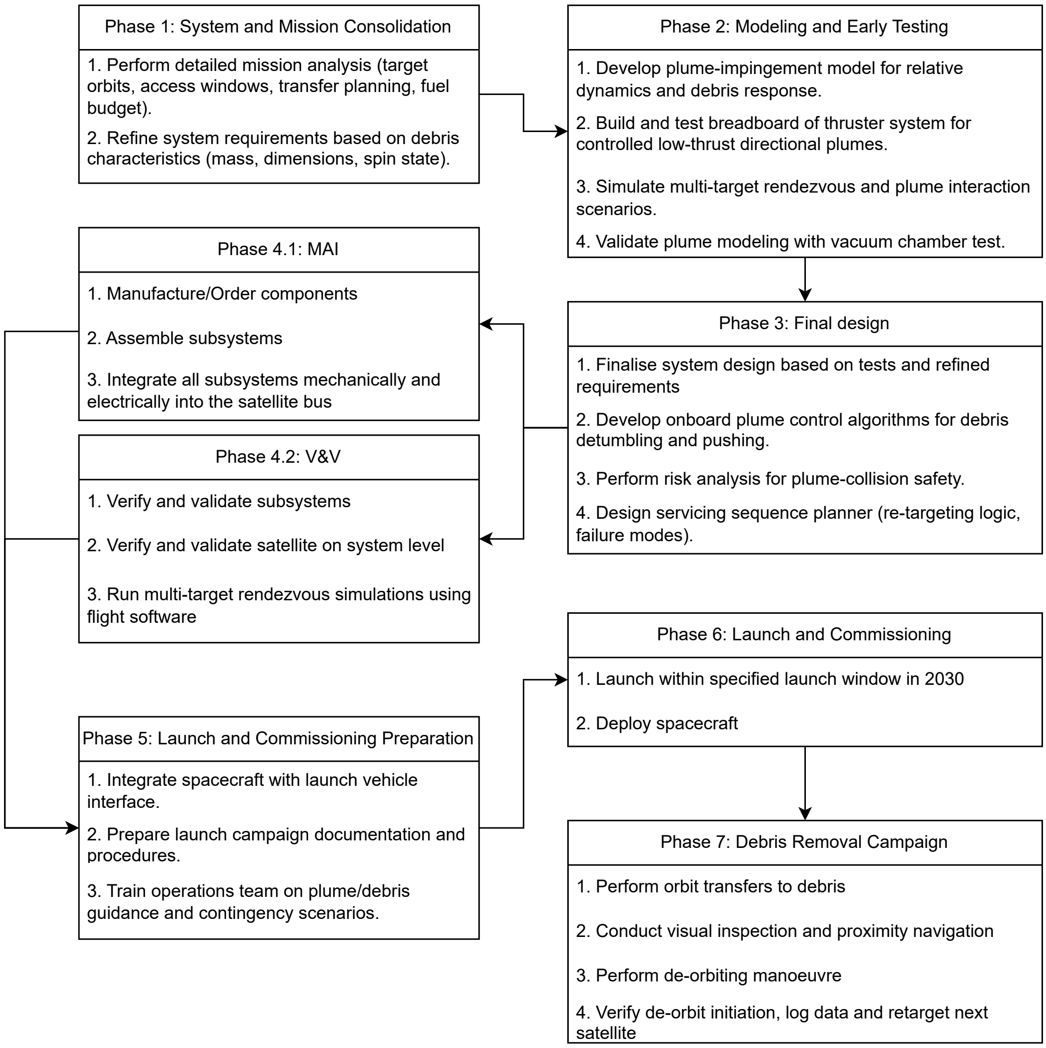

Phase 1: System and Mission Consolidation

1. Perform detailed mission analysis (target orbits, access windows, transfer planning, fuel budget).
2. Refine system requirements based on debris characteristics (mass, dimensions, spin state).

Phase 2: Modeling and Early Testing

1. Develop plume-impingement model for relative dynamics and debris response.
2. Build and test breadboard of thruster system for controlled low-thrust directional plumes.
3. Simulate multi-target rendezvous and plume interaction scenarios.
4. Validate plume modeling with vacuum chamber test.

Phase 3: Final design

1. Finalise system design based on tests and refined requirements
2. Develop onboard plume control algorithms for debris detumbling and pushing.
3. Perform risk analysis for plume-collision safety.
4. Design servicing sequence planner (re-targeting logic, failure modes).

Phase 4.1: MAI

1. Manufacture/Order components
2. Assemble subsystems
3. Integrate all subsystems mechanically and electrically into the satellite bus

Phase 4.2: V&V

1. Verify and validate subsystems
2. Verify and validate satellite on system level
3. Run multi-target rendezvous simulations using flight software

Phase 5: Launch and Commissioning Preparation

1. Integrate spacecraft with launch vehicle interface.
2. Prepare launch campaign documentation and procedures.
3. Train operations team on plume/debris guidance and contingency scenarios.

Phase 6: Launch and Commissioning

1. Launch within specified launch window in 2030
2. Deploy spacecraft

Phase 7: Debris Removal Campaign

1. Perform orbit transfers to debris
2. Conduct visual inspection and proximity navigation
3. Perform de-orbiting manoeuvre
4. Verify de-orbit initiation, log data and retarget next satellite

Figure 14.6: Project Design and Development Logic of Starfixers Satellite.

15 Conclusion

The rapid expansion of satellite constellations, such as Starlink and OneWeb, has transformed Low Earth Orbit (LEO) into a crowded and increasingly hazardous environment. The resulting rise in collision risk and accumulation of orbital debris poses a major challenge to the long-term sustainability of space operations. In response, Starfixers, Inc. has developed a mission concept for active debris removal (ADR), targeting multiple uncooperative objects in LEO with an efficient, scalable solution. The Project Objective Statement on which the development of the mission was based is as follows:

> Design an ADR mission to de-orbit at least 10 spacecraft from 550–630 km within one year, under a €100 million budget, by a team of 10 students working full-time for 10 weeks.

This objective was shaped by a combination of market conditions, regulatory trends, and sustainability goals to be used as design drivers for the whole design process. Additionally, an increasing global concern about orbital debris has led to more pressure on regulation updates for organisations such as ESA, NASA, and the U.S. Space Force to introduce stricter post-mission disposal requirements. Insurance providers are also demanding clearer end-of-life plans. While many of these guidelines are currently non-binding, they are already influencing national regulations and shifting industry norms.

In this context, market forecasts project significant growth for the ADR sector, with estimates rising from €1.13 billion in 2023 to €4.76 billion by 2032 [94]. Investments from government agencies and commercial players signal a strong interest in early solutions. Starfixers Inc.'s approach, which targets uncooperative debris using a flexible, easily adaptable spacecraft, positions it to secure a share of the growing market. Based on this, Starfixers decided that the business model would be centred on offering de-orbiting services to satellite operators, space agencies, and commercial stakeholders who seek reliable, cost-effective solutions for end-of-life satellite disposal. Rather than selling the hardware, we intend to be hired to provide such a service on a per-mission or subscription basis in a sustainable and scalable way.

The design option chosen to carry out the de-orbiting service is gas shepherding: a novel technique in which the spacecraft's thruster plume is used to slow down debris into lower, denser atmospheric layers where they would passively de-orbit, avoiding physical contact. This method eliminates the need for complex mechanical systems, such as nets or robotic arms, reducing risk, mass, and operational complexity. By transferring momentum through repeated plume interactions, the spacecraft enables debris to decay naturally due to atmospheric drag.

Despite also investigating an optimisation on any possible debris' characteristics combination within the given user requirements, and offering a high adaptability for any combination of such, this report mainly focuses on the design of a spacecraft aiming to de-orbit 10 Starlink V1 satellites, with 260kg of mass, 19.5577m^2 average area, and orbiting Earth at an altitude of 600km with 53deg inclination. This specific combination led to the following results displayed in Table 15.1:

Table 15.1: Summary of Starfixer mission.

M_{dry}	M_{wet}	rdv per debris	Total mission rdv	Operational time	Mission time
264 kg	646 kg	14 - 17	153	37.4 days	10.4 months

These results are achieved by performing a complex operational sequence consisting of selecting the proper target and performing repeated rendezvous with the same debris at the correct relative velocity until moved to an orbit where it passively de-orbits within 9 months. Between each of these rendezvous, a time and fuel-optimal orbit combination is used to meet again with the same debris with the correct velocity. After de-orbiting each debris, a transfer manoeuvre is carried out to bring the ADR to the orbit of the next debris and the operation is repeated.

The design of the spacecraft was driven to a great extent by sustainability and market demands. The choice of the gas shepherding option was strongly influenced by the aim of not creating any additional debris, having a reliable spacecraft and de-orbiting operation, as well as being cost-effective. After scoring well in each of these categories, the operational procedure was established. To do so, an optimisation was carried out to choose the solution minimising fuel mass, while satisfying all of the defined safety features, including a minimum allowed approach distance to the debris of 3m, as well as a maximum allowed relative velocity of 8m/s at 9m distance when performing rendezvous. This ensured that the final design of the ADR had the minimum possible mass, resulting in the lowest possible launch cost. This is of great importance to the proper scalability of Starfixers Inc. in the ADR market. Additionally, the safety measures will greatly increase the sustainability of the whole mission. This was also enhanced with the implementation of the developed risk mitigation strategies.

The design of the spacecraft subsystem was also driven by cost-efficiency and sustainability. In addition to minimising cost and environmental impact, each subsystem prioritises redundancy to ensure mission reliability, as well as high precision and coordination with other subsystems.

The Command and Data Handling (C&DH) subsystem is essential to the mission's operations, particularly from the systems engineering standpoint. It acts as the centre of integration, tying together different subsystems through command execution, data flow management, and platform-wide response coordination. This integration guarantees that subsystems such as propulsion, power, and communication work together and in unison with mission goals. C&DH acts as the central nervous system of the spacecraft, facilitating problem detection, real-time decision-making, and system-level autonomy, which are all crucial for successful ADR execution.

The Guidance, Navigation, and Control (GN&C) system features GNSS receivers, LiDAR units, and infrared cameras, allowing for high-precision tracking and safe rendezvous operations. Redundancy is provided through the Attitude Determination and Control Subsystem, which includes star trackers, inertial sensors, reaction wheels, and cold gas thrusters to maintain or alter orientation.

Propulsion is delivered by a 465N bi-propellant thruster using non-toxic fuels: hydrogen peroxide and kerosene. The thruster's narrow exhaust cone is optimised for efficient plume contact. A smaller adverse thruster, at the opposite face of the main thruster, enables precise control of relative velocity, improving the accuracy and repeatability of each momentum transfer.

Power is generated by twin solar arrays and supported by a lithium-ion battery pack for eclipse periods. The Electrical Power Subsystem includes a power regulation unit and a maximum power point tracker to maintain energy balance throughout the mission. Thermal control is achieved passively using reflective coatings and insulation, keeping all components within operational temperature limits. The spacecraft structure, built from a lightweight aluminium alloy, also serves as a load-bearing frame that houses fuel tanks and critical subsystems. Figure 15.1 presents the structural layout of the Starfixer spacecraft.

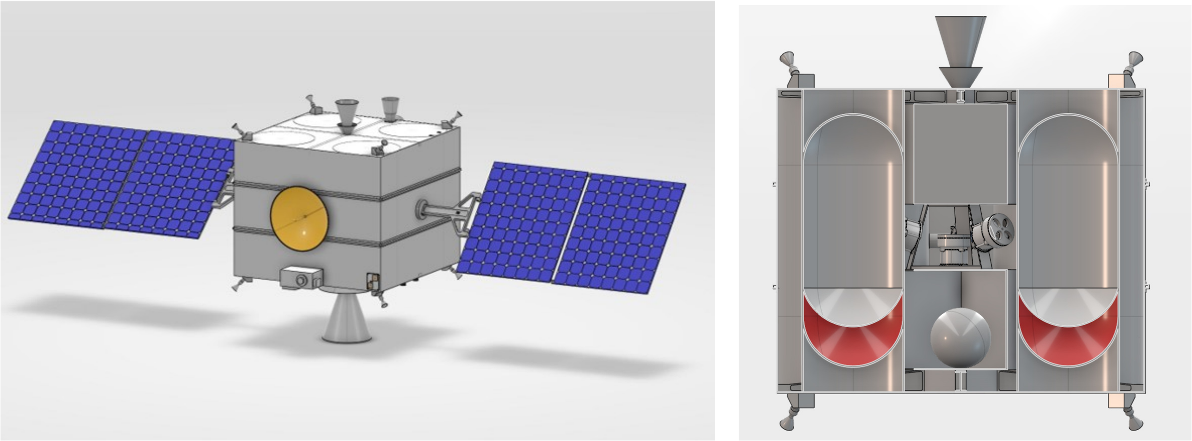

(a) 3D Render of the Starfixer Spacecraft.

(b) Cross Section of the Starfixer Spacecraft.

Figure 15.1: Structural Layout.

To ensure the robustness of the mission, a detailed risk assessment was conducted. This process informed key design and operational decisions. A comprehensive RAMS (Reliability, Availability, Maintainability, and Safety) analysis concluded with an overall spacecraft reliability of 90%, reflecting a balanced approach to technical performance and mission resilience.

Verification and validation activities were planned in a rigorous requirements matrix and were also performed for the model developed. This ensures that each mission requirement is clearly linked to a method of verification, whether through analysis, testing, demonstration, or inspection, ensuring that all safety and operational standards are satisfied prior to deployment. Moreover, a sensitivity analysis was conducted to estimate how changes in the user requirements could affect the final results.

The mission underwent a Space Sustainability Rating (SSR) assessment, achieving a Platinum rating with an additional Gold star for innovation. These results reflect both the responsible mission design and the spacecraft's potential to support long-term orbital sustainability.

Cost analysis placed the total budget at €100 million, including a €15 million contingency. The spacecraft's design focuses on simplicity and high adaptability, enabling future units to be manufactured at an estimated €6 million each. A market-aligned pricing strategy sets the commercial rate at €7.2 million per debris removal, supporting long-term financial viability.

A development roadmap has been established to target a 2030 launch. This includes refinement of subsystems, component procurement, integration, testing, and final launch preparations. Risk mitigation and verification activities are embedded throughout the schedule to maintain technical readiness and ensure design maturity.

In conclusion, Starfixers' mission presents a sustainable, reliable, and commercially relevant approach to active debris removal. Its use of gas shepherding provides a streamlined alternative to traditional capture methods, offering simplicity, adaptability, and cost-efficiency. While challenges remain, particularly in regulation, funding, and market adoption, the mission lays a strong foundation for future ADR missions.

To build on the gas shepherding method and further improve the design, some recommendations are proposed. Firstly, there is very little research in the field of applying gas plumes for momentum transfer in space. To improve the reliability of the gas shepherding efficiency as a function of distance, a model should be made that makes use of computational fluid dynamics in a vacuum environment. This model should have the option of applying different plume half-cone angles, exhaust velocities, distances up to 15 m to the debris and shapes of the debris. Secondly, it is recommended to update the knowledge of the proposed thruster's properties. The Padova University's thruster has limited public information, and new developments are crucial for an accurate indication of the thruster's de-orbiting use. Thirdly, physical experiments can be performed with the proposed thruster on surrogate test models of Starlink's V1 satellite. These should be performed in a vacuum chamber, if possible, at a distance of 2m to test whether Starfixer's proposed method does not cause additional debris by damaging the target. Additionally, the functioning of the LiDAR should be tested in a 0.5m vicinity of an active 465N thruster. The radiation of the active thruster potentially has a negative influence on the LiDAR's accuracy and functioning. Regarding the survival of Starfixer's structure and critical loads during launch, a full finite element method (FEM) analysis has to be performed. Lastly, the model of orbital mechanics, used for rendezvous calculations, should be improved by implementing additional effects such as J2, solar pressure, etc.

Together, these next steps will help transition Starfixers from a promising concept to a deployable mission, contributing meaningfully to the future of sustainable space operations.

References

[1] 3D PLUS. *Radiation Tolerant NAND Flash Memory*. Accessed: 2025-06-17. 2022.

[2] 3D PLUS. *Radiation Tolerant SRAM*. Accessed: 2025-06-17. 2022.

[3] I.M. Abdalugatov and N.D. Azizov. ‘‘Density of rocket propellant (RP-1 fuel) at high temperatures and high pressures’’. In: *ESA* 89 (July 2010).

[4] Mahmoud R. Abusrea et al. ‘‘Bending strength of CFRP laminated adhesive joints fabricated by vacuum-assisted resin transfer molding’’. In: *Composites Part B: Engineering* 156 (2019), pp. 8–16. ISSN: 1359-8368. DOI: `https://doi.org/10.1016/j.compositesb.2018.08.041`.

[5] European Space Agency. *ESA'S ANNUAL SPACE ENVIRONMENT REPORT*. 2025.

[6] European Space Agency. *GRAVES Radar System*. Details on European radar detection capabilities. 2021.

[7] AgilSpace. *OBC-15 Onboard Computer*. Accessed: 2025-06-17. 2023.

[8] AgilSpace and MCSE. *OBC-15 and MCSE Onboard Systems Specifications*. Accessed June 2025. 2022.

[9] C. Bombardelli et al. ‘‘Ariadna Call for Ideas: Active Removal of Space Debris Ion Beam Shepherd for Contactless Debris Removal’’. In: *ESA* (2011).

[10] Hansjörg Dittus et al. ‘‘Attitude and Orbit Control of the BIROS Satellite using Cold Gas Propulsion’’. In: *Small Satellite Conference*. Accessed June 2025. 2017.

[11] M. Santi et al. ‘‘Design and Testing of a Hydrogen Peroxide Bipropellant Thruster’’. In: *Aerospace Research Central* (2020). DOI: `10.2514/6.2020-3827`.

[12] T. Peters et al. ‘‘SPACE DEBRIS ORBIT MODIFICATION USING CHEMICAL PROPULSION SHEPHERDING’’. In: 6 (1 2013). 6th European Conference on Space Debris.

[13] W. Mijnendonckx et al. ‘‘Baseline Report’’. DSE.

[14] W. Mijnendonckx et al. ‘‘Midterm Report’’. DSE.

[15] B.J. Anderson. ‘‘Guidelines for the Selection of Near-Earth Thermal Environment Parameters for Spacecraft Design’’. In: (Oct. 2001).

[16] K. Anderson-Wedge et al. ‘‘Characterization of the evolution of 2219-T87 aluminum as a function of the friction stir welding process’’. In: *International Journal of Fatigue* 142 (2021), p. 105954. ISSN: 0142-1123. DOI: `https://doi.org/10.1016/j.ijfatigue.2020.105954`.

[17] Luciano Anselmo. *Evolution of the Space Debris environment*. 2001. (Visited on 10/01/2001).

[18] Adam Archuleta and Michael Nicolls. ‘‘Space Debris Mapping Services for Use by LEO Satellite Operators’’. In: *Proceedings of the Advanced Maui Optical and Space Surveillance Technologies Conference (AMOS)*. Accessed June 11, 2025. AMOS. 2018.

[19] J.A. Ávila-Rodríguez. *Galileo Signal Plan*. Last accessed: 2025-06-11. Navipedia – ESA. 2011.

[20] F. Barato et al. ‘‘Update on green chemical propulsion activities and achievements by the University of Padua and its spin-off T4I’’. In: *Aeronautics and Astronautics* (2023). DOI: `10.21741/9781644902813-140`.

[21] L. Boldt-Christmas. *Low Earth Orbit*.

[22] NASA Ames Research Center. *Fault Detection, Isolation, and Recovery (FDIR) for SmallSats*. Accessed June 2025. 2020.

[23] Sierra Nevada Corporation. *EH25 Bi-axis Gimbal*. Last accessed: 2025-06-18. 2011.

[24] CubeSpace. *Aquila-H01 Sun Sensor Datasheet*. CubeSat-compatible sun sensor technical specifications. 2021.

[25] S. D'Amico and O. Montenbruck. ''Proximity operations of formation-flying spacecraft using an eccentricity/inclination vector separation''. In: *The Journal of the Astronautical Sciences* 56.3 (2008), pp. 349–371. DOI: `10.1007/s40295-008-0034-5`.

[26] Safran Electronics & Defense. *STIM318 Tactical Grade IMU*. Tactical grade MEMS IMU datasheet. 2020.

[27] TU Delft. *Spacecraft Design*. 2013.

[28] eSpace EPFL. *Space Sustainability Rating*. Accessed: 2025-06-11. 2023.

[29] ESA. *ESA'S ANNUAL SPACE ENVIRONMENT REPORT*. 2025. (Visited on 03/31/2025).

[30] ESA. *Objects*. Online; accessed 2025-06-03. 2025.

[31] ESA. *Propulsion Subsystem Design Handbook*. TEC-MCS/2008/130, European Space Agency. 2008.

[32] ESA. *Update of the ESA Space Debris Mitigation Handbook*. 2002. (Visited on 07/02/2002).

[33] eSpace. *Space Sustainability Rating (SSR)*. Accessed: 2025-06-11. 2023.

[34] European Space Agency. *ESA Redu Centre*. Accessed: 2025-06-06. 2023.

[35] European Space Agency. *ESA's Annual Space Environment Report*. Technical Report GEN-DB-LOG-00288-OPS-SD. Darmstadt, Germany: European Space Agency, 2023.

[36] European Space Agency. *ESA's Annual Space Environment Report*. Technical Report GEN-DB-ENV-REP-2024. Darmstadt, Germany: European Space Agency, 2024.

[37] European Space Agency. *Estrack - ESA's Global Ground Station Network*. Accessed: 2025-06-06. 2023.

[38] European Space Agency. *Upgrade of DRAMA's Spacecraft Entry Survival Analysis Codes*. ESA. Accessed May 2025. 2019.

[39] European Space Agency (ESA). *ESA Report on the Space Economy 2024*. Tech. rep. Accessed: 2025-06-16. European Space Agency, 2024.

[40] Tzu-Wei Fang. *Space Weather Environment During the SpaceX Starlink Satellite Loss in February 2022*. 2022. (Visited on 11/02/2022).

[41] J. Garcia-Rodriguez, M. Rybak, and M. Fernandez. ''Reliability and Lessons Learned from CubeSat Missions''. In: *Proceedings of the 4S Symposium (Small Satellites Systems and Services)*. Accessed June 2025. ESA. 2020.

[42] German Aerospace Center (DLR). *Weilheim Ground Station*. Accessed: 2025-06-06. 2023.

[43] Jena Optronik GmbH. *RVS3000-3D Lidar for Non-Cooperative Rendezvous*. Technical Product Datasheet. 2020.

[44] NASA Goddard. *Multi-Layer Insulation (MLI) Handbook*. Accessed: 2025-06-17. 2021.

[45] D.M. Goebel and I. Katz. ''Fundamentals of Electric Propulsion: Ion and Hall Thrusters''. In: *JPL SPACE SCIENCE AND TECHNOLOGY SERIES* (Mar. 2008). p. 403.

[46] GomSpace. *Solar Panel Substrate Technical Overview*. Accessed: 2025-06-17. 2023.

[47] Christian A. Gueymard. ‘‘A reevaluation of the solar constant based on a 42-year total solar irradiance time series and a reconciliation of spaceborne observations’’. In: *Solar Energy* 168 (July 2018), pp. 2–9. ISSN: 0038092X. DOI: `10.1016/j.solener.2018.04.001`.

[48] Ir. R.J. Hamann and dr. ir. M.J.L. van Tooren. *Systems Engineering & Technical Management Techniques, Part 1*. 2th ed. Delft University of Technology, Faculty of Aerospace Engineering, 2006.

[49] ESA Handbook. *Spacecraft Harness Design and Guidelines*. Accessed: 2025-06-17. 2021.

[50] John H. Henninger. *Solar Absorptance and Thermal Emittance of Some Common Spacecraft Thermal Control Coatings*. Reference Publication GEN-DB-ENV-REP-2024. Maryland: NASA, 1984.

[51] Siamek Hesar. ‘‘Growing risks in low Earth orbit demand more responsible space behavior’’. In: *SpaceNews* ().

[52] B. Hoffmann and A. Zinecker. *USING THERMAL DESKTOP TO MODEL THE EFFECTS OF PLUME HEATING ON MLI*. Technical Report TFAWS 2023. Houston: NASA, 2023.

[53] Moog Inc. *Moog 58E163A Cold Gas Thruster*. Technical datasheet and space heritage. 2020.

[54] Moog Inc. *Moog Cold Gas Thrusters Technical Sheet*. Accessed June 2025. 2021.

[55] Sinclair Interplanetary. *Libra-6 Reaction Wheel*. Product datasheet and reliability specifications. 2019.

[56] ISISPACE. *PCU-110 Power Control Unit*. Accessed: 2025-06-17. 2023.

[57] ISISpace. *ISIS Antennas and Communication Subsystems*. `https://www.isispace.nl/product/s-band-telemetry-transmitter/`. Accessed: 2025-06-17. 2020.

[58] ISISpace. *ISIS GNSS Patch Antenna*. Component datasheet and CubeSat integration info. 2020.

[59] J. J. Puschell et al. J. R. Wertz D. F. Everett. *Space Mission Engineering: The New SMAD*. Vol. 28. Microcosm Press, 2011.

[60] Siegfried W Janson. *Brane Craft (A 2016-2017 NIAC Phase I Project)*. Tech. rep. 2016.

[61] Japan Aerospace Exploration Agency. *JAXA Ground Stations*. Accessed: 2025-06-06. 2023.

[62] T.S. Kelso. *Satellite Tracking and Radar Detection Capabilities*. Includes data on radar cross-section detection limits in LEO. 2020.

[63] Huong G. Le and Dudley L. O’Brien. *Process for Producing a High Emittance Coating and Resulting Article*. Technical Article 5,217,600. California: NASA, 1992.

[64] Francesca Letizia, Davide Izzo, and Alberto Rossi. ‘‘Extending the ECOB Space Debris Index with Likelihood and End–of–Life Scenarios’’. In: *Proceedings of the 7th European Conference on Space Debris*. Ed. by T. Flohrer and F. Schmitz. ESA Space Debris Office. Paper 417. ESA. Darmstadt, Germany, Apr. 18, 2017, pp. 400–428.

[65] J.-C. Liou. ‘‘An active debris removal parametric study for LEO environment remediation’’. In: *Advances in Space Research* 47.11 (2011), pp. 1865–1876. ISSN: 0273-1177. DOI: `https://doi.org/10.1016/j.asr.2011.02.003`. URL: `https://www.sciencedirect.com/science/article/pii/S0273117711000974`.

[66] Jericho Locke et al. *Cost and Benefit Analysis of Mitigating, Tracking, and Remediating Orbital Debris*. Technical Report NASA/TP-20240003484. Washington, DC: NASA Office of Technology, Policy, and Strategy, 2024.

[67] A. Ruggiero M. Andrenucci P. Pergola. *Active Removal of Space Debris: Expanding foam applications for active debris removal*. Tech. rep. ESA, 2011.

[68] Gérard Maral and Michel Bousquet. *Satellite Communications Systems*. 6th ed. Wiley, 2020.

[69] MCSE. *MCSE Spacecraft Monitoring Electronics*. Accessed: 2025-06-17. 2021.

[70] MOOG. *Electric Propulsion Gimbal Thruster Assembly*. Last accessed: 2025-06-18. 2025.

[71] NASA. *Deep Space Network (DSN)*. Accessed: 2025-06-06. 2023.

[72] NASA. *Reliability Design and Cost Handbook*. NASA-HDBK-217. 1991.

[73] NASA Orbital Debris Program Office. ‘‘Orbital Debris Quarterly News, Volume 22, Issue 3’’. In: *Orbital Debris Quarterly News* 22.3 (July 2018).

[74] NASA Orbital Debris Program Office. ‘‘Orbital Debris Quarterly News, Volume 29, Issue 1’’. In: *Orbital Debris Quarterly News* 29.1 (Jan. 2025).

[75] Organisation for Economic Co-operation and Development (OECD). *Space Economy Investment Trends*. Tech. rep. Accessed: 2025-06-16. OECD Publishing, 2024.

[76] United Nations Office for Outer Space Affairs. *GUIDELINES FOR THE LONG-TERM SUSTAINABILITY OF OUTER SPACE ACTIVITIES OF THE COMMITTEE ON THE PEACEFUL USES OF OUTER SPACE*. 2021.

[77] Panasonic. *Li-ion 18500 Battery Cell Specifications*. Accessed: 2025-06-17. 2022.

[78] 3D PLUS. *3D PLUS 8GB NAND Flash 16MB SRAM Space-Qualified Memory*. Accessed June 2025. 2022.

[79] Timothy Pratt, Charles W. Bostian, and Jeremy E. Allnutt. *Satellite Communications*. 2nd ed. Wiley, 2003.

[80] Matt Pyrak and Joseph Anderson. ‘‘Performance of Northrop Grumman’s Mission Extension Vehicle (MEV) RPO imagers at GEO’’. In: *Autonomous Systems: Sensors, Processing and Security for Ground, Air, Sea and Space Vehicles and Infrastructure 2022*. Ed. by Michael C. Dudzik, Stephen M. Jameson, and Theresa J. Axenson. Vol. 12115. International Society for Optics and Photonics. SPIE, 2022, 121150A. DOI: `10.1117/12.2631524`.

[81] Aerojet Rocketdyne. *Aerospace Propulsion Components: Isolation and Flow Control Valves*. Component datasheets and product catalog. 2020.

[82] Leonardo S.p.A. *ECAM-IR3A: Compact Thermal Infrared Camera*. Technical specifications and product use cases. 2019.

[83] Sodern. *ST16-RT2 Star Tracker*. Product reliability and space mission data. 2021.

[84] QJ Solar. *QJ 4G32C Triple-Junction Solar Cell Datasheet*. Accessed: 2025-06-17. 2022.

[85] South African National Space Agency (SANSA). *Hartebeesthoek Ground Station*. Accessed: 2025-06-06. 2023.

[86] AAC Clyde Space. *Clyde Space Electrical Power Systems Overview*. Accessed June 2025. 2020.

[87] Clyde Space. *CubeSat Structure Data Sheet*. Accessed: 2025-06-17. 2023.

[88] Consultative Committee for Space Data Systems (CCSDS). *Image Data Compression*. CCSDS 122.0-B-1, Blue Book, Issue 1. 2005.

[89] Space Exploration Technologies Corp. *SpaceX Gen 1 Semi-Annual Report: December 1, 2023 – May 31, 2024*. July 2024.

[90] SpacePNT. *NaviLEO POD GNSS Receiver for Small Satellites*. Product documentation and reliability data. 2021.

[91] SpaceX. *Falcon Payload User’s Guide*. 2025.

[92] Spectrolab. *Space Solar Panels*. Accessed: 2025-06-10. 2010.

[93] Richard Speed. *Space insurers make record-breaking loss as orbit gets cramped*. Accessed: 2025-06-24. URL: `https://www.theregister.com/2024/05/01/space_insurer_record_loss/?utm_source=chatgpt.com`.

[94] Future Data Stats. *Space Debris Removal Market Size, Share, Trends Competitive Analysis By Type: Contact Debris Removl, Contactless Debris Removal By Orbit: By Solution: Robotic Arms, Harpoons, Nets, Lasers, Tethers, Ion Beams By End-User: Government Military, Commercial By Service: By Regions, and Industry Forecast, Global Report 2025-2033*. 2025.

[95] S. Surawdhaniwar and R. Diwan. ‘‘Study of Maximum Power Point Tracking Using Perturb and Observe Method’’. In: *Orbital Debris Quarterly News* 1.5 (July 2012).

[96] Swedish Space Corporation. *Esrange Space Center*. Accessed: 2025-06-06. 2023.

[97] G. Wusk T.J. Colvin J. Karcz. *Cost and Benefit Analysis of Orbital Debris Remediation*. Tech. rep. NASA, 2023.

[98] W.H. Tam. *CONCEPTUAL DESIGN OF SPACE EFFICIENT TANKS*. Tech. rep. ATK Space Systems, Inc., July 2006.

[99] Heidi Thelander. *Design and Implementation of TT&C Systems for SmallSats*. Accessed June 2025. 2018.

[100] J. Tuttle et al. *Thermal Properties of Double-Aluminized Kapton at Low Temperatures*. Tech. rep. 20080045503. Technical Report. Maryland, USA: NASA, 2007.

[101] James R. Wertz, David F. Everett, and Jeffery J. Puschell. *Space Mission Engineering: The New SMAD*. Microcosm Press, 2011.